PROCEEDINGS OF 2nd INTERNATIONAL CONFERENCE ON ADVANCED MATERIALS AND PROCESS ENGINEERING (AMPE)

12 & 13 DECEMBER

Editors: Dr. Muhammad. Sohail, Dr. Rafiq Ahmed, Dr. Zahoor Awan

ORGANIZED BY

FACULTY OF CHEMICAL AND PROCESS ENGINEERING

NED UNIVERSITY OF ENGINEERING & TECHNOLOGY,

KARACHI PAKISTAN

PRO-VICE CHANCELLOR'S MESSAGE

It is indeed a matter of honor and great pleasure for me to write a message for the 2nd International Conference on Advanced Materials and Process Engineering (AMPE-2017). In industrially developed nation, a university's role in multidisciplinary research is a well established fact. Every research conducted pushes the boundaries of knowledge and contributes to the progress of nation. Dissemination of this knowledge is of prime importance. Conferences are generally an essential part of academic discourse. It is a platform which facilitates discussion on new knowledge and its dissemination. It is also my great pleasure to welcome researchers from all over Pakistan, Australia, England, Malaysia and South Korea.

The successful organization of conference requires the talents, dedication and time of many volunteers and strong support from sponsors. I am confident that the faculty of Chemical & Process Engineering would hold this conference to the expectations of the world academic community. I would like to express my thanks to all authors for their outstanding contributions and in particular the members of the program board for their competent evaluation of the large number of submissions. Likewise I would also like to express my appreciation to the program committee, as well as to the invited chairs for their careful preparation of the invited sessions.

I extend my congratulations to the organizers of the conference & wish them all success.

Prof. Dr. M. Tufail
Pro Vice Chancellor
NED University of Engineering
& Technology,
Karachi

Proceedings of the 2nd International Conference on Advanced Materials and Process Engineering

Table of Contents

Behavioural Analysis and Arx Model Identification of Distillation Column

S. A. Taqvi[1,2], F. Uddin[1,2,*], A. A. Hashmi[1], Y. Aslam[1], M. Owais[1] and M. Mustafa[1]

[1]Chemical Engineering Department, NED University of Engineering & Technology, Karachi, Pakistan

[2] Chemical Engineering Department, Universiti Teknologi PETRONAS, 32610 Bandar Seri Iskandar, Perak Darul Ridzuan, Malaysia

[*]Corresponding author. Tel.: +92-21-99261261-8 Ext: 2286; fax: +92-21-99261255*E-mail address*: fahimuddin@neduet.edu.pk (F. Uddin)

ABSTRACT

System identification is a technique to build an accurate model of system behaviour in order to represent the input-output relationship. It can be applied in various fields of applications. This study is basically focused on the system identification of a pilot scale of Acetone–Isopropyl alcohol distillation column by relating the control variables (top and bottom compositions) with the manipulated variables (reflux and reboiler steam flow rates). System identification is carried out using MATLAB® System Identification Toolbox to develop linear low-order model. Model validation has been done to compare performance between the mathematical models with the actual plant. The identified model can be further used in the advanced process control applications to improve the performance of the process control in the system.

***Keywords*:** System identification; Distillation; Dynamic Behaviour; Model; MATLAB

1. INTRODUCTION:

System identification deals with many restraints during designing, conducting and interpreting the results from identification experiments. In other words, system identification could be described as to design, conduct, process and interpret the results from the experiment applied to the system to get an accurate model of its dynamic behaviour [1-3]. The purpose of this system identification is to derive models from available input and output data of the system. System identification includes dealing with various tasks of parameter estimation based on the observations originating from a dynamic system [4]. It is also used to determine the dynamic behaviour of physical object or process based on the mathematical relations between the inputs and outputs [1,2].

The techniques for system identification can be applied in various system and applications. For example, in industrial plants the feed stocks undergo various complicated processes in order to produce the desired yield. This internal mechanism of the industrial plant processes is focused on the detail. System identification could be applied in this condition as it will make simpler model by relating the input and output which is easier and can be directly tuned based on our needs. This also allows for better adjustments and handling of unforeseen disturbances [3].

System identification is one of the modelling method which deals with problem on how to estimate the model of a system from a measured input and output signals. The system can be described as linear or non-linear depending on the estimation of the model itself and the type of system used in the process [2].

System identification could be beneficial in many ranges of fields and mechanisms in life. It could be used in various applications such as petrochemical plant, multimedia system, signal system and even human body system [1].

Distillation is a physical separation process commonly used for purifying liquids and separating mixtures of liquids into their individual components. Most of the process industries use distillation column for the separation operation. In this study, acetone and isopropyl alcohol are to be separated in a fractionation column operating at certain pressure [5-10]. The model structure and constituent variables are similar to those used by the conventional Wood and Berry model, and the model parameters such as steady-state gains, time constants and lags are determined. Model validation is carried out in order to demonstrate the accuracy of the identified model.

2. PROCESS DESCRIPTION:

A fully instrumented distillation column is used to separate a binary mixture of Acetone and IPA (Isopropyl Alcohol). Firstly a steady state simulation is developed in Aspen Plus® using RADFRAC column as shown in Figure 1. CHAO-SEA has been selected as the thermodynamic property package. The column specifications and feed conditions are used as presented in Table 1 and Table 2.

Table 1: Column Specification

Parameter	Value
Internal Diameter (m)	5.5
Height of the Column (m)	0.15
Type of tray	Bubble Cap Tray
Number of trays	15
Tray Spacing (cm)	35
Feed Stage	Variable
Condenser Type & Area (m^2)	Plate type, 1.2
Reboiler Type & Area (m^2)	Kettle type, 0.6
Reflux Drum (m)	0.25(D) x 0.6(H)

Later on the designed column is converted to dynamic state using Aspen Plus Dynamics® so that the dynamic behaviour of the system can be observed and mapped using continuous and discrete linear models via MATLAB. The controllers fixed in the designed distillation were:

1. Flow Controller (FC): It controls the flow from inlet stream by manipulating the valve.
2. Pressure Controller (PC): It maintains the column pressure by regulating the condenser duty.
3. Composition Controller (CC*_TOP): It controls the purity of acetone by manipulating the reflux flow.
4. Composition Controller (CC*_BOTTOM): It controls the purity of IPA by manipulating the reboiler duty.
5. Level Controller (LC_TOP): It controls the level of distillate.
6. Level Controller (LC_ BOTTOM): It controls the level of bottom product.

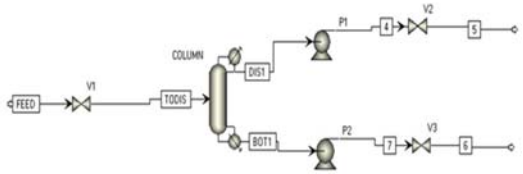

Figure 1: Steady-state Simulation of Distillation Column

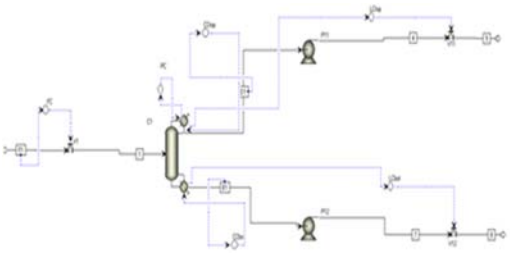

Figure 1: Dynamic Simulation of Distillation Column

Table 2: Feed Conditions and Utilities Specifications

Parameter	Value
Temperature (C)	30.0
Pressure (kPa)	105.6
Molar Flow (kmole/h)	3600.0
IPA mole fraction	0.4
Acetone mole fraction	0.6
Reflux Ratio (molar)	3.0
Distillate Rate (kmole/hr)	1080
Condenser Pressure (kpa)	101.3
Reboiler Pressure (kpa)	105.7

3. Identification Experiment

Simple step increments and decrements are used for the identification of the system. This is because it has been the preferred method of the practitioners due to its simplicity and ease of the understanding. Step changes of 5% and 10% in the reflux and reboiler duty were introduced to the system.

3. Model Developed from MATLAB

Using the responses of the purity of Acetone and IPA obtained from the identification experiments, the models were developed using the System Identification Toolbox in MATLAB® and were recorded. Hence, there are run for each purity of top and bottom composition respectively. The Autoregressive Exogenous (ARX) model was identified with an order of [2,2,1] i.e. [2×ones(2,2), 2×ones(2,2), ones(2,2)].

The identified model was validated with a different experimental data and was found to fit it accurately.

5. RESULTS

The steady state Aspen Plus® model determines the initial state of the system. It presents the vapour-liquid equilibrium and the degree of separation obtained by the system. The pressure and composition profiles of the system at the steady state are presented in Figure 3.

The dynamic model of the system successfully presents the transient behaviour of the system, which is crucial for the identification of the system. The input perturbations and the output responses can be observed in Figure 4.

As a result, the system behaviour was used to obtain ARX models, and the Equations representing the model are:

Model for output y_1:

$$A_{(z)}y_{1(t)} = -A_{i(z)}y_{i(t)} + B_{(z)}u_{(t)} + e_{1(t)} \quad (1)$$

Where,

$$A_{(z)} = 1 - 1.90z^{-1} + 0.90z^{-2}$$

$$A_{i(z)} = -7.94 \times 10^{-6}\, z^{-1} + 5.85 \times 10^{-5}\, z^{-2}$$

$$B_{1(z)} = 8.49 \times 10^{-9}\, z^{-1} - 1.68 \times 10^{-9}\, z^{-2}$$

$$B_{2(t)} = 0.19z^{-1} - 0.18z^{-2}$$

(2)

Model for output y_2:

$$A_{(z)}y_{2(t)} = -A_{i(z)}y_{i(t)} + B_{(z)}u_{(t)} + e_{2(t)}$$

(3)

Where,

$$A_{(z)} = 1 - 1.99z^{-1} + 0.99z^{-2}$$

$$A_{i(z)} = 2.47z^{-1} - 2.44z^{-2}$$

$$B_{1(z)} = 6.83 \times 10^{-8}\, z^{-1} - 1.16 \times 10^{-7}\, z^{-2}$$

$$B_{2(t)} = 3.60z^{-1} - 3.56z^{-2}$$

(4)

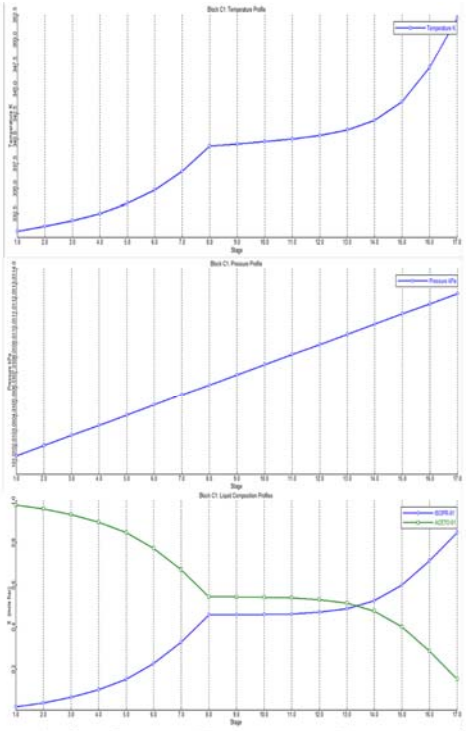

Figure 3. Steady-state Temperature, Pressure and Composition Profiles

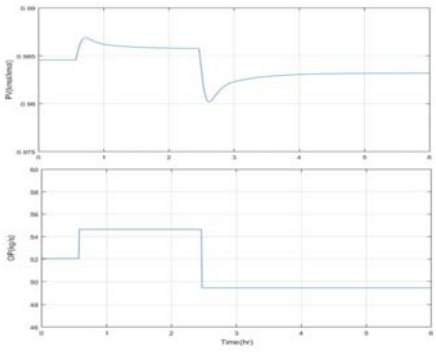

(a) 5% Change in Reflux

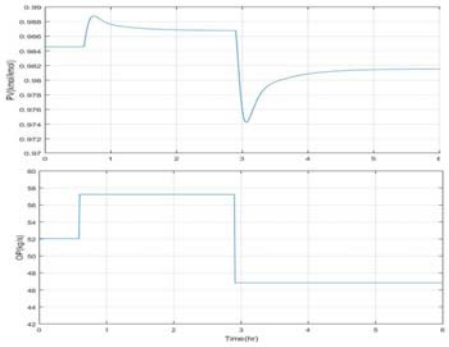

(b) 10% Change in Reflux

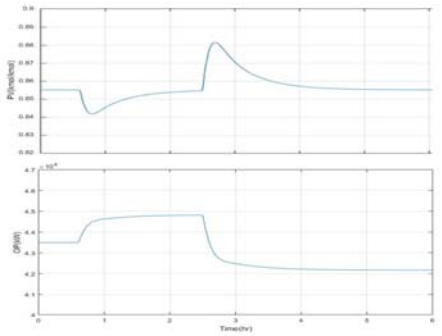

(a) 5% Change in Reboiler Duty

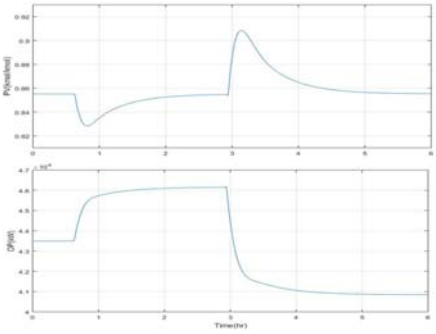

(b) 10% Change in Reboiler Duty

Figure 4. Top Composition responses to t
Changes in Reflux flowrate and Reboiler D

The identified model was found to fit the data appropriately. The fit % was found to be 74.4% as shown in Figure 5, which is acceptable.

To improve the model accuracy, higher orders of the models (i.e. [4,2,1] and [4,4,1] were used, however, none of those were able to bring significant improvement in the fit%. Therefore, the model of order [2,2,1] was selected due to its simplicity to represent the system, which was presented in equations 1-4.

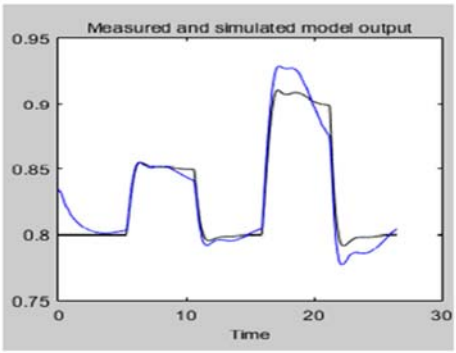

Figure 5. Validation of Model [2,2,1]

CONCLUSIONS:

This work summarizes the estimation of dynamic behaviour and basic identification procedure of distillation column by using Aspen PLUS Dynamics® and MATLAB®. A pilot-scale binary distillation column of IPA-Acetone mixture is used for the study. Steady-state and dynamic simulations have been developed with rational results. Control scheme has been designed and then the system is identified and validated as ARX models using MATLAB® System Identification Toolbox. The procedure is explained in general terms and can be applied to many other control-relevant processes. Moreover, this identification can be used to devise appropriate model based controllers.

ACKNOWLEDGEMENTS

The authors would like to thank the Department of Chemical Engineering, NED University of Engineering and Technology,

Pakistan for the guidance and support provided throughout this study.

REFERENCES:

[1] Nagarajaiah, S. (2009). Introduction to system identification. *System Identification*

[2] Schoukens, R. P. a. J. (2012). *System Identification-A Frequency Domain Approach* (IEEE Press Editorial Board ed.). Canada: John Wiley & Sons

[3] Douglas, B. (2013). System identification method

[4] U. Forssell, *Closed-loop Identification.* Link¨oping Studies in Science and Technology. Dissertations, Sweden 1999.

[5] S. M. Safdarnejad, J. R. Gallacher and J. D. Hedengren, Dynamic parameter estimation and optimization for batch distillation, *Computers and Chemical Engineering* 86, 18-32, 2016.

[6] W. L. Luyben, Aspen Dynamics simulation of a middle-vessel batch distillation process, *Journal of Process Control* 33, 49-59, 2015.

[7] A.A. Bachnas, R. Tóth, J.H.A Ludlage and A. Mesbah, A review on data-driven parameter-varying modeling approaches: A high purity distillation column case study, *Journal of Process Control* 24, 272-285, 2014.

[8] A. D. Assandri, C de Prada, A. Rueda and J. L. Martínez, Non-linear parametric predictive temperature control of a distillation column, *Control Engineering Practice* 21, 1795-1806, 2013.

[9] F. Bezzo and M. Barolo, Understanding the dynamic behavior of middle-vessel continuous distillation columns, *Chemical Engineering Science* 60, 553–563, 2005.

[10] S. Skogestad and M. Morari, Understanding the Dynamic Behavior of Distillation Columns, *Industrial & Engineering Chemistry Research,* 27, 1848-1862, 1988.

FULLERENE BASED NANOCOMPOSITES FOR ADVANCED OIL/GAS APPLICATIONS

C. Okolo[1] and F. Inam[1*]
[1] Northumbria University, Faculty of Engineering and Environment, Department of Mechanical and Construction Engineering, Newcastle upon Tyne, NE1 8ST, United Kingdom

[*]Corresponding author. Tel.: +44 1912273741
E-mail address: fawad.inam@northumbria.ac.uk (F. Inam)

ABSTRACT

Fullerenes, novel forms of super carbonaceous materials are subject of significant research for their utilization in an increasing number of applications like petrochemical, energy, transportation, automotive, aerospace, defence, sporting goods and infrastructure development. In particular, carbon nanotubes and graphene are some of the common types of fullerenes that offer unique combinations of superlative chemical and physical properties. This keynote speech will look into how a simple chemical manipulation at nano-scale of a superlative chicken wire structure of graphene can be exploited to address major engineering challenges we are now encountering in the development of subsea engineering products used for oil/ gas applications. Substituting monolithic materials with nanofiller reinforced composites would not just bring major performance uplift but also significant reduction in manufacturing and related economics. However, there are several key challenges prior to this forthcoming substitution which will be detailed in this work.

Keywords: Graphene; alumina; fracture toughness; electrical conductivity; SPS.

1 INTRODUCTION

Advanced ceramics are having many applications in the very challenging oil and gas applications. As current reservoirs and other national resources of oil and gas are being depleted, the technology is being pushed to explore ever more severe and demanding environments for future supplies. New materials, like fullerenes, offer unique combination of extraordinary properties to such materials. Owing to the superlative nature of atomically thin graphene [1], its incorporation in ceramics has become a focal point for many ceramics researchers globally. For example, with the addition of just 1.5 vol% of graphene in silicon nitride, a remarkable 235% improvement in fracture toughness was achieved [2]. The graphene was found to be wrapped around the silicon nitride grains and formed a continuous network along the grain boundaries [2]. Kim et al. [3] reported an increase of one order of magnitude with the addition of only 0.25 vol% of graphene in alumina. Similarly, Zhou et al. [4] reported an increase of 8 orders of magnitude and 3.7 times in the electrical and thermal conductivity of ceramic-graphene nanocomposites respectively. The percolation threshold for the alumina – graphene nanocomposites was researched for the first time in 2010 [5], which was found to be around 3 vol.%. Fan et al. [5] reported increased electrical conductivity for the nanocomposites with increasing the amount of graphene, reaching a value of around 5710 S/m for alumina - 15 vol% graphene.

From the analysis of the literature studying ceramic – graphene nancomposites, it can be noted that majority of the research papers in the field of ceramic-graphene nanocomposites study the effect of the graphene content on the properties of the final ceramic – graphene nanocomposite [3]. In this study, we systematically report a novel and effective strategy for engineering the mechanical and electrical properties of ceramic – graphene nanocomposites without changing the amount of graphene.

2 EXPERIMENTAL DETAILS

Chopped graphene nanoribbons flakes were produced by the CVD pyrolysis of a solution containing ethanol, ferrocene and thiopene as reported in [6]. Freshly produced (raw) graphene was then aggressively tip-sonicated for 20-60 mins in distilled water using Z511463 Sigma-Aldrich ultrasonic tip-sonicator (750

W). The supernatant was collected and dried in an oven at 60 °C for 24 h prior to Raman spectroscopy. The Raman spectra for raw and damaged/ tip-sonicated graphene were obtained on a Renishaw Raman Imaging Microscope System. Sample masses ranged from 25 to 30 mg. Raman spectra were excited with a 488 nm Ar+ laser line at a power of 35 mW. Spectra were detected with an imaging photomultiplier (1024 x 1024) with 5 cm-1 resolutions. Typical collection time was 30 minutes for each sample and at least 5 batches of each sample were examined for accurate quantification of the ratios of the intensities for different bands (i.e. D, G and G'). Thermogravimetric analysis (TGA) was conducted for all nanocomposites to evaluate graphene oxidation temperature using TA Instruments SDT Q600. Q500 (TA instruments) was used with a heating rate of 5 °C/min to 1000 °C in air. All specimens were examined on platinum pans in the range 30–1000 °C. A heating rate of 5 °C/min in flowing air (at 180 ml/min) was used. Sample masses ranged from 40 to 50 mg and at least 3 samples were oxidised for each composition of selected nanocomposites.

For mechanical and electrical characterisations, alumina nanocomposites containing 0.5 vol% graphene (raw and damaged) were Spark Plasma Sintered (SPSed) respectively. Graphene nanopowder (chopped nanoribbons flakes produced by the CVD pyrolysis of a solution containing ethanol, ferrocene and thiopene as reported in [6] were dispersed in dimethylformadie, DMF [7] using high power tip ultrasonication for 45 minutes and then hand-mixed with alumina nanopowder (Sigma–Aldrich, UK: gamma phase; particle size <50 nm; surface area 35–43 m2 g−1; melting point 2040 °C; and density 3.97 g cm−3) for 10 min. The liquid mixture was rotation ball milled for 10 h. It was then dried at 70 °C for 12 h using a rotary drier containing milling media (4 mm alumina balls), followed by vacuum oven drying at 100 °C for 50 h. To avoid re-agglomeration of graphene during lengthy drying, the alumina balls (milling media) was added during rotary drying. The dried nanocomposite powder was ground and sieved at 150 mesh and then placed again in the vacuum oven at 100 °C for another 50 h to thoroughly extract the solvent. Nanocomposite pellets (diameter 20 mm and thickness 5 mm) were prepared by Spark Plasma Sintering (SPS) using LABOX 350 (Sinter Land Inc, Japan) furnace. A pressure of 100 MPa was applied concurrently with the heating (rate 60 °C min−1) and released at the end of the sintering period, which was 10 mins. Sintering temperature for all nanocomposites was 1250 °C. A pulsed DC current with 5 µsec ON and 5 µsec OFF was used without any pause.

All of the sintered samples were ground using SiC paper down to 4000 grit. The density of the ground samples was measured using the Archimedes' water buoyancy method and also verified by a manual Heliulm multipycnometre (Quantachrome UK). All samples were then thoroughly dried in an oven for 24 hours and then diamond polished using 1-micron paste. Sintered nanocomposite samples were gently fractured and their micro structures were examined in an FE-SEM. Cross-sectional surfaces were gold coated and observed in an ultra-high resolution analytical FE-SEM (Hitachi, SU-70) using 20 keV.

For mechanical and electrical characterisations, at least 5 samples of each composition were examined. Fracture toughness characterisations were carried out for alumina and nanocomposite samples according to standard ASTM C1421 (standard test method for determination of fracture toughness of advanced ceramics at ambient temperature). Single Edge V-notch Beam (SEVNB) method was employed using parallelepiped samples (3 x 4 x 30 mm2) and a loading span distance of around 17 mm. All samples were machined and notches were produced using a diamond saw (Accutom-50). For all samples, the notch was in the range of 0.7-1.1 mm in depth and around 195 µm in width. The root radius of the notch for each sample was about 9-10 µm with a V-notch angle of around 19o. For evaluating electrical conductivity, a bar (dimensions: 17 x 3 x 5 mm) was cut from each sintered pellet using precision and deformation-free cutting machine (Accutom-50). Around 500 microns of material was removed from all surfaces of sample by fine grinding. Four-point method [8] was employed by using a resistivity/ Hall measurement system (Quantum Design, PPMS, Model 6000) for measuring electrical conductivities of nanocomposites. For pure alumina samples, high resistance meter (HP 4329A) was used to measure the conductivity. The connecting wires in the experimental setup were permanently bonded by using silver paste in order to avoid any contact resistance for this analysis.

3 RESULTS AND DISCUSSION

Raman spectroscopy is a well-known and widely used characterisation technique for analysing carbon materials [9-15]. For graphene, the D-band near 1370 cm-1 and the D' shoulder band near 1630 cm-1 are, respectively, the disorder-induced features that are representing the intervalley K→K' and intervalley K (or K') double resonance scattering processes [9, 10]. G band, appearing at around 1620 cm-1, is associated with the doubly degenerate phonon mode at the Brillouin zone centre or tangential vibration of carbon atoms [9]. The sharpening of G band peak will shorten FWHM (Full Width at Half Maximum) line which confirms the establishment of larger crystalline areas [9, 11]. Similarly, the D band is the signature of defects and increase in ID/IG and ID/IG' corresponds to an increase in the amount of 'unorganised' carbon and/or decrease

in the mean crystal size as reported elsewhere [11-15]. During graphitisation, the ID becomes smaller than IG, which indicates a more perfect graphene structure [11, 13, 15]. Therefore, in this study, the authors used the ID/IG and ID/IG' ratios and FWHM line widths from Raman spectroscopy supported by electrical conductivity and oxidation temperature analyses to study the degradation of graphene after sintering.

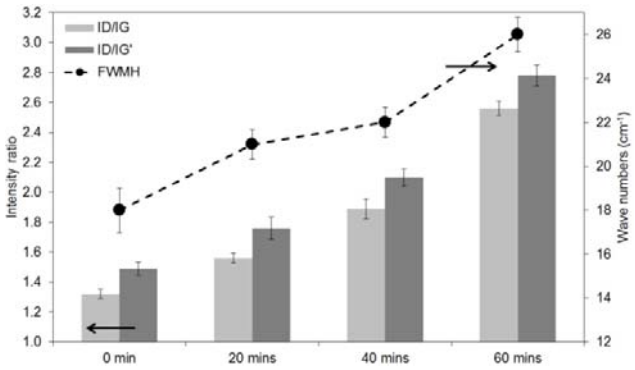

Figure 1. Raman spectroscopy analysis of as-produced and tip-ultrasonicated graphene showing intensity ratios and FWHM line widths (G band).

Figure 1 shows severe damaging of chicken wire structure in graphene due to severe ultrasonication. Qualitative information on purity, crystallinity and structural health of graphene was obtained from the Thermogravimetric analysis (TGA) of the sintered nanocomposites. Higher the content of oxidisable residue and amorphous carbon, lower the onset of oxidation temperature or thermal stability and vice versa [16, 17]. The crystallinity was also significantly reduced as confirmed from the TGA analyses as well (figure 2). Because of this damage, as confirmed via figures 1 and 2, fracture toughness and electrical properties were also found to be severely affected (figure 3). It can be seen that with the increase in the damage or the amorphous content within graphene, lower fracture toughness and electrical conductivities were observed.

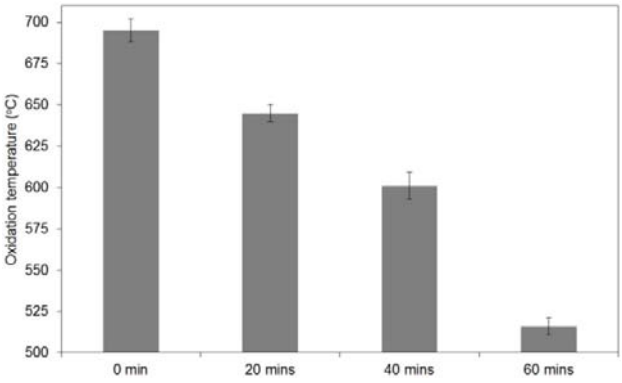

Figure 2. Thermogravimetric analysis (TGA) of as-produced and tip-ultrasonicated graphene.

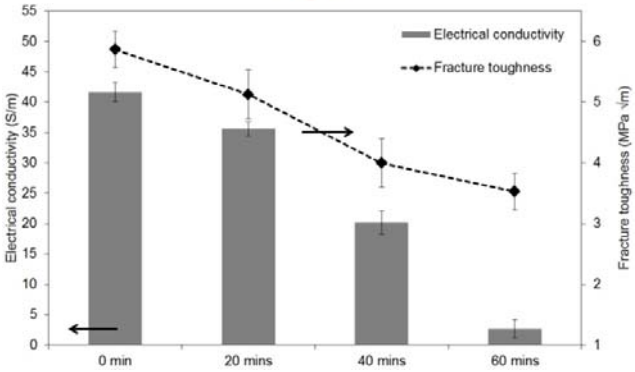

Figure 3. Electrical conductivity and fracture toughness values of the nanocomposites measured by four-probe and Single Edge V-notch Beam (SEVNB) techniques respectively. For electrical and mechanical characterisations, alumina nanocomposites containing 0.5 vol% graphene (raw and damaged) were sintered respectively.

Fig 4 shows the FE-SEM images of fractured surfaces of the representative sintered nanocomposite samples (i.e. alumina – 0.5 vol% graphene). Individual layers of graphene are pointed and found crushed between alumina grains. Good dispersion of graphene in the alumina matrix can be observed (fig 4). Individual grains and intergranular fracture mode along with pulled out graphene from the alumina grains can be visualised. With the addition of carbon nanofillers in ceramics, finer microstructures are produced as previously reported [18, 19]. For example, Wang et al. [18] observed that the addition of 2 wt% graphene in the alumina matrix resulted in grain size refinement. The grain size of pure alumina was 1 μm, while the grain size of composites was around 500 nm [18]. From the analysis of figure 4, no structural or grain size differences can be observed. Therefore, it can be concluded that the quality of graphene has no influence on the grain size refinement.

For enhancing electrical or mechanical properties of alumina nanocomposites, researchers have always added more graphene and proposed new effective dispersion strategies. Such enhanced properties can only be achieved if graphene is thoroughly homogenised/ dispersed, i.e. having maximum surface area in contact with the ceramic grains. There is always a limit for adding graphene in ceramic nanocomposites because higher the concentration of graphene, the more difficult it becomes to homogenise. As we mix more and more graphene with ceramic powder in a liquid solvent, the viscosity of the solution increases. Therefore, new experimental variables (related to dispersion) are required if different amounts of graphene are mixed with ceramic powder. With this new method, there is no need to optimise experimental variables related to dispersion prior to the wet processing for homogenisation, because we can customise the properties of final composite

material by changing the quality of incorporated graphene.

4 CONCLUSION

A novel strategy for producing ceramic – graphene nanocomposites with customisable mechanical and electrical properties without changing the amount of graphene has been presented. Structural and crystalline defects were produced in graphene using high-power tip ultrasonication for 20, 40 and 60 minutes. Raman spectroscopy and thermogravimetric analyses were conducted to characterise degradation in graphene. Alumina – graphene nanocomposites were then prepared using Spark Plasma Sintering. Fracture toughness and electrical conductivities were measured for alumina nanocomposites containing 0.5 vol% graphene respectively. Electrical conductivity and fracture toughness values of alumina – graphene nanocomposites decreased with the increase in structural defects in graphene. The quality of graphene has no influence on the grain size of the alumina nanocomposites.

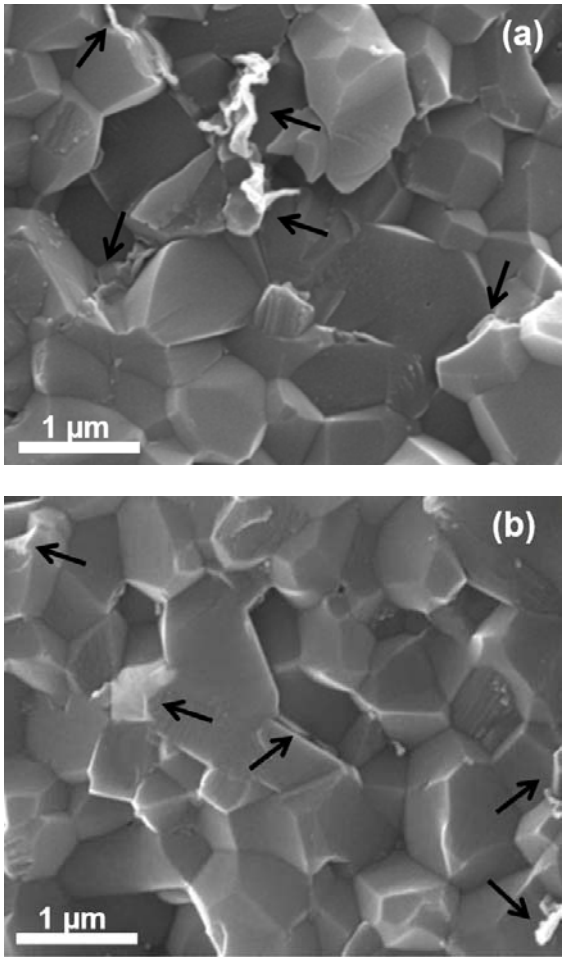

Figure 4. Representative FE-SEM images showing alumina – 0.5 vol% graphene nanocomposite having graphene tip-ultrasonicated for: a) 0 minute (as produced); and b) 60 minutes.

ACKNOWLEDGEMENTS

The authors would like to thank funding from the Dstl (MoD), UK and Innovate UK for carrying out part of this work.

REFERENCES

[1] K. S. Novoselov, A. K. Geim, S. V. Morozov, D. Jiang, Y. Zhang, S. V. Dubonos, I. V. Grigorieva, A. A. Firsov, Electric field in atomically thin carbon films. Science 306(5696), 666-669, 2004.

[2] L. S. Walker, V. R. Marotto, M. A. Rafiee, N. Koratkar and E. L.Corral, Toughening in graphene ceramic composites, ACS Nano 5(4), 3182–3190, 2011.

[3] H.J. Kim, S.M. Lee, Y.S. Oh, Y.H. Yang, Y.S. Lim, D.H. Yoon, C. Lee, J.Y. Kim and R.S. Ruoff, Unoxidized Graphene/Alumina Nanocomposite: Fracture- and Wear-Resistance Effects of Graphene on Alumina Matrix, Scientific Reports 4, 5176, 2014.

[4] M. Zhou, H. Bi, T. Lin, X. Lü, F. Huang, J. Lin, Directional architecture of graphene/ceramic composites with improved thermal conduction for thermal applications, J. Mater. Chem. A 2, 2187-2193, 2014.

[5] Y.C. Fan, L.J. Wang, J.L. Li, J.Q. Li, S.K. Sun, F. Chen, L.D. Chen, W. Jiang, Preparation and electrical properties of graphene nanosheet/ Al_2O_3 composites, Carbon 48, 1743–1749, 2010.

[6] J. Campos-Delgado et al., Bulk Production of a New Form of sp2 Carbon: Crystalline Graphene Nanoribbons, Nano Lett. 8 (9), 2773-2778, 2008.

[7] F. Inam, H. Yan, M. Reece and T. Peijs, Dimethylformamide: an effective dispersant for making ceramic–carbon nanotube composites. Nanotechnology 19 (19), 195710, 2008.

[8] F. Inam, R. B. Bhat, T. Vo, and W. M. Daoush, Structural health monitoring capabilities in ceramic – carbon nanocomposites, Ceramics International 40 (2), 3793-3798. ISSN 0272-8842, 2014.

[9] L. M. Malard, M. A. Pimenta, G. Dresselhaus, M. S. Dresselhaus, Raman spectroscopy in graphene, Physics Report 473, 51-87, 2009.

[10] R. Saito, A. Grüneis, G. G. Samsonidze, V. W. Brar, G. Dresselhaus, M. S. Dresselhaus, A. Jorio, L. G. Cançado, C. Fantini, M. A. Pimenta and A. G. Souza Filho, Double resonance Raman spectroscopy of single-wall carbon nanotubes, New J. Phys. 5, 1571, 2003.

[11] J. Campos-Delgado, Y. A. Kim, T. Hayashi, A. Morelos-Gomez, M. Hofmann, H. Muramatsu, M. Endo, H. Terrones, R. D. Shull, M. S. Dresselhaus, M. Terrones, Thermal stability studies of CVD-grown graphene nanoribbons: Defect annealing and loop formation, Chemical Physics Letters 469, 177–182, 2009.

[12] F. Inam, H. Yan, M. J. Reece and T. Peijs, Structural and chemical stability of multiwall carbon nanotubes in sintered ceramic nanocomposite, Advances in Applied Ceramics 109 (4), 240-247, 2010.

[13] M. Endo, Y. A. Kim, T. Hayashi, Y. Fukai, K. Oshida, M. Terrones, T. Yanagisawa, S. Higaki, M. S. Dresselhaus, Structural characterization of cup-stacked-type nanofibers with an entirely hollow core, Appl. Phys. Lett. 80, 1267, 2002.

[14] F. Tuinstra and J. L. Koenig, Raman Spectrum of Graphite, J. Chem. Phys. 53, 1126–1130, 1970.

[15] P. Delhaes, M. Couzi, M. Trinquecoste, J. Dentzer, H. Hamidou, and C. V. Guterl, A comparison between Raman spectroscopy and surface characterizations of multiwall carbon nanotubes, Carbon 44, 3005–3013, 2006.

[16] K. E. Hurst, A. Van Der Geest, M. Lusk, E. Mansfield, J. H. Lehman, Quartz–crystal microbalance for in situ monitoring of laser cleaning of carbon nanotubes. Carbon 48(9), 2521–2525, 2010.

[17] Dilip K. Singh, Parameswar K. Iyer and P. K. Giri, Diameter dependence of oxidative stability in multiwalled carbon nanotubes: Role of defects and effect of vacuum annealing, Journal of Applied Physics 108, 084313, 2010.

[18] K. Wang, Y. F. Wang, Z. J. Fan, J. Yan and T. Wei, Preparation of graphene nanosheet/alumina composites by spark plasma sintering, Mater. Res. Bull. 46(2), 315–318, 2011.

[19] F. Inam, T. Peijs and M. J. Reece, The production of advanced fine-grained alumina by carbon nanotube addition J. Eur. Ceram Soc. 31(15), 2853–2859, 2011.

CONVERSION-BASED CATHODE MATERIALS FOR LITHIUM ION BATTERIES

Hameed Ullah [a], Shah Nawaz[a], Pierre Bonnet[*b], Muhammad Irfan[a]

[a] Department of Chemistry, Hazara University, Mansehra-21300, Pakistan
[b] Institut de Chimie de Clermont-Ferrand, University Clermont Auvergne, Clermont-Ferrand, France

ABSTRACT

High energy density storage devices are highly desirable today than ever to deal, on one hand, with the energy shortages, and on the other hand, to overcome the fossil fuel created environmental problems. Renewable energy resources are the only abundant and clean alternatives to fossil fuels but their exploitation to full potential is limited by the absence of energy storage devices for large scale applications *i.e.,* in electric vehicles (EVs) and grids. Intercalation-based Lithium ion batteries (LIBs) emerged as viable energy storage devices. However, their storage capacities are far lower than the required for future large scale applications. The inherited limitation of the commercial LIBs is the low number of transferable electrons (maximum 0.5-1.0) per redox site, and thus could only be overcome by employing cathode materials having the ability to furnish two or more than two transferable electrons per redox site. Transition metal fluorides (TMFs) can serve well as conversion-type cathode materials for LIBs if two of the major issues *i.e.,* poor conductivity of metal fluorine bond and large volume changes during conversion reaction are tackled intelligently. We anticipate, in light of the reported literature, that the metal fluorine bond conductivity could be improved and the volume changes during conversion reaction could be buffered by employing carefully engineered and viably architectured TMFs hollow nanospheres. Here, we report some of the preliminary results upon fabrication of TMFs, anhydrous nickel fluoride (NiF_2), hollow nanospheres by a purposely designed synthesis protocol. The successfully synthesized NiF_2 hollow nanospheres are anticipated to have improved electrochemical properties as conversion-type cathode material for LIBs.

Keywords: LIBs, SiO_2, Fluorination, NiF_2, Hydrothermal

1. INTRODUCTION:

Lithium ion batteries (LIBs) have made the society more mobile today than ever before, and the global demand for lithium (Li) is growing annually by about 7% to sustain the growth in production of LIBs as energy storage devices to power the portable gadgets [1]. Owing to its enormous demand, it is anticipated that Li could emerge as economy indicator in future. By now the uses of LIBs as energy storage devices are extended to automobile sectors and even electricity grids, though with limited successes. In fact, powering automobiles by electricity, electric vehicles (EVs) commercialization, is the need of the time to combat the ever growing greenhouse gases threatening the environment. It is reported that nearly 20% carbon dioxide (CO_2), one of the main greenhouse gases, emission into the environment is due to the burning of fossil fuels in automobiles (approximately 45% of the total fossil fuels are used globally in vehicles) [2]. Transforming, completely, the automobiles on electric power will lessen significantly the emission of greenhouse gases, and thus the global warming.

However, to achieve the target of powering vehicles with electricity, and for grid applications, LIBs having high energy storage capacities are needed. The present day commercial LIBs are unable to meet the challenges of future applications *i.e.,* powering vehicles and grids with rechargeable batteries. One of the main and inherited problems is the

low energy storage capacity of the prevailing LIBs. The maximum theoretical capacity of the present commercial LIBs is in the range of 140 – 170 $mAhg^{-1}$ [3], and thanks to the efforts of the producers of LIBs, the maximum is already achieved. Further increase in energy storage capacity of these LIBs is not possible owing to an inherited problem wrapped-in in the discharge/charge mechanism. In fact, the prevailing LIBs for Li insertion/deinsertion in cathode materials base on intercalation mechanism, and involve transfer of less than one (1.0) electron during the discharge/charge cycle [4, 5].

Therefore, the only way forward is to exploit cathode materials having the ability to provide two or more than two transferable electrons per redox site, and this will allow manifold increase in energy storage capacities of the LIBs. It has been observed that the ability to furnish two or more than two electrons per redox site could be found in materials which undergo conversion mechanism, instead of intercalation, during discharge/charge cycle [6, 7]. The conversion-type cathode materials, in fact, transform from one material to another as a result of redox process. The transformation between two materials during redox process is accompanied by the movement of electrons equal in number to the change in oxidation state of the element, generally metal. The compounds undergo conversion mechanism have central metal atom having the ability to change its oxidation state by two or more than two, and thus allow transfer of two or more than two electrons per redox reaction [6, 7].

Transition metal compounds have been exploited as potential conversion-type electrode materials owing to their high oxidation state changes during conversion reactions. Generally, the conversion mechanism involves reaction of the transition metal compound (M_aX_b where M is transition metal, X is anion which may be H, N, O, F, P or S) with Li in discharge, and of metal with lithium compound in charge as given in equation below (Eq. 1) [6].

$$M_aX_b + (b.n)Li \leftrightarrow aM + bLi_nX \qquad (1)$$

Here n refers to the formal oxidation state of X.

Of the many transition metal compounds exploited as conversion-type cathode materials [8], transition metal fluorides (TMFs) are of particular interest corresponding to their two main advantages over the others: (a) TMFs have high redox potentials (>2V) [9], and (b) TMFs have high specific capacity reaching several hundred $mAhg^{-1}$ [10]. But, the main challenge in commercialization of TMFs based LIBs is their poor cycle performance [11]. The TMFs based LIBs lose large capacity in the successive discharge/charge cycles [12]. The poor reversibility of TMFs is corresponded to two visible factors *i.e.,* poor conductivity of the metal fluorine bond and large volume changes during conversion reactions [13, 14]. For commercial success of the TMFs based LIBs, control over these factors is of utmost importance.

The challenges of poor conductivity of metal fluorine bond and decohesion of cathode materials due to internal compounded strain as a result of large volume changes during conversion reaction could be overcome by nanostructuration of the materials through careful engineering and viable architecturing [15]. One such engineered nanostructures are the hollow spheres which are decorated with exceptional features like low Li^+ diffusion path lengths, high surface area, and above all ability to buffer the large volume changes during conversion reaction [16]. However, owing to the difficulty in fabrications, TMFs hollow spheres have not been reported so far, and thus applied as cathode material for conversion-type LIBs.

Here we come up with new idea to fabricate TMFs hollow spherical nanostructures following a purposely designed protocol. The

preliminary results show successful fabrication of TMFs (NiF_2) hollow spheres by this very designed and developed protocol. In this paper the preliminary results upon fabrication of TMFs hollow spheres are presented, while the complete study will be published later in a comprehensive research article.

2. Experimental

2.1. Materials and Methods

All the chemicals used in this study were purchased from commercial suppliers and used as received without further purifications. The water (H_2O) was doubly distilled in our own laboratory. The characterizations of the sample were performed by using different analytical techniques including FTIR spectrophotometer (Varian 2000 FT-IR spectrometer), powder X-rays diffractometer (XPert PRO diffractometer), scanning electron microscope (JSM-6490A), transmission electron microscope (TEM) and TGA/DTA analyzer.

2.2. Fabrication of Anhydrous NiF_2 Hollow Nanospheres

The NiF_2 hollow nanospheres were fabricated by a three step protocol. In first step of the experimental process, SiO_2 spheres were prepared by following the well know Stöber method [17]. In second step, the SiO_2 spheres were pasted with $Ni(OH)_2$ in autoclave to get SiO_2@$Ni(OH)_2$ core-shell spherical structures. Typically, the SiO_2 spheres (0.1g) were suspended in appropriate amount of distilled H_2O, and to this suspension was added $Ni(NO_3)_2.6H_2O$ (0.5g) followed by addition of NH_4OH (10mL). The reaction mixture was transferred to Teflon lined stainless steel autoclave which was placed in laboratory oven at the desired temperature (150^0C) and time (6 hours). The retrieved sample was washed thoroughly, and dried in oven at 100^0C overnight. In third step of the fabrication protocol, the core-shell structure was subjected to online fluorination at 350°C for 5 hours to remove the SiO_2 core and get anhydrous NiF_2 hollow nanospheres. The color of sample upon fluorination changed from light green to dark brown.

3. Results and Discussion

Figure 1(a) presents XRD patterns of SiO_2 prepared by Stöber method, and of SiO_2@$Ni(OH)_2$ core-shell structure. The large hump in XRD pattern of SiO_2 indicates its amorphous nature. However, the XRD pattern of SiO_2@$Ni(OH)_2$ core-shell structure gives well developed peaks imposed over the broad hump of SiO_2. These peaks were indexed by matching with standard powder diffraction files (PDF) [00-003-0177] and [00-049-1859] for hexagonal $Ni(OH)_2$ and monoclinic $Ni_3Si_2O_5(OH)_4$ phases, respectively, in JCPDS database. The appearance of the new phase $Ni_3Si_2O_5(OH)_4$ could be the result of reaction between SiO_2 core and $Ni(OH)_2$ shell at the interface.

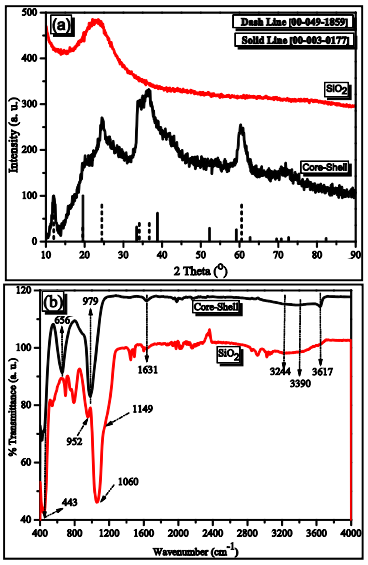

Figure 1 PXRD patterns (a) and FTIR spectra of SiO_2 and SiO_2@$Ni(OH)_2$ core-shell structures

The FTIR spectra of SiO_2 and SiO_2@$Ni(OH)_2$ core-shell structure are given in Figure 1(b). The FTIR spectrum of SiO_2 corresponds to the reported [18, 19], while FTIR spectrum of

SiO_2@$Ni(OH)_2$ core-shell structure gives peaks for all the necessary stretching and bending vibrations of SiO_2, and new peaks for the $Ni(OH)_2$. Peaks owing to the new phase $Ni_3Si_2O_5(OH)_4$ are seen in the FTIR spectrum of the core-shell structure [20]. Furthermore, the peculiar peaks of SiO_2 have shifted significantly to low energy in the SiO_2@$Ni(OH)_2$ core-shell structure spectrum.

The formation of SiO_2 spheres were confirmed by SEM, and the image is presented in Figure 2(a). As shown in the SEM image (Figure 2(a)), the SiO_2 spheres formed are uniform in size and narrowly distributed (200 nm – 220 nm). The SEM result of SiO_2@$Ni(OH)_2$ core-shell structure are still awaited. However, the SiO_2@$Ni(OH)_2$ core-shell structure was investigated for its morphology by TEM. As shown in Figure 2 (b), uniform spherical structures having rough surfaces are formed. The spheres are self organized, and the average size (237.14 ± 21.44 nm) is larger than the size of the SiO_2 spheres (214.36 ± 7.47 nm). From these measurements, the shell thickness is roughly estimated in the range of 20 nm to 25 nm.

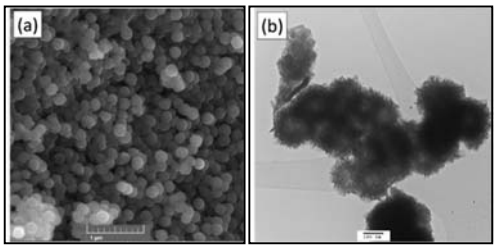

Figure 2 SEM image of SiO_2 spheres obtained following the Stöber method (a), and TEM image of SiO_2@$Ni(OH)_2$ core-shell structure (b)

The temperature regime for the fluorination of SiO_2@$Ni(OH)_2$ core-shell structure to get anhydrous NiF_2 hollow spheres was selected based on the thermogravimetric analysis (TGA). The thermogram of the SiO_2@$Ni(OH)_2$ core-shell structure is given in Figure 3(a) showing three main stages of weight loss. The first stage of weight loss (~4.17%) in the temperature range of 25°C to 120°C is corresponded to the removal of adsorbed water molecules. The second significant weight loss of about 6.67% in the temperature range of 120°C to 425°C is corresponded to the removal of lattice OH groups. The weight loss of about 5.83% in the temperature range of 425°C to 650°C corresponds to the phase transformation. Further heating of the sample showed no weight loss.

The fluorinated sample was characterized by PXRD, and the diffractogram is presented in Figure 3(b). The PXRD patterns of the fluorinated sample shows well defined diffractions which are indexed by matching with standard PDF [01-081-2269] in the JCPDS database for anhydrous NiF_2 in the tetragonal crystal system. The PXRD diffractogram confirms on one hand complete transformation of $Ni(OH)_2$ to pure NiF_2, and on the other hand, complete removal of SiO_2 under the given fluorination parameters.

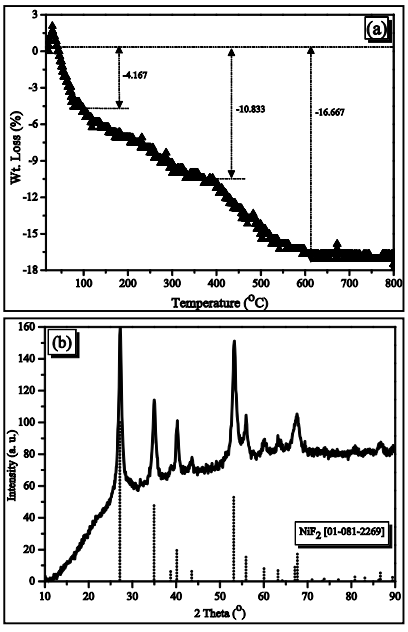

Figure 3 Thermograms of SiO_2@$Ni(OH)_2$ core-shell structure (a), and PXRD pattern of the sample obtained by fluorination of SiO_2@$Ni(OH)_2$ core-shell structure at 350°C for 5 hours

FTIR spectrum was recorded for the NiF_2 sample in the range of 4000 cm^{-1} to 400 cm^{-1}, and is presented in Figure 4(a). As shown in the FTIR spectrum of NiF_2 (Figure 4(a)), all the peaks for SiO_2, $Ni(OH)_2$ and $Ni_3Si_2O_5(OH)_4$ phases are absent indicating the removal and/or transformation of these phases. In fact there are now significant peaks in the FTIR spectrum of NiF_2 except a sharp tail around 400 cm^{-1} which could be corresponded to the Ni – F bond vibration. Furthermore, the resulting NiF_2 material is highly anhydrous as there are no peaks observed for H_2O or OH vibrations.

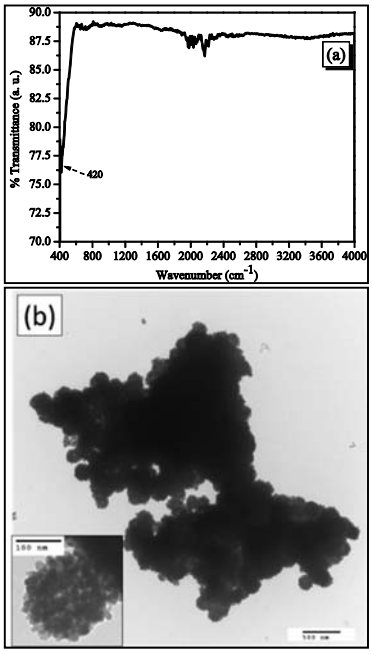

Figure 4 FTIR spectrum of NiF_2 sample obtained by fluorination of SiO_2@$Ni(OH)_2$ core-shell structure at 350°C for 5 hours (a), TEM image of NiF_2 hollow structure (inset is shown single hollow sphere) (b)

The TEM image of the NiF_2 sample obtained by fluorination of SiO_2@$Ni(OH)_2$ core-shell structure at 350°C for 5 hours is given in Figure 4(b). The TEM image shows self organized spherical structures having empty centers. The average size of the sphere is measured about 186.06 ± 17.72 nm. The size of the NiF_2 hollow sphere is quite smaller than the SiO_2@$Ni(OH)_2$ core-shell spheres (237.14 ± 21.44 nm). The decrease in size of the NiF_2 spheres further confirms the formation of NiF_2 hollow spheres. It is assumed that as the core is removed the shell nanoparticles move inwards. This inward movement of nanoparticles results in size decrease of the resulting hollow spheres. The shell of the hollow spheres is composed of tiny nanoparticles (Figure 4(b) inset) having average size of 14.90 ± 2.45 nm. This indicates that the elongated nanoparticles which have composed the shell in the precursors are no more exist. The transformation of shell particles to tiny nanoparticles could also be one of the reasons to stabilize the shell.

4. Conclusion

In conclusion, TMFs hollow spheres of NiF_2 have been fabricated following the proposed synthesis protocol. The SiO_2 spheres which were used as hard templates were achieved by following the well known Stöber method, and strict control over the size and distribution have been obtained. The $Ni(OH)_2$@SiO_2 core-shell structures have shown tremendous integrity between the shell and the core. From the better integrity of shell with core has been benefited during the core removal step, and stable and coherent shells of the hollow structures have been achieved. This would be the first time to prepare hollow spheres of any TMF. The complete study will be reported along the galvanostatic measurements in a comprehensive paper.

References

1. Lithium, Lithium Minerals and Lithium Chemicals, Chemical Economics Handbook (CEH) Marketing Research Report, **2014**.

2. (a) EIA. 2009. Annual energy outlook **2009**. Washington, DC: Energy Information Administration, U.S.

Department of Energy; (b) IEA. **2009**. CO_2 emissions from fuel consumption. Paris France: International Energy Agency; (c) IEA. **2010**. Review of international policies for vehicle fuel efficiency. Paris France: International Energy Agency.

3. C. M. Julien, A. Mauger, K. Zaghib, H. Groult, *Inorganics* **2014**, *2*, 132-15.

4. M. S. Whittingham , *Chem. Rev.* **2004** , *104* , 4271 .

5. B. L. Ellis , K. T. Lee , L. F. Nazar , *Chem. Mater.* **2010** , *22* , 691 .

6. J. Cabana, L. Monconduit, D. Larcher, M. R. Palacin, *Adv. Energy Mater.* **2010**, *22*, E170-E192.

7. M. Armand, J.-M. Tarascon, *Nature* **2008**, *451*, 652.

8. R. Malini, U. Uma, T. Sheela, M. Ganesan, N. G. Renganathan, *Ionics* **2009**, *15*, 301-307.

9. (a) G. G. Amatucci, N. Pereira, *J. Fluorine Chem.* **2007**, *128*, 243-262; (b) H. Li, G. Richter, J. Maier, *Adv. Mater*. **2003**, *15*, 736-739; (c) S.-W. Kim, D.-H. Seo, H. Gwon, J. Kim, K. Kang, *Adv. Mater*. **2010**, *22*, 5260-5264; (d) P. Liu, J. J. Vajo, J. S. Wang, W. Li, J. Liu, *J. Phys. Chem*. C **2012**, *116*, 6467-6473; (e) L. Li, F. Meng, S. Jin, *Nano Lett*. **2012**, *12*, 6030-6037.

10. (a) P. Poizot, S. Laruelle, S. Grugeon, L. Dupont, J.-M. Tarascon, *Nature* **2000**, *407*, 496-499; (b) T. A. Yersak, et al. *Adv. Energy Mater*. **2013,** *3*, 120-127.

11. D. H. Lee, K. J. Carroll, S. Calvin, S. Jin, Y. S. Meng, *Electrochim. Acta* **2012**, *59*, 213.

12. X. Hua, R. Rober, L.-S. Du, K. M. Wiaderek, M. Leskes, K. W. Chapman, P. J. Chupas, C. P. Grey, *J. Phys. Chem. C* **2014**, *118*, 15169-15184.

13. J. Zaanen, C. Westra, G. A. Sawatzky, *Phys. Rev. B: Condens. Matter Mater. Phys.* **1986**, *33*, 8060.

14. (a) M. M. Thackeray, J. T. Vaughey, C. S. Johnson, A. J. Kropf, R. Benedek, L. M. L. Fransson, K. Edstrom, *J. Power Sources* **2003**, *113* , 124; (b) A. Timmons, J. R. Dahn, *J. Electrochem. Soc.* **2006**, *153*, A1206.

15. J. Liu, W. Liu, S. Ji, Y. Wan, M. Gu, H. Yin,.Y. Zhou, *Chem. Eur. J.* **2014**, *20*, 5815-5820.

16. a) X. W. Lou, L. A. Archer, Z. Yang, *Adv. Mater*. **2008**, 20, 3987-4019; (b) J. Liu, Y. Wan, C. Liu, W. Liu, S. Ji, Y. Zhou, J. Wang, *Euro. J. Inorg. Chem.* **2012**, *24*, 3825-3829; (c) W. M. Zhang, J. S. Hu, Y. G. Gou, S. F. Zheng, L. S. Zhong, W. G. Song, L. J. Wan, Adv. Mater. **2008**, 20, 1160-1165; (d) L. Yu, H. B. Wu, X. W. Lou, Adv. Mater. **2013**, 25, 2296 –2300.

17. W. Stöber, A. Fink, E. Bohn, Controlled Growth of Monodisperse Silica Spheres in the Micron Size Range, Journal of Colloid and Interface Science, 26 (1968) 62 – 69.

18. W. Y. D. Yong, Z. Zhang, G. Cristobal, W. S. Chin, One-pot synthesis of surface functionalized spherical silica particles, Colloids and Surfaces A: Physicochem. Eng. Aspects, 460 (2014) 151 – 157.

19. M. Qasim, J. Ananthaiah, S. Dhara, P. Paik and D. Das, Synthesis and Characterization of Ultra-Fine Colloidal Silica Nanoparticles,

Advanced Science, Engineering and Medicine, 6 (2014) 965–973.

20. R. L. Frost, B. J. Reddy and M. J. Dickfos, Raman spectroscopy of the nickel silicate mineral pecoraite – an analogue of chrysotile (asbestos), J. Raman Spectrosc., 39 (2008) 909 – 913.

Multi-property computational material optimization for solar cells

Ahmer A.B. Baloch[1,*], M.I. Hossain[2], Fedwa El Mellouhi[2], Nouar Tabet[1,2], Fahhad Alharbi[1,2]
[1]College of Science and Engineering, Hamad bin Khalifa University, Qatar
[2] Qatar Environment and Energy Research Institute, Hamad bin Khalifa University, Qatar
[*]Corresponding author. Tel.: +97433157462;
E-mail address: ahmbaloch@hbku.edu.qa (Ahmer A.B. Baloch)

ABSTRACT

Recently, photovoltaic field has progressed on many fronts mainly due to the pressing need for alternative energy resources. While these devices are continuously being maturing, a survey has showed that most of the used charge transport materials in solar cells are similar in different technologies. For example, several solar cells use TiO_2 and CdS as electron transport material. So, it is reasonable to assume that there is a possibility of better matching materials for high efficiency. Therefore, a systematic enhancement for solar cell demands an in-depth analysis of individual device layers and their cumulative effect. This can be expensive experimentally and hence computational design can be useful. Therefore, a multi-property materials optimization method is developed and implemented. Drift-diffusion calculations are performed to obtain microscopic material properties which are coupled with multi-property design to specify the optimum configuration of solar cell. For an absorber, the method optimizes the device structure and identifies the optimum properties that can achieve the maximum efficiency. For example, an application to hybrid perovskite solar cells showed an efficiency of 26.63% can be achieved by optimizing 23 variables. The resulted data set can then be used for material screening and for devising multiple descriptors.

Keywords: solar cells; photovoltaic; material optimization; computational

1 INTRODUCTION

Recently, hybrid perovskite solar cells (PSC) have appeared as a very promising candidate for next generation solar cell technologies, as exhibited by the very rapid surge in their efficiency within a very short time span. But a number of issues (such as the poor stability of perovskite and the inclusion of an expensive hole transport material (HTM)) need to be resolved, before being able to commercialize PSC [1,2]. It is believed that an alternative inorganic HTM to replace the expensive Spiro-OMeTAD shall allow better stability of the cell and a reduction in the production cost without compromising the efficiency. So, some less expensive and robust alternates of spiro-OMeTAD have been studied. Likewise, the Electron Transport Material (ETM) has been evolving to increase the existing efficiencies. Currently the maximum power conversion efficiency (PCE) is 22.1% [3].

The general device architecture of PSC is shown in Fig. 1 besides its energy band diagram. It comprises of the absorber layer, two carrier transport layers, and two contacts. More sophisticated designs can be used for some specific purposes. Besides the light absorber layer, the ETM and HTM layers permit selective extraction of charges at their respective contacts. Remarkably, there is a diverse collection of efficient PSCs. On one hand, this large variety illustrates how rich the field is; on the other, it is a clear manifestation that the devices are not optimized. Also, most of the used materials for ETM and HTM and contacts are based –understandably- on commonly used ones; for example, here is a non-inclusive list of such used materials (Ref. [1,4] and the references within):

- ETM: TiO_2, Al_2O_3, ZnO, ZrO_2, and BCBM,
- Organic HTM: Spiro-OMETAD, P3HT, PTAA, PEDOT:PSS, and DPP-TT,
- Inorganic HTM: Cu_2O, CuI, NiO, and CuSCN,
- Contact: Au, Ag, Al, FTO, and ITO.

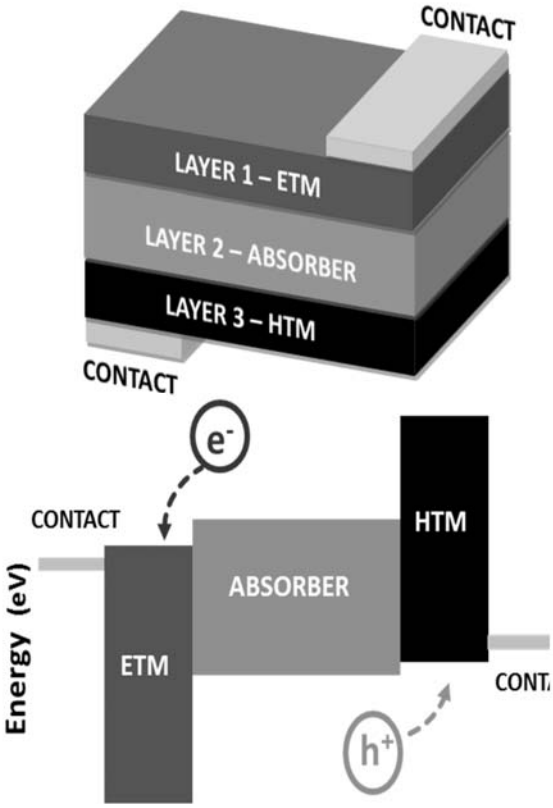

Figure. 1 The general device structure and the associated energy level diagram of PSC. Here, ETM and HTM shows Electron Transport Material and Hole Transport Material, respectively.

These materials are commonly used in other solar cell technologies and they are simply reused for PSCs along with the device concepts as well. So, it is reasonable to assume that there is a possibility for better matching materials. Also, a systematic enhancement in PSC demands an in-depth analysis of individual device components and their cumulative effect on the global performance. The band gap, electronic and energetic landscapes of each layer in PSC, and many other parameters should be considered for better understanding and performance improvement of solar cells.

Simulation-wise, there are some reported works [1,2,5-9], which can be classified in two categories. The first one is known-materials driven and covers the optimization of solar cells using common ETMs, HTMs, and contacts. The optimization targets mostly the layer thickness and doping [1,2,5-8]. The second category is toward some specific device parameters like band-offset [9] and contact work functions [7] with no preference for a specific material. Interestingly, most of the simulations show that the efficiency of PSCs can exceed 23% with moderate optimization.

In this work, we conduct a multi-property material optimization for full space of solar cell, where the essential device parameters are optimized as shown in the next section. Full space methods are performed where the complete design space is required to be optimized rather than the single variable optimization. For this reason, this method is also called as one-shot, all-at-once, or simultaneous-analysis-and-design method. An application to hybrid perovskite solar cells showed an efficiency of 26.63% can be achieved by optimizing 23 variables. The resulted data set can then be used for material screening and for devising multiple descriptors.

2 DEVICE OPTIMIZATION METHOD

Here, we present a multi-property optimization approach, in which the effects of the various physical parameters in PSC on the output efficiency have been studied. The optimization space covers the electron and hole transport materials (undefined), both contacts, and the thickness of the absorbing perovskite layer. The motive behind the study is to identify suitable matching materials for the hybrid perovskite absorber, on a global scale. The optimized parameters cover the device five layers, namely: front contact, ETM, perovskite absorber, HTM, and back contact. The presented approach optimizes the device structure and identifies the properties of the optimal matching materials (except obviously for the perovskite absorbing layer) by selecting 23 optimum design parameters. This method can potentially guide the selection of new better matching materials for ETM, HTM, and contacts. Moreover, the full-scale optimization methodology applied will provide pathways to accomplish >25% efficiency PSC.

Drift-Diffusion equation are solved numerically using SCAPS [10] which is coupled with an optimization algorithm. All of the parameters are varied within very wide, yet physically reasonable, ranges to maximize the efficiency based on the following objective function

$$\max \eta : (v_l \le v \le v_u) \quad (1)$$

where, η is the efficiency, ν is a vector of input parameters used for optimization. It is bounded between the lower limit ν_l and the upper limit ν_u. The multivariate optimization is performed using the rich optimization toolbox in MATLAB.

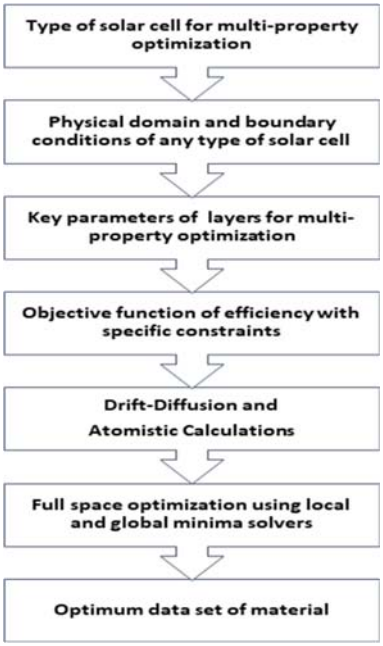

Figure. 2 Multi-property optimization framework for solar cell design using local and global optimization algorithm solvers.

For the absorbing $CH_3NH_3PbI_3$ properties, experimental values were obtained from literature [1,4] such as: bandgap (E_g) of 1.5 eV and electron affinity(χ) of 3.9 eV were considered for the simulations. Relative dielectric permittivity(ε) of 10 , CB DOS of 3.9×10^{18} 1/cm^3 and VB DOS of 2.75×10^{18} 1/cm^3 were selected from literature. Electron and hole mobility denoted as μ_n and μ_p respectively were chosen to be 2 cm^2/VS whereas donor density (N_D) and acceptor density (N_A) were 1×10^9 1/cm^3. Electron and hole thermal velocity were taken as 1×10^7 cm/s along with Radiative recombination coefficient of 2×10^{-9}. For PSC with defects, neutral defects at intrinsic fermi level (mid gap) was considered. Trap density was taken as 1×10^{14} whereas capture cross section was considered as 1×10^{-14} with a charge carrier life time of 100ns and diffusion length of 720 nm. All the simulations are conducted in AM 1.5 solar spectrum, temperature of 300 K and an absorption spectra for perovskite absorber layer taken from reference.

Constraints applied in the simulation code for the physically acceptable material properties and band alignments are shown by Eq. (2-5).

$$\chi_{ETM} - \varphi_{front\ contact} \leq 0 \tag{2}$$

$$\chi_{HTM} - \chi_{Perovskite} \leq 0 \tag{3}$$

$$\varphi_{back\ contact} - \chi_{HTM} - E_{g,HTM} \leq 0 \tag{4}$$

$$\chi_{ETM} + E_{g,HTM} - \chi_{Perovskite} - E_{g,Perovskite} \leq 0 \tag{5}$$

For the non-intrinsic recombination, two cases are independently considered; with and without defects.

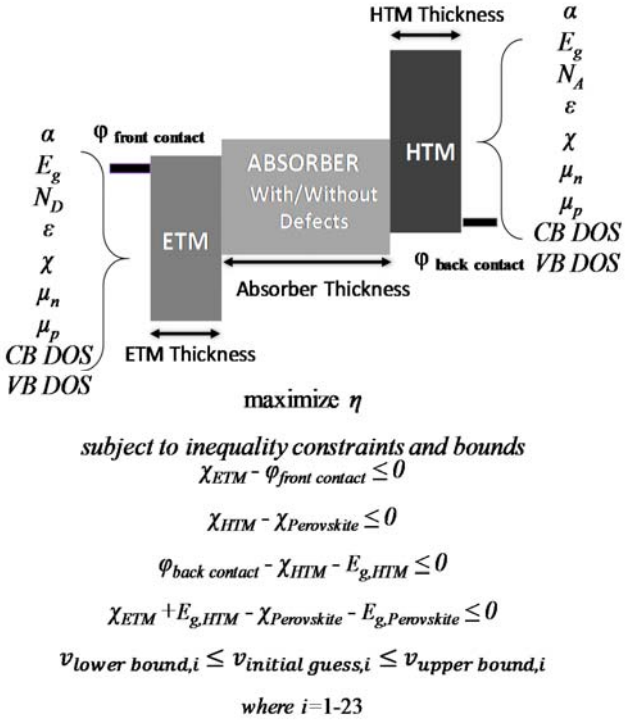

Figure. 3 Parameters and constraints considered for Perovskite Solar Cell optimization with and without extrinsic defects for different layers of solar cells.

3 RESULTS AND DISCUSSION

All optimization problems are not identical and the inherent nature of the physics enables us to choose the right tool. Moreover, the complexity of a device optimization is governed by the quantity of variables and constraints required

for search space optimization which in this case are 23 design parameters for perovskite solar cells (PSC) as outlined in the previous section. Figure 4 shows the comparison of local and global optimization algorithms for objective function of efficiency of perovskite solar cell. This will show the robust nature of the proposed method by converging to the same solution.

This procedure guarantees that the optimized material properties has found the global minima of the objective function with the lowest computational cost. Additionally, the comparison is used to examine the optimization efficiency in term of maximum efficiency and minimum computational time (expressed as function counts). Figure 4 shows a comparison of different optimizers for the number function counts obtained by PSC with and without defects. Gradient based optimizer (fmin) performed better in terms of computational cost when compared with global optimizers such as genetic algorithm, particle swarms and pattern search at the same efficiency value i.e. 26.6% for solar cell without defects and 23.4% with defects. It is a result of the convex nature of the objective function which has local and global minima coincided in the 23-dimensional space. The best performance was of fmin algorithm that resulted in the minimum function counts of 238 for PSC with defects and 1384 for PSC without defects. On the contrary, hybrid pattern search to fmin algorithm resulted in 169.44% higher computational cost than gradient based fmin method. For solar cell without intrinsic defects, this effect was more pronounced for genetic algorithm to fmin where an increase of 1361.34% in computational cost was observed compared to gradient based fmin.

The standard deviation of efficiency attained by seven employed optimization methods was 7.35×10^{-3} for case with defects and 7.50×10^{-3} for case without defects. This shows that the convergence of the target criteria for both local and global optimizers were approximately same. However, global optimizers yielded in a slow convergence due to its nature of initial guesses. This should be noted that hybrid optimizers such as pattern search to fmin and particle swarm to fmin showed less number of iterations due to the initial guesses already calculated by preceding optimizer.

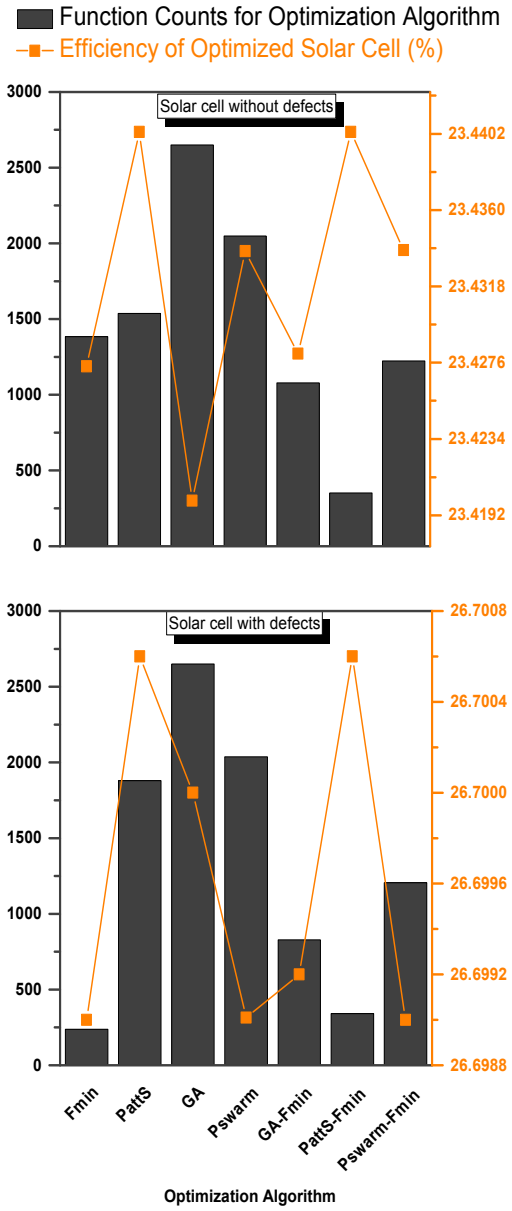

Figure. 4 Comparison of local and global optimization algorithms for objective function of efficiency of perovskite solar cell. Two cases with and without defects were considered.

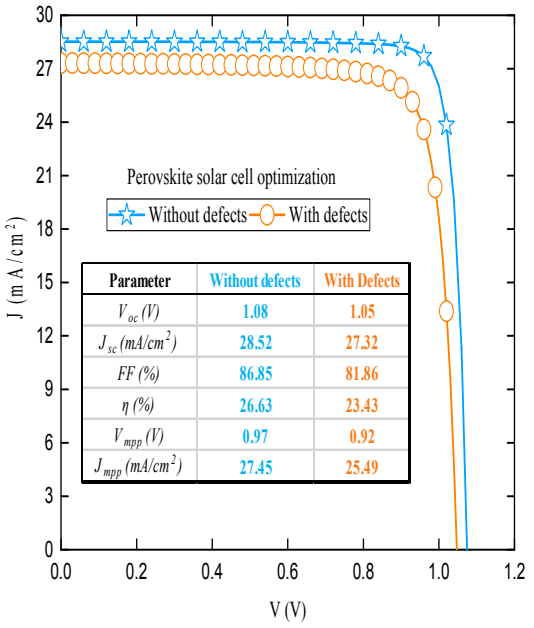

Figure. 5 Current (J) / Voltage (V) characteristics of solar cells with 23 optimized parameters.

The optimization identifies the properties of the device layers (other than the absorber) that can achieve the maximum conversion efficiency of 26.63% without defects under AM 1.5 spectrum and this is reduced to 23.43% if the defects are considered. The IV curves of the simulations are shown in Fig.5. The main change due to the defect is the open circuit voltage (V_{oc}) as it's directly a measure of recombination losses. Moreover, short circuit current (J_{sc}) was enhanced due to higher absorber thickness and low recombination in the case of solar cell without defects. As a result of optimization, a data set of 23 variable were predicted which can be used to guide the selection of new better matching materials for ETM, HTM, and contacts.

Thickness of solar cell is the key figure of merit as it determines the absorption and recombination in the absorber layer. The optimum thickness ensures that maximum charge are collected while losses are minimized by ensuring that charge carrier reach the terminals. This in turn increases the collection efficiency. Most of the performance indicators are not far from the experimentally reported values except for J_{sc}, which is around 24 mA/cm^2. There are many factors that contributed to this. But, one of the most important ones is the thickness of the absorber layer. Fig. 6 shows that J_{sc} peaks around 1100 and 700 nm thicknesses for the two studied cases because of the balance between the absorption and recombination of the perovskites. This is larger than the thicknesses currently used which is around 450 nm. Therefore, as the material quality increases of PSC, ideally thicker absorbers can be employed for sufficient charge collection.

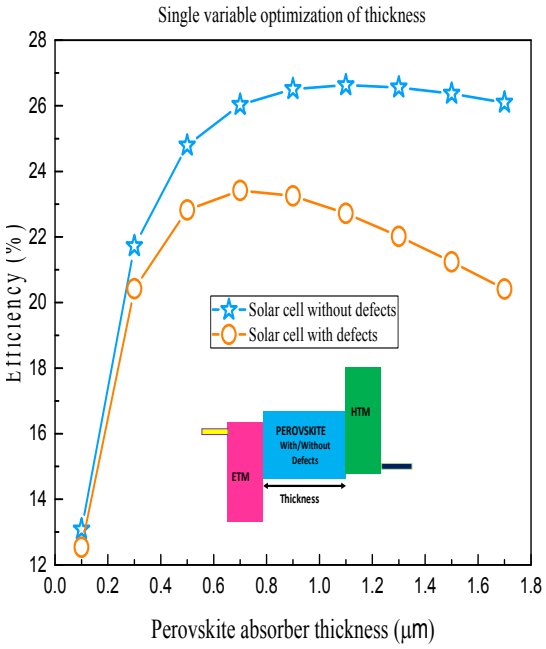

Figure. 6 Single variable optimization for perovskite absorber thickness and its effect on efficiency.

Band offsets i.e. the energy band difference from vacuum for HTM and ETM with absorber is extremely important to improve the charge transfer inside the solar cells. Conduction band offset (CBO) is defined as the difference between electron affinity between ETM and perovskite absorber. Valence band offset (VBO) shows the difference between the sum of electron affinity and band gap of perovskite

and ETM material. Energy gap of perovskite ($E_{g,PEROVSKITE}$) was considered to be 1.5 eV with $\chi_{PEROVSKITE}$ as 3.9 eV whereas $E_{g,HTM}$ was constant at 3.3 eV. Both band offsets were varied from 0.0 to 0.5 eV for analysis of performance contours as shown by Figure 7 for PSC with/without defects. These performance contours are a good measure to determine the optimum band offsets for both interfaces and to search for local and global minima in the design space. The maximum conversion efficiency of 23.4 % and 26.6 % for both cases, PSC with/without defects, was found for a perfect interface alignment of CBO (ΔE_c =0) and VBO (ΔE_v=0) as expected [9]. The effect of CBO and VBO on the Voc and Jsc is a pure optimization problem due to a conflicting nature of each on objective function. Voc was found to have positive correlation with CBO and VBO whereas the effect of Jsc was found to be primarily governed by saturation current Jo which is in direct relation with barrier height and comparable thermal energy of charge carrier to room temperature. By increasing the band offset, Voc was found to be increasing from 1.04 to 1.06 V due to the reduction of leakage current because of high barrier height, in the case of PSC with defects. On the opposite side, Jsc was found to be reduced slightly from 27.3 to 27.2 mA/cm^2 by increasing band offsets. Consequently, the optimum range of CBO and VBO based on the simultaneous optimization yielded a range of 0.0 to 0.2 eV which agrees well with the literature [9].

$$\chi_{ETM} \geq \chi_{PEROVSKITE} \rightarrow CBO \quad (6)$$

$$\chi_{PEROVSKITE} + E_{g,PEROVSKITE} \geq \chi_{ETM} + E_{g,ETM} \rightarrow VBO \quad (7)$$

It should be noted at CBO and VBO of 0.0, flat bands configuration is developed with respect to contacts which if further increased may increase the saturation current and reduce the performance of the solar cell.

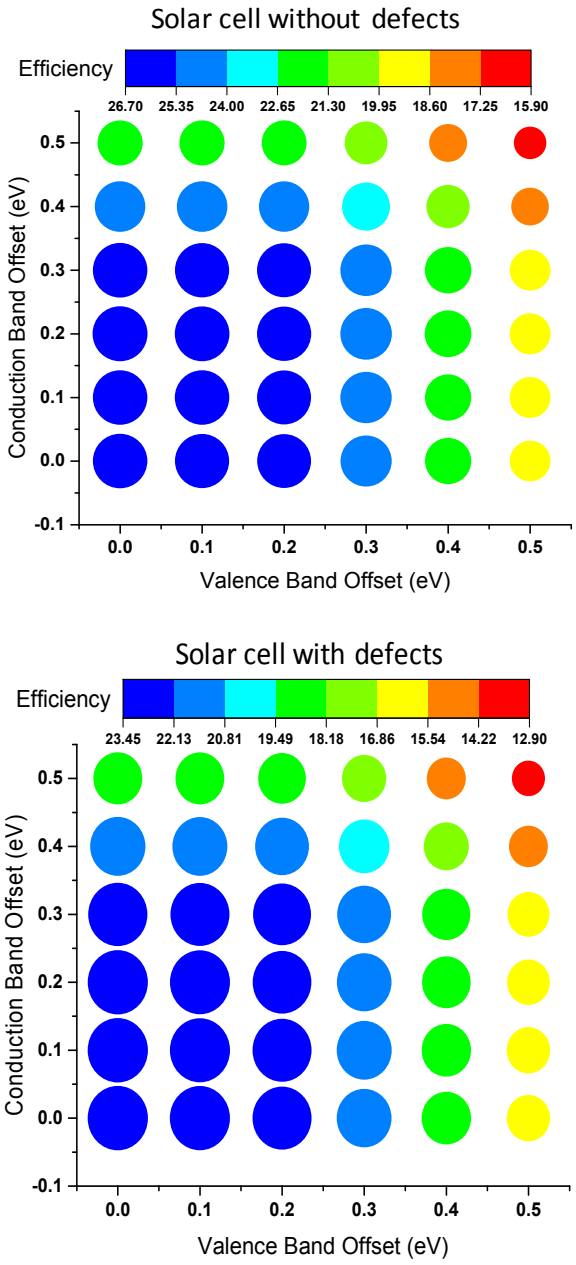

Figure. 7 Two variable optimization for valence band offset (VBO) and conduction band offset (CBO) for proper collection at contacts.

ACKNOWLEDGEMENTS

This work has been funded by Qatar National Research Fund under a Qatar National Priority Project, NPRP-6-931-2-382. We also thank the support of Qatar Environment and Energy Research Institute, Hamad Bin Khalifa University, Qatar Foundation.

REFERENCES

[1] M.I. Hossain, F.H. Alharbi, N. Tabet, Copper oxide as inorganic hole transport material for lead halide perovskite based solar cells, Sol. Energy. 120 (2015) 370–380.

[2] P. Yadav, K. Pandey, P. Bhatt, D. Raval, B. Tripathi, C. Kanth P., et al., Exploring the performance limiting parameters of perovskite solar cell through experimental analysis and device simulation, Sol. Energy. 122 (2015) 773–782.

[3] Research Cell Efficiency Records, NREL.

[4,] J. Cui, H. Yuan, J. Li, X. Xu, Y. Shen, H. Lin, et al., Recent progress in efficient hybrid lead halide perovskite solar cells, Sci. Technol. Adv. Mater. 16 (2015) 036004.

[5] K.R. Adhikari, S. Gurung, B.K. Bhattarai, B.M. Soucase, Comparative study on MAPbI3 based solar cells using different electron transporting materials, Phys. Status Solidi C 17 (2015) 13–17.

[6] F. Liu, J. Zhu, J. Wei, Y. Li, M. Lv, S. Yang, et al., Numerical simulation: Toward the design of high-efficiency planar perovskite solar cells, Appl. Phys. Lett. 104 (2014) 253508.

[7] T. Minemoto, M. Murata, Impact of work function of back contact of perovskite solar cells without hole transport material analyzed by device simulation, Curr. Appl. Phys. 14 (2014) 1428–1433.

[8] T. Minemoto, M. Murata, Device modeling of perovskite solar cells based on structural similarity with thin film inorganic semiconductor solar cells, J. Appl. Phys. 116 (2014).

[9] T. Minemoto, M. Murata, Theoretical analysis on effect of band offsets in perovskite solar cells, Sol. Energy Mater. Sol. Cells. 133 (2015) 8–14.

[10] M. Burgelman, P. Nollet, S. Degrave, Modelling polycrystalline semiconductor solar cells, Thin Solid Films. 361 (2000) 527–532.

Optimization Of Chemical Composition Of Acids And Inhibitors For De-Scale From Heat Exchanger

[1]M. Suleman Tahir, [1]Afaq Hassan,
[1]Department of Chemical Engineering University of Gujrat. Pakistan

Abstract

Scaling in boiler/heat exchangers badly affect the efficiency of equipment's and process. Various techniques were applied to remove the deposited scale inside the boiler to determine the cost effective technique.
This project investigates the analysis of scale and effect of different acids on dissolving the scale with time. Effect of HCl, H_3PO_4, HNO_3, CH_3COOH and H_2SO_4 is investigated with various concentrations to dissolve the scale of heat exchangers taken from industry located in Faisalabad region. An experimental data/results show that 2.5M HCL mixed with 0.80 g of glutamine as inhibiters has the maximum dissolving potential of scale than other acid concentrations. Process was also evaluated with time of 1hr, 1.5hr and 2 hours. The solubility potential of different acid is as follow: HCl > H_3PO_4> HNO_3> CH_3COOH>H_2SO_4.Percentage of scale removal was also investigated and results shows

HCl > H_3PO_4> HNO_3> CH_3COOH>H_2SO_4
92% >91% > 83% > 78% > 30.8%

This project has potential to rescale the

Key words: descaling, effect of inhibitors, effect of concentration of acids

1. Introduction:

Boilers are designed to produce steam or heat water. About 83% of world electricity is produced by boilers. Scale can reduce the lifetime of the boiler and the working of the boiler. Other drawbacks of scale formation are increase of cost, replacement of the boiler again and again, and a very high energy usage i.e. up to 25% [1]. In some worst scenarios the pressure of boilers may raise and damage the working place if any accident occurs. Fouling tubes of internal condenser/boiler are unfavorable to heat transfer; therefore condensing efficiency of steam decreases, which may cause a lesser vacuum pressure (higher stress) and decreases the steam turbine operations. In intense conditions bad vacuum situations inside the condensing unit could diminish electric generation efficiency by extra 50% [2].

Deposited salts decreases the thermal heat transfer efficiency and normally effects the tubes operation because of overheating which may also bring about plugging fouling of the system [3].

Figure 1 Scale of Boiler

The scale of different compositions at the boiler surfaces can be documented as:

- Corrosion parts which includes oxides of copper and iron.
- Alkaline scale of calcium hydro oxide and MgO.

- Additive scales of calcium and magnesium in combination with additive which might be typically soft and could be removed easily, and Calcium-Sulphate.

The deposition of $CaCO_3$is a main problem of many industrial operations. In many heat exchangers, scale deposits are used which behave as thermal insulator, appreciably lowering the boiler efficiency at the same time as inflicting heating element to overheat, and may cause to early component breakdown. The flow rates of flowing compounds decreases because of scale canal. Aside from manufacturing units, daily life equipment's which are used in homes consisting of water geysers, solar collectors, and many other area also effected by deposition of scale. Formation of scale in these areas can drastically decrease the efficiency of equipment and life. Other results are service charges increase, regular replacement of equipment's and may consume high energy up to 25% [4].

Chemical inhibitors and also de-scalers are currently, the very capable manner to save from scaling. But this could be very expensive and have bad effect on environment [5-6].

The inhibitors consisting of hetero atoms like oxygen, nitrogen, sulfur, and phosphorus are experimental as very efficient rust controlling compounds. The efficiency of those inhibitors change upon the density of electron which are around the hetero atoms, the wide variety of molecules having activated adsorption centers and their charge density, size of molecule, adsorption mode, metallic complexes that are formed [7]. Inhibitors used for scale are third largest product in water treatment up till 2016 of worth $ 3.6 billion.

The boiler thermal efficiency will be restored after cleaning cycle and it also reduces the cost of fuel consumption, but the cleaning costs will increase the total cost of boiler operation [8].

Cleansing of boiler mostly has the following stages [10].

- Cleaning by mechanical means
- Flushing through water
- Treatment through alkaline solution
- Cleaning by solvent
- neutralization and passivation

K. Anthony Selby [9] proposed that for chemical cleaning it is required to examinethe particular region of the boiler through scheduled checkups.

Cleaning the scale with the solvent i.e. different acids are used to clean the scale of different compositions. One of the best solvent used is hydrochloric acid. Mostly the scale contained the Fe_2O_3, $CaCO_3$,CaO, Al_2O_3, MgO and ZnO salt. Equation 1-6 shows the reactions observed when the scale is treated with the HCl acid.

$$6\ HCl + Fe_2O_3 \longrightarrow 2\ FeCl_3 + 3\ H_2O \quad (1)$$

$$CaCO_3(s) + 2\ HCl\ (aq) \longrightarrow H_2O(l) + CO_2(g) + CaCl_2(aq) \quad (2)$$

$$CaO + 2\ HCl \longrightarrow CaCl_2 + H_2O \quad (3)$$

$$Al_2O_3(s) + 6\ HCl\ (aq) \longrightarrow 2\ AlCl_3(aq) + 3\ H_2O(l) \quad (4)$$

$$2\ HCl + MgO \longrightarrow MgCl_2 + H_2O \quad (5)$$

$$ZnO + 2\ HCl \longrightarrow H_2O + ZnCl_2 \quad (6)$$

2. Materials and methodology:

The scale was collected from the "Sitara Chemicals Industries PVT Limited". The experiments were performed in the lab of university of Gujrat, Pakistan. The scale sample were treated chemically in the laboratory.

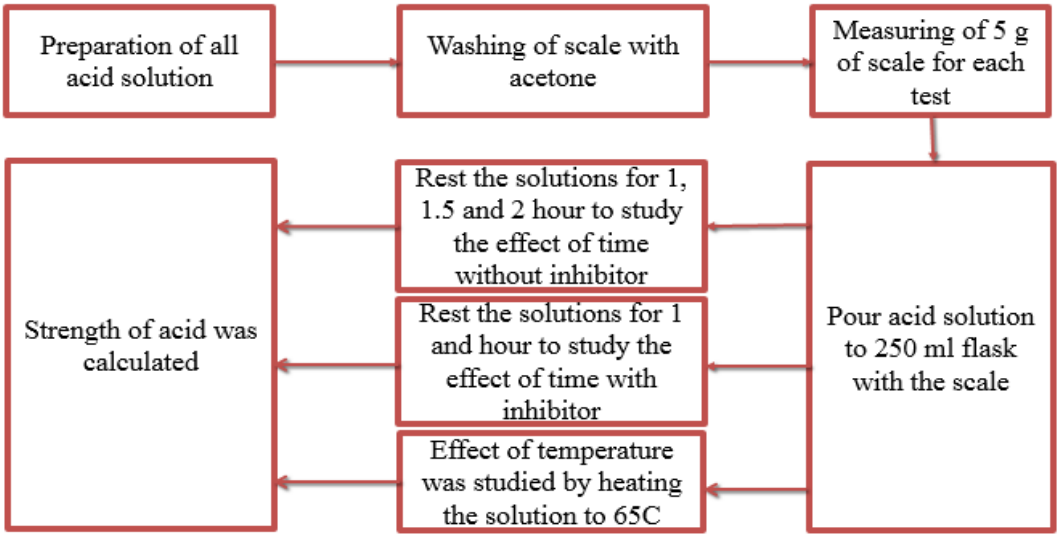

Figure 2 Block Diagram of Methodology

Different molar solution of Hydrochloric acid (HCL), Acetic acid (CH_3COOH), Nitric acid (HNO_3), Sulfuric acid (H_2SO_4) and Phosphoric acid (H_3PO_4) were prepared to check the weight loss in scale.
Firstly 0.5 M HCl solution was taken in 250 ml conical flask. Then the scale was washed with acetone and weighted 5 grams of scale was poured in the flask. The solution with the scale was left for one hour for descaling. After one hour the solution was filtered and the weight of the leftover scale was measured.
The same sample were again examined for the1.5 and 2 hour immersion time to study the effect of the time on the dissolution rate %. The same procedure was repeated for all the acids (HCl, H2SO2) at various concentrations, 0.5M, 1M, 1.5M, 2M, and 2.5 M.
To observe the effect of inhibitors i.e. glutamine and hexamine, different concentrations of the inhibitors was used (0.2 grams, 0.4 grams, 0.6 grams and 0.8 grams). To same amount of acid solution that was used for immersion time effect was selected andinhibitors were added and left the solution of hydrochloric acid and phosphoric acid for 1 hour to examine the change in the dissolution rate %.The temperature effect was also studied by the heating the sample up to 65 degree Celsius.

3. Results:

This study involves the effects of temperature, time and acid concentration on scale removal.

3.1.Effect of concentration and time:

Acids were tested in five concentrations of 0.5 M, 1 M, 1.5 M, 2 M and 2.5 M table 1 shows the results. It was found that increasing the concentration of acid scale removal efficiency increases. It was observed that 92.4 % of scale removal at concentration of 2.5 M of hydrochloric acid and 91.2 % with phosphoric acid at constant 2 hr time and 25°C temperature.
Other acids show lower dissolution rate % as compared to HCl and H3PO4 acids. Theincrease in the scale removal with increasing acid concentration is due to the increase in concentration gradient between the bulk and the solid solution interface which increase the reaction rate of the acid with scale.Figure 4-8 shows the effect of concentration of dissolution rate%.
The effect of time on scale removal was also observed findings are given in table 1 for all the acids respectively at different concentrations and at 25°C temperature. It was observed that the percentage of scale

removal increases with reactions time at a constant concentration and temperature

At 2 hours of reaction time with all concentrations of hydrochloric acid more than 70% scale removal was accomplished while with phosphoric acid maximum 65% scale removal was obtained. Increase in the time cause the scale removal to increase due to increasing the action time of the acid to break the bound between the scale particles.

For immersion tests, different molar solutions of HCl, H_3PO_4, HNO_3, CH_3COOH and H_2SO_4 in distilled water without inhibitor was used during testing at 25°C. The dissolution rates % were determined and the results are summarized in Table 1.

Table 1*Dissolution rate % of scale with different acids concentration, 0.5, 1, 1.5, 2, 2.5 molar*

Conn. acid	HCl 1 hr	HCl 1.5 hr	HCl 2 hr	H_3PO_4 1hr	H_3PO_4 1.5hr	H_3PO_4 2 hr	HNO_3 1 hr	HNO_3 1.5 hr	HNO_3 2 hr	H_2SO_4 1 hr	H_2SO_4 1.5 hr	H_2SO_4 2 hr	CH_3COOH 1 hr	CH_3COOH 1.5 hr	CH_3COOH 2 hr
0.5	68.6	70.5	72.6	64.6	68.1	70.2	50	57.8	67	2.6	2.9	3.8	29.6	32.9	35.6
1	71.8	83.9	89.4	68.2	79.7	85.4	58	62.3	69.8	13.4	13.6	13.8	42.4	48.7	57.8
1.5	77	86.8	90.4	74.2	82.1	87.8	72.4	73.6	74.2	17	17.8	19.8	53.8	68.7	70.8
2	80	90.2	91.6	79.8	84.3	88.6	76.6	78.9	79.8	22.4	23.1	24	64.4	71.3	77.2
2.5	84	91.4	92.4	83.1	88.5	91.2	79.6	82	83	29	29.9	30.8	78.2	79.1	80.0

Table shows the performance of all the five acids in the scale removal, it is clear that hydrochloric acid appears to be the better acid for scale removal than all other acids. Among all acids sulphuric acid's efficiency waspoor. All the acids shows better efficiency at 2 hours immersion time compared to 1 and 1.5H time.

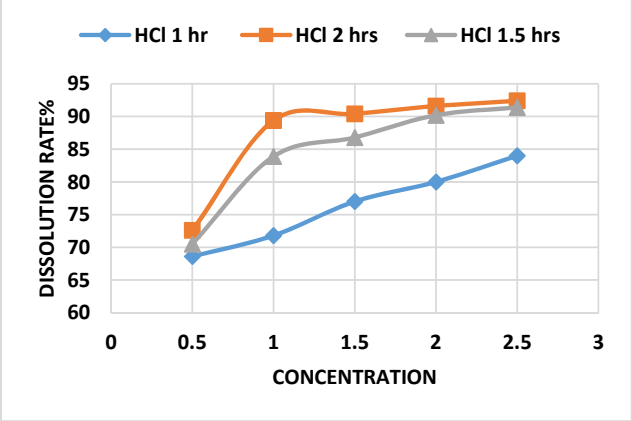

Figure 3Effect of HCl concentration on dissolution rate

Figure 3 shows the effect of different HCl concentration on scale removal under the condition of 1, 1.5 and 2hr. Experimental results shows that 2.5 M solution at 2 hour immersion time the dissolution rate% is 8.4% more than and 1 hour time. Hydrochloric acid in concentrations from 5 to 15 mass % at temperatures up to 80°C, is most favorable solvent for water-formed precipitates, it reduces the amount of the calcium and iron deposits.

Figure 4 shows the results obtained from H_3PO_4. At 2 hour time and 2.5 M concentration the dissolution rate% was found almost 8.1%higher than at 1 hour immersion time, while for 0.5 M solution a rise of 5.6% was recorded at 2 hour time. This shows that the increase in concentration and time the efficiency improved positively.The overall efficiency was lower than HCl efficiency under same experimental conditions. At 1 M concentration of acid a rapid increase was observed for 1 and 1.5 hour.

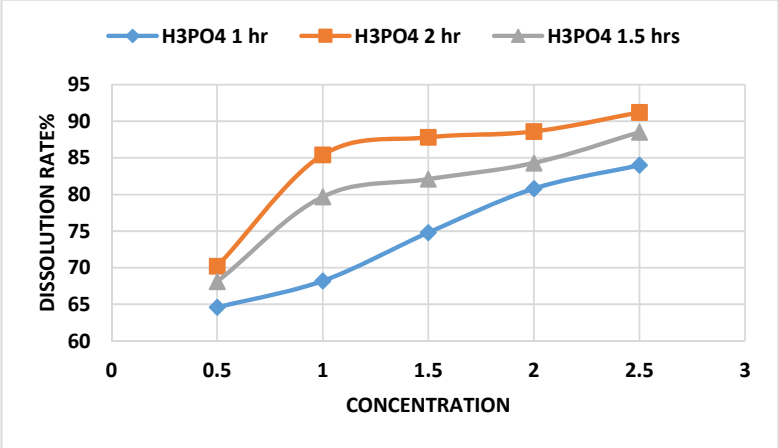

Figure 4 Effect of H3PO4 on DR%

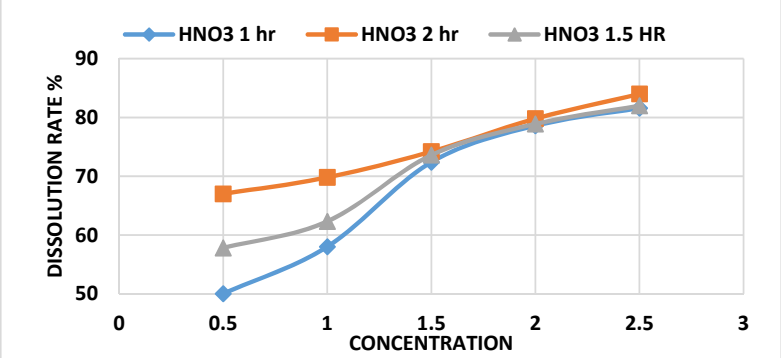

Figure 5 Effect of HNO3 on DR%

HNO_3 shows a very rapid increase in the dissolution at low concentrations of almost 17% but at higher concentrations the results are almost same at all time periods as shown in Figure 5. Thus using this acid at lower concentration give significant change in result but at high concentrations the results were not significant. At 2.5 M concentration the acid shows only 1.4% increase in dissolution rate %. Nitric acid is although not advisable to use for acid cleaning of scale but are usually used for stainless steel equipment's and with 65% HNO_3 solution. Nitric acid shows a dissolution rate % of 83% at 2hour which is even lower than HCl 1 hour rate i.e. 84%.

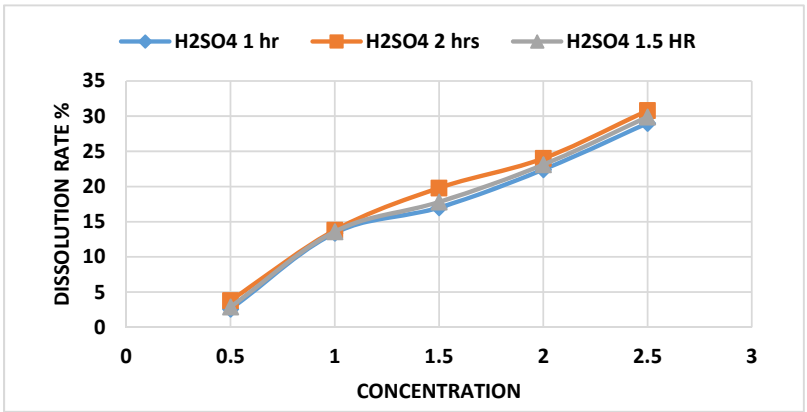

Figure 6 Effect of H2SO4 on DR%

H_2SO_4 shows a very low dissolution rate at all the concentrations as shown in figure 6. The graph shows that H_2SO_4 have low efficiency among the other acids. Time also have negligible effect on all concentrations thus giving the low dissolution rate even after 2 hours. Concentrated (98%) sulphuric acid is used to remove the iron oxide in the scale. It is about 60% low efficiency compared to 0.5 M HCl.

Figure 7 shows that CH_3COOH offer 26% dissolution at 0.5 concentrations that is very low with respect to other acids. With 1.5 M concentrations 14.9% increase in dissolution rate at 1.5 hour immersion time. Acetic acid is another solvent for chloride-free acid removal of carbonate scales in equipment, especially those made from aluminum. At higher concentrations of acid immersion time does not affect the rate of dissolution showing 1.1% increase for 2 hours and 0.8% for 1.5 hour.

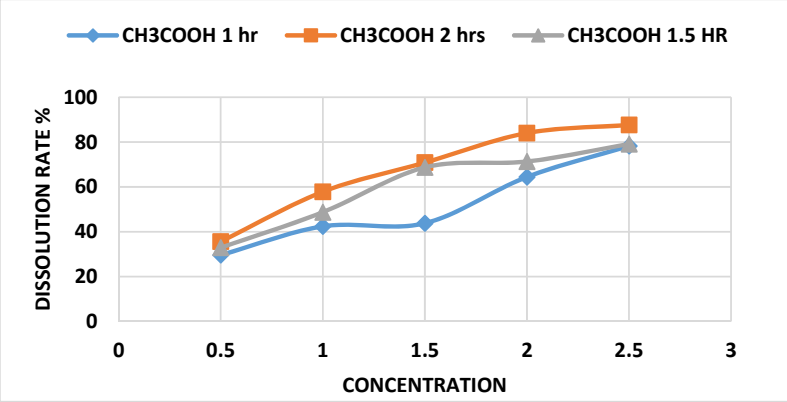

Figure 7 Effect of CH3COOH on DR%

3.1.1. Comparison of all acids on dissolution rate %

Comparison of all the acid at 1, 1.5 and 2 hour is shown in figure 8. The graph shows that HCl offers the best results among all the acids at every concentration. With the increase in time the dissolution rate % also increases. The highest rate % obtained was for HCl i.e. 92.4% at 2.5 M concentration at 2 hour immersion time. The lowest rates % were obtained from H_2SO_4 at every concentrations and every time.

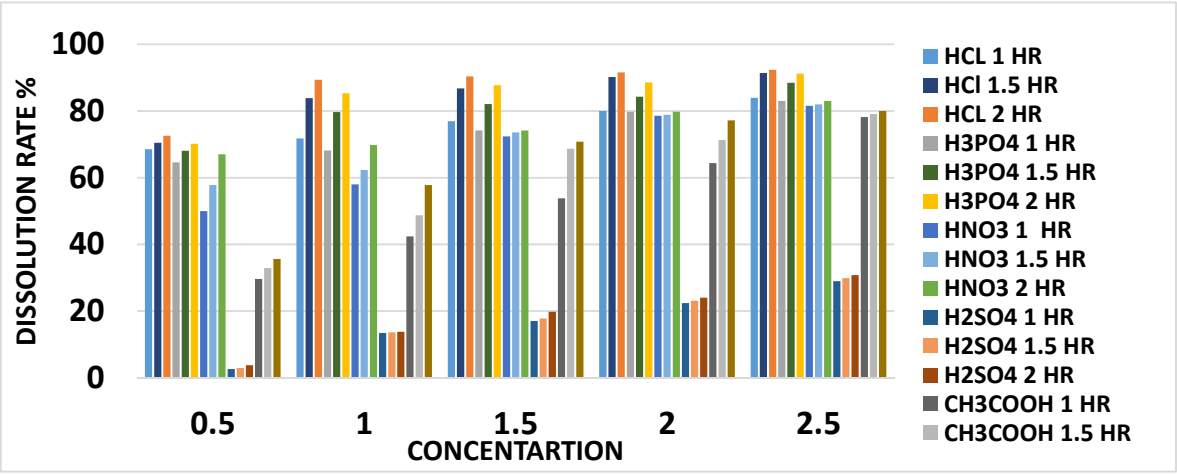

Figure 8 Comparison of all acids

3.2.Effect of inhibitors:

Adding an inhibitor to the acids is essentially to diminish its corrosive effect on metals

Scale inhibitor action is that the inhibiting compounds serve as blanket to the entire metal surface with a protective layer of compound used; this occurs as simple adsorption of the inhibitor ion on the metal surface.

Table 2-5 shows the effect of glutamine and hexamine on the dissolution rate % of the HCl and H_3PO_4. Different concentrations of inhibitors were used i.e. 0.2, 0.4, 0.6 and 0.8 grams to calculate the dissolution rate % in HCl and H_3PO_4.All the resultswere obtained by the addition of different concentrations of inhibitors for 1 hour immersion time. Only two acids were examined with inhibitors i.e. hydrochloric acid and phosphoric acid. At 0.2g of hexamine shows increase in the dissolution rate % from 68.6 % to 68.8 %. With 0.8g of hexamine the rate % increases to 70.2 % with 0.5 M HCl solution. Glutamine increased the rate to 71% with 0.5M HCl solution. Same pattern was observed with phosphoric acid. The results obtained from the hexamine inhibitor in HCl are almost same with the result obtained for 2 hour immersion time thus saving the extra time of immersion as shown in Table 3. And glutamine offer more than that obtained form 2 hour time.

For phosphoric acid the hexamine shows 88.6% efficiency which is almost same for 1.5 hour immersion time without inhibitor, with glutamine it shows 5% increase.

Table 2 Effect of Hexamine on the Dissolution rate % of HCl

Conc.acid	0.20 g hexamine	Dissolution rate %	0.40 g hexamine	Dissolution rate %	0.60 g hexamine	Dissolution rate %	0.80 g hexamine	Dissolution rate %
0.5	3.39	69	3.44	69.4	3.47	70	3.53	70.6
1	3.68	72.6	3.65	73	3.71	74.2	3.79	75.8
1.5	3.85	77	3.90	78	3.92	78.4	4.10	85.2
2	4.10	82	4.16	83.2	4.22	84.4	4.38	90
2.5	4.22	84.4	4.27	85.4	4.39	87.8	4.80	97.8

Table 3 Effect of glutamine on the Dissolution rate % of HCl

Conc.acid	**0.20g glutamine**	**Dissolution rate %**	**0.40g glutamine**	**Dissolution rate %**	**0.60g glutamine**	**Dissolution rate %**	**0.80g glutamine**	**Dissolution rate %**
0.5	3.32	70.8	3.45	71.8	3.45	73.8	3.49	75
1	3.71	74.2	3.72	74.4	3.78	78.9	3.79	80
1.5	3.91	78.2	3.93	79.8	3.96	83.9	4.10	85
2	4.12	82.4	4.18	85.3	4.48	91	4.89	96.5
2.5	4.28	85.6	4.32	87.6	4.59	95	8	100

Table 2 shows the results obtained from hexamine added to HCl solution for 1 hour immersion time, the result shows that by increasing the amount of inhibitor the rate also increases. All the rates even at 0.2 grams of hexamine were greater than those obtained without inhibitor.

Table 3 shows the results obtained from glutamine added to HCl solution for 1 hour immersion time. The results obtained were better than those obtained from hexamine. At 0.20 grams of hexamine and 0.5 M concentration of acid the rate obtained was 2.2% greater than that obtained without inhibitor. 0.8 grams of glutamine in 2.5 M concentration of acid show 100% rate showing complete dissolution of the scale.

Table 4 shows the results obtained from hexamine added to the phosphoric acid solution. 0.2 grams of hexamine shows 2.2% increase in dissolution rate at 0.5 M concentration of acid. Increased amount of hexamine shows the increased rate of dissolution. At 2.5 M concentration and 0.8 grams of hexamine an increase of 5.5% was observed at 1 hour immersion time.

Table 5 shows the result obtained from glutamine added to phosphoric acid. The results obtained from glutamine in phosphoric acid were less than those obtained from glutamine in HCl. At 2.5 M concertation of acid with 0.8 grams of glutamine added shows a rate of 89% showing that phosphoric acid demand more amount of inhibitor to dissolve the scale completely.

3.2.1. Comparison of inhibitors

Figure 9 shows the comparison of the glutamine and hexamine effect in hydrochloric and phosphoric acid. Glutamine offers better result in removal of scale than hexamine, at 2.5 M concentration of HCl 0.8 grams of glutamine shows 100% rate of scale removal while in H_3PO_4 0.8 grams shows 89% removal. At all the concentrations of acids glutamine in HCl shows better results.

3.3.Strength of the acid

Figure 11 shows the strength of the acid remaining after the immersion test.
The strength of the remaining acid after descaling was calculated for all acids of different acids by doing the titration and then calculating the K_a value for each acid. All the acids at 1 hour shows better results as the scale content is less in acid solution for 1 hour thus having better strength. The order of strength was also the same as recorded for the acid for scale removal.

Table 4 Effect of hexamine on the Dissolution rate % of H3PO4

Conc. acid	0.20g hexamine	Dissolution rate %	0.40g hexamine	Dissolution rate %	0.60g hexamine	Dissolution rate %	0.80g hexamine	Dissolution rate %
0.5	3.44	68.8	3.45	69	3.47	69.4	3.51	70.2
1	3.60	72	3.62	72.4	3.66	73.2	3.72	74.4
1.5	3.71	74.2	3.82	76.4	3.87	77.4	3.91	78.2
2	4.08	81.6	4.11	82.2	4.18	83.6	4.22	84.4
2.5	4.21	84.2	4.23	84.6	4.30	86	4.43	88.6

Table 5 Effect of glutamine on the Dissolution rate % of H3PO4

Conc. acid	0.20g glutamine	Dissolution rate %	0.40g glutamine	Dissolution rate %	0.60g glutamine	Dissolution rate %	0.80g glutamine	Dissolution rate %
0.5	3.44	68.8	3.44	68.8	3.51	70.2	3.55	71
1	3.61	72.2	3.65	73	3.72	74.4	3.75	75
1.5	3.86	77.2	3.86	77.2	3.91	78.2	4.01	80.2
2	4.10	82	4.15	83	4.25	85	4.30	86
2.5	4.22	84.4	4.27	85.4	4.35	87	4.45	89

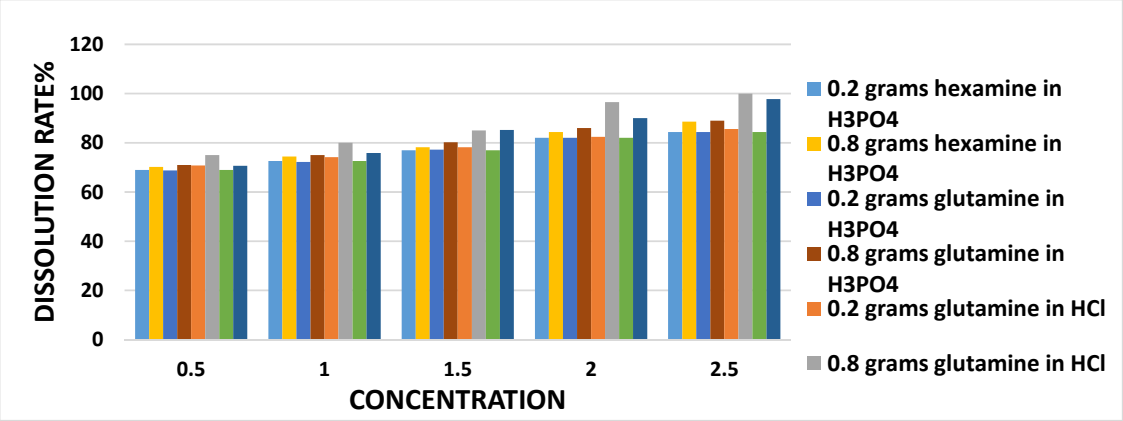

Figure 9 Comparison of inhibitors

Table 6 Effect of temperature on DR%

Acid con	HCl at 65 °C	HCl at 25 °C	H_3PO_4 at 65 °C	H_3PO_4 at 25°C	HNO_3 at 65 °C	HNO_3 at 25 °C	CH_3COOH at 65 °C	CH_3COOH at 25 °C	H_2SO_4. at 65 °C	H_2SO_4. at 25 °C
0.5	68.6	68.6	68	64.6	66	50	31.8	29.6	4.0	2.6
1	72.2	71.8	71.2	68.2	69.6	58	46.2	42.4	14.6	13.4
1.5	76	77	75	74.2	74	72.4	48	43.8	18.2	17
2	89	80	84	79.8	79.9	79.8	66.4	64.4	24	22.4
2.5	91	84	84.4	83.1	84.6	84	79.6	78.2	32	29

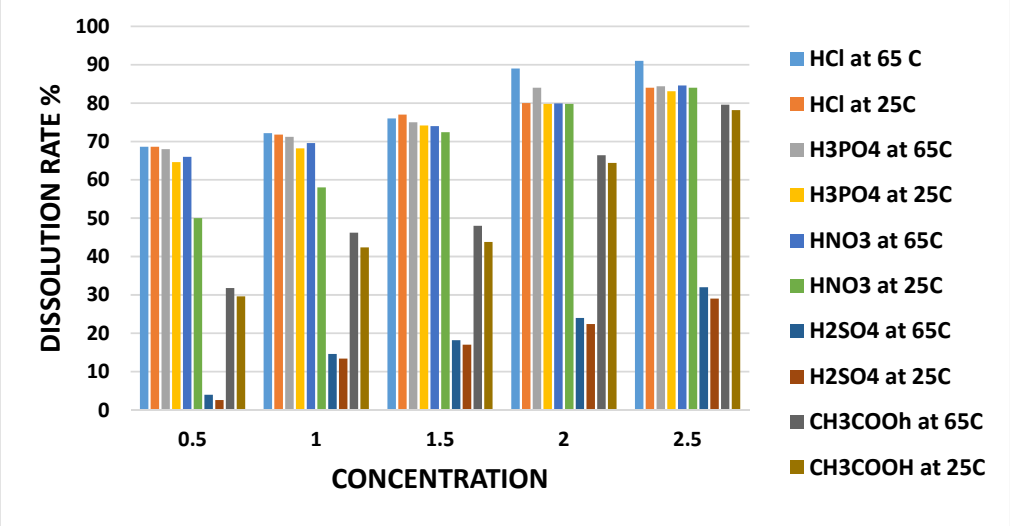

Figure 10 Effect of temperature on the DR%

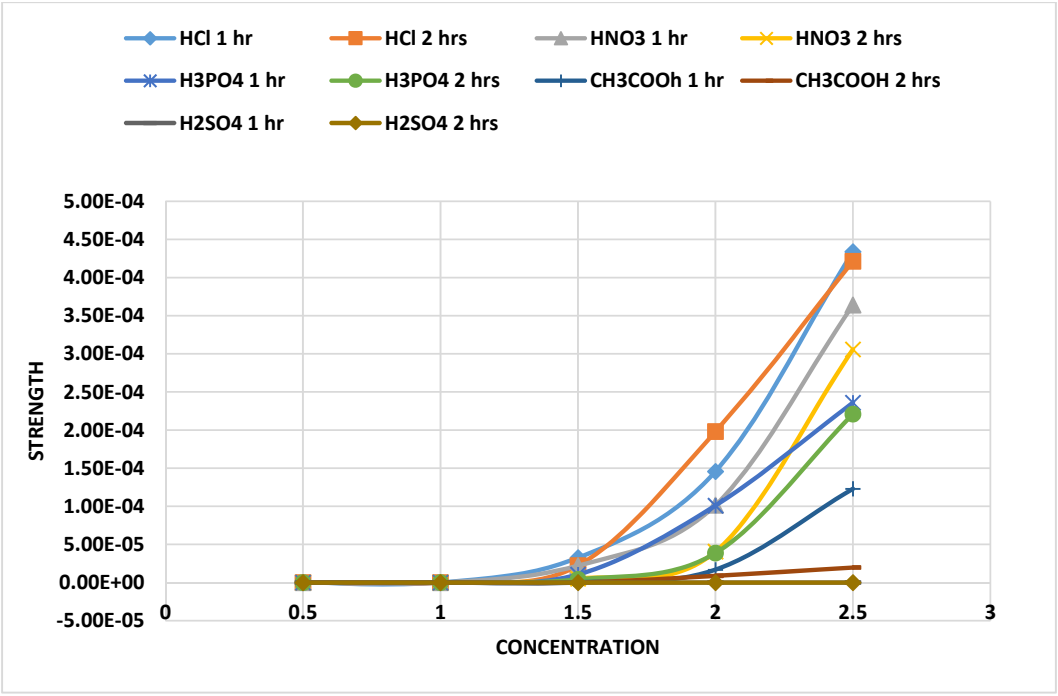

Figure 11 Strength of the acids

3.4.Effect of temperature:

Increase in temperature imparts kinetic energy to molecules causing them to move faster and collide with more frequency and causing the rate of reaction to increase, this may be due to the effective penetration of acids at high temperature to internal structure of the scale. Also the reaction rate constant increases as the temperature increases, and has its maximum value at the highest temperature. Temperature 25°C and 65°C have been used for the process of scale removed.

Figure 10shows the effect of temperature on the scale removal process for all the acids. It was observed that the higher the temperature the better the percentage of scale removal when other conditions of the process (time, concentration) remained constant. HCl at 2.5 M concentration shows about 7% increase at 65°C. At lower concentration of acid the effect of temperature is almost negligible for HCl acid.

4. Conclusions:

i. Increasing the concentration of acid the dissolution rate% increase, for HCl acid the rate for 1 hour immersion time was 68.6% for 0.5 M, 71.8 for 1 M, 77% for 1.5 M, 80 % for 2 m and 84 % for 2.5 M.

ii. $HCl > H_3PO_4 > HNO_3 > CH_3COOH > H_2SO_4$ is the order of the better acid for cleaning of the boiler, dissolution rate % for 2 hour immersion time at 2.5 M concentration was 92.4 > 91.2 > 83 >80.0 >30.8.

iii. H_2SO_4 is not recommended for the use for descaling as its scale removal power is very low even at high concentration or greater immersion time.

iv. Inhibitors offer high scale removal in less time, Glutamine offers better results than hexamine inhibitor

v. HCl in hexamine and glutamine shows 97.8% and 100% rate respectively with 1 hour immersion time and at 2.5 acid concentration, without inhibitor the rate was 84% for 1 hour at 2.5 M concentration

vi. H_3PO_4shows 88.6% and 89 % dissolution rate respectively for 1 hour , while without inhibitor it was 83.1% at 2.5 M concentration

vii. Immersion time will be reduced by adding inhibitors

viii. Increase in temperature increases the dissolution rate % e.g. for HCl at 25 C the rate was 84% while at 65C it was 91%

ix. The order of acids strength is $HCl>HNO_3>H_3PO_4>CH_3COOH>H_2SO_4$

5. Acknowledgements

The author's acknowledgeDr. Muhammad Suleman Tahir, who was the greatest source of inspiration; his efforts and valuable suggestions are truly commendable.The financial support and analytical facilities provided by university of Gujrat, Pakistan. The cooperation of Sitara Chemicals Industries PVT Limited is also acknowledged.

6. References

[1] Schmitt G., et al. (2009). Global Needs for Knowledge Dissemination, Research, and Development in Materials Deterioration and Corrosion Control. World Corrosion Organization.

[2] Andy Howell and George Saxon, Jr. "The Practical Application and Innovation of Cleaning Technology for Condenser", Proceeding of Power 2005: ASME Power2005, Chicago, Illinois, PWR2005-50173, April5-7, 2005.

[3] Vessakosol P., Charoensuk J. (2010). Numerical analysis of heat transfer and flow field around Cross-flow heat exchanger tube with fouling. Applied Thermal Engineering 30(10): 1170–1178.

[4] DOE, Energy Savers: Tips on Saving Money & Energy at Home, US Department of Energy, Office of Energy Efficiency and Renewable Energy (2011)1–44

[5] D. Hasson, H.Shemer, A.Sher, State of the art of friendly "green" scale control inhibitors: are view article, Ind.Eng.Chem.Res.50 (12) (2011)7601–7607.
[6] J.T.Hansen, G.E.Saxon, Improving condenser efficiency with innovative scale removal system technology, in ProceedingsofASME2004Conference, 2004, pp. 19–23.
[7] M. A. Qureshi, A. Singh, V. K. Singh, D. K. Yadav, A. K. Singh, Mater. Chem. Phys. 122 (2010) 114.
[8] Chen, H. (2005). Research of high scale inhibitor in boiler water treatment. Master's thesis, Tianjin University, Tianjin
[9] K. Anthony Selby, "Determining the Need for Chemically Cleaning a Boiler," International Water Conference, paper no. IWC-00-32, Pittsburgh, 2000.
[10] Mel J. Esmacher and George H. Bodman, "Use of Comprehensive Deposit Analysis Techniques to Evaluate Boiler Deposits Prior to Chemical Cleaning," International Water Conference, paper no. IWC-00-33, Pittsburgh, 2000.

[11] M. Suleman Tahir, Mahmood Salem, Experimental Study of Chemical De-scaling-I: Effect of Acid Concentration, Journal of Faculty of Engineering & Technology, 2007-2008, pages, 1-9
[12] Dr.Najwa S. Majeed, study the performance of sulfamic acid and citric acid in removal the scale deposited on the dura refinery heat exchange piping system, Number1 Volume 16 march 2010 Journal of Engineering
M. F. Bady, H. M. Hassanien, S. A. S. Mousa, A. M Hussein, A. M. K. El-Dean, study of the effects of using acetic acid in condenser de-scaling on the exhaust emissions and the performance of assist thermal power plant, PP. 971 –

Effect of Low Grade Coal Fly Ash As Adsorbent For Municipal Wastewater Treatment Coupled With Post Treatment

Syed Haseeb Sultan[1], Dr. Suleman Tahir [2], Muhammad Amin[1]

[1] Department of Chemical Engineering, Faculty of Engineering, Balochistan University of Information Technology, Engineering and Management Sciences Quetta, Pakistan. Email: engr_amin63@yahoo.com
[2] Department of Chemical Engineering, University of Gujrat, Pakistan.

ABSTRACT

Wastewater is one of the major candidates which have largest contribution in polluting the environment. The main sources of its includes domestic, industrial and agricultural, which if untreated have adverse environmental effects. Treatment of wastewater has a historical background in terms of methodology, equipment, standard parameters, but still it is of major interest to find out new improved techniques, that should be cost effective and should satisfy the desired parameters set down by environmental regulation authority. Wastewater treatment by using adsorbent such as fly ash is old but very effective technique. Researchers are engaged to find out the new sources, methods to obtain fly ash which should satisfy the range of desired quality, compare to traditional activated carbon materials such as alum etc.

This study focus on the wastewater treatment by using low grade coal fly ash as adsorbent. Balochistan is very rich in minerals especially coal resources are of much interest. This coal has wide range of applications in the region such as domestic and industrial sectors for heat and power generation. After generating the heat ash produced is thrown as waste which has serious environmental issues. This low grade coal fly ash is abundantly available and is utilized as adsorbent in this study. Waste water of two sites namely Shell vehicle service stations Jinnah town, Balochistan slaughter house situated in Quetta, Balochistan are selected for the case studies. Low grade coal fly ash as adsorbent having particle size 355 µm and 500 µm was utilized for the treatment of respective waste water samples. In vehicle service station waste water case by using 355 µm particle size of adsorbent reduction in color is highest 98%, similarly in Turbidity 99 % , BOD 89, COD 87, TDS 96, TSS 91 respectively was observed.

***Key words*:** Waste water, Low Grade coal fly ash, Adsorbent, Vehicle Service, Poultry waste, Balochistan, Coal, Particle size

1. INTRODUCTION

Clean water is very essential component for survival on earth planet to maintain the activities mainly for domestic, industrial and agricultural. With increase in population and consumption of water it is global to challenge to save the resources and to find out the new one's as well. With increase to obtain desired facilities human activities has large impact on polluting the water. This polluted water is known as waste water. To maintain the aquatic life and sustainability this waste water must be treated so that it can be recycled for reuse. Quetta is capital city of largest province (by area) of Pakistan. This is valley and situated in western part of country. Now a days water shortage emerge as major issue in city due to increasing demand with increase in population.1935 earthquake in city ruined everything, thousands of peoples dead in natural disaster. Other crises can emerge soon if steps towards upgradation of water table are not

taken as per current and future requirement in Quetta. The researchers and analyzer activists have believe that water level has been down 1000 feet from 45-50 feet in last three decades [1]. The water scenario in the province including capital is appearing a major issue with every passing day and necessary initiatives must be taken ultimatley for preserving the available resources," said the President (Balochistan) of Association of Geoscientists, A. Raziq Khan Khilji.[1]. Pakistan is one of the countries in the globe which heavily rely on agriculture especially in Asia. ALMIGHTY ALLAH has gifted this country with a lot of water sources, rivers flowing down the world largest mountains heights from the world‟s largest glaciers and free and unique bounty for this land. Pakistan is basically an agrarian economy. Out of its total geographical area of 79.61 million hectares, cultivated area is 22.05 million hectares. The total area under irrigation is 19.02 million hectares (Agricultural Statistics of Pakistan 2005-06). Irrigated land supplies more than 90 percent of agricultural production and most of the country food. Agriculture sector is regarded as the backbone of the Pakistan economy. It shares 25 percent of the country GDP. Approximately 50 percent of labor is engaged in specified sector. Agriculture field is major candidate of consumption of this source. It is also mainly used to generate energy such as hydro power generated by water stored in large capacity dams. Therefore water sources has major contribution in economy of any country [2].

The availability of fresh water source per capita in Pakistan has been observed in declining order by over 406 % from 5,260 m^3 in 1951 to 1,038 m^3 in 2010, thousand cubic meter per person only available as per global threshold limit. A report states that "If the status quo continues, then by 2020, the water availability in Pakistan would further plummeted to 877 m^3 per annum, which will further go down to an alarmingly level of 575 ft^3 in 2050.

Pakistan has capability to store water for only thirty day while in comparing with India which has storage capacity of around 120 days [3]

Contamination of water bodies by the activities of living organisms which may leads to environmental degradation is termed as water pollution. These contamination may occurs directly or indirectly discharge of effluents to fresh sources. These sources may include domestic, agricultural, industrial waste. Major waste water treatment technologies are classified as physical, chemical and biological. Each has its own significance in terms of utilization of material and process. Common phenomena for pollutants removal by using surface mechanism is known as adsorption [4]. The solution which has absorbing solute can be contacted with solid surface. The absorbable substance gets deposited on solid surface by inter molecular forces action among the molecules. [4]. The substance remains in processes is called as adsorbate, whereas, the substance on which it remains known as an adsorbent. The phenomenon of accumulating of adsorbate on solid surface is called adsorption. The newly phase might have different composition from the bulk phase. All bonding requirements are attained by another atom, molecule for constituent atom in bulk case. While atoms on the face of the adsorbent are not completely covered by other adsorbent atoms and hence might attract adsorbate [4]. Nature of bonding is dependent on characteristics of species but

commonly it is due to physio or chemo action. Approximately six hundred million tons of ash produced by coal power plant in the world in a year. Lack of proper utilization of this waste may leads to damage the environment[5]. Abundant availability from different sources, cheap and adsorptive substance qualities support this material to be used as an alternative substance for removal of contaminations from aqueous solution [8]. Low grade coal fly ash emerged as special candidate who can be produced from different process as product or by product. Incomplete combustion process may leads to produce fly ash persist in residual coal ash. Due to the increasing applications of activated carbon , researchers are engaged to find out new sources , materials which can be utilized as activated carbon, which must compete with traditional one in terms of desired quality.

2. MATERIALS & METHODOLOGY

2.1. Waste Water Samples

Waste water samples for current study were collected in 10 liter bottles from the source. Including Shell vehicle service station located in Jinnah Town Quetta. It is in the middle of Quetta city. Around 80-100 vehicles including bikes, cars and heavy vehicles get service from the point and a lot of waste water drained without its recycling. Baluchistan slaughter house is located in main street of this area. A lot of water they are utilizing for cleaning purpose and directly drained waste water into Habib Nala.

2.2. Low Grade Coal Fly Ash

The aim was to collect and utilize this material as adsorbent for waste water treatment. 5 bags each of 1 kg Low Grade coal fly ash was collected from MACH nearby area of Quetta city, which is very famous due to its coal production and supply all over the country. After collecting it was sized and screened to get the particle size of 355 µm and 500 µm respectively. After sizing this low grade sized coal fly ash was activated using standard procedure. Air dried activated granules were then checked by using electron microscope as shown in Fig 1. Analysis showed that pores were open and increase in porosity was observed. After performing this highly activated adsorbent was kept in controlled dry conditions for further application in treatment of waste water.

Fig 1: Analysis by using Electron Microscope

2.3. Experimental Procedure

Jar test standard method was applied for chemical treatment of the waste water. Tests were carried out using 355 µm and 500 µm particle size of activated low grade coal fly ash. 200 ml Samples of wastewater were taken into the beaker along with variable weight of activated low grade coal fly ash (40, 60,80 and 100g/200ml of sample) to measure the effect of weight and particulate size on percentage reduction of pollutants. In the second step as post treatment physical process was selected to ensure the purity.

Physical treatment is a pre requisite in this Physico-Chemical treatment process to get the final water quality required. Filtration is common process carried out for treatment purpose in final stage as a removal process, which has the capability to reduce fine particles from the wastewater. Mostly Sand filters can be utilized for treatment of wastewater to remove fine particles, which are not possible to be reduce by sedimentation in economic. This type of filtration depends on proper arrangement of sand bed consist of different granules size particle. The main applications in water treatment are rapid sand filtration and slow sand filtration. Rapid sand filter was used in this study and effective particle size suggested was in between 0.5 and 0.9mm, which is larger than in slow sand filters. This was only done due to low quantity of water samples used. The performance of sand filter is not only retaining used carbon particles / sludge or flocs it can also retain trace of organic contaminants that left during chemical treatment. Three different layers were made layer 1 of sand with particle size 1mm and the thickness of the bed 200mm, Layer 2 of small gravels of silica stone with particle size 20mm and thickness of the bed was 120mm and finally the layer of gravels of biggest particle size with thickness of the bed 200mm.Filter clothes type Polypropylene woven filter cloth of size 50µm were placed in between each layer for better performance. Due to small amount of filter media used washing was performed after every batch of 5 samples filtration. Sands and gravels were removed washed and placed again. For large scale, the, more convenient and method applied is the backwash cleaning method which is more reliable, less time consuming, and not much human work is involved.

3. RESULTS

Waste water samples collected from both sites were analyzed to find out its characteristics which are shown in Table 1 and Table 2below.

Table 1: Vehicle Service Station Waste water Analysis

Sr. No	Parameter	
1	Total Solids	1588.8mg/L
2	Total Suspended Solids	1000 mg/L
3	Total Dissolved Solids	590.9 mg/L
4	Turbidity	260 NTU
5	pH	6.5
6	Oil	27 mg/L
7	Color (Pt-Co)	2750
8	BOD	690
9	COD	970

Table 2: Poultry Slaughter House Waste water Analysis

Sr. No	Parameter	
1	Total Solids	1636.5mg/L
2	Total Suspended Solids	850 mg/L
3	Total Dissolved Solids	733.9 mg/L
4	Turbidity	335NTU
5	pH	7.3
6	Oil	864 mg/L
7	Color (Pt-Co)	Brownish
8	BOD	872
9	COD	2750

After analysis adsorbent and post treatment method was applied ,results of which are presented below individually for each sample.

3.1. Vehicle Service Station Waste Water

3.1.1. Using 355 micron Particle Size

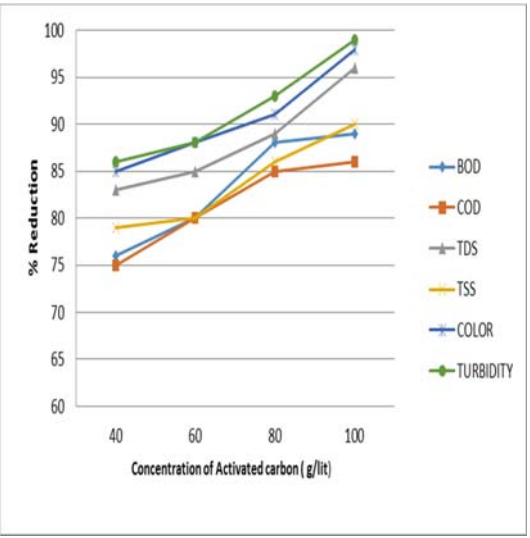

Fig 2: % removal of BOD, COD, TDS, TSS

Figure 2 shows that by using activated carbon of 355 mn particle size the % reduction in color is highest 98%, similarly in Turbidity 99 % , BOD 89, COD 87, TDS 96, TSS 91 respectively. When we used 40 gm. Of activated carbon the reduction in terms of percentage was observed as 86, 85, 76,75, 83 & 78 for Color, Turbidity BOD, COD, TDS & TSS respectively. Similarly when adsorbent was used 60 gm. 88, 87, 80, 80, 84 & 89 % reduction for Color, Turbidity BOD, COD, TDS & TSS respectively was observed. When weight of fly ash was increased to 80 gm. Reduction in parameters was 92, 91, 87, 85, 87 & 83 for Color, Turbidity BOD, COD, TDS & TSS respectively

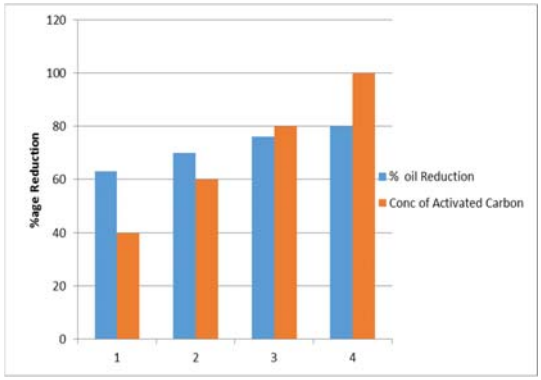

Fig 3: % reduction in oil with adsorbent weight

Figure 4.2 above describes the oil contamination reduction in terms of percentage when the particle size of adsorbent was 355 µm . Different weight of activated fly ash such as 40 , 60,80 and 100 were used to study .It has been observed that when we used 40 gm. activated fly ash color reduction was around 60 % while when we increased the weight to 60 gm. reduction in oil contents was observed about 65%.

Similarly increase in weight to 80 and 100 gm. oil contents reduced about 75 & 80 % respectively. This analysis concludes that with particle size of 355 micron when used for vehicle service station waste water, increase in adsorbent weight shown the increase in reduction of oil contamination.

3.1.2. Using 500 micron Particle Size

Figure 4 shows that by using activated carbon of 500 mn particle size the % reduction in color is highest 94%, similarly in Turbidity 95 % , BOD 87, COD 86, TDS 86, TSS 87 respectively.

When we used 40 gm. Of activated carbon the reduction in terms of percentage was observed as 85, 86, 73,75, 81 & 73 for Color, Turbidity BOD, COD, TDS & TSS respectively. Similarly when adsorbent was used 60 gm. 88, 88, 76, 80, 83 & 80 % reduction for Color, Turbidity BOD, COD,

TDS & TSS respectively was observed. When weight of fly ash was increased to 80 gm. Reduction in parameters was 91, 91, 84, 84, 87 & 84 for Color, Turbidity BOD, COD, TDS & TSS respectively

Following first set of experiments the results are shown in (Figure 4.3). This Indicate that when using 100 % pure fly ash as adsorbent (500 µm particle sizes and 100 gram of weight) gives the percentage reduction in color is 94 while in turbidity is 95 % while in reduction in BOD , COD , TDS and TSS is 87 , 86, 93 and 88 % respectively.

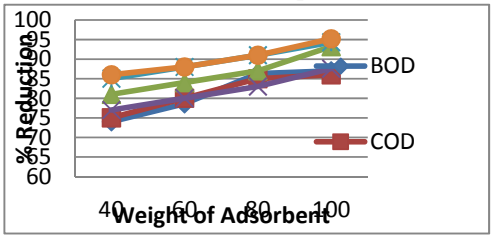

Fig 4: % removal of BOD, COD, TDS, TSS

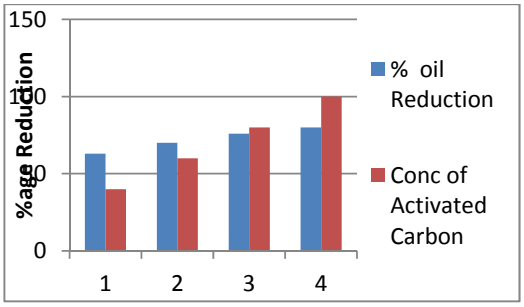

Fig 5: % reduction in oil with adsorbent weight

Figure 5 above describes the oil contamination reduction in terms of percentage when the particle size of adsorbent was 500 µm . Different weight of activated fly ash such as 40 , 60,80 and 100 were used to study .It has been observed that when we used 40 gm. activated fly ash color reduction was around 61 % while when we increased the weight to 60 gm. reduction in oil contents was observed about 67%.

Similarly increase in weight to 80 and 100 gm. oil contents reduced about 76 & 79 % respectively. This analysis concludes that with particle size of 500 micron when used for vehicle service station waste water, increase in adsorbent weight shown the increase in reduction of oil contamination.

3.2 Poultry Slaughter House Waste Water

3.2.1 Using 500 micron Particle Size

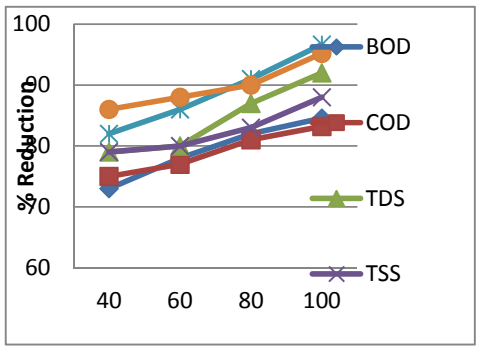

Fig 6: % removal of BOD, COD, TDS, TSS

Figure 6 shows the results obtained by using water sample obtained from Slaughter house (poultry). It is representation b/w %age reduction of pollutants against the weight of fly ash used. Above figure describes that by using activated carbon of 500 mn particle size the % reduction in color is highest 96%, similarly in Turbidity 95 % ,BOD 83, COD 84, TDS 92, TSS 87 respectively.

When we used 40 gm. Of activated carbon the reduction in terms of percentage was observed as 85, 82, 72,74, 77 & 77 for Color, Turbidity BOD, COD, TDS & TSS respectively. Similarly when adsorbent was used 60 gm. 87, 86, 77, 76, 79 & 80 % reduction for Color, Turbidity BOD, COD, TDS & TSS respectively was observed. When weight of fly ash was increased to 80 gm. Reduction in parameters was 92, 90, 82, 81, 87 & 88 for Color, Turbidity BOD, COD, TDS & TSS respectively. Hence it depicts that same as in precious case weight of

adsorbent increased results in higher reduction of pollutants.

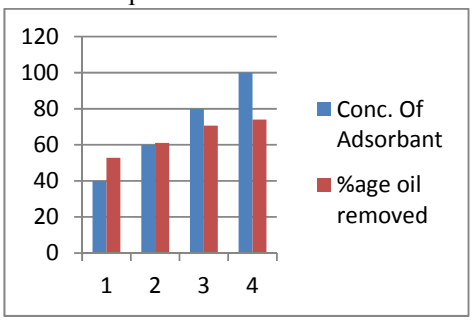

Fig 7: % reduction in oil with adsorbent weight

Figure 7 above describes the oil contamination reduction in terms of percentage when the particle size of adsorbent was 500 µm . Different weight of activated fly ash such as 40 , 60,80 and 100 were used to study .It has been observed that when we used 40 gm. activated fly ash color reduction was around 55 % while when we increased the weight to 60 gm. reduction in oil contents was observed about 61%.

Similarly increase in weight to 80 and 100 gm. oil contents reduced about 70 & 78 % respectively.

3.2.2. Using 355 micron Particle Size

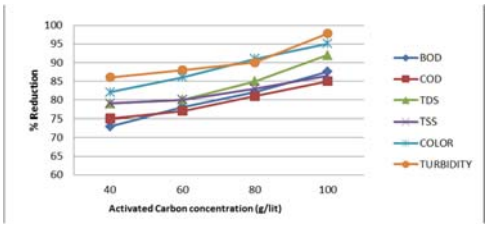

Fig 8: % removal of BOD, COD, TDS, TSS

Figure 8 shows that by using activated carbon of 355 mn particle size the % reduction in color is highest 96%, similarly in Turbidity 98 % , BOD 87, COD 85, TDS 93, TSS 87 respectively.

When we used 40 gm. Of activated carbon the reduction in terms of percentage was observed as 83, 86, 74,75, 79 & 79 for Color, Turbidity BOD, COD, TDS & TSS respectively. Similarly when adsorbent was used 60 gm. 86, 89, 78, 77, 80 & 80 % reduction for Color, Turbidity BOD, COD, TDS & TSS respectively was observed. When weight of fly ash was increased to 80 gm. Reduction in parameters was 91, 90, 82, 81, 85 & 84 for Color, Turbidity BOD, COD, TDS & TSS respectively. Increase in adsorbent weight reflects considerable reduction in contamination.

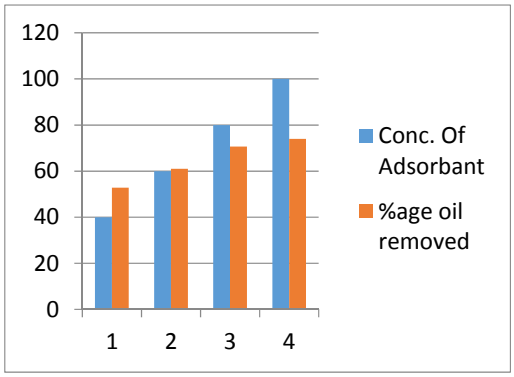

Fig 9: % reduction in oil with adsorbent weight

Table3 : % Reduction after Post treatment for Vehicle Service station waste water

Sr.No	Parameter	% Reduction
1	Total Solids	99.5
2	Total Suspended Solids	99
3	Total Dissolved Solids	99.2
4	Turbidity	3 NTU
5	pH	7.3
6	Oil	97
7	Color (Pt-Co)	98.7
8	BOD	96
9	COD	95

Table 4: : % Reduction after Post treatment for Vehicle Service station waste water

Sr.No	Parameter	% Reduction
1	Total Solids	95
2	Total Suspended Solids	96.3
3	Total Dissolved Solids	98
4	Turbidity	5 NTU
5	pH	8.3
6	Oil	94.6
7	Color (Pt-Co)	97
8	BOD	96
9	COD	98

4. CONCLUSION

From all results obtained it has been concluded that low grade coal fly ash can be utilized as adsorbent for commercial waste water treatment which is not only the economical but also covers less area(unit assembly). Smaller units can be installed in city to treat waste water and reuse which helps to save the water for future generation.

6. REFERENCES

[1] "Quetta to face water crisis soon."

[2] M.A.Qureshi, "Water Resources of Pakistan," National University of Modern Languages, Islamabad2012.

[3] "Crops grown in contaminated water sold unchecked in Quetta."

[4] M. N. Rashed, *Adsorption technique for the removal of organic pollutants from water and wastewater*: INTECH Open Access Publisher, 2013.

[5] F. Noli, G. Buema, P. Misaelides, and M. Harja, "New materials synthesized from ash under moderate conditions for removal of toxic and radioactive metals," *Journal of Radioanalytical and Nuclear Chemistry,* vol. 303, pp. 2303-2311, 2015.

Physico-Mechanical and Thermal Properties of Engineering Purpose Composite Material

S. J. Mahmood & AFK Ifrahim

PCSIR Laboratories Complex Karachi.

ABSTRACT

Natural fibers such as jute, coir, sisal, pineapple, ramie, bamboo, banana etc., are getting attention from reserachers and academicians to utilize in polymer compoistes due to their eco- friendly, biosustainibility and biocompatibility. Natural fibers have been focussed in the development of natural fiber composites primarily in value added applications specifically for engineering materials and domestic purpose. In this study polymer/ thermoset resin reinforced with natural cotton fiber was characterized physicomechanically by Universal Testing Machine (UTM) with 1000 kN load cell provided with different cross heads attachments while thermal properties were studied with thermogravimetric analyzer (TGA). Fiber contents in given matrix not only enhances the mechanical parameters such as tensile strength, compressive strength and modulus of elasticity but also made resistant against chemicals (acid/ alkali/ salt), organic solvents and lubricants as compred to natural wood. TGA- thermogram was showed that the material has remarkable temperature resiatance. It was found that the fiber reinforced polymer material was significant tear resistant as well as distinguished rigidity under various solvent systems.

Key words: Fiber Reinforced Polymer, UTM, TGA & Thermals.

1. INTRODUCTION:

Composite materials are made up of two or more phases where the properties are distinct from the individual combining materials. Polymer matrix composite materials are composed of matrix polymer (continuous phase) and reinforcing material(s) (dispersed phase). Natural fibers, glass fiber, carbon fiber, organically modified clay, inorganic fillers are few examples of reinforcing materials [1].

Highly-cross linked thermosetting polymers are well known for the production of polymer matrix based engineering materials [2]. Phenol-Formaldehyde (PF), a synthetic thermoset resin, is used in the production of molding compounds, laminates, lacquers and varnishes [3,4]. Phenol-formaldehyde composite have been prepared with wheat straw [5], Capparis Decidua (ker) Fiber [6], inorganic fillers [4,7-8], banana fiber [9], oil palm empty fruit bunch fiber [10], cellulose fiber [11-13], jute fabric and sisal random mat [8,14] and varying the phenol-formaldehyde ratio [3].

Mechanical, thermal and physico-chemical properties of the cured polymer matrix composite not only depends on the curing variables such as time, temperature, and pressure [5] but also affected by the type of the reinforcing material and the application environment [15].

As far as the authors' knowledge is concerned only few literatures are devoted to the study of phenol-formaldehyde impregnated with cotton fabric laminates. Woven cotton fabric/Phenol-formaldehyde (CF/PF) composites may find applications in those environments where high dimensional stability and good mechanical properties are required in the presence of organic solvents, oils and water are encountered such as wear-ring.

2. EXPERIMENTAL:

2.1 Materials

Details of the raw materials are shown in table 1.

S. No.	Raw material	Properties
1.	Cotton woven fabric	10 g/m^2
2.	Phenol-formaldehyde resin	Mesh size = 200 Water content = 0.5-2.0% Free phenol = 1.5-4.0%

2.2 Preparation of CF/PF Composite Samples

Compression molded samples were prepared using hand-layup process on a laboratory press (Gibitre, Italy). The panel samples were prepared by sandwiching the two cotton fabric layers in the three layers of power phenol-formaldehyde resin. The samples were prepared in the dimension of 200 mm x 100 mm x 50 mm in two steps. In the first step panel was pressed for about 7 min at 120 °C and 50 bar. In the second step the temperature and pressure were raised to 150 °C and 100 bar, respectively. The sample was held for 2 min at the second step. The second step was included to reach the high degree of cross-linking as reported by the supplier. The samples were cooled to room temperature under ambient conditions and stored in a desiccator for further characterizations.

3. METHODOLOGY

The main objective is to select natural fibers which are available easily and eco-friendly. Hence we have selected the widely available cotton fiber. Islamic Republic of Pakistan is the largest producer of cotton and included in leading cotton producing countries of the world[e]. The statistic shows that Pakistan amounted to around 1.68 million metric tons in crop year 2016/2017. Phenol formaldehyde resins were from David Zhang Jiaxing Honing Co. Ltd., China used for the production of panels. The resins were subjected to standard lab analysis for the determination of the specifications. The lab analysis included the determination of curing time, free phenol, water content and screening (200 mesh). Fourier Transform Infrared Spectroscopy was carried out with AVATAR 320 FT IR Thermo Nicolet. Spectrum was characterized that the deformation vibrations of –C-H bonding in aromatic units correspond to the absorption bands in the 600-900 cm^{-1}. The bands at 997 and 1025 cm^{-1}, characteristic of C-O bonds in hydroxymethyl groups attached to aromatic ring. The bands at 1060 cm^{-1}, characteristic of C-O bands in an ether group. The band at1110 cm^{-1}, characteristic of the deformation vibration of aromatic –CH bonds, 1205 cm^{-1} for phenolic hydroxyl and at 1275 cm^{-1} for sodium salt of phenolic hydroxyl [f] as shown in Figure 1. Sample panel was produced at lab scale for physicomechanical characterization of the composite. The sample preparation and characterization conducted at the premises of Pakistan Council of Scientific & Industrial Research (PCSIR) Karachi Laboratories Complex (Applied Chemistry Research Center- ACRC). The panel sample was muliple layers of cotton fabric and henol formaldehyde resins alternately having dimensions 200 mm × 100 mm × 50 mm. Sample was pressed with Laboratory Press (Gibitre, Italy) provided with controlled pressure (upto 250 bar) and temperature (upto 300 ^{o}C).

The assembled panel was initially pressed at 120 ±5 ^{o}C for 7 minutes with 50 bar pressure and then increased pressure upto 100 bar at 150 ±5 ^{o}C for 5 minutes. Physicomechanical characterization such as tensile test, modulus of elasticity and compression test was performed on a computer controlled Universal Testing Machine (UTM measuring 1000 kN Load Cell made Tinius Olsen, USA) according to the guidelines of ASTM D638 standard and ASTM D790 standard. Six sample specimens

were tested to for each test and their average values are used to determine tensile strength, modulus of elasticity and compression strength. Separation rate of cross heads for tensile test, modulus of elasticity and compression test was maintained at 10 mm.minute^{-1}. Instrumental Hardess test was determined with Rockwell Hardness Tester made INDENTEC Hardness Testing Machine Limited United Kingdom provided with ball indenter 1/16" Dia at 60 kgF load. Thermal properties of the samples were monitored by Thermo Gravimetric Analyzer (TGA). Composites were taken using a computer controlled eSTAR software TGA/ SDTA851e METTLER TOLEDO Switzerland. The TGA/DTA module uses a horizontal system micro balance machine. The experiment was carried out from 30 oC to 700 oC. The heating rate was adjusted at 5 oC / minute. The experiment was proceed in the presence of Nitrogen gas (Linde Pakistan) maintained at the rate of 70 ml per minute alongwith constant circulation of water – ethylene glycol mixture from chiller kept at 21 ^{o}C temperature.

4. RESULTS AND DISCUSSION:

The physico- mechanical properties such as tensile test, modulus of elasicity, compression test and instrumental hardness (Rockwell) are determined. The results obtained from the various tests are presented and possible reasons for the mechanical behavior of the composite are discussed.

Tensile test was performed on a computer controlled universal testing machine according to the guidelines of ASTM D638 standard with a specimen having dimensions of 150 mm length, 25 mm width and 20 mm thickness. Various mechanical properties such as maximum load, displacement at maximum load and maximum stress with and without solvents were determined and tabulated in Figure 1. Figure 1 shows a comparison of the maximum load, displacement and maximum tensile stress of various solvents system at 30 ^{o}C for 1000 minutes. By Table 2, results are clear that, composite material is resistant against various solvent systems.

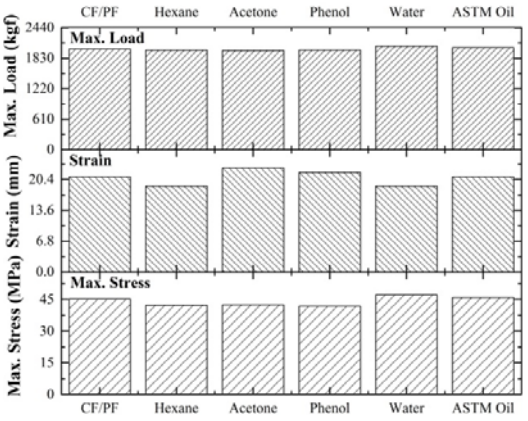

Figure 1: Effect of organic solvents (Hexane, Acetone, and Phenol), water, and ASTM Oil on the tensile properties of CF/PF composites.

Compressive load was applied on the composite material using UTM Machine according to the guidelines of ASTM D695 standard and the parameters under compression were determined. The mechanical properties such as maximum load, displacement at maximum force and maximum stress were determined with and without solvents were determined with a specimen having dimensions of 56 mm length, 55 mm width and 17 mm thickness and are shown in figure 2.

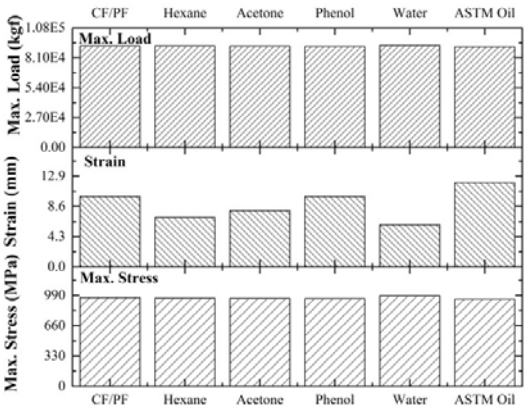

Figure 2: Effect of organic solvents (Hexane, Acetone, and Phenol), water, and ASTM Oil on the compression properties of CF/PF composites.

Figure 2 shows a comparison of the maximum load, displacement and maximum compressive stress of various solvents system at 30 ^{o}C for 1000 minutes. By figure 3, it becomes clear that, composite material under compression test is resistant against various solvent systems.

The instrumental Rockwell hardness was determined by using Rockwell hardness tester according to ASTM D785 standard specimen size of 25 mm × 25 mm × 19.5 mm. The results of Rockwell hardness (HRF) and specific gravity with and withour various solvents after 1000 minutes at 30 ^{o}C are tabulated in figure 3. Specific gravity was determined according to ASTM D792 standard specimen size of 25 mm × 25 mm × 19.5 mm. Results of instrumental Rockwell hardness and specific gravity show resistant/ inert behaviour of composite material against various solvent systems at 30 ^{o}C for 1000 minutes.

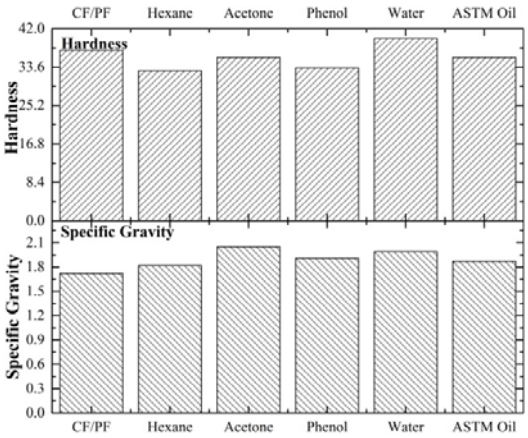

Figure 3: Effect of organic solvents (Hexane, Acetone, and Phenol), water, and ASTM Oil on the hardness and specific gravity of CF/PF composites.

The TGA thermograph of composite material is presented in Figure 2. Objectives of TGA analysis are to investigate the samples' decompoistion performance and determine the highest temperature that can be safely applied during sampling/ pressing of the composite panel. The thermogram of 10.24 mg composite material out of 17.24 mg is mentioned above while the remaining would be the residue of sample. Thermograph shows two (2) patterns i.e. a & b. In Figure 5, (**a**) shows the actual graph of TGA i.e. mass loss versus temperature of composite material while (**b**) is the manipulation in term of mathematical derivative i.e. derivative mass loss (1st order-one of the important software *STAR^{e} SW 9.10*, application function) versus temperature.

TGA graph of composite material shows clearly that the mass loss implemented in two steps. The first mass loss is performed at temperature between 41 ^{o}C and 377 ^{o}C where about 63 % of the initial mass is lost, while a further 39.5 % of the mass is lost at the temperature range of 377 ^{o}C and 592 ^{o}C. The above findings are in consistency with liteature references where TGA measurements show the composite material sample perform endothermically two degradation peaks temperatures at 378 ^{o}C and 532 ^{o}C accordingly. The first mass reduction is attributed to water loss that occurs close to 100 ^{o}C. It is even more clearly indicated by derivative endothermic peak at about 105 ^{o}C (i.e. **b**). The major mass loss of sample takes place at the temperature range of 200 ^{o}C and 390 ^{o}C as the temperature approaches the transition point. The derivative plot (i.e. **b**) shows this phenomenon by a curve in this vicinity with endothermic peak at the temperature of 379 ^{o}C. The mass loss over the tempertaure at 200 ^{o}C is due to the evolution of various organic compounds [g].

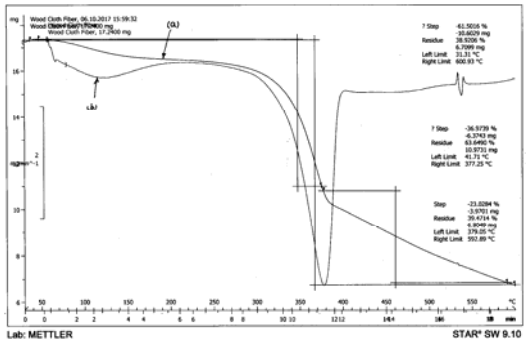

Figure 4: Thermogravimetric Analysis Thermogram of Composite Material: Mass loss (mg) versus Temperature (^{o}C) and Time (minutes)

CONCLUSIONS:

Natural Fibers are renewable raw materials, environmentally friendly material and they are recyclable. Extensive uses of this material will save wood resources and thus protect forests. In this study, the composite materials are reinforced with natural fibers. The developed natural fiber composite used in various applications in the field of Automobile, construction and manufacturing and being adopted in aircraft interior decoration, designing body parts.

1. Based on physico-mechanical investigations such as maximum load, maximum stress and displacement at maximum force during tensile, compression and modulus of elasticity tests are being determined with and without different solvent systems at 30 ^{o}C for 1000 minutes.
2. Consistency in physico-mechanical results i.e. tensile, modulus of elasticity and compression test showed that the composite material has excellent solvents resistant
3. Consistency in instrumental Rockwell hardness and specific gravity revealed that the sample chemistry and dimensions remain unchanged under given solvent syustems at 30 ^{o}C for 1000 minutes.
4. On the basis experimental findings and obervations it is evaluated that the composite material is recommended for masking the teared material specifically pressure and clutch plates of automobiles.

5. REFERENCES:

1. Wang Ru-Min, Zheng Shui-Rong, Zheng Y., Polymer Matrix Composites and Technology, 1st Ed., Woodhead Publishing, 2011.
2. Chawla K K., Composites Materials: science and engineering, 2nd Ed., Springer-Verlag New York, Inc., 1998.
3. Kaith B.S., Chauhan A., E-Journal of Chemistry, 2008, 5(S1):1015-1020.
4. Szałajko R., Oleksy M., Oliwa R., Budzik G., Polimery, 2016, 61(11-12):855-858.
5. Kumar M. Sinha A.S.K., Applied Polymer Composites, 2014, 2(1):37-44.
6. Singh G.P., Mangal R., Bhojak N., Dixit M., Saxena N.S., AIP Conference Proceedings, 2010, 55:CP1249.
7. Strecková M., Füzer J., L' Medvecký., Bureš R., Kollár P., Fáberová M., Girman V., Bull. Mater. Sci., 2014, 37(2):167-177.
8. Francucci G.M., Rodriguez E.S., Vázquez A., 2010, The 10th International Conference on Flow Processes in Composite Materials (FPCM10).
9. Joseph A., Baby B., Thomas A.B., Krishnan S.S, Euro. J. Adv. Engg. Tech., 2015, 2(5):85-90.
10. Jaafar S.N.S., Amran U.A., Roslan R., Hua C.C., Zakaria S., International Journal of Energy and Power Engineering, 2015, 9(1):171-174.
11. Athijayamani A., Das M.C., Ramanathan K., BioResources, 2017,12(1):1960-1967.
12. Pugazhenthi N., Thamilarasan J., Kumar A.S., International Journal of Mechanical Engineering and Technology, 2017, 8(5):59-64.
13. Satyanarayana S., cement concrete composites,1990,12(2):117-
14. Joseph K., J Appl. Poly. Sci., 1999, 3:367-
15. Mallick P.K., Fiber-Reinforced Composites: Materials, Manufacturing, and Design, CRC Press, 3rd Ed., 2008.

Self-Reduction Of Magnetite Ore Mixed with Bitumen

A. K. Ansari[1], H. L. Soni[1]*, Zubair A. Chandio[1], Mukhtiar A. Mallah[1], Zeeshan A Hameed[2]

[1]Chemical Engineering Department, Quaid-E-Awam University of Engineering, Science & Technology, Nawabshah, Sindh, Pakistan
[2]Department of Quality Assurance, Peoples Steel Mills Ltd., Karachi, Pakistan

*Corresponding author. Tel.: +92-33-22984883
E-mail address: soni.hiralal@quest.edu.pk

ABSTRACT

The utilization of magnetite bitumen briquettes considered to be efficient in reduction of ore in the blast furnace. In this paper the direct reduction data of concentrate magnetite ore mixed with bitumen is presented, focusing on self-reduction. Results showed that the reduction is likely to be influenced by the chemical kinetics of both carbon oxidation and magnetite reduction in the temperatures range 400-1100 ºC. Basically, the bitumen was used as a binder to produce high crushing strength magnetite pellets. The additional advantage of using bitumen is that it is an integral source of reducing potential which significantly contributes to the overall reduction of iron oxide in hydrogen at temperatures above 800°C. The carbonization show self-reducing properties of iron oxides and weight loss was observed to increase by using bitumen as high as 9.4 % at 1100 °C.

Keywords: Magnetite Ore, Bitumen, Pellet, Non-Isothermal Reduction process, Blast Furnace

1 INTRODUCTION

Steel can be produced by two major routes: Basic Oxygen Furnace (BOF), uses primary sources such as iron oxide with addition of base chemical, and Electric Arc Furnace (EAF), called secondary steelmaking process which is used primarily to re-melt scrap steel for making special type of steel [1]. The production of hot metal in Blast Furnace (BF) is dependent significantly on metallurgical coke as a source of heat and reducing agent while it dependent on oxygen blowing in EAF process [2]. In this development over the last decades, technologies categorized as efficiency improvers for existing blast furnaces (BFs) have emerged as green short-term growing technologies in the iron and steel industry [3]

Pellet production using composite of iron ore, carbon and binder has become increasingly more prevalent with the increased manipulation of low-grade iron ores and increased iron and steel consumption around the world. It has been claimed that the pellet production process has been enhanced by addition of binders. In 2010, world iron ore pellet production was 388 Mt. [5].

The need to agglomerate small particles of iron ore into larger lumps first arose because particles smaller than 20 mesh are nearly all blown out of the blast furnace as flue dust. The agglomeration not only allowed fine iron ores to be used as a feed charge but also brought about substantial increases in output and consequently lowered the cost of iron making. There are generally four processes in the use for agglomerating iron ores and concentrates; Sintering, nodulizing, briquetting and Pelletizing. Pelletizing generally involves two operations. The first stage is the formation of green pellets at room temperature. Fine grained wet iron ores are rolled with or without a binder in suitable equipment. These pellets are fired to increase their strength. Bitumen bonded iron oxide pellets are to be investigated, firstly because it was not known what the effect would be of using bitumen as binder and secondly because interpretation of the effect, if any could give valuable information regarding the direct reduction of pellets. This may be done by using single pellets for crushing and reduction tests at various conditions of temperature and time.

The most reported benefit of organic binders is a reduction in pellet silica content. The traditional binder, bentonite clay, generally

increases iron ore pellet silica content by 0.5%; the true value depends on bentonite dose and composition [5]. Organic binders are combusted during the high-temperature firing process, and may leave virtually no ash residue among the pellet structure for slag formation. Heavy hydrocarbons such as bitumen, naphthalene, and fuel oil have been considered for iron ore pelletization. They are available naturally or as oil and coal refining products and residue. Bitumen was used as a binder on high purity concentrates for direct reduction iron ore (DRI) use. Bitumen was softened at 180 °C and mixed with concentrate in a high energy mixer for 1 hour of mixing and cooling. 5% bitumen was used; higher doses became too sticky to pelletize. Pellets were hardened at low temperatures to polymerize the bitumen and bake out volatile components. Maximum pellet performance was achieved at 200 °C: 250 kg compression strengths were achieved on 1.27 cm diameter pellets during conventional pelletizing; compression strengths over 220 kg were achieved on 6 mm diameter pellets after a double baking treatment (200 °C for 16 hrs. followed by 200 °C for 1 or 4 hrs.) [6], [7].

Baharian iron ore and a locally produced heavy oil fraction were mixed and agglomerated into pellets approximately 15 mm in diameter. Fuel oil dosages were kept below 15 % to limit the creation of a "sticky massive product". Pellets were cold bonded at 120 °C for 24 hours, but no strengths were reported [8].

It is reported that the reduction rate is much faster when intimate contact established by number of reaction sites between iron oxide and carbon fines [4]. It was further established that at lower reduction temperatures, the kinetics of the carbon gasification reaction in CO_2 controlled the overall reduction rate. Deviations in the rate from the carbon gasification-controlled regime were observed by Fruehan [9] at higher temperatures. This was because of the lower temperature dependence of the reduction of wustite by CO than the gasification of carbon by CO_2. Additives such as Li_2O, $NaCO_3$, etc. can significantly affect the reduction rate by enhancing the rate of carbon gasification [10] .

The reduction mechanism is controlled by a combined effect of both gaseous-diffusion and chemical reaction processes.

El-Geassy *et al.* [11] obtained activation energies 18.81-28.42 $kJ.mol^{-1}$ for non-isothermal reduction of composite pellets in N_2 atmosphere. It is reported that in beginning, development was observed and the reduction rate was controlled by the gaseous diffusion mechanism. Dutta found activation energy obtained for final stage reduction, values varies of the order of 183.1 to 268.5 KJ / mol, which mean overall reduction is controlled by gasification reaction [12].

2 EXPERIMENTAL WORK

The iron oxide used in the form of magnetite (Fe_3O_4) super concentrate, the chemical composition of sample is shown in Table 1. A binding material; the 5 % brown bitumen (Table 2) was used to prepare the magnetite pellets (composite pellet) in a sigma bladed mixer at a temperature of 180 ^oC.

Table 1. Chemical analysis of magnetite super concentrate [13]

Constitute	Wt. %
Fe	71.9
Fe_3O_4	97.0
Fe_2O_3	2.30
SiO_2	0.66
MgO	0.15
Al_2O_3	0.15
TiO_2	0.14
V_2O_5	0.20
Na_2O	0.023
K_2O	0.015
P	0.004
Cu	0.005

After cooling and drying, particles can easily flow, coated material was compressed in compression testing machine to produce compact cylindrical pellets (6, 9 and 12 mm). These pellets were backed in an oven at 200 ^oC. When a composite pellet is heated, either under isothermal or non-isothermal conditions, the reduction starts taking place at numerous sites due to evenly distributed carbon particles (reductant) all throughout the matrix.

Table 2. Ultimate analysis of bitumen

Composition Analysis	Wt. (%)
Carbon	82.8
Hydrogen	10.0
Oxygen	2.7
Nitrogen	0.5
Sulphur	4.6
Ash at 550 °C	0.12
Fixed carbon	20.5

3 RESULTS & DISCUSSION

3.1 Magnetite-Bitumen Reduction

Fresh bitumen was heated in nitrogen stream, before studying the effect of bitumen on magnetite reduction (in H_2). Volatilization started at about 300 °C, and total weight loss at 400 °C was around 75%. On further heating to 1000 °C, the volatiles evolved faster that results in total weight was about 79 %. This volatile loss was in accordance with the chemical analysis of bitumen Table 2 which also gives 20.5 % fixed carbon and 0.12 % ash.

Table 3. Weight loss on hydrogen reduction of magnetite powder mixed with and without bitumen

Reduction Time (min)	Temperature (°C)	Without Bitumen (%)	With Bitumen (5 %)	Difference (%)
180	400	21. 58	25.3	3.7
50	500	21.8	25.48	3.68
60	600	25.25	26.55	1.3
40	700	14.5	18.25	3.75
20	800	15.5	19.27	3.77
10	900	14.0	19.6	5.6
7	1000	16.0	25.0	9.0
6	1100	19.5	28.9	9.4

When the mixture was reduced in the range 400 to 1100 °C in a Linseis thermo gravimetric balance, the total weight loss recorded was greater than the weight loss resulting from magnetite reduction alone. The weight loss of powder and pellet sample was recorded as a function of time until a steady state in weight change achieved. The difference in weight loss between these two powders reduced in hydrogen atmosphere at the same temperature, was due to bitumen (Table 3). At 400-500 °C (Figure 1 and 2), the increased weight loss due to the bitumen, was about 3.7 %. This amount was slightly lower than the original volatile contents of bitumen-magnetite concentrate.

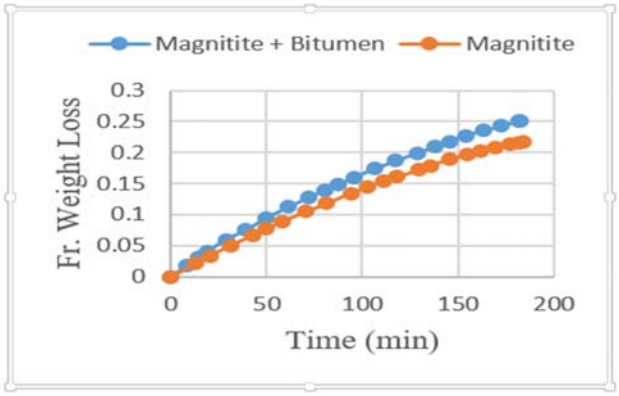

Figure 1. Comparative wt. loss of magnetite powder with and without 5 % bitumen on reduction in H_2 at 400 °C

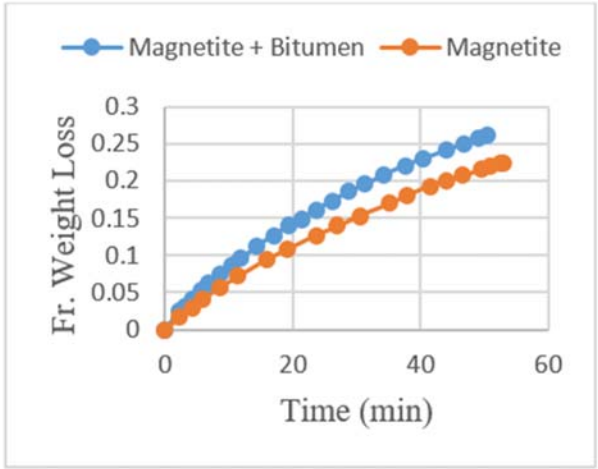

Figure 2. Comparative wt. loss of magnetite powder with and without 5 % bitumen on reduction in H_2 at 500 °C

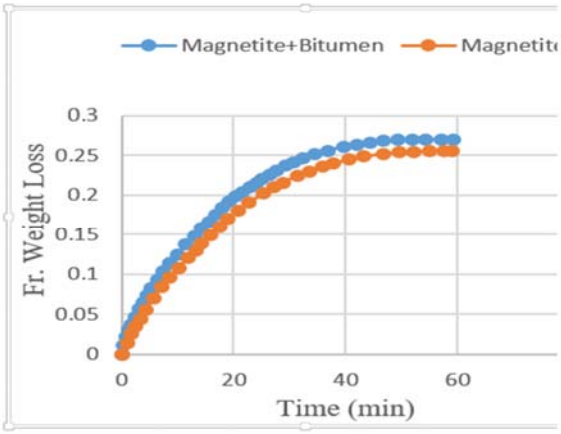

Figure 3. Comparative wt. loss of magnetite powder with and without 5 % bitumen on reduction in H_2 at 600 °C

Table 4. Carbon and Sulphur contents (magnetite + 5 % bitumen) samples

Temperature (reduction °C)	% Carbon	% Sulphur
400	1.38	0.197
500	1.25	0.172
600	1.46	0.106
700	1.17	0.039
800	0.134	0.019
900	0.064	0.015
1000	0.017	0.012
1100	0.011	0.01
unreacted sample	4.14	0.23

At 600 °C (Figure 3), the increase was only 1.3 %. This drop-in weight loss could be due to two reasons. Firstly, since the maximum rate of magnetite reduction occurs at 600 °C, the fast diffusion of H_2 and H_2O to and from the reacting sample may be inhibiting the rate of volatilization.
Secondly, the carbon deposition reaction may well be taking place at this thermodynamically favourable temperature resulting in less weight loss than at 400-500 °C.

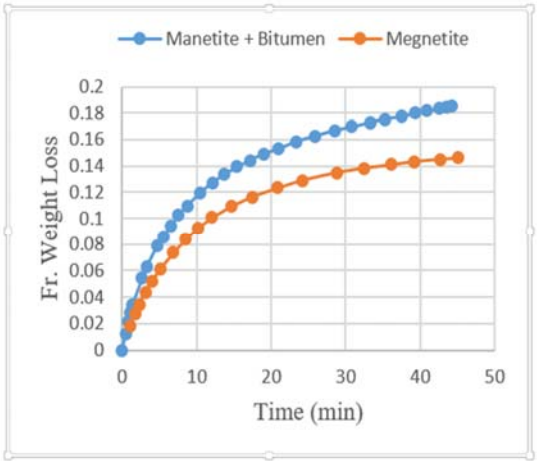

Figure 4. Comparative wt. loss of magnetite powder with and without 5 % bitumen on reduction in H_2 at 700 °C

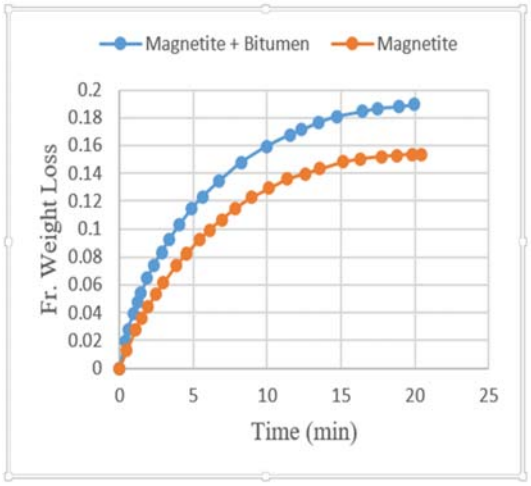

Figure 5. Comparative wt. loss of magnetite powder with and without 5 % bitumen on reduction in H_2 at 800 °C

At 700 °C and 800 °C (Figure 4 and 5), the increased weight loss was about the same as at 400 °C and 500 °C. Above 800 °C, this increase reaches over 5, showing that the fixed carbon of bitumen was also taking part in the reduction besides hydrogen. As the temperature increase from 900 °C to 1100 °C, the rate of weight loss of the mixture rose faster than magnetite alone. For instance, at 1000 °C (Figure 6), the difference between the weight losses after 7 minutes of reduction, was about 9 %.

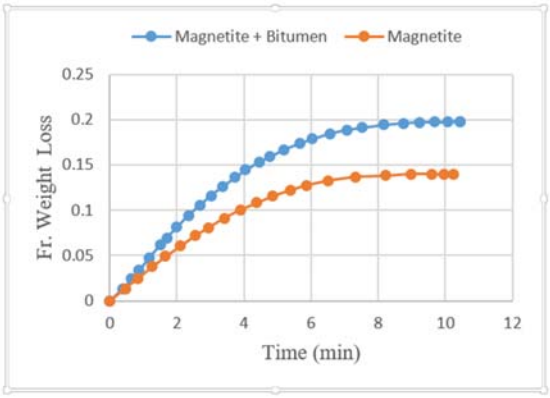

Figure 6. Comparative wt. loss of magnetite powder with and without 5 % bitumen on reduction in H_2 at 1000 °C

Analysis of kinetic data

In the present work only a small amount of bitumen 5 % was mixed with magnetite and this mixture was then reduced in hydrogen atmosphere. Under these conditions, the high molecular weight bitumen molecule would decompose to a variety of saturated and unsaturated hydrocarbons which in comparison to hydrogen would have little affinity for oxygen. Both solid reduction products are favourable for hydrocarbon oxidation at high temperatures, but the volatiles (hydrocarbons) are liberated at the beginning of the reaction where most iron oxide is still magnetite. In addition, these volatile products are almost immediately swept away by the flowing hydrogen gas (with product H_2 O) to the atmosphere.

The kinetics equation can be applied to understand the reduction mechanism of iron ore–coal pellets in different atmospheres. The iron ore-coal pellets were reduced by the following reactions in N_2 atmosphere:

$$FexOy(s) + C(s) = FexOy - 1(s) + CO(g) \quad (1)$$

$$FexOy(s) + CO(g) = FexOy - 1(s) + CO_2(g) \quad (2)$$

Reaction (1) represents direct reduction and reaction (2) represents the indirect reduction of iron oxide by gaseous CO. The rate of the indirect reduction reaction is much faster than the direct reduction reaction in the presence of CO, therefore reduction reaction is mainly due to reaction (2) and (3) [14] . At temperature, lower than 700 °C, the decomposition of carbon monoxide to carbon and carbon dioxide is well known reaction (3). In addition the H_2 present in bitumen cause reaction (4)

$$2CO = C + CO_2 \quad (3)$$

$$CO + H_2 = C + H_2O \quad (4)$$

The product gas H_2O, while diffusing out from interior of the sample would come in contact with the carbon and a water gas reaction would occur.

$$CO + H_2O = CO_2 + H_2 \quad (5)$$

Studies confirmed that the rate of carbon deposition in H_2 -CO mixture reaches a maximum value at 600-700 °C. It is at this temperature that the hydrogen reduction of magnetite plus bitumen powder showed a smaller increase in weight loss than at all other temperatures (Figure 3). In iron ore reduction the rate minima occurs between 600-700 °C. This is reported by all authors and also witnessed in this study.

In H_2 atm, at temperature higher than 800 °C the bitumen contributed to the reduction of a magnetite-bitumen powder mixture by increasing it's rate of reduction as compared with the magnetite alone. At low temperature (400- 500 °C), the overall reduction rate of both was controlled by the chemical reaction with activation energy of 13- 16 Kcal/mol for whole range of reduction. At high temp from 700 to 1100 °C with 29 % reduction of magnetite the activation energy was between 5-6 Kcal/mole, this low value suggests that with chemical reaction the gas diffusion through pores was also rate limiting factor. At later stages of reduction the solid state diffusion was rate controlling step.

The curves given in the Figure 1-5 clearly show an increase in weight loss of 5.6 %, 9 % and 9.4 % at 900 °C, 1000 °C, and 1100 °C respectively. These losses were combination of the amounts of bitumen and oxygen removed at the respective temperature. By assuming that all bitumen 5% has been driven off, the approximate reduction of magnetite due to the bitumen can be calculated as 2.3 % at 900 °C, 15.6 % at 1000 °C and 16.8 % at 1100 °C by the following expression:

$$\%\, Self\ reduction = \frac{(Total\ \%\ wt.loss - 5\ \%)(100)}{(\%\ oxygen\ in\ iron\ oxide)(0.95)}$$

$$\%\, weight\ loss = \frac{(wt.loss)(100)}{(initial\ wt.of\ pellet)}$$

On the basis of elemental analysis (Table 4), the sulphur and carbon contents of the 5%

bitumen-magnetite mixture were 0.2 % and 4 % respectively.

4 CONCLUSIONS

This paper reports direct reduction process of iron ore mixed with bitumen under the H_2 atmosphere, the following conclusions can be drawn from this study:

- For the same time interval of reduction in H_2 atmosphere, the magnetite-bitumen samples produced higher levels of reduction than the magnetite alone. At the same reduction temperature, the weight loss f magnetite with bitumen was relatively higher than those without bitumen.
- The reduction temperature had a significant effect on the weight loss. Below 900 ^oC the bitumen containing sample gave more weight loss due to volatile losses. At temperature 900 ^oC and above the reduction was more pronounced with bitumen as the fixed carbon of bitumen took part in the reduction of magnetite.
- By using bitumen binder it is found that pellet inside achieve a reducing potential which supplements the reduction of iron oxide in hydrogen by about 17 % at 1100^oC. This reflects the better reducibility of bitumen mixed magnetite samples at high temperatures.

ACKNOWLEDGEMENTS

The authors would like to acknowledge the financial support by ministry of Education, Islamabad, and computer and literature facilities of Quaid-E-Awam University, Nawabshah, Sindh Pakistan.

REFERENCES

[1] F. F. Grillo, J. L. Coleti, D. C. R. Espinosa, J. R. Oliveira and J. A. S. Tenório, "Zn and Fe Recovery from Electric Arc Furnace Dust", *Materials Transactions*, vol. 55, pp. 351-356, 2014.

[2] E. A. Mousa, A. Babich, and D. Senk, "Reduction behavior of iron ore pellets with simulated coke oven gas and natural gas," *Steel Res. Int.*, vol. 84, no. 11, pp. 1085–1097, 2013.

[3] B. D. Flores, A. Guerrero, I. V. Flores, A. G. Borrego, M. A. Díez, E. Osório, and A. C. F. Vilela, "On the reduction behavior, structural and mechanical features of iron ore-carbon briquettes," *Fuel Process. Technol.*, vol. 155, pp. 238–245, 2017.

[4] R. S. S. K. Dutta, "Kinetic Studies of Iron Ore – Coal Composite Pellet Reduction by TG – DTA,"., vol. 64, no. December, pp. 583–591, 2011.

[5] J. Halt and S. Kawatra, " 'Review of organic binders for iron ore agglomeration," *Miner. Metall. Process.*, vol. 31, no. 2, pp. 73–94, 2013.

[6] K. A. et al. Abdul, "Crushing strength & reduction of bitumen bonded magnetite super concentrate," *Ironmak. Steelmak.*, vol. 11, no. 5, 1984.

[7] A. S. SJ Ahier, "Use of high-purity sponge iron in possible new steelmaking route," *Ironmak. Steelmak.*, 1981.

[8] K. S. Abdel-Halim, M. I. Nasr, and A. A. El-Geassy, "Developed model for reduction mechanism of iron ore pellets under load," *Ironmak. Steelmak.*, vol. 38, no. 3, pp. 189–196, 2011.

[9] R. J. Fruehan, "The rate of reduction of iron oxides by carbon," *Metall. Trans. B*, vol. 8, no. 1, pp. 279–286, 1977.

[10] H. M. Ahmed, N. Viswanathan, and B. Bjorkman, "Composite pellets-a potential raw material for iron-making," *Steel Res. Int.*, vol. 8, no. 1, pp. 293–306, 2014.

[11] M. H. Khedr, M. I. Nasr, M. S. Aly, M. H. Khedr, M. I. Nasr, and M. S. Aly, "Behaviour of iron ore – fuel oil composite pellets in isothermal and non-isothermal reduction conditions," *Ironmak. Steelmak.*, vol. 28, no. 3, pp. 237–243, 2001.

[12] S. K. Dutta, "Kinetics and mechanism of iron ore - Coal composite pellets reduction," *Trans. Indian Inst. Met*, vol. 58, no. May, pp. 801–808, 2005.

[13] K. A. et al. Abdul, "A new manufacturing process of iron and steel." 2001.

[14] Y. Man and J. Feng, "Effect of iron ore-coal pellets during reduction with hydrogen and carbon monoxide," *Powder Technol.*, vol. 301, pp. 1213–1217, 2016.

Regioselective synthesis under external electric field and electrochemical band broadening of Poly(3-hexylthiophene)

Muhammad Azhar Ansari[a*], Shaikh Mohiuddin[a], Fatma Kandemirli[b], Muhammad Imran Malik[c]

[a]Department of Chemistry, University of Karachi, Karachi, Pakistan.
[b]Biomedical Engineering Department, Faculty of Engineering and Architecture, Kastamonu University, Kastamonu, Turkey.
[c]H.E.J Research Institute of Chemistry, University of Karachi, Karachi, Pakistan.
*Corresponding author: 786muhammadazharansari@gmail.com

ABSTRACT

Renewable energy sources are important target of modern world and solar energy is most abundant source of energy. Keeping keen eyes on the environmental and economic issues, only organic solar cell (OSC) can play a major role to capture huge amount of energy. But there is the big capacity of improvement in OSC regarding efficiency. The major component of OSC is electron acceptor material such as fullerene and electron donor material such as Poly(3-hexylthiophene), P3HT. Fullerene is an ideal accepter material but engineering of P3HT is required to enhance the efficiency of OSC. Optoelectronic properties of P3HT can be improved by controlling the regioregularity, Energy band gap, molar mass of polymer and by p-doping of conjugated polymer. The optimal reaction conditions for synthesis of efficient P3HT are studied. For commercialization of OSC, the cost effective and stereoselective method is proposed. Regioregular P3HT is synthesized by oxidative coupling of monomer with ferric chloride $FeCl_3$ under uniform external electric field (EEF) and its mechanism is discussed. Energy band gap of synthesized polymer can also be compressed by voltammetric p-doping. This research is the collection of knowledge for efficient p-doped donor regioregular P3HT; synthesis and characterization in context of Organic solar cell.

1 INTRODUCTION

Semiconducting polymers have gained tremendous research interest in last decades because it opened the door of organic electronics in modern technological world [1]. Since semiconducting organic macromolecules, specially Polythiophene is environmental friendly, cost effective, easy solution processable and thermally stable so it can be perfectly utilized for the manufacturing of organic electronic devices [2]. In the fast growing era energy crisis and global warming are the major world problems. In many under developed countries such as Pakistan, there is no electricity for people in many villages. It is estimated that 0.25 % coverage of Baluchistan by these photovoltaic devices, having 20 % power conversion efficiency [3], can produce surplus electricity beyond our needs. It is now the need to manufacture commercially, power efficient devices and green electricity for the sustainable technological livings. The energy coming on the surface of the earth from the sun in an hour is ~120,000 TW and the world needs only ~15 TW for the whole year [4]. Solar energy is clean and high enough to derive this world for centuries. Only the action to capture this huge amount of energy is required. For this purpose, harvesting solar energy and converting it into electricity is the global interest for the development of modern green world. Sun is the best renewable source of energy against environmental destroying fossil fuel's resources. Perfect designing of organic photovoltaic devices can provide the higher solar energy conversion into electricity at low cost. Poly(3-hexylthiophene) is one of the excellent conjugated polymer p-type donor material and Fullerene is an ideal n-type accepter material in bulk heterojunction solar cell. Regioregularity of P3HT has a very important role in enhancing the optical absorption and mobility of exitons in the photovoltaic device [5,6]. Great efforts are made in the scientific community for molecular designing of low band gap regioregular P3HT [7]. Regioregularity of polymer can be controlled by External electric field and band gap can be decreased by p-doping.

2. METHODOLOGY:

2.1 SYNTHESIS OF POLYMER:

P3HT was synthesized by oxidative coupling (scheme 1) of 3-hexylthiophene with anhydrous ferric chloride in chloroform and reported previously [8]. Method is used here under different external electric field.

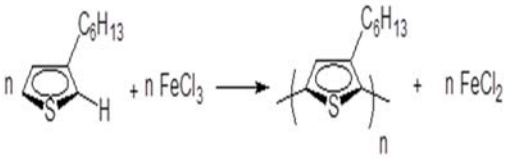

Scheme 1: Synthesis of P3HT.

2.2 P-doping of polymer:

P3HT was coated on the glass slide which was acted as a working electrode. Three electrodes voltammteric system was used in which platinium counter electrode and silver/silver chloride electrode reference electrode was used. Tetrabutyl ammonium perchorate was used as supporting electrolyte. Doping potential was applied for 1min. For determination of optical band gap the UV/Visible absorption spectrum was recorded from 350 nm to 1100nm.

3. Results and discussion:

3.1 Effect of electric field:

P3HTs synthesized under external electric field were characterized by Proton nuclear magnetic resonance for the determination of regioregularity. Results of H-NMR are shown in table for polymers prepared under different electric field. It is found that by increasing electric field the regioregularity of the polymers is increased. This effect may be due to the alignment of cationic radicals (which formed during reaction) under uniform electric field.

Table 1: Effect of external electric field:

Polymer No.	EEF (V)	HT (%)	HH (%)
P1	0	57	43
P2	24	65	35
P3	100	74	26

3.2 Spectroelectrochemistry:

Oxidation (p-doping) of coated polymer was carried out by voltammetric experiment. UV/Visible spectrum recorded for undoped (Figure 1A) and p-doped (figure 1B) polymer is shown in figure 1. It can be seen in the spectrum A of undoped polymer that there is only one optical band while in spectrum B of p-doped polymer contains two bands. An extra band at around 800nm in spectrum B is generated due to effect of p-doping. P-doping oxidizes some of the units in the polymers and some polarons are produced within the polymer chain. These polarons have lower energy related to those elctrons present in undoped units of the same chain.

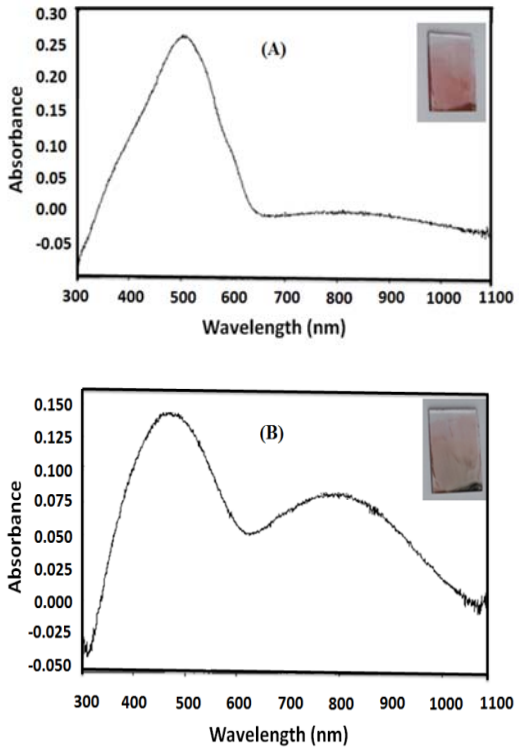

Figure 1: Optical spectrum A of undoped and spectrum B of p-doped polymer.

4. Conclusion:

Regioselectivity of unsymmetrical conjugated polymer such as poly(3-hexylthiophene) is controlled under external electric field and optical energy bandgap of conjugated polymer can decreases by p-doping (oxidation) at fixed potential at a given time. Polymer synthesized in this way can be efficient in context of

organic solar cell and hence improve the overall efficiency of the device.

5. References

[1] Bobade, R. S. (2011). Polythiophene composites: a review of selected applications. *Journal of PolymerEngineering , 31*, 209–215.

[2] Chang Liu, K. W. (2015). Low bandgap semiconducting polymers for polymeric photovoltaics. *Chemical Society Reviews*. doi:10.1039/c5cs00650c

[3] Ovais Mangalwala, Alternative energy Plan B, Spider Magazine, published on August 20, 2013, https://www.dawn.com/news/1037113, accessed on 3rd January 2016.

[4] Forrest, S. R. (2004). The path to ubiquitous and low-cost organic electronic appliances on plastic. *Nature, 428*, 911-918.

[5] McCullough, R. D. (1998). The Chemistry of Conducting Polythiophenes. *Advance Material, 10*(2), 93-116.

[6] Muhammad Yasin, T. T. (2014). P3HT:PCBM blend based photo organic field effect transistor. *Microelectronic Engineering, 130*, 13–17.

[7] Robert S. Loewe, P. C. (2001). Regioregular, Head-to-Tail Coupled Poly(3-alkylthiophenes) Made Easy by the GRIM Method: Investigation of the Reaction and the Origin of Regioselectivity. *Macromolecules, 34*, 4324-4333.

[8] SATORU AMOU, O. H. (1999). Head-to-Tail Regioregularity of Poly(3-hexylthiophene) in Oxidative Coupling Polymerization with FeCl3. *Journal of Polymer Science: Part A: Polymer Chemistry, 37*, 1943–1948

AN IN VITRO EVALUATION OF MICROLEAKAGE AMONG RESIN BASED RESTORATIVE MATERIALS AT DIFFERENT TIME INTERVALS

Afreen Bilgrami[1], Fazal-ur-Rehman Qazi[1], Kausar Ali Syed[2]

[1]Department of Operative Dentistry, Dr, Ishrat-ul-Ebad Khan Institute of Oral Health Science, Dow University of Health Sciences Karachi, Pakistan

[2]Department of Polymer & Petrochemical Engineering, NED University of Engineering & Technology, Karachi, Pakistan.

ABSTRACT

Microleakage between resins based restorative materials in a sandwich manner with and without the intermediate bonding layer was compared. Materials used were Composite Z350, Resin Modified Glass Ionomer Cement (RMGIC), Ceram X Mona plus, Smart Dentine Replacement (SDR), Bond XT and Universal Bond. Samples were cured with Light Emitting Diode(LED) and stored in artificial saliva. Samples were thermocycled to 500 cycles / 30 sec and 1000 cycles / sec as per ISO 11405. Results were concluded based on Grading Tool for microleakage by WHO.

Keywords: Resin based restorative materials, Microleakage, Class II Open sandwich technique.

1. INTRODUCTION:

Composite resins were introduced in the middle of 1960s since then a lot of augmentation in performance and esthetic traits of composite resins occurred[1-3]. An essential aspect of restorative dentistry is the bonding of the restorative material to the remaining part of the tooth structure, in order to restore the peripheral seal of dentine which is discontinued when enamel is lost as a result of developmental squeal, trauma, caries or dental treatment[4]. Ideally a restorative material should create a permanent seal between the restoration margin and tooth structure. "An imperfect bonding results in a microscopic gap through which bacteria, fluids, molecules and ions can infiltrate between the restoration and tooth structure[5]. This phenomenon is known as Microleakage which causes hypersensitivity, recurrent caries, pulpal pathoses and marginal discoloration [6-10]. Many factors [11-13] are responsible for microleakage in restorative materials such as, polymerization shrinkage, thermal contraction, water absorption, mechanical stress, and alteration in tooth structure.

There are various techniques for decreasing microleakage of material. These include application of blended, direct or indirect restorative methods and various curing protocols. Some studies, however, show that incremental technique produce less leakage[14, 15], but others think that amount of leakage remained same with both increments and bulk fillings[16, 17]. The polymerization shrinkage affects all the three layers i.e., viscous bonding material, resilient lining cements and bulk restorative materials[18-20]. Flowable composite flexible lining was suggested to reduce the polymerization shrinkage of class V cavities[21]. Restorative substances are made of micro-hybrid resins which have low modulus of elasticity which causes elastic deformation[22, 23]. Another method for decreasing the microleakage in class II is modification in composite as light cure hybrid composites compared to the chemically cured composite resins[10, 24] . Despite the technological progress, polymerization shrinkage remains one of the main drawbacks of composite resins. Polymerization shrinkage produces contraction which distorts the bonding in the direction of cavity walls[2, 8, 25]and is probably a major cause of caries more

specifically Class II cavities in proximal box deep part[7, 26-28]. Many techniques are recommended for preventing class II secondary caries of composite resins. This include incremental layering, increasing amount of fillers, C factor analysis, use of low shrink material, dentine bonding agents, reapplication of unfilled resin and a "Sandwich Technique" using glass ionomer material[3, 7, 8, 29].

McLean and Wilson introduced open and closed sandwich technique in class II dental caries[30, 31],[32]. Open Sandwich technique is a process in which dentine is replaced by GIC and composite resins replaces the enamel [3, 8, 13, 33-37] and Glass Ionomer (GI) margins are left exposed to produce fluoride at gingival level [9, 12, 31, 38]. The quantity of dental composite is reduced by using GIC [13, 35]. Most favorable attributes of both substances are utilized by this technique including caries resistance, chemical adhesion to dentine, fluoride release, thermal compatibility with tooth enamel,[8, 34, 39, 40], re-mineralization, lower interfacial shrinkage stress of GI, enamel bonding, surface finish, durability and tooth-color matching of composite resins[3, 41]. GIC is a dentine substitute in sandwich technique. Resin Modified Glass Ionomer Cement (RMGIC), and Smart Dentine Replacement (SDR) etc. On one side RMGIC is bonded chemically with the tooth and on other side it is micromechanically linked to bulk filling composite restorative material[42, 43]. Smart dentine replacement (SDR) is the latest improvement in light cure resin based restoratives, which can give the depth of cure of 4mm. It develops less stresses and flowability is better in restorative procedures[43].

Connection of substrate and tooth structure is guaranteed by bonding through micro-mechanical association, chemical bonding as well as linkage among restorative materials and substrate through wetting and penetration process[44, 45].

The purpose of this study is to validate the hypothesis that "there is no microleakage between the two-resin based restorative materials in a sandwich manner, with and without the intermediate bonding layer after immersion in 2% Methylene blue dye at different time intervals." This research follows the class II cavity restored with open sandwich technique.

2. Materials and Methods:

2.1 Materials

Following materials were used in the study: Vitremer (3M), Z350 (3M), SDR(DENTSPLY), Ceram X Mono+ (DENTSPLY), Prime & Bond NT(DENTSPLY), Single Bond Universal (3M).

2.2 Sample Preparation

The mold was fabricated in three pieces, consisting of a metallic base with hooks to hold two Teflon sheets of 2mm thick each containing nine holes of 4mm diameter as per ISO 10650 [46, 47] .

The base material (Vitremer or SDR) was mixed using a plastic instrument then filled in the first Teflon sheet and cured for 40sec using LED light curing unit[48].The other Teflon sheet was fixed over the first sheet taking care that its holes should overlap the already filled holes of first sheet. Composite material was filled with or without bond application, in the other Teflon sheet using plastic instrument and cured for 40 seconds with LED unit. In group A base material Vitremer or SDR was placed and cured for 40sec. Base was then etched using 37% phosphoric acid gel for 20 sec, rinsed for 10sec and dried for 5 sec[49]. Second Teflon sheet was placed over the first one, the holes were filled with bulk filling material (Z350 or Ceram X). Whereas in group B the same protocol was followed with addition of bonding agent (Vitrebond plus or Single Bond Universal) was applied on the base material and then the second Teflon sheet was placed over the first one. The holes were filled with bulk filling material(Z350 or Ceram X)[51]. The Teflon sheets were removed from the metal

base. Each sample was removed from the Teflon sheet holes by applying finger pressure or taking help from a plastic instrument (figure 1 and 2).

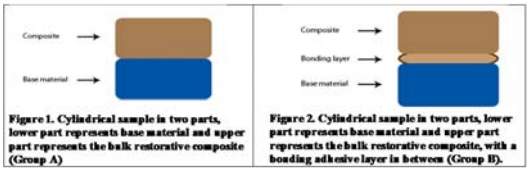

Figure 1. Cylindrical sample is two parts, lower part represents base material and upper part represents the bulk restorative composite (Group A)

Figure 2. Cylindrical sample is two parts, lower part represents base material and upper part represents the bulk restorative composite, with a bonding adhesive layer in between (Group B).

Samples were stored in artificial saliva pH. = 6.7, in tagged brown bottles to avoid light interference. Samples were fully dipped in the saliva. Each bottle was tagged with group number and the name of the material of that group.

Samples were placed in the incubator within half an hour in order to provide control temperature of 26 ºC for 48 hours to allow complete polymerization[49]. Samples from incubator were placed in small tube containing artificial saliva, to place them in thermocycler machine.

The thermocycling tube were filled with artificial saliva to prevent drying of the samples and simulate the oral cavity temperature (5ºC - 55 ºC) according to ISO standard 11405[35, 36, 52-57].These small tubes were also color coded so the samples of different materials will not be mixed.

All groups were divided in three sets:

- Control groups were stored at room temperature (26 ºC). No temperature variation was given to this group (not thermocycle).
- Second set of samples was given temperature variations for 500 cycles/30sec.
- Third set of samples was given the temperature variations for 1000 cycles/30sec.

500 cycles/30sec are equivalent to six-month aging of material [34, 35, 52, 53]. While, 1000 cycles/30sec are equal to one-year aging process [34, 52, 53] , according to ISO 11405[56, 58]. Sample tubes were then placed in the thermocycler.

Samples were taken out of the thermocycling tubes, dried with tissue paper and left on the table to dry completely. Two coats of nail varnish were applied from time to time, on the three quarters of the circular samples[49]. The three sides of both the materials were covered in the longitudinal manner whereas one side that is the dye penetration site (DPS) (one third of sample); was left open to allow the dye penetration to check any leakage present.

After drying the samples were again placed in their tagged brown bottles and fully immersed in 2% methylene blue dye solution buffered at pH=7 completely[48, 58, 59]. Samples were left in dye solution for 24 hours to allow the leakage between the materials[34].

After 24 hours, samples were removed from the bottles and washed thoroughly under running tap water. Sectioning was done using micro-motor ultra-thin ceramic disc (22.2mm×0.3mm) in longitudinal manner. Division was done taking care that DPS should be divided into two halves. Samples were placed in the bottles again and the bottles were covered with the plain white paper to avoid any bias.

Samples were then finally observed under stereomicroscope at the magnification between 10X – 40X[48], which was counterchecked by another observer.

2.3 Tools for Microleakage Testing

The examination tool of Microleakage Index by World Health Organization(WHO) is as following, which is according to (ISO/TS 11405:2003)[40]:

Grade 0 0.0 mm
Grade 1 up to 0.5 mm micro leakage
Grade 2 up to 1 mm micro leakage
Grade 3 up to 2 mm micro leakage
Grade 4 ≥ 2 mm

2.3 Statistical Technique

The present study has employed Kruskal-Wallis ANOVA for non-parametric analysis, Post Hoc (Tukey Test) based on Rank Data and Descriptive statistics to analyze whether

there is microleakage or not between groups A and group B. Moreover, the study further analyzed the cross-grouping comparison of group A and group B to gain more insight about the existence of microleakage at three different levels including (control, 500 cycle/30sec and 1000 cycles/30sec).

3. RESULTS AND DISCUSSION:

3.1 Results

3.1.1 Group-wise Assessment for WHO Microleakage Index Grading

Table 2 presents statistical information about the group-wise assessment of samples with respect to classification as per WHO Microleakage Index Grading.
The groups were categorized as group A and group B along with WHO Microleakage Grading Index method (Table 2)

Table 2: Detailed analysis of Group-wise Assessment for WHO Microleakage Index Grading.

Group-wise Assessment for WHO Micro Leakage Index Grading											
Row Labels	Control (n)		Group 2 (n)		Group 3 (n)		Group 4 (n)		Group 5 (n)		Grand Total (n)
	A	B	A	B	A	B	A	B	A	B	
Grade 0	15	19	1	2	10	10	0	9	10	9	85
Grade 1	2	0	1	5	0	0	0	1	0	1	10
Grade 2	1	1	1	2	0	0	2	0	0	0	7
Grade 3	2	0	5	1	0	0	8	0	0	0	16
Grade 4	0	0	2	0	0	0	0	0	0	0	2
Grand Total	20	20	10	10	10	10	10	10	10	10	120

A = without bond B = with bond

Among the total 34 samples from control categorized as Grade 0 (0.0 mm microleakage), there were 15 samples of group A and 19 samples of group B. Likewise, in group 2, there were total 3 samples as Grade 0 including 1 group A and 2 of group B. Similarly, total 20 samples were categorized as Grade 0 in group 3 including 10 of group A and 10 of group B. All the 9 samples of group 4 classified as Grade 0 were of group B. However, 10 samples of group A and 9 samples of group B from group 5 were categorized as Grade 0.
Additionally, 2 samples of group A from the control group were classified as Grade 1 (up to 0.5 mm microleakage), whereas, 1 sample of group A and 5 samples from group 2B were categorized as Grade 1. In group 4B and group 5B, there was only 1 sample in each group categorized as Grade 1 respectively.
Grade 2 (up to 1 mm microleakage) classification includes 1 sample of group A and 1 sample of group B from control group, whereas, 1 sample of group 2A and 2 samples from group 2B, also, 2 samples from group 4A.
Similarly, Grade 3 (up to 2 mm microleakage) classification included 2 samples of group A from control group, five samples of group A and one sample of group B from group 2, whereas, 8 samples from group 4A. And lastly, in Grade 4 (($\geq$ 2 mm) only 2 samples were categorized from group 2A.

3.1.2 Descriptive Details of Micro leakage values at control and experimental (500 cycles/30sec and 1000 cycles/30sec) groups levels.

Table 3 provides detailed information about the descriptive statistics of samples of group A and group B compared between cycles and materials.

Table 3: Comparison of group A and group B Microleakage (mm) of specimen by Materials.

Material		Control Group	500 Cycles/30sec	1000 Cycles/30sec
Group 2	(A)	0.82 ± 0.86	1.25 ± 0.13	1.26 ± 1.22
	(B)	0.00	0.50 ± 0.36	0.30 ± 0.31
	Mean Difference (p-value)	0.82 (0.05*)	0.75 (0.016*)	0.95 (0.17)
Group 3	(A)	0.00	0.00	0.00
	(B)	0.00	0.00	0.00
	Mean Difference (p-value)	0 (> 0.99)	0 (> 0.99)	0 (> 0.99)
Group 4	(A)	0.18 ± 0.24	1.22 ± 0.39	1.14 ± 0.30
	(B)	0.00	0.06 ± 0.14	0.00
	Mean Difference (p-value)	0.18 (0.14)	1.16 (0.01*)	1.15 (0.17)
Group 5	(A)	0.00	0.00	0.00
	(B)	0.00	0.00	0.62 ± 0.14
	Mean Difference (p-value)	0 (> 0.99)	0 (> 0.99)	0.06 (0.32)

* significant at 5%A = Without Bond; B = With Bond

P-value less than 0.05 are significant. Although a result of not having a significant is in favor of our research, thus we can state that statistical insignificant results are in favor of clinically significant (no leakage). The mean difference values of specimens at control level

that is without any intervention were found to be 0 (zero) in groups 3 and 5 with the p-value > 0.99 which is not significant (no leakage) (Figure 3, 4, 5 & 6).

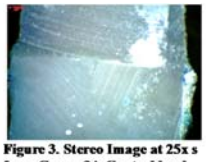

Figure 3. Stereo Image at 25x s from Group 3A Control level

Figure 4. Stereo image at 30x from Group 3B Control level

Figure 5. Stereo image at 30x from Group 5A Control level

Figure 6. Stereo image at 40x from Group 5B Control level

In groups 2 and 4 values are 0.82 and 0.18 with the p-value of 0.05 and 0.14 respectively (Figure 7, 8, 9 & 10).

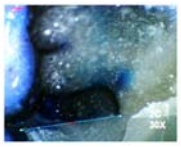

Figure 7. Stereo image at 30x from Group 2A Control level

Figure 8. Stereo image at 45x from Group 2B Control level

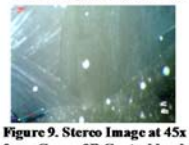

Figure 9. Stereo Image at 45x from Group 2B Control level

Figure 10. Stereo Image at 45x from Group 4A Control level

However, statistics showed that mean difference of group 2 at 500 cycles/30sec has 0.75 and group 4 has 1.16 with p-values 0.016 and 0.01 highly significant respectively. Whereas, group 2, 4 and 5 at 1000 cycles/30sec have shown mean differences of 0.95, 1.15 and 0.06 with p-values 0.17, 0.17 and 0.32 respectively to each group.

In group 2 A at 500 cycles/30sec and 1000 cycles/30sec the specimens have mean 1.25 and 1.26 with standard deviation of 0.13 and 1.22 respectively. The control of this group has the value of 0.82 with the standard deviation of 0.86(Figure 11 & 12).

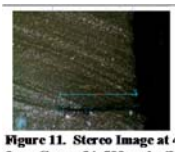

Figure 11. Stereo Image at 45x from Group 2A 500 cycles/30sec

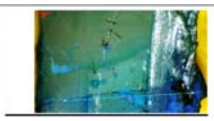

Figure 12. Stereo image at 45x from Group 2A 1000 cycles/30sec

Similarly, the mean values of group 2 B at 500 cycles/30sec and 1000 cycles/30sec are 0.50 and 0.30 and standard deviation 0.36 and 0.31. The control of this group has the value of 0 (zero) with standard deviation of 0 (zero) (Figure 13 & 14).

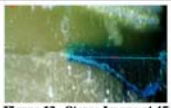

Figure 13. Stereo Image at 45x from Group 2B 500 cycles/30sec

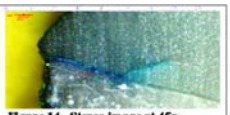

Figure 14. Stereo image at 45x from Group 2B 1000 cycles/30sec

The group 3 A and B at 500 cycles/30sec and 1000 cycles/30sec indicated mean value of 0 (zero) for both the interventions with standard deviation of 0 (zero) (Figure 15, 16, 17 & 18). The control of this group also showed 0 (zero) mean value with standard deviation of 0 (zero). The group 4 A at 500 cycles/30sec and 1000 cycles/30sec showed the mean of 1.22 and 1.14 with standard deviation of 0.39 and 0.30 (Figure 19 & 20).

Figure 15. Stereo Image at 45x from Group 3A 500 cycles/30sec

Figure 16. Stereo Image at 45x from Group 3A 1000 cycles/30sec

Figure 17. Stereo Image at 45x from Group 3B 500 cycles/30sec

Figure 18. Stereo Image at 45x from Group 3B 1000 cycles/30sec

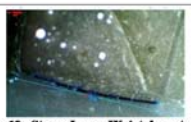

Figure 19. Stereo Image IX A taken at 45x stereomicroscope from Group 4A 500 cycles/30sec

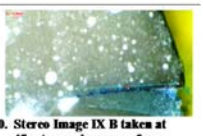

Figure 20. Stereo Image IX B taken at 45x stereomicroscope from Group 4A 1000 cycles/30sec

In group B mean is 0.06 and 0 (zero) and standard deviation is 0.14 and 0 (zero) (Figure 21 & 22). However, group 5 B at 1000 cycles/30sec has mean value of 0.62 with standard deviation of 0.14, whereas, all other interventions were having 0 (zero) mean values with 0 (zero) standard deviation. (Figure 23, 24, 25 & 26).

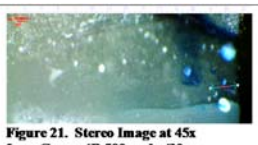

Figure 21. Stereo Image at 45x from Group 4B 500 cycles/30sec

Figure 22. Stereo Image at 45x from Group 4B 1000 cycles/30sec

Figure 23. Stereo Image at 45x from Group 5A 500 cycles/30sec

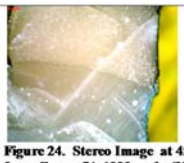

Figure 24. Stereo Image at 45x from Group 5A 1000 cycles/30sec

Figure 25. Stereo Image at 45x from Group 5B 500 cycles/30sec

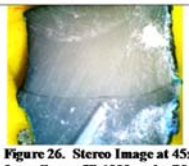

Figure 26. Stereo Image at 45x from Group 5B 1000 cycles/30sec

3.1.3 Cross-Comparison between Groups A

Table 4 shows cross-comparison of groups A at control, 500 cycles/30sec and 1000 cycles/30sec at 5 percent confidence interval. The study has employed Kruskal-Wallis ANOVA for non-parametric analysis, Post Hoc (Tukey Test) based on Rank Data and Descriptive statistics to analyze. Also, the cross comparison of groups was also carried out. No significant difference found among materials in control group.

Table 2: Cross-comparison of group A

Material	Control	500 Cycles/30sec	1000 Cycles/30sec
Group 2	0.82 ± 0.86	1.25 ± 0.13	1.26 ± 1.23
Group 3	0	0	0
Group 4	0.18 ± 0.25	1.22 ± 0.40	1.15 ± 0.30
Group 5	0	0	0

Mean & Standard deviation of groups 2,3,4 & 5 A .

However, at 500 cycles/30sec significant difference was found when group 2 & 4 was compared with group 3 & 5. Significant difference was found when group 2 was compared with 3 & 4 at 1000 cycles/30sec. It clearly shows that only group 2 and 4 at control has mean values of 0.82 and 0.18 with standard deviation of 0.86 and 0.25 respectively. Whereas, at 500 cycles/30sec, the results showed that group 2 has mean value of 1.25 with standard deviation of 0.13 and group 4 has mean value of 1.22 with standard deviation of 0.40. Moreover, at 1000 cycles/30sec, group 2 has mean value of 1.26 with standard deviation of 1.23 and group 4 has mean value of 1.15 with standard deviation of 0.30. However, group 3 and 5 were having 0 (zero) mean value with 0 (zero) standard deviation at control, 500 cycles/30sec and 1000 cycles/30sec.

3.1.4 Cross-Comparison between Groups B

Table 5. shows cross-comparison of groups B at control, 500 cycles/30sec and 1000 cycles/30sec at 5 percent confidence interval.

Table 2: Cross-comparison of group B

Material	Control	500 Cycles/30sec	1000 Cycles/30sec
Group 2	0	0.50 ± 0.36	0.31 ± 0.32
Group 3	0	0	0
Group 4	0	0.07 ± 0.15	0
Group 5	0.11 ± 0.24	0	0.06 ± 0.14

Mean & Standard deviation of groups 2, 3, 4&5 B

No significance was found at control and 1000cycles/30sec. However, in group thermocycled at 500cycles/30sec significant difference was found when group 2 was compared with all other groups. The statistics showed that group 2 was having mean value of 0.50 with standard deviation of 0.36 at 500 cycles/30sec, whereas, mean value of 0.31 with standard deviation of 0.32 was found at 1000 cycles/30sec. Further, group 4 was having 0.07 mean values with standard deviation of 0.15 at 500 cycles/30sec. Additionally; group 5 was having mean value of 0.11 and 0.06 at 500 cycles/30sec and 1000 cycles/30sec respectively with standard deviation of 0.24 and 0.14 respectively.

3.2 Discussion

In this study, the microleakage between the two sandwiched materials has been investigated. The statistical analysis revealed non-significant result (i.e. no microleakage) was found in groups 3 (A and B) and group 5 (A and B). This indicates the better bonding capability of SDR with other resin materials.

Similar results were reported by Nicola Scotti [48] . No leakage in SDR could be because of better marginal seal and improved adhesion at enamel and dentine obtained due to the flowable nature of the resin and decreased modulus of elasticity creating less stresses. Swelling behavior of some bulk fill materials could also be one reason of not showing any leakage, as claimed by Leprince JG et al[62]. All groups along with sub groups showed non-significant results (no leakage) on different cycles. In group 3, half cylinder was fabricated using the Ceram X. No microleakage was statistically found in sub-groups containing Ceram X composite either in control group, at 500 cycles/30sec or 1000 cycles/30sec.

No leakage with Ceram X was also reported by Schirrmeister et al;[64], Ahmadi et al;[65], and Eden and co-workers[66]

On the contrary, Sing et al; [68] had statistically proved the presence of microleakage in extracted tooth cavity using Ceram-X composite. Similarly microleakage was found in coronal and apical region [69] of cement-enamel junction in Ceram X nanocomposite, at occlusal margin [65] , and in class 2 cavities[70]. Agrawal [58] and colleagues reported that substantial reduction in the microleakage had been found in Nano-ceramic and Silorane composite with the usage of Ribbond fiber. High microleakage was found in Nano-composite resins as compared to micro-hybrid composites [72]. Due to these controversial findings of Ceram X, our study is focused on the base materials used in sandwich technique. In current study, Ceram X was used in combination with the Vitremer (group 4) showing leakage.

The gold standard in adhesive system is still etch and rinse three step formulation thus we used the same protocol, by etching the base materials for better micro- mechanical retention of composite resin[73]. Our results are almost in agreement with the above-mentioned studies, where the groups 3 & 5 showed no leakage in control group or at 500 and 1000cycles. Literature is available showing bonding efficacy of bulk restorative materials (composites), the Ceram X and the Z350 in class 2 open sandwiched technique but as it is clear in the results among groups 3 and 5 that presence of SDR had shown the difference. Thus, no change had been observed when the bulk restorative materials were interchanged for comparison. Hence the better bonding ability of SDR was evident.

The comparative groups 2 (Vitremer and Z350) and 4 (Vitremer, 3M and Ceram X), of the study showed some leakage in all sub-groups (with and without bond, 500 and 1000 cycles as well as in control groups). In contrast to those studies which stated no difference in sealing ability of bonded and unbonded restorations, the control group, 2A and 4A showed leakage. This might be due to internal voids formation as shown in a study with nearly similar methodology [74].

The control group 2B and 4B, 2 (Vitremer, Bond and Z350) and 4 (Vitremer, Bond, and Ceram X) with bond showed no leakage. But the testing groups of 2B and 4B which were subjected to thermocycling showed some evidence of leakage at 500 cycles/30sec. Leakage was also observed in 2B at 1000cycles/30sec but comparatively no leakage was found in group 4B subjected to 1000 cycles/30sec. This indicates that application of adhesives between two resin based materials, bonds the materials initially well but the process of aging (increase number of cycles) can reduce the bonding capacity of adhesive resin perhaps due to thermal changes. The reason for 4B not showing any leakage at 1000cycles/30sec can be good sealing bonding agent with bulk resin based materials (Ceram X) with aging phenomena. Some amount of leakage was found in 4B at 500cycles/30sec which could be due to weakening of bonding strength with initial aging or error in sample.

According to Gerdolle et al;[75] the thermocycled material showed greater leakage due to disruption of bond but at greater number of cycles bonds may again be formed due to thermal expansion and contraction process.

Comparing the base materials SDR and Vitremer. It was observed that Vitremer did not produced good enough sealing with other resin material as compared to its bonding affinity for dental hard tissues. A reasonable explanation of this adversity could be the brittle nature of RMGIC(Vitremer) that forms thick layer which cracks due to thermal stresses.[76]

In past studies adhesion was evaluated with enamel and dentine where as in current study, it was evaluated between two resin based materials and not among restoration and hard tooth tissues. Overview of past studies, using different modification of GIC showed the reduced leakage and better bonding when RMGIC was used as base material where it was evaluated at the interface of enamel or dentine and restoration. Reduced leakage may be due to the effect of water sorption in unfilled resin materials[77-80]. Nano-RMGI and Nano-composite sandwich technique had been found with least microleakage. El-Ashiry [81]and AB Malik[82] reported that gingival margin had evidently higher microleakage degree than occlusal margin specifically for Nano-RMGI, conventional RMGI and sandwich of Nano-RMGI and Nano-composite C.Beznos[83] gave reason that the restoration lined with RMGIC reduces the volumetric shrinkage of RBC restorations by 41%. RMGIC proved to be best in preventing microleakage [84]. This is in contradiction with our results. It may be due to the evaluation site which is different in both the studies. In RMGIC bonding to tooth dentine, the hydrophilic end of the material bond to the dentine well thus no leakage was found, whereas the hydrophobic end bonds with the other resin material. In our study higher leakage was shown by RMGIC groups (group 2& 4). The reasons for more leakage in RMGIC lined restorations could be: (i) polymerization shrinkage at the time of curing which leads to gap formation, (ii) lack of elastic deformation at the interface, (iii) higher viscosity due to particle size, (iv) two component system of RMGIC can leading to porosities, and (v) loss of severe water from RMGIC due to water sensitivity[83, 85].The other reason for RMGIC leakage could be; two phase setting reaction initially by acid base reaction and then by light curing as compared to SDR which sets through light activation only and bonds with other resin restoration well[75, 86].

The results of the present study revealed that microleakage had been found in Filtek Z350 in group 2 except in 2B control level. This indicates the poor bonding between the two resin based materials (Vitremer, and Z350). No leakage in 2B at control level indicates good bonding initially with the application of bonding layer before thermocycling. In group 5 no leakage was found except in group 5B at 1000cycles. The reason could be the effect of thermocycling where bond strength decreases showing leakage, or it could be due to error in specimen preparation. Praveen et al [87], Alqahtani et al [88, 89], Bugalia et al[90] have reported microleakage shown by Z350 for the Class II composite restoration. The results of Singh et al[68] are in agreement with some of this study set up. Similar findings were presented by Gupta, K.V [91] , Gowda et al [92] and Narayana et al[93] showing least microleakage as compared to other groups in those particular studies. Additionally, microleakage was detected by Ahmadi et al;[65] for Nano-filled composite at occlusal and gingival margin. However, they also explained the presence of least microleakage in flowable composite as compare to Nano-ceramic composite, the reason given was the easy adaptability of the flowable composite. In addition, Filtek Silorane composite shows significantly lower microleakage value compared to Nano-ceramic composite because of less than 1% shrinkage in the silorane composite [71].

In present study, the dye penetration method was used as it is the most common method of evaluation of microleakage. The differences in readings of the results were perceived. In spite of the disadvantages of dye penetration, it is not yet confirmed that errors can occur in

results[94]. In class II sandwich technique resin-dentine adhesive properties are of significant importance[95, 96]. Simplicity in laboratory methods and authenticity of results has been proved recently [94, 97]. The convenient detection of 2% methylene blue dye under visible light made it usable, it has high water solubility and is readily diffusible[98]. Methylene blue have dye penetration comparable to butyric acid (metabolic product of microorganisms) as suggested by Starkey et al [99]. Dye and radioisotope penetration methods have been used in approximately 82% of microleakage studies [100]. It is a good indicator of leakage of microorganisms and bigger toxins and as well as low molecular weight toxic agents[101]. Hence it is logical to select a technique which is considered most effective among all in vitro methods. Though it is yet not understood that how the dye movement is comparable to tissue fluid flow and bacterial movement in vivo [98]. Based on past studies showing accurate results of methylene blue, it was used it in this study [102, 103]. In this regard a recently conducted study found positive association between microleakage and the presence of voids [104], whereas another study reported no correlation between them [105],[106].

Polymerization shrinkage and stresses play a role in gap formation resulting in microleakage, still in discussion. Bond strength and marginal seal of restorative materials like composite resin can be controlled by combination of materials, application of bonding layer and techniques like incremental layering technique [16, 83, 107], application of lining or base material, sandwich technique, control of C-factor and use of low shrink materials[108] to prevent microleakage as discussed in literature. In class II sandwich technique resin- dentine adhesive properties are significant. But according to Anupriya Bugalia et al; Aguiar et al;[109-111] microleakage is yet not completely prevented by any restorative method or any adhesive application, although it can only be reduced by some techniques or materials.

Thus, in this study we tried to add a new aspect in success and failure of Class II open sandwiched technique restoration, by evaluating the resin-resin interface microleakage. Eight different combinations were tested for leakage and the control groups of each combination were observed under stereomicroscope.

4. CONCLUSIONS:

Within the limitations of the study following conclusion can be drawn:

1. SDR with Ceram X and with Z350 exhibited no leakage, indicating that SDR would have better bonding affinity with resin composites at different time intervals.
2. Bonding with the resin composite was not strong enough.
3. It was an in vitro study, which followed all the protocols to mimic in vivo processes but still we cannot completely co-relate variables encountered in in-vivo practices of materials.
4. The specimens were used in this study instead of restored teeth, to simulate class II open sandwich technique to avoid any operator bias method of filling and materials used for restorations.

5. REFERENCES:

1. Bowen, R.L., Dental filling material comprising vinyl silane treated fused silica and a binder consisting of the reaction product of bis phenol and glycidyl acrylate. 1962, Google Patents.
2. Sharafeddin, F. and H. Moradian, Microleakage of class II combined Amalgam-Composite restorations using different composites and bonding agents. Journal of Dentistry of Tehran University of Medical Sciences, 2008. **5**(3): p. 126-130.
3. Vilkinis, V., P. Hörsted-Bindslev, and V. Baelum, Two-year evaluation of class II resin-modified glass ionomer

cement/composite open sandwich and composite restorations. Clinical Oral Investigations, 2000. **4**(3): p. 133-139.
4. Magne, P. and W.-S. So, Optical integration of incisoproximal restorations using the natural layering concept. Quintessence international, 2008. **39**(8).
5. Parveen, N., et al., The effects of mechanical stresses on the comparative microleakage of two different restorative materials. J Univ Med Dent Col, 2012. **3**(1): p. 48-53.
6. Magne, P. and T. Kim, Magne P, So WS. Optical integration of incisoproximal restorations using the natural layering concept. Quintessence Int. 2008 Sep; 39 (8): 633-43. Magne M, Magne I, Magne P. Diagnostic waxing transfer from diagnostic casts to soft tissue definitive casts. J Prosthet Dent. 2008 Jul; 100 (1): 70-1. Reshad M, Cascione D, Magne P. Diagnostic mock-ups as an objective tool for predictable outcomes with. Quintessence Int, 2008. **39**(8): p. 633-43.
7. Usha, H., et al., Comparing microleakage and layering methods of silorane-based resin composite in class V cavities using confocal microscopy: An in vitro study. Journal of Conservative Dentistry, 2011. **14**(2): p. 164.
8. Simi, B. and B. Suprabha, Evaluation of microleakage in posterior nanocomposite restorations with adhesive liners. Journal of Conservative Dentistry, 2011. **14**(2): p. 178.
9. within Dentin, E., Applied. 2007.
10. Bagis, Y., I. Baltacioglu, and S. Kahyaogullari, Comparing microleakage and the layering methods of silorane-based resin composite in wide Class II MOD cavities. Operative Dentistry, 2009. **34**(5): p. 578-585.
11. Usha, H., et al., Comparing microleakage and layering methods of silorane-based resin composite in class V cavities using confocal microscopy: An in vitro study. Journal of conservative dentistry: JCD, 2011. **14**(2): p. 164.
12. Fabianelli, A., et al., The relevance of microleakage studies. International Dentistry SA, 2007. **9**(3): p. 64-74.
13. Fourie, J. and C. Smit, Cervical microleakage in Class II open-sandwich restorations: an in vitro study: scientific. South African Dental Journal, 2011. **66**(7): p. 320-324.
14. Cooley, R.L. and W.W. Barkmeier, Dentinal shear bond strength, microleakage, and contraction gap of visible light-polymerized liners/bases. Quintessence International, 1991. **22**(6).
15. Crim, G. and K. Chapman, Effect of placement techniques on microleakage of a dentin-bonded composite resin. Quintessence international (Berlin, Germany: 1985), 1986. **17**(1): p. 21.
16. Coli, P. and M. Brännström, The marginal adaptation of four different bonding agents in Class II composite resin restorations applied in bulk or in two increments. Quintessence International, 1993. **24**(8).
17. Affleck, M., et al., Microleakage with incremental vs bulk placement utilizing condensable composites. J Dent Res, 1999. **78**: p. 155.
18. Carvalho, R.M.d., et al., A review of polymerization contraction: The influence of stress development versus stress relief. Operative dentistry, 1996. **21**(1): p. 17-24.
19. Kemp-Scholte, C.M. and C.L. Davidson, Marginal integrity related to bond strength and strain capacity of composite resin restorative systems. The Journal of prosthetic dentistry, 1990. **64**(6): p. 658-664.

20. Oliveira, A.L.B.M.D., et al., Effect of finishing and polishing on color stability of a nanofilled resin immersed in different media. Revista de Odontologia da UNESP, 2014. **43**(5): p. 338-342.
21. DAVIDSON, C.L., Glass-Ionomer Bases Under Posterior Composites. Journal of Esthetic and Restorative Dentistry, 1994. **6**(5): p. 223-226.
22. Unterbrink, G.L. and W.H. Liebenberg, Flowable resin composites as" filled adhesives": literature review and clinical recommendations. Quintessence International, 1999. **30**(4).
23. Fabianelli, A., A study into the significance of tracing microleakage by color die infiltration. Dental Materials and Clinical Applications, University of Siena: Italy, 2004.
24. Mali, P., S. Deshpande, and A. Singh, Microleakage of restorative materials: an in vitro study. Journal of Indian Society of Pedodontics and Preventive Dentistry, 2006. **24**(1): p. 15.
25. Sawani, S., et al., Comparative evaluation of microleakage in Class II restorations using open vs. closed centripetal build-up techniques with different lining materials. Journal of conservative dentistry: JCD, 2014. **17**(4): p. 344.
26. Loguercio, A.D., et al., Microleakage in class II composite resin restorations: total bonding and open sandwich technique. Journal of Adhesive Dentistry, 2002. **4**(2).
27. Hewlett, E.R. and G.J. Mount, Glass ionomers in contemporary restorative dentistry--a clinical update. Journal of the California Dental Association, 2003. **31**(6): p. 483-492.
28. Koubi, S., et al., Effect of dual cure composite as dentin substitute on the marginal integrity of class II open-sandwich restorations. Operative Dentistry, 2010. **35**(2): p. 165-171.
29. EFES, B.G., et al., The effects of glass ionomer and flowable composite liners on the fracture resistance of open-sandwich class II restorations. Dental materials journal, 2013. **32**(6): p. 877-882.
30. Kopperud, S.E., Treatment decisions on approximal caries and longevity of Class II restorations. 2013.
31. Al-Jobair, A., In vitro evaluation of microleakage in contaminated fissures sealed with GC Fuji Triage glass ionomer cement. J King Saud Univ, 2010. **22**(1): p. 25-32.
32. Arora, V., et al., THE OPEN SANDWICH TECHNIQUE WITH GLASS IONOMER CEMENT – A CRITICAL EVALUATION. International Journal of Innovative Research in Science, Engineering and Technology, 2013. **2**(8): p. 3875-3882.
33. Bona, Á.D., C. Pinzetta, and V. Rosa, Effect of acid etching of glass ionomer cement surface on the microleakage of sandwich restorations. Journal of Applied Oral Science, 2007. **15**(3): p. 230-234.
34. Bona, A.D., C. Pinzetta, and V. Rosa, Micro leakage of acid etched glass ionomer sandwich restorations. J Appl Oral Sci, 2007. **15**: p. 230-4.
35. Hewlett, E.R. and G.J. Mount, Glass Ionomers in contemporary restorative dentistry—A Clinical update. Journal of the California Dental Association (CDA), 2003. **2003**.
36. Koubi, S., A. Raskin, and J. Dejou, Effect of dual cure composite as dentin substitute on the maginal integrity of class 2 open-sandwich restoration. Operative Dentistry, 2010. **35**(2): p. 165-171.
37. Moraes, R., et al., Nanohybrid resin composites: nanofiller loaded materials or traditional microhybrid resins? Operative Dentistry, 2009. **34**(5): p. 551-557.

38. Al-Jobair, A., In vitro evaluation of microleakage in contaminated fissures sealed with GC Fuji triage glass ionomer cement. J.King Saud Uni, 2009. **22**(1): p. 25-32.
39. Simi, B. and B.S. Suprabha, Evaluation of microleakage in posterior nanocompositeretorations with adhesive liners. J Consery Dent, 2011. **14**(2): p. 178-181.
40. Fourie, J. and C.F. Smit, Cervical microleakage in class 2 open-sandwich restorations: An in vitro study. SADJ, 2011. **66**(7): p. 320-324.
41. Vilkins, V., P.H. Bindslev, and V. Baelum, Two year evaluation of class 2 resin modified glass ionomer cement/composite open sandwich and composite restorations. Clin Oral Invest, 2000. **4**: p. 133-139.
42. Gupta, K.V., P. Verma, and A. Trivedi, Evaluation of microleakage of various restorative materials: An in vitro study. J life Sci, 2011. **3**(1): p. 29-33.
43. Poggio, C., et al., Microleakage in Class II composite restorations with margins below the CEJ: In vitro evaluation of different restorative techniques. Medicina oral, patologia oral y cirugia bucal, 2013. **18**(5): p. e793.
44. Spencer, P., et al., Adhesive/dentin interface: the weak link in the composite restoration. Annals of biomedical engineering, 2010. **38**(6): p. 1989-2003.
45. Irari, K.W., An in-vitro evaluation of repair protocols applied to composite resin. 2016.
46. Alshali, R.Z., N. Silikas, and J.D. Satterthwaite, Degree of conversion of bulk-fill compared to conventional resin-composites at two time intervals. Dental materials, 2013. **29**(9): p. e213-e217.
47. Flury, S., A. Peutzfeldt, and A. Lussi, Influence of increment thickness on microhardness and dentin bond strength of bulk fill resin composites. Dental materials, 2014. **30**(10): p. 1104-1112.
48. Scotti, N., et al., Microleakage at enamel and dentin margins with a bulk fills flowable resin. European journal of dentistry, 2014. **8**(1): p. 1.
49. Lawrence W. Stockton, S.T.T., Microleakage of class2 posterior composite restorations with gingival margins placed entirely within Dentine. JCDA, 2007. **73**(3).
50. Lindberg, A., J.W. van Dijken, and M. Lindberg, Nine-year evaluation of a polyacid-modified resin composite/resin composite open sandwich technique in Class II cavities. Journal of Dentistry, 2007. **35**(2): p. 124-129.
51. Fabianelli, A., et al., Microleakage in class II restorations: open vs closed centripetal build-up technique. Operative dentistry, 2010. **35**(3): p. 308-313.
52. Usha, H.L., A. Kumari, and D. Mehta, Comparing microleakage and layering methods of silorane-based resin composite in class 5 cavities using confocal microscopy: An in vitro study. J Conserv Dent, 2011. **14**(2): p. 164-168.
53. Bagis, Y.H., I.H. Baltacioglu, and S. Kahyaogullari, Comparing microleakage and the layering methods of silorane–based resin composite in wide class 2 MOD cavities. Operative Dentistry, 2009. **34**(5): p. 578-585.
54. Poggio, C., M. Chiesa, and A. Scribante, Microleakage in class 2 composite restorations with margins below the CEJ : In vitro evaluation of different restorative techniques. Med Oral Patol Oral Cir Bucal, 2013. **18**(5): p. e793-8.
55. Malik, N.A.B., et al., Effect of Liners on Microleakage in Class II

Composite Restoration. Sains Malaysiana, 2013. **42**(1): p. 45–51.
56. Standards, I., ISO 11405 Dental materials—Testing of adhesion to tooth structure Geneve: International Organisation for Standardization for 500 cycles at 5°C-55°C with a 30-second dwell time. 2003.
57. Gale, M. and B. Darvell, Thermal cycling procedures for laboratory testing of dental restorations. Journal of Dentistry, 1999. **27**(2): p. 89-99.
58. Agrawal, V.S., V.V. Parekh, and N.C. Shah, Comparative Evaluation of Microleakage of Silorane-based Composite and Nanohybrid Composite With or Without Polyethylene Fiber Inserts in Class II Restorations: An In Vitro Study. Operative Dentistry, 2012. **37**(5): p. E23-E29.
59. Bona A D, P.C., Rosa V., Microleakage of acid etched glass ionomer sandwich resttoration. J Minim Interv Dent 2009. **2**(1).
60. Sadeghi, M., Influence of flowable materials on microleakage of nanofilled and hybrid Class II composite restorations with LED and QTH LCUs. Indian Journal of Dental Research, 2009. **20**(2): p. 159.
61. El-Safty, S., N. Silikas, and D. Watts, Creep deformation of restorative resin-composites intended for bulk-fill placement. Dental materials, 2012. **28**(8): p. 928-935.
62. Leprince, J.G., et al., Physico-mechanical characteristics of commercially available bulk-fill composites. Journal of Dentistry, 2014. **42**(8): p. 993-1000.
63. Frankenberger, R., et al., Bulk-Fill vs. Layered Resin Composite Restorations in Class II Cavities: Six-Month Results. University Medical Center Giessen and Marburg, 2012.
64. Schirrmeister, J.F., et al., Two-year evaluation of a new nano-ceramic restorative material. Clin Oral Invest, 2006. **10**: p. 181–186.
65. Ahmadi, R., et al., In vitro Comparison of Microleakage of Nanofilled and Flowable Composites in Restoring Class V Cavities in Primary Molars. Zahedan Journal of Research in Medical Sciences, 2013. **15**(1): p. 47-51.
66. Eden, E., D. Cogulu, and T. Attin, The Effect Of Finishing And Polishing Systems On Surface Roughness, Microhardness And Microleakage Of A Nanohybrid Composite. Journal of International Dental and Medical Research, 2012. **5**(3): p. 155-160.
67. Schmidt, M., et al., Marginal adaptation of a low-shrinkage silorane-based composite: A SEM-analysis. Tandlaegebladet, 2012. **116**(10): p. 736-742.
68. Singh, S.V., et al., Microleakage Evaluation of Nano-Ceramics and Nano-Composite Resins using Self Etch Adhesive in Class V Cavities using Single Increment Technique. Dental Journal of Advance Studies, 2013. **1**(II): p. 106-111.
69. Bogra, P., S. Gupta, and S. Kumar, Comparative evaluation of microleakage in class II cavities restored with Ceram X and Filtek P-90: An in vitro study. Contemporary Clinical Dentistry, 2012. **3**(1): p. 9-14.
70. Kumar , V., A. Devi , and R. Bhargava Comparative Evaluation of Microleakage in Class 2 Cavities Restored with A Nanohybrid Composite Using Three Different Increment Techniques- An in vitro Stereomicroscopic Study. Journal of Oral Health & Community Dentistry, 2014. **8**(3): p. 143-147.
71. Kermanshah, H., et al., Microleakage evaluation of Silorane-Based Composites versus Low Shirinkage Methacrylate-Based Composites. Journal of Islamic Dental Association

of IRAN (JIDAI), 2013. **25**(3): p. 147-154.
72. Sharafeddin, F., F. Koohpeima, and B. Palizian, Evaluation of Microleakage in Class V Cavities Filled with Methacrylate-based versus Silorane-based Composites. Journal of Dental Biomaterials, 2015. **2**(2): p. 67-72.
73. Owens, B. and W. Johnson, Effect of single step adhesives on the marginal permeability of Class V resin composites. Operative dentistry, 2007. **32**(1): p. 67-72.
74. Payne, J.H., The marginal seal of Class II restorations: Flowable composite resin compared to injectable glass ionomer. The Journal of clinical pediatric dentistry, 1998. **23**(2): p. 123-130.
75. Gerdolle, D.A., E. Mortier, and D. Droz, Microleakage and polymerization shrinkage of various polymer restorative materials. Journal of Dentistry for Children, 2008. **75**(2): p. 125-133.
76. Mitra, S.B., et al., Long-term adhesion and mechanism of bonding of a paste-liquid resin-modified glass-ionomer. Dental materials, 2009. **25**(4): p. 459-466.
77. Attin, T., et al., Curing shrinkage and volumetric changes of resin-modified glass ionomer restorative materials. Dental materials, 1995. **11**(5-6): p. 359-362.
78. Feilzer, A.J., et al., The influence of water sorption on the development of setting shrinkage stress in traditional and resin-modified glass ionomer cements. Dental materials, 1995. **11**(3): p. 186-190.
79. McLean, J.W., Dentinal bonding agents versus glass-ionomer cements. Quintessence International, 1996. **27**(10).
80. Yap, A.U., Resin-modified glass ionomer cements: a comparison of water sorption characteristics. Biomaterials, 1996. **17**(19): p. 1897-1900.
81. El-Ashiry, E.A., et al., Microleakage Evaluation of Two Different Nano-Restorative Materials in Primary Molars: In Vitro Study. Life Science Journal, 2012. **9**(3): p. 2292-2300.
82. Ab Malik, N., et al., Effect of liners on microleakage in class II composite restoration. Sains Malaysiana, 2013. **42**(1): p. 45-51.
83. Beznos, C., Microleakage at the cervical margin of composite Class II cavities with different restorative techniques. Operative Dentistry, 2001. **26**(1): p. 60-69.
84. W.G.Walls, J.F.M.C.a.A., Applied dental materials. 2012. **chapter 25**: p. 260.
85. Bore Gowda, V., et al., Evaluation of Gingival Microleakage in Class II Composite Restorations with Different Lining Techniques: An In Vitro Study. Scientifica, 2015. **2015**.
86. Gladys, S., et al., Marginal adaptation and retention of a glass-ionomer, resin-modified glass-ionomers and a polyacid-modified resin composite in cervical Class-V lesions. Dental materials, 1998. **14**(4): p. 294-306.
87. Praveen , M.R.K., et al., Evaluation Of Gingival Microleakage Of Composite Restorations With Glass Fiber Inserts, Polyethylene Fiber Inserts And Prepolymerized Composite Inserts: An In Vitro Study. Imperial Journal of Interdisciplinary Research (IJIR), 2016. **2**(3): p. 627-630.
88. Oliveira, A.L.B.M.d., et al., Eff ect of fi nishing and polishing on color stability of a nanofi lled resin immersed in diff erent media. Rev Odontol UNESP, 2014. **43**(5): p. 338-342.
89. Alqahtani, M.Q., Tooth-bleaching procedures and their controversial effects: A literature review. The Saudi Dental Journal, 2014. **26**: p. 33–46.

90. Bugalia, A., et al., Effect of Placement Techniques, Flowable Composite, Liner and Fibre Inserts on Marginal Microleakage of Class II Composite Restorations. Journal of Evidence Based Med & Hlthcare, 2015. **2**(32): p. 4779-87.
91. Gupta, K.V., P. Verma, and A. Trivedi, Evaluation of Microleakage of Various Restorative Materials: An in Vitro Study. Life Science Journal, 2011. **3**(1): p. 29-33.
92. Gowda, V.B., et al., Evaluation of Gingival Microleakage in Class II Composite Restorations with Different Lining Techniques: An In Vitro Study. Scientifica, 2015. **2015**: p. 1-6.
93. Narayana, V., et al., Assessment of Microleakage in Class II Cavities having Gingival Wall in Cementum using Three Different Posterior Composites. Journal of International Oral Health, 2014. **6**(4): p. 35-41.
94. Camps, J. and D. Pashley, Reliability of the dye penetration studies. Journal of Endodontics, 2003. **29**(9): p. 592-594.
95. Kronman, J.H., et al., Microbiologic evaluation of poly-HEMA root canal filling material. Oral surgery, oral medicine, oral pathology, 1979. **48**(2): p. 175-177.
96. Vaidyanathan, T. and J. Vaidyanathan, Recent advances in the theory and mechanism of adhesive resin bonding to dentin: a critical review. Journal of Biomedical Materials Research Part B: Applied Biomaterials, 2009. **88**(2): p. 558-578.
97. Liu, Q., et al., Preparation of macroporous poly (2-hydroxyethyl methacrylate) hydrogels by enhanced phase separation. Biomaterials, 2000. **21**(21): p. 2163-2169.
98. Waltimo, T.M., et al., Clinical performance of 3 endodontic sealers. Oral Surgery, Oral Medicine, Oral Pathology, Oral Radiology, and Endodontology, 2001. **92**(1): p. 89-92.
99. Starkey, D.L., R.W. Anderson, and D.H. Pashley, An evaluation of the effect of methylene blue dye pH on apical leakage. Journal of endodontics, 1993. **19**(9): p. 435-439.
100. Goldberg, F. and J. Gurfinkel, Analysis of the use of Dycal with gutta-percha points as an endodontic filling technique. Oral surgery, oral medicine, oral pathology, 1979. **47**(1): p. 78-82.
101. Ahlberg, K., P. Assavanop, and W. Tay, A comparison of the apical dye penetration patterns shown by methylene blue and India ink in root-filled teeth. International endodontic journal, 1995. **28**(1): p. 30-34.
102. Kocll, K., P.S. Min, and G.G. Stewart, Comparison of apical leakage between Ketac Endo sealer and Grossman sealer. Oral surgery, oral medicine, oral pathology, 1994. **78**(6): p. 784-787.
103. Ximenez-Fyvie, L.A., et al., Accuracy of endodontic microleakage results: autoradiographic vs. volumetric measurements. Journal of endodontics, 1996. **22**(6): p. 294-297.
104. Olmez, A., N. Oztas, and H. Bodur, The effect of flowable resin composite on microleakage and internal voids in class II composite restorations. Oper Dent, 2004. **29**(6): p. 713-9.
105. Chuang, S.-F., J.-K. Liu, and Y.-T. Jin, Microleakage and internal voids in Class II composite restorations with flowable composite linings. Operative dentistry, 2001. **26**(2): p. 193-200.
106. Alqahtani, M.Q., Tooth-bleaching procedures and their controversial effects: A literature review. The Saudi dental journal, 2014. **26**(2): p. 33-46.
107. Aranha, A. and L. Pimenta, Effect of two different restorative techniques using resin-based composites on

microleakage. American journal of dentistry, 2004. **17**(2): p. 99-103.
108. Giachetti, L., et al., A review of polymerization shrinkage stress: current techniques for posterior direct resin restorations. J Contemp Dent Pract, 2006. **7**(4): p. 79-88.
109. Aguiar, F., et al., Quantitative evaluation of marginal leakage of two resin composite restorations using two filling techniques. Operative dentistry, 2002. **27**(5): p. 475-479.
110. Aguiar, F., K. Ajudarte, and J. Lovadino, Effect of light curing modes and filling techniques on microleakage of posterior resin composite restorations. Operative dentistry, 2002. **27**(6): p. 557-562.
111. Bugalia, A., et al., EFFECT OF PLACEMENT TECHNIQUES, FLOWABLE COMPOSITE, LINER AND FIBRE INSERTS ON MARGINAL MICROLEAKAGE OF CLASS II COMPOSITE RESTORATIONS.

Effect of Xanthan Gum Concentration on the Rheological Properties of Commercial Tomato Ketchup

R. Ahmed[1], R.M. Khan[1], A. Nafees[1], H. Arif[2], A. Bari[1], M. Suhaib[1], N. Abdul Raheem[1], M. Waseem[1], M. Sufyan[1], K.A. Syed[1]

[1]Polymer & Petrochemical Engineering Department
NED University of Engineering & Technology, Karachi, Pakistan
ahmedr@neduet.edu.pk; drkausarali@neduet.edu.pk

[2]Department of Industrial & Manufacturing Engineering,
NED University of Engineering & Technology, Karachi, Pakistan
hammad_aaa@hotmail.com

ABSTRACT

In this study the effect of xanthan gum concentration on rheological properties of commercial tomato ketchup has been investigated. Xanthan gum was added to the tomato ketchup at various concentrations ranging from 0.05 to 0.2 % (w/v) under vigorous mixing. The Brookfield viscometer data was converted into the rheological parameters using Mitschka's method. All the samples showed pseudoplastic behavior with yield stress. Although in all samples the power law index, ranging from 0.51 to 0.82, was less than unity but the samples becomes more Newtonian as the concentration of the xanthan gum is increased. Yield stress increases and consistency coefficient decreases with increase in the xanthan gum concentration. The yield stress, power law index, and consistency coefficient values reported here are in accordance with the values reported in the literature.

Keywords: rheology, tomato ketchup, xanthan gum, Herschel-Bulkley model, yield stress.

1. INTRODUCTION:

Rheology is the science of flow and deformation notably non-Newtonian fluids [1]. Rheological characterization provides opportunity to the quality control of raw materials, intermediate products and finished products [2,3].

Tomato is volitionally consumed raw or in the processed tomato product such as tomato ketchups, tomato paste, juice, and many more. The acceptance of these tomato processed products by the consumers largely depends on it quality of tomato variety and ripeness, water soluble and insoluble solid contents, particle size and distribution, consistency, and other rheological properties [4-7]. The determination of rheological properties, for example yield stress and viscosity, are essential for tomato processing such as mixing, pumping and heating [8]. Various thickeners [9] are added to tomato ketchups to meet the consumer thick product demand. Starch [10], modified starch [11], tomato pulp powder [12], and various hydrocolloids [13].

Xanthan gums are anionic polysaccharides and are preferred industrially as thickening agents [14].

The purpose of this study is to understand the effect of xanthan gum concentration on the rheological behavior of a commercial tomato ketchup sample notably on yield stress and consistency coefficient. Both of the parameters are important for the acceptance of tomato products.

2. EXPERIMENTAL:

2.1 Materials

A commercial sample of tomato ketchup was purchased from the local market and stored at room temperature. As per manufacturer the ketchup ingredients are water, sugar, tomato pulp, salt, vinegar, stabilizer, citric acid, mixed

spices, and preservatives. Table 1 shows the properties of the raw materials.

S.No	Raw material	Properties
1.	Tomato ketchup	[a] Specific gravity: 1.14 [b] Solid content: 27%
2.	[c]Xanthan gum	pH : 6.0-8.0 Ashes = < 12

a: Sp. Gravity = mass of the tomato pulp/mass of water; b: Solid content = (mass of sample - loss of mass on drying)/ (mass of samples); c: E415 (Changzhou Kamadi Trading Co., Ltd., China).

2.2 Sample Preparation

Xanthan gum in various percentage ranges (0.05 – 0.2 % w/v) were mixed in the commercial Ketchup at 80 °C under vigorous mixing using overhead stirrer. The mixture was cooled to room temperature under ambient conditions and stored in PVC bottles at room temperature for rheological characterization.

2.3 Characterizations

2.3.1 Rheological Characterization

Rheological measurements were performed at room temperature, 30 °C, using Brookfield RV viscometer (Brookfield Engineering Laboratories, Inc., USA). All the ketchup samples were covered with aluminum foils during rheological measurements to avoid the loss of moisture and other undesirable changes in the pastes.

Flow curves were developed for all the ketchup samples using Mitschka's method [15]. All the measurements were reproduced in triplicate for each sample.

3. RESULTS AND DISCUSSION:

3.1 Determination of Flow Curve

Figure 1 shows that all the ketchup samples show non-Newtonian, pseudoplastic flow behavior and yield stress. The similar flow behavior is reported by many researchers for their ketchups [16-17].

The flow parameters were determined using Herschel-Bulkley rheological model [6]:

$$\tau = \tau_0 + k\dot{\gamma}^n$$

Where τ_0 (Pa) – yield stress (or flow limit), k (Pa s^n) – consistency coefficient, and n (–) flow behavior index.

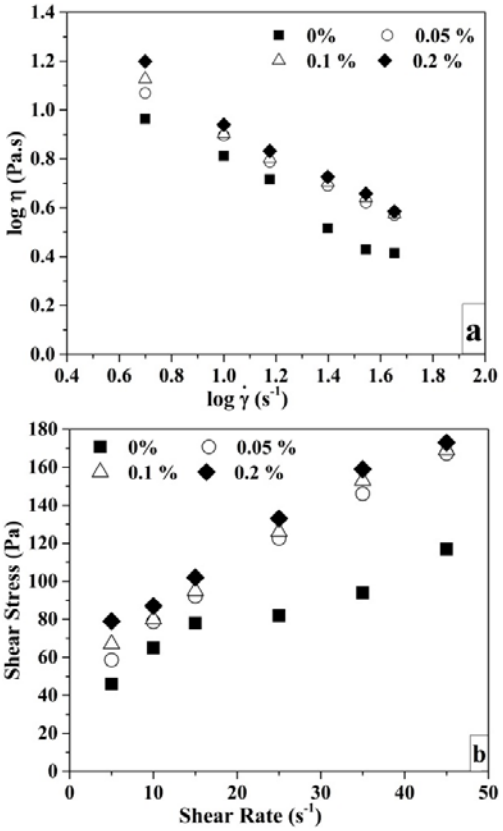

Figure 1: Flow curves for the commercial ketchup (0%) and Xanthan gum added ketchup samples (0.05%, 0.1 %, and 0.2% w/v). (a) Plot of log(viscosity) versus log(shear rate), (b) Plot of shear stress versus shear rate.

A representative curve for the determination of rheological parameters is shown in figure 2. The rheological parameters were determined using Herschel-Bulkley model and are mentioned in the figure.

All the samples were fitted with same model, see figure 3, and the determined parameters are plotted in figure 4 (a, b, and c).

It is evident from the figure 4a that all the samples showed power law index, a parameter

that indicates the deviation from the Newtonian fluid behavior, value less than unity. The lower values show pseudoplastic flow behavior and are in good agreement with other reported work [9,17].

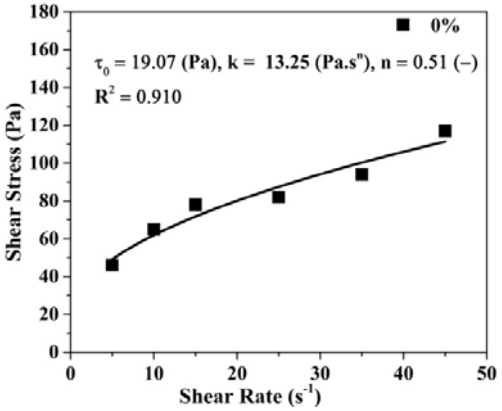

Figure 2: A representative curve show the Herschel-Bulkley rheological model fit to the commercial sample (0%) for the determination of rheological parameters. The R-squared (R^2) value shows the regression coefficient.

However, it is interesting to note that increasing the concentration of xanthan gum leads to the higher values of power law index values. It indicates that the tomato ketchup becomes more Newtonian in contrast to the expected non-Newtonian behavior as reported by the researchers [9,13,18]. A similar increasing trend in power law index was also reported by Romanos et al. [19] but the authors did not provide the explanations for the observed trend.

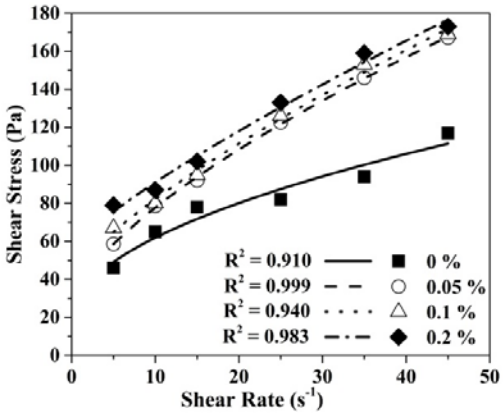

Figure 3: Flow curves fitted with Herschel-Bulkley model.

We believe that due to the anionic nature and long chains xanthan gum do not facilitate thermodynamic miscibility and hence inefficient intermolecular interactions required for thickening [20].

The yield stress, a major rheological parameter for the acceptability of tomato ketchup, increases with increase in xanthan gum concentration, see figure 4b. This observation is in line with the reported trend [9,13,18]. Figure 4c shows the effect of xanthan gum concentration on the consistency coefficient, a measure of the viscosity. A similar decreasing trend in the consistency coefficient is also reported by Romanos et al.. The decreasing trend of consistency coefficient might be attributed to the inefficient interactions between the xanthan gum and tomato pulp ingredients [20]. The values reported in this work are within the range reported by Dak et al. [21] for their tomato concentrates.

The decreasing trend of consistency coefficient predicts that once the tomato ketchup, loaded with higher xanthan gum concentration, will be sheared (shaking or tapping the tomato ketchup sample) its viscosity will decreases. After the shear is removed the sample thickens to its initial viscosity as suggested by the higher yield stress values for the tomato ketchup samples with higher concentration of xanthan gum.

CONCLUSIONS:

1. Brookfield data was successfully converted into the rheological parameters using Mitschka's method.
2. The rheological data was modeled with three parameter Herschel-Bulkley rheological model.
3. All the samples used in this study showed non-Newtonian flow behavior with yield stress.
4. The observed flow behavior index (0.51 to 0.82) was less than unity for all the samples revealing pseudoplastic behavior. The increasing values of flow behavior index with increasing xanthan gum oncentrations

show the tendency of the samples towards Newtonian fluid behavior.

5. Yield stress increases with the increase in xanthan gum concentration. This increasing trend in yield stress is in accordance with the reported trend in the literature.
6. The decreasing consistency coefficient observations are attributed to the inefficient interactions between the xanthan gum and tomato pulp ingredients.

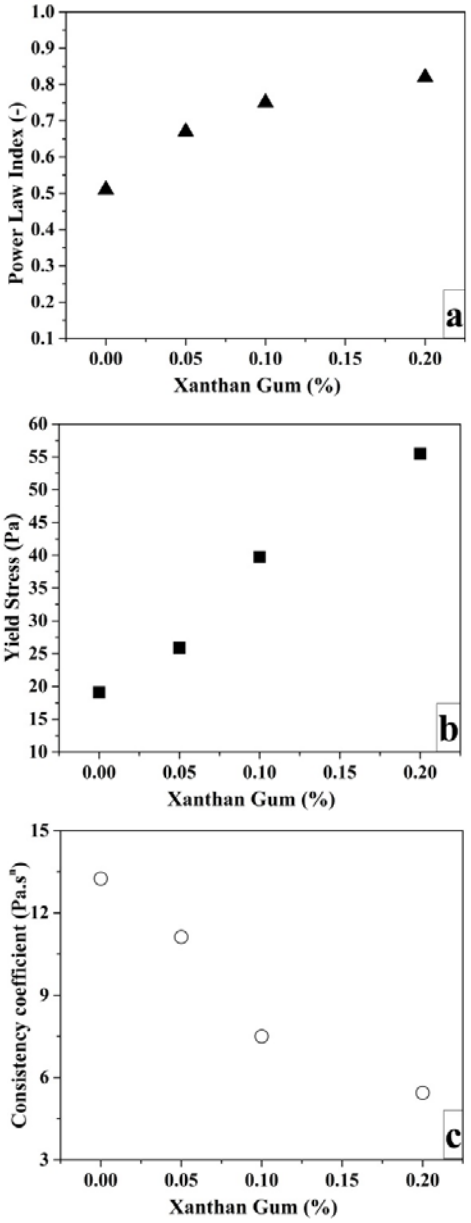

Figure 4: Effect of Xanthan gum concentration on (a) flow behavior index, (b) yield stress, and (c) consistency coefficient.

5. REFERENCES:

1. Macosko C.W., "Rheology: Principles, Measurements and Applications", 1994.
2. Steffe J.E., "Rheological Methods in Food Process Engineering", 2nd Ed., 1996, Freeman Press.
3. Tabilo-Munizaga G., Barbosa-Cánovas G.V., Journal of Food Engineering, 2005, 67:147–156.
4. Tibäck E.A., Svelander C.A., Colle I.J.P., Altskär A.I., Alminger M.A.G., Hendrickx M.E.G., Ahrné L.M., Langton I.B.C., J. Food Sc., 2009, 74:1750–3841.
5. Bayod E., Willers E.P., Tornberg E., LWT, 2008, 41:1289–1300.
6. Sharoba A.M., Senge B., EL-Mansy H. A., Bahlol H. E., Blochwitz R., Europ. Food Res. Techn., 2005, 220:142–151.
7. Claybon, K.T., Barringer, S.A., Journal of Food Science, 2002, 67 (6): 2380-2384.
8. Sharma S.K., Le Maguer M., Italian Journal of Food Science, 1996, 2: 107–113.
9. Varela P., Gambaro A., Gimenez A.M., Duran I., Lema P., Journal of Texture Studies,2003,34:317–330.
10. Bonnefin G., International Food Ingredients, 2000, 2:29–30.
11. Lee Y.I., Lee S.J., Noh W.S., Agricultural Chemistry and Biotechnology, 1997, 40:48–52.
12. Farahnaky A., Abbasi A., Jamalian J., Mesbahi G., Journal of Texture Studies, 2008, 39: 169–182.
13. Sahin H., Ozdemir F., Food Hydrocolloids, 2004, 18: 1015–1022.
14. Glicksman,M, "Food Hydrocolloids" Vol. 1, CRC Press. 1982
15. Mitschka P., Rheologica Acta, 1882, 21: 207–209.
16. Probola G., Zander L., Haponiuk E., Pol. J. Natur.Sc. , 2015, 30(3):297–305.
17. Upasana-Rani, Bains, G.S., Journal of Texture Studies, 1987, 18: 125-135.
18. Singh H., Sharma A., Singh H., International Journal of Food Properties, 2000, 5(1):179-191.
19. Romanos S., Karina S., Noelia S., Andrea V., Gatsón A., Ana G., Patricia L., 2nd Mercosur Congress on Chemical Engineering, 4th Mercosur Congress on Process Systems Engineering.

20. Gibinski M., Kowaski S., Sady M., Krawontka J., Tonasik P., Sikora M., J Food Engg, 2006,75:407–414.
21. Dak M., Verma R.C., Jaaffrey S.N.A., Int International Journal of Food Engineering, 2008, 4(7):1-17.

REMOVAL OF METHYLENE BLUE AND MALACHITE GREEN BY ADSORPTION ON BARK OF GUAIACUM OFFICINALE TREE

Ghazala Aftab[1], Hira Sultan[1], Ghazanfar Hussain[2], Shaista Perveen[3]

Ned University of Engineering and Technology[1], Ned University of Engineering and Technology[1], Ned University of Engineering and Technology[2]

ABSTRACT

Wastewater effluents contain synthetic dyes which cause an impending hazard to the environment hence these dyes need to remove from the water bodies. The several dye removal techniques are classified into Chemical, Physical, and Biological methods. Adsorption found to be very effective and cheap method among the all available dye removal methods. Therefore, studies associated to searching for efficient and low cost adsorbents derived from existing resources are gaining importance for the removal of dyes. Experimental studies proved that the effective removal of dyes is obtained using several cheaply available non-conventional adsorbents also. Therefore, studies related to searching for efficient and low cost adsorbents derived from existing resources are gaining importance for the removal of dyes. Bark of the tree (guaiacum officinale) was found to be effective for the removal of methylene blue from the water. pH 7was suitable for the removal of 50 ppm of methylene blue from aqueous solution. 0.2 g of adsorbent dosage was selected for maximum removal in 30min. 89% removal was achieved at these optimal conditions.

Key words: Dyes, Adsorption, low cost adsorbents

1. INTRODUCTION:

High production and use of dyes generates colored wastewater and pollute the environment. Dyes are used on many consumer products due to their coloring properties. Paints, textiles, inks, pharmaceutical, food, cosmetics, plastics, photographic and paper industries discharge colored wastewater. The increase demand in textile products and increase in their production with the use of synthetic dyes resulting in wastewater effluent has become serious pollution problem in recent times. Most of these dyes fails to go through a wastewater treatment processes and remains in the environment for a very long period due to their high stability to light, temperature, water, detergents, chemicals, soap, bleach and perspiration. Dyes can remain for an extended period of time in the environment due to their high thermal and photo stability to resist bio degradation.

Most of the dyes and their breakdown products are carcinogenic, mutagenic and toxic. Primary cancers of kidney, urinary bladder and liver were reported in workers working with dyes. Dyes can cause allergies like contact dermatitis, respiratory disease, and irritation in eyes, irritation in skin, irritation in mucus membrane and irritation in upper respiratory tract.

The methods of color removal from industrial effluents include coagulation, precipitation, biological treatment, irradiation, ion exchange, oxidation and adsorption. Among these options, adsorption is most preferred method and activated carbon is most effective adsorbent widely employed to treat wastewater containing different classes of dyes, recognizing the economical drawback of commercial activated carbon Various inexpensive materials like tree barks, fly ash, ground nut shell powder, red soil, bauxite, etc., are used for removal of acid, basic direct and disperse dyes. The present study commenced

to assess the efficiency of *guaiacum officinale* bark powder as an adsorbent for the removal of MB dye from aqueous solutions. The effect of adsorption parameters such as initial dye concentration, pH, adsorbent dose, agitation time has been studied to obtain optimum conditions for the process of adsorption.

2. EXPERIMENTAL:

2. Materials and Methods

2.1 Adsorbent

Adsorbent used in the present study is mature dried bark of Guaiacum officinale obtained from the Botanical Garden of the University of Karachi in Karachi, Pakistan. It was washed thoroughly with distilled water to remove dust and other impurities. Washed bark was dried for 2 days in sunlight. It was then dried in oven at 110.2 °C and powdered in a hammer. The powdered biomass was divided into various particle sizes by using different sieves and then stored in plastic container for further use.

2.2 MB and MG Dye (Adsorbate)

Methylene blue (MB) and Malachite green (MG) are monovalent cationic dyes. Molecular weight of MB and MG are 373.9 and 364.911 g/mol respectively. The laboratory grade MB and MG dyes were obtained from Merck and used without further purification. A stock solution of 1000 ppm was prepared in deionized water and the experimental solutions of the desired concentration were obtained by successive dilutions.

2.3 Adsorption Experiments

The wavelength corresponding to the maximum absorbance λmax of methylene blue and malachite green were determined from the plot of absorbance verses wavelength, and this wavelength were used for measuring the absorbance of residual concentration of dye. For MB and MG it were found to be 612 and 616nm respectively. The initial pH values of the solutions were pre-set with 0.1 M hydrochloric acid or sodium hydroxide using the *DEEP VERSION (EI) pH meter*. Batch adsorption experiments were performed on an orbital shaker at 150 rpm using 250 ml flask containing 50 ml coloring solutions of specific concentration at desired pH value. Specific adsorbent dose (measured in g) was added to each flask. After mixing the flask for a predetermined time, the dye solutions were separated from the adsorbent by filtration after centrifugation. The concentration of dyes in supernatant solutions was determined by measuring the absorbance at the wavelength of maximum absorbance using *Spectrophotometer-Systronics104*. Effect of various factors such as pH, contact time and adsorbent dose were determined. The amount of dyestuff adsorbed by biomass was calculated using the following equation:

$$q = (C_0 - C_t) \times V/W$$

The Removal % of dye was determined by

$$R\% = [(C_o - C_t)/ C_o] \times 100$$

Where q (mg/g) is the amount of dye adsorbed per unit mass of biomass, C_0 and C_o (mg/L) are the initial and equilibrium liquid phase concentration of dye. V (L) the initial volume of dye solution, and W (g) the weight of the biomass.

The influence of each parameter (pH, contact time, adjuvant dose and initial dye concentration) was evaluated in the experiment by changing the parameter that was evaluated while all other parameters in the experiment were kept constant.

3. Results and Discussions

3.1 CHARACTERIZATION OF ADSORBENT

3.1.1 POINT OF ZERO CHARGE

The point of zero charge for an adsorbate is defined as pH value at which, the net charge at

the surface of the adsorbent is zero. The adsorbent taken in a specific amount in a specific concentration of salt solution. Different initial pH values were preset before giving it the agitation up to a point at which the final pH becomes constant. The values are plot in a graph to attain a PH_{PZC} value. Fig 1 shows the graph of the values attained. The pH_{PZC} value of GOB was found to be ''5.3''. As discussed , the net charge at PH_{PZC} is zero , the available charged sites (net charge) at pH value lower than that are positive , whereas, the available charged sites (net charge) at pH value higher than this value are negative.

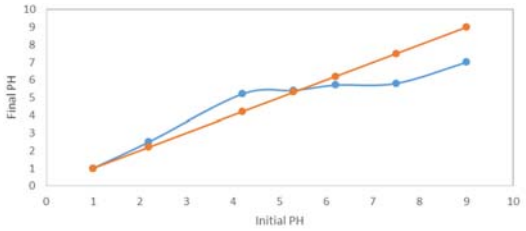

Figure 1: Plots of the values for PZC

3.2 Influence of sorption parameters

3.2.1 Effect of pH

pH of the adsorbate solution is the most influencing variable factor in the adsorption mechanism. The reason for that is partly because of the Hydrogen ion which itself is a powerful enough ion to hinder the mechanism and partly because pH of the solution also tends to influence the dye as well as it tends to change the structure (ionize the functional groups) of the adsorbent.

Methylene blue and Malachite Green being a cationic dye, the increasing H^+ concentration (due to the decreasing pH) decreases the availability of the dye cations. Due to this very fact, the dye adsorption is not favorable at lower pH. However, this increased H^+ ion concentration increases the positive sites available at the adsorbate surface. The pH_{PZC} of the GOB adsorbent was found to be 5.3 , as shown in Fig 1,which means that, the GOB surface has overall positive charge at pH value lower than ''5.3'' and negative at pH value higher than ''5.3'' . Positive sites are not favorable for the uptake of a cationic dye, which needs increased negative sites to be adsorbed on to the adsorbent surface. All of these factors favors the higher pH (towards neutral) of the solution rather than the acidic (lower) PH.

Fig 2 shows the removal% of the methylene blue and malachite green at different pH. The effect was observed for the 50ppm of dye concentration for 30mins with 0.5gms of adsorbent dose. Fig 2 shows the removal% of the Methylene Blue Dye solution was increased with increased in pH and was highest at the pH value equal to ''7 '' ,after which, a slight decrease was observed.

The same phenomenon was observed for the Malachite Green dye solution. However, a sharp decrease was observed at PH value of ''2''.this was due to the above discussed facts. The removal% was found to be maximum at PH value of 7 here as well.

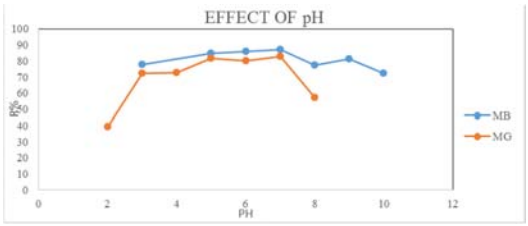

Figure 2: Experimental conditions: Initial dye concentration=50ppm, adsorbent dose = 0.5g, contact time = 30min, temperature 24 ºC.

3.2.2 Effect of Adsorbent Dose

The effect of adsorbent dosage holds an importance as it tells about the capacity of an adsorbent allowing the adsorption onto its surface. The effect was checked at a 50ppm MB and MG dye concentration for 30mins at 7 pH. Fig 3 shows the removal% of MB and MG dye solutions respectively at different adsorbent dose. Both of the dye solutions showed maximum removal% with the GOB amount of 0.2gms, after which, the removal% decreased or remained constant.

The increase in the adsorbent dose increases the overall surface area of the adsorbent, which increases the removal%. However, the

adsorbent surface has a specific affinity for every particular adsorbate after which it does not uptake any more of the adsorbate. Due to this reason the removal% becomes constant after a certain point.

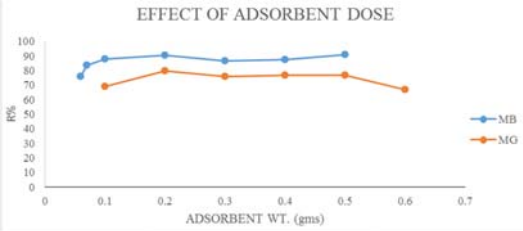

Figure 3: Effect of Adsorbent Dose. Contact time =30mins, pH=7 and Initial dye concentration=50ppm

3.2.3 Effect of Contact time

The effect of contact time is related with the cost effectiveness of the adsorbent. This physical parameter is to attain the shortest possible time with best possible results. The Dye solutions of the 50ppm MB and MG were used with PH of 7. Fig 4shows the removal% of the MB and MG solutions respectively in different contact time. The removal% was checked up to 60mins of contact time with the dye solution. The removal% was found to be best (most cost effective) at the 30mins of contact time with the Adsorbate solution. The removal% remained almost constant or below that afterwards. Whereas, the removal% was constant after 30mins of contact time in MG solution with 40mins of contact time showing the slightly better removal%. However, 30mins of contact time was still most cost effective due to the fact of it being lesser in time and still providing with almost the same efficiency if dye removal.

The dye solutions of both MB and MG showed almost a similar trend of dye adsorption. This trend can be divided into 2 step processes. First, the adsorbate being rapidly attached onto the adsorbent surface showing a high removal% in very short time. Both of the dye solutions showed about 75-80% of dye uptake in a very short span of 5mins. However, in the second step process, the removal% increased slightly and gradually to a point it became almost constant. This was due to the fact that at first, the GOB surface had active sites readily available for adsorption. After these readily available sites were saturated with the dye molecules, further dye molecules were left to diffuse in-between the particles to the interior of the porous adsorbent surface.

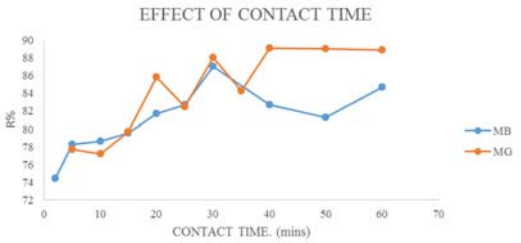

Figure 4: Experimental conditions: Initial dye concentration=50ppm, adsorbent dose = 0.2g, pH = 7, temperature 24 ºC.

CONCLUSIONS:

Our study proposed to use an economic and environmental-friendly walnut shell as the adsorbent to remove methylene blue for the first time. The effects of contact time, pH, adsorbent dosage, were investigated. 5.3 point of zero charge was determined by pH drift method. The solution pH was found to be a very important factor controlling the adsorption processes: the adsorption was favored at pH 7. This can be explained by the electrostatic forces between GOB particles and (MB and MG dyes). At pH 7, more attractive forces existed between cationic dyes and GOB particles, resulting in more adsorption of dyes on GOB particles. Under the optimized experimental conditions, the removal efficiency of 88% for both dyes by GOB can be achieved, indicating that bark of guaiacum officinal was a promising and environmental-friendly adsorbent to remove cationic dyes.

GALVANIZING ON DIFFERENT HEAT TREATED STEEL AND THEIR EFFECT ON MICROSTRUCTURAL PROPERTIES

Muntazer Ayaz[1], Kouser[1], Shahzad Khan[2], and Ayesha Shabbir[2]

Metallurgical Engineering Department, NED University of Engineering & Technology, Karachi, Pakistan
Corresponding author. Tel.: +923422122879, +923343122726
E-mail address: Engr.Muntazer2015@gmail.com , kouser.metallurgical12@gmail.com

ABSTRACT

In the modern era of industrialization, where contribution of different gases and chemicals in the environment have increased the Pollutions in the environment and has accelerated the corrosion rate of materials there by demands of corrosion resistant materials have been increased. Hot dip galvanizing is one of the effective and an ancient method to produce such a corrosion resistant material by coating zinc on steel. In this study, AISI 1014 Mild Steel was galvanized before and after heat treatments. The main heat treatments includes; Annealing (550^{o}C - 650^{o}C), Normalizing (550^{o}C - 650^{o}C) and Quenching (900^{o}C – 910^{o}C).The aim of study was to investigate the effect of microstructure on coating (Zinc) quality. The results suggest that the best coating quality was observed in annealed sample. In contrast worst coating quality was observed for quenched sample. The coating quality is assessed in terms, the level of porosity. Further discussion is presented in the light of available results.

Keywords: Galvanizing; normalizing; annealing; quenching

1. INTRODUCTION

The demand of zinc coated steel is increasing day by day due to the increasing effect of the chemicals and gases which contribute the rapid increment of the corrosion rate and fatalities on the large scale can be done in term economic losses or human injuries or even death can be done by this corrosion. Research and development has been contributing to avoid these losses in term of improving the corrosion resistance of the material. There are multiple method by which surface of the material can be protected being corrode. One of these methods is Hot Dip galvanizing process in which Zinc layer is coated on the surface of material. This process is usually recommended for Steels and many other Iron alloy. It is an economical way to protect the atmospheric sensitive material like steel and other iron alloys from corrosion by immersing the clean and oxide free steel into molten zinc. This produce zinc coating on the surface comprises of multiple layers. Which have improved properties and led to a drastic enhancement in its applications over the last ten years. In general, the coatings formed from the hot-dip method present outstanding corrosion resistance and paint adhesion. The formability and coating adhesion suffer as in the form of increased thickness. However, the characteristic of these layers are controlled by the iron-zinc inter metallic compounds that form in the coating. The corrosion resistance, coating adhesion and ductility, formability, weld-ability and paint ability depends on the composition and structure of the phases present in the coating.

The mild steel is a low iron-carbon alloy which contains less than 0.3% carbon. This percentage of carbon makes it more ductile and soft. Due to the defect in the oxide film on the mild steel, these defects are caused by mechanical damage like scratches or from the natural discontinuities in the Film, these include: inclusions, grain boundaries, or networks of dislocation at the surface of the steel, Mild steel vigorously reacts and reverts back to iron oxide (rust) in the readiness of the mild steel to oxidize on exterior exposure means, that is, it should be adequately protected from rusting. Hot dip galvanizing is a type of zinc coating .It is an economical way to

protect the atmospheric sensitive material like steel and other iron alloys from corrosion by immersing the clean and oxide free steel into molten zinc.

During hot dip galvanizing different Iron zinc alloy layers are formed. These layers exhibit different chemical composition, hardness and morphologies.

Heat treatment is a process to obtain desired microstructure of a material by controlled cooling and heating time and temperature. This is usually done to obtain desired mechanical properties. Annealing, Quenching and normalizing are the heat treatment processes. In this study we have annealed, quenched and normalized different sample of mild steel in order to study the effect on morphology and chemical properties of a hot dip galvanized layer.

The present investigation is an effort to have a better understanding of the hardness of the hot dip galvanized coatings on the heat treated (annealed, normalized, quenched) mild steel. These investigations are performed by hot dip galvanizing the samples and then study the microstructures by conventional metallography techniques. For further information we have determined the hardness of different layers by micro hardness tester. The morphology of the grains are studied by SEM and optical microscope.

The hot dip galvanizing process affect the microstructure of the mild steel and form the metallurgical bonding galvanizing layers (eta, zeta, delta and gamma) with the base metal (mild steel). Hot dip galvanizing not only increases the corrosion resistance but also increase the abrasion resistance of the material.

We have also observed that Due to the heat treatment hardness of different layers (Delta and Gamma) changes.

The Gama phase is usually is hard and a thin layer with higher iron content. It is therefore easily weld able but hard to form, and the resistance to corrosion also decreases. If the thickness of the Gamma phase is increased it leads to a harder coating but will favor the entire coating to crack.

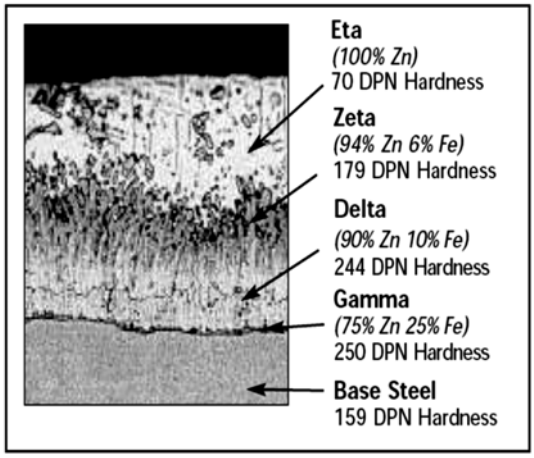

Figure 1 Photomicrograph of galvanized coating (source: American Galvanizers Association report 2000)

2. EXPERIMENTAL PROCEDURE

2.1 Materials

As discussed earlier iron and its alloys are recommended for Hot Dip galvanizing therefore the material used in this experiment was a mild steel sheet of 12 mm thickness. For this experiment, the mild steel sheets were cut into square shaped with dimensions 12 mm x 12 mm x 76.2 mm. as shown in the fig:

Figure 2. Figure 2 Sample of Mild Steel grades1014 for galvanizing

To ensure average bulk composition of the material spectroscopic testing is carried out from Pakistan Steel Mill and results are plotted in the table.

Table 1. Chemical composition of mild steel

Element	Composition (wt. %)
C	0.14
Si	0.02
Mn	0.35
P	0.019
S	0.014
Cr	0.009
Ni	0.01
Al	0.13
Cu	0.02
Fe	Balanced

2.2 Heat Treatment cycles.

This experiment mainly covered the study of galvanizing process on different heat treated steel. For this experiment, the mild steel sheets were cut into square shaped with dimensions 12 mm x 12 mm x 76.2 mm. First sample was annealed, the sample was heated to above the upper critical temperature (550 -650) °C for 1 hour and then cooled in a furnace at the rate of 38 °C per hour. Second sample was normalized, it consist of heating the sample to 30 to 50 °C above the upper critical temperature and then remove from the furnace and cooled at room temperature. Third sample was quenched and heated in a furnace up to 900 °C and sock for 30 min and then quenched in water.

2.3 Galvanizing of Mild Steel

The mild steel samples were degreased in 10% detergent and NaOH solution at 60 °C for 15 min, and after degreasing the samples were washed in a water bath to prevent transfer of degreasing solvent to the next stage. Next the pickling were done in 100 - 200 g/l dilute hydrochloric acid for 15 min at room temperature, and then rinsed in a water bath. Next the samples were dipped in a flux bath which consists of 75 wt. % ammonium chloride and 25 wt. % zinc chloride of 500 g/l solution at a temperature of 80 °C, after immersion in the flux bath the samples were dried for 30 min at a temperature of 70°C. Then the samples were completely immersed in a zinc bath consisting of 99.99 % pure molten zinc for 8 min, the bath temperature is maintained at about 530 °C and samples were taken off from the bath and apply an air pressure of 2 bars on galvanized samples for the formation of bright shiny and an even coating. Then samples were quenched to cool in a sodium di chromate solution at room temperature the purpose of quenching in sodium-di-chromate is to avoid formation of white powder on zinc.

2.4 Microstructure Observations

Figure 3 Hot Dip Galvanized samples of Mild Steel Grade 1014

Before and after galvanizing, the samples were cut to study the microstructure ofthe cross sectioned part by performing subsequent grinding, polishing with Al_2O_3 and etched in 1 % nital (99 % ethanol and 1% HNO3). The microstructure of mild steel after heat treatment and galvanized coating and thickness were observed by using SEM, Spectroscopy microscope and Optical microscope. And hardness of each galvanized layer was investigated with the help of micro Vickers hardness machine.

3. RESULT AND DISCUSSION

3.1. Microstructure Before Galvanizing

The above microstructure of the four samples revealed differences in the distribution and uniformity of the interstitial elements like carbon and also grain growth of ferrite during different heat treatment.

In figure (A), microstructure of annealed sample contains two phases; pro eutectoid ferrite and pearlite. The formation of proeutectoid ferrite is because of less carbon content. The ferrite phase is prominent and has a higher growth rate as compared to the other

microstructures in figure (C) & (D) except (B) as it is an as received microstructure. There is a slower grain growth in a quenched sample, having finer grains and multiple grain boundaries. The carbon constituents were trapped inside the ferrite phase due to its less diffusion time. As far as the normalized microstructure is concerned, there is a moderate grain growth of the two phases. Grain boundries can easily be viewed in a normalized and annealed microstructure; it is because of the diffusional transformation which took place during the heat treatment.

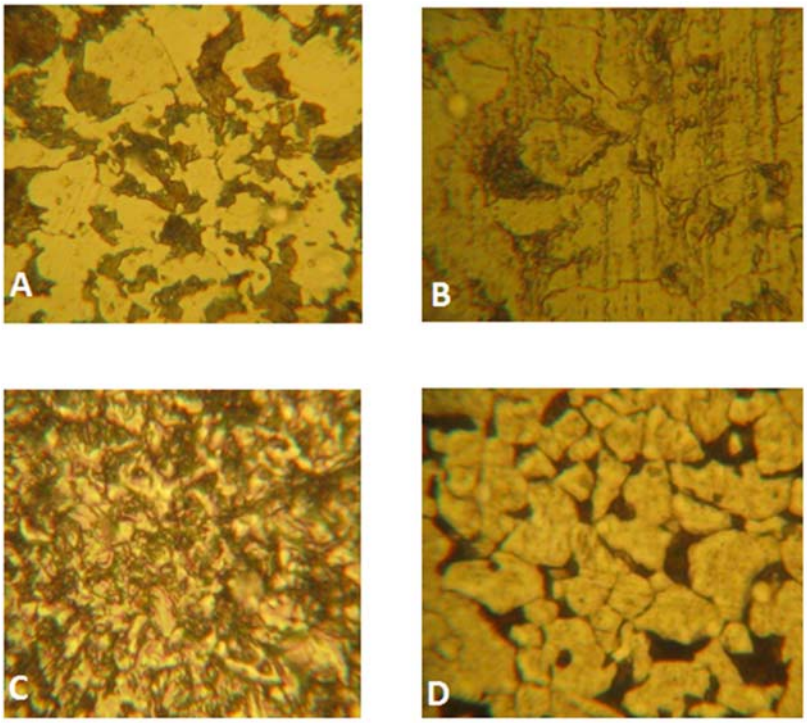

Figure 4 Microstructure of Mild Steel grade 1014,etched by 1% picral (1% picric acid+99% ethanol), Mag 400X (a) Annealed (b) As Recieved (c) Quenched (d) Normalized

3.2. Microstructure After Galvanizing

After Hot-Dip Galvanization, the microstructures of different heat treated samples were studied. A Hot-Dip Galvanized coating contains a heterogeneous assembly of multiple phases which are caused as a reason of metallurgical reactions between iron and zinc when a iron substrate is dipped into a molten zinc. [4]. When the coating is solidified, the outer layer consists of 100% zinc eta layer(1) and inner layers called alloy layers consists of intermetallic phases of iron and zinc such as zeta (2) layer(94% Zn-6%Fe), delta (3) layer (90% Zn-10% Fe) and gamma (4) layer (75% Zn-25% Fe) [5-7] (fig 1). The intermetallic phases formed are relatively harder than the outer layer and offer exception safeguard against coating damage. The distinctiveness of the intermetallic phases of hot dip zinc coatings are compared in table. [8. 11].In fig (a) and (c), the eta layer is not visible clearly where as they are identifiable in (b) and (d). It might be because of the withdrawing speed of sample from molten zinc, it can also be the effect of extra etching time.

3.3. SEM Photography

Results obtained from the microstructures of optical microscope were almost similar. Any significant change in the microstructure was not identified. Therefore the need for Scanning Electron Microscope arised. Fig shows the microstructres of Galvanized layer in which both pure phases (Eta and Base metal) and

intermatellic compounds are shown. The growthand morphologies of these intermetallic compounds (Zeta, delta Gamma layers) are still similar.

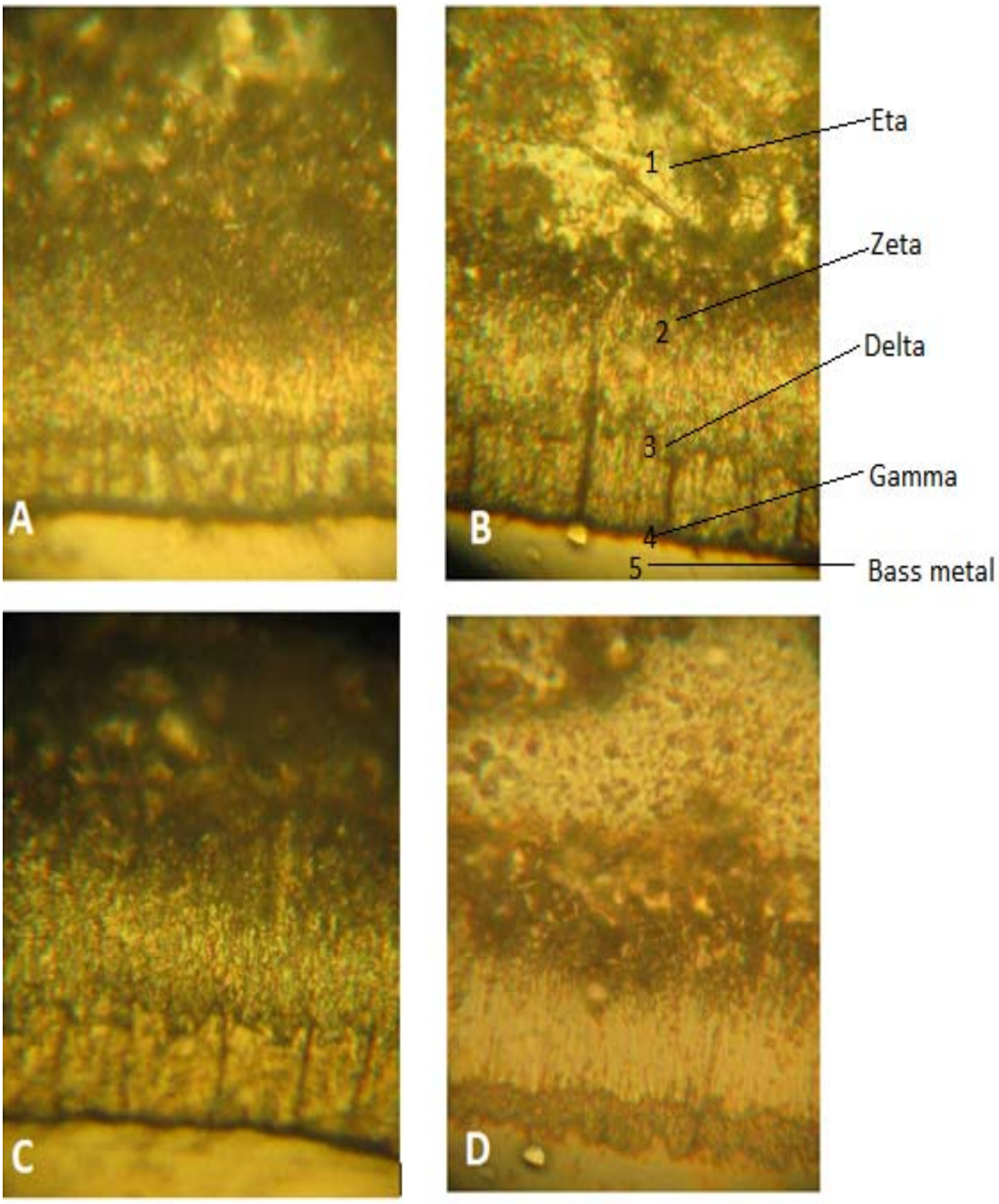

Figure 5. Microstructure of galvanized mild steel, grade 1014, etched by 1% nital (1% nitric acid + 99% ethanol), Mag 400X (a) Annealed (b) As received (c) Quenched (d) Normalized

Table 2.Characteristics of Fe–Zn intermetallic phases of hot dip zinc coatings [8–11].
Source: Comput. Mater. Sci., Vol. 50, 2011, pp. 2502

	η phase	ζ phase	δ phase	Γ1 phase	Γ phase
Stoichiometry	Zn	FeZn13	FeZn10	Fe5Zn21	Fe3Zn10
Wt.% of iron	0	5-6	7-11.5	17-19.5	23.5-28
Crystal structure	HCP	Monoclinic	Hexagonal	FCC	BCC
Atoms/unit cell	6	28	555	408	52

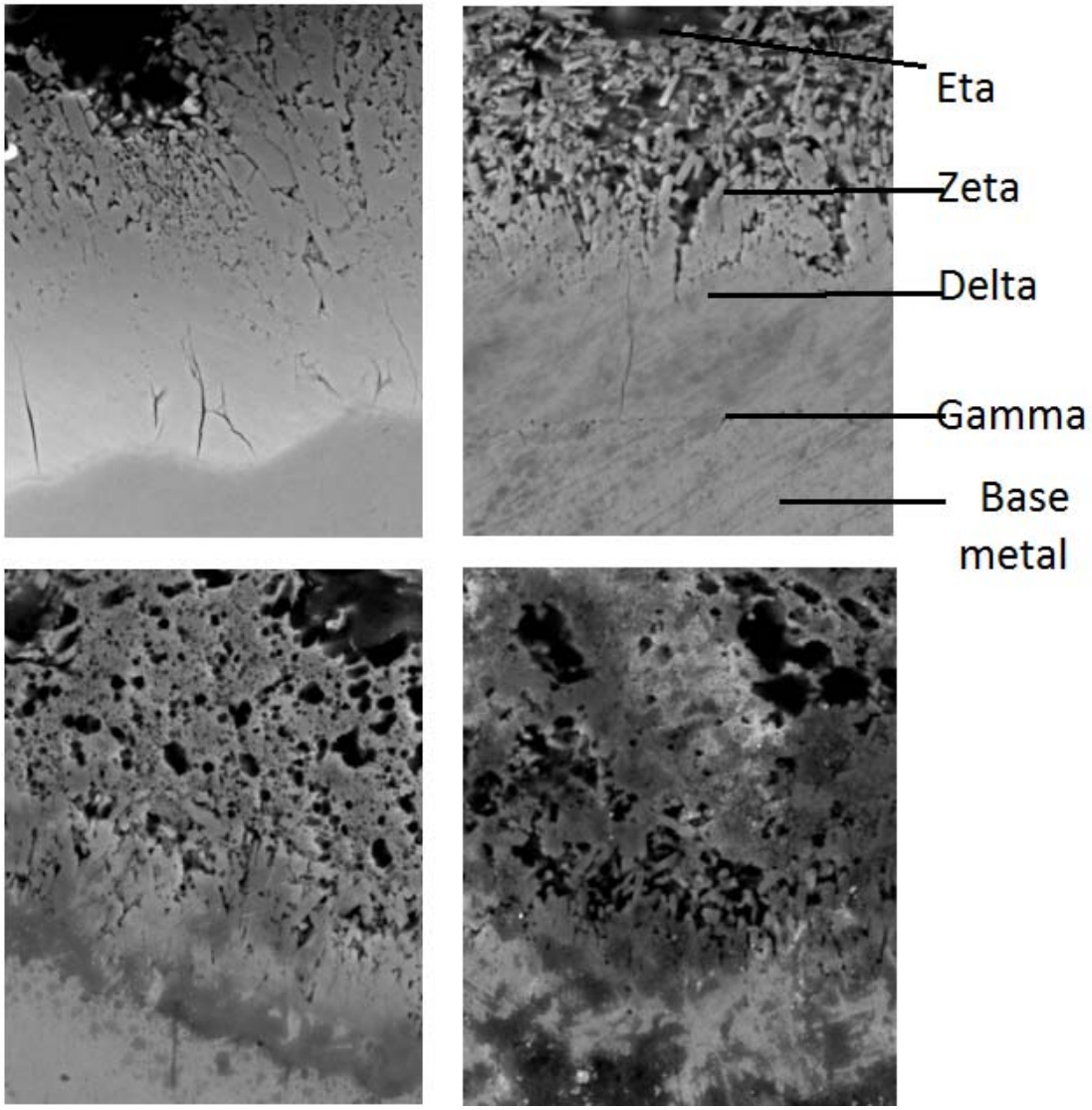

Figure 6. SEM photographs of galvanized mild steel, grade 1014, etched by 1% nital (1% nitric acid + 99% ethanol), Mag 400X (a) Annealed Mag 1194X, At 30KV (b) As received, Mag 1200X, at 30KV (c) Quenched, Mag 1606X, 30KV (d) Normalize

3.4.Microhardness Testing

Since the microstructures obtained by metallographic techniques and SEM were not giving any positive indications for the change of morphology. Therefore, in third stage we have determined microhardness of these different layers by knoop hardness tester and the results are plotted in the table.

It can be seen that there is a change in the hardness of the ZETA and Delta layer of the all samples. The change in hardness values of the sample indicate that the heating process before Galvanizing influences the strength of the different heat treated sample.

Table 3. Hardness of annealed, normalized and quenched samples

Serial number	Eta	Zeta	Delta	Gamma	Base
Annealed	61.6	90.5	113	162	127
Normalized	61.6	70	127	161.5	127.5
Quenching	62.2	108	135	160	179
As-Recieved	61	90.9	127	167	112

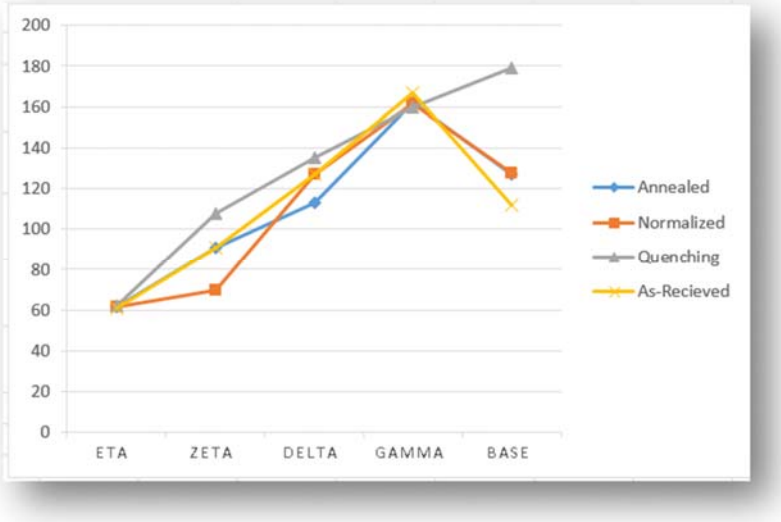

Figure 7 Graph showing the trend of hardness of galvanized layers of heat treated steel

CONCLUSIONS

By the above experiments and results it should be noted that, non-porous areas of all the samples were taken into consideration. It is observed that if the samples are Heat treated for Hot Dip Galvanizing process, there is no identifiable change in the microstructures, morphologies. There could be many reasons which account to resist the change in the adhesion property. The most important reason is low carbon content in the mild steel. Since, Carbon influences the hardness of iron and steel, but here the insufficient amount of carbon may increase the stability of Ferrite and Austenite region which prevent the diffusion of carbon into the Intermetallic layers but there is a small change in Micro hardness of the ZETA and DELTA Phase. There is a possibility that the Phase energy of different layers causes the change in Micro hardness of these layers, where as in other (ETA, GAMA) layer the access quantity of Zinc And Iron Respectively did not show such variation.

ACKNOWLEDGEMENTS

A special thanks to Dr.Ali Dad Chandio and Engr.Muhammad Rizwan who have been an inspirational teacher and gave their credible insight in this work and a sincere thanks to my office collegue Engr.Mansoor Dawson and the administration of Department of Metallurgical

Engineering and Materials Engineering, NEDUET.

REFERENCES

[1] American Galvanizers Association 6881 South Holly Circle, Suite 108 Centennial, CO 80112 USA 1-800-HOT-SPEC, Hot-Dip Galvanizing for Corrosion Prevention. A Guide to Specifying and Inspecting Hot-Dip Galvanized Reinforcing Steel.p3-4

[2]Beverly Kerr, Taking action against hot-dip galvanizing pollution. Duke University: Blue Ridge Environmental Defense League.p3

[3]F. Porter, Zinc Handbook, Properties, Processing and Use in Design, Marcel Dekker(1991)

[4]H. E. Townsend, Continous Hot Dipped Coatings, ASM Handbook, Volume 5: Surface Engineering (1994) C.M. Cotell, J.A. Sprague, and F.A. Smidt, Jr., editors, p 339-348

[5]E. Diler, B. Rouvellou, S. Rioual, B. Lescop, G. Nguyen Vien , D. Thierry Corrosion
Science 87 (2014) 111–117

[5]M. SalgueiroAzevedo, C. Allély, K. Ogle, P. Volovitch, Corrosion Science 90 (2015)472–481

[6]E.A. Anderson, The atmospheric corrosion of rolled zinc, ASTM STP 175, ASTM,Philadelphia, 1956, pp. 126–134.

[7]G. Schikorr, Werkst. Korros. 15 (1964)
537–543.

PREPARATION AND STABILITY EVALUATION OF TYRE WATER SLURRY

Aniqa Moin1*, Alia Ahrar[1], Hafiza Sujood Khan[1]
[1]Chemical Engineering Department, NED University of Engineering & Technology, Karachi, Pakistan
*Corresponding author.
E-mail address: winanq@hotmail.com (Aniqa Moin)
aliaahrar@neduet.edu.pk

ABSTRACT

Much of Pakistan's energy generation depends on imported oil and the rising oil prices are forcing a hard look on how the energy needs are tackled in the future. Coal slurry as an alternative fuel is an attractive option but the high viscosity, lower calorific value at high mass loadings and usage of additives to stabilize it, poses problems. In order to overcome these drawbacks we present a new alternative fuel technology - tyre water slurry. In our study we would also compare coal water slurry with tyre water slurry on basis of stability, rheology and calorific value. Tyre's higher volatile-to-fixed carbon ratio enhances its ability to combust rapidly and completely. Their lower sulphur content (especially in terms of pounds/million Btu) offers the potential advantage of decreasing SOx emissions compared to coal. Lower inherent nitrogen content decreases NOx emissions. The burning temperature of tyre is lower than that of coal which means less energy requirements for burning and enhanced burning efficiency. In our study we have used bus tyre. The optimum size 212 μm and mass loading 25% of tyre has been determined on basis of static stability results. Furthermore, three rheological tests were conducted determining type of fluid, time dependent behaviour and variation of viscosity with temperature. It was concluded that the slurry exhibits a viscosity range of 182-955 cP and non-Newtonian- psuedoplastic behaviour as value of n<1. The viscosity decreases with time, temperature and shear rates. The calorific value of the slurry is found to be 2024 Kcal/kg.

Keywords: Alternative fuel; coal water slurry; tyre water slurry; comparison

1. INTRODUCTION:

In an ideal world, we would endlessly recover and reuse all resources - and we would do so without detrimental impact on our environment. Tyres represent a significant resource. Ideally, a tyre's polymerized rubber mixture would be perpetually reused. However, today's applications for this material consume less than 15% of the waste tyres generated annually in North America.

Unless other applications are embraced and developed, the remainder of this resource will be squandered through landfilling or become a stockpiled public liability posing public health and environmental hazards. Since no one consciously wants to waste a valuable resource, other applications that are compatible with our environment should be developed. Avoiding unnecessary consumption of natural energy resources through alternative use of waste tyres is a worthy objective if it can be done without a Counter-balancing negative impact on our environment**.**

Slurry fuels have the advantages of being convenient to handle (similar to heavy fuel oil) as liquid fuel and processing high energy density. Coal slurries have been investigated as potentially efficient replacement for oil in boilers and furnaces, fuel in internal combustion engines, and recently energy feedstock for cofiring of coal fines in utility boilers. Not only some of the industrial units and equipment, e.g. IC diesel engines accept just the liquid fuels, but also liquid fuels have

more advantages over than solid fuels. Cheap and easy transportation, ease of maintaining and storage, and finally low emission of pollutants of their combustion are the points should be considered when comparing solid and liquid fuels.[1]

Landfilling or stockpiling of scrap tyres has several disadvantages. Tyres do not biodegrade and tend to float to the periphery in a landfill. They also consume relatively large amounts of space. Tyre stockpiles are potentially subject to arson; emissions of hazardous air pollutants from an arson-caused fire of a tyre stockpile are potentially very damaging to the environment and nearby receptors. Finally, uncovered tyre dumps are breeding grounds for mosquitoes, other insects, and rodents. Potentially resulting in the spread of a number of diseases to nearby human population.

Table 1:Comparison of Coal and Tyre

TYRES	COAL
Density of tyres: 140kg/m^3	Lignite: 641-865 kg/m^3
Heat content:7800-8600 Kcal/kg	Heat content, Lignite: 3883-4438 Kcal/kg
Moisture and Ash (%) Moisture: 0.3-2 Ash : 3.9	Moisture and Ash (%) Lignite , Moisture: 30-40 Ash : 7.4-25

Tyres are a hydrocarbon-based material derived from oil and gas. Some inorganic materials are added to enhance reactions or performance properties. Tyres have a heat content of 7,800 to 8,600 kcal/kg (14,000 to 15,500 Btu/pound), depending on the type of tyre and degree of wire removal. By comparison, coal that may be displaced by use of tyres typically contains 5,550 to 7,200 kcal/kg (10,000 to 13,000 Btu/pound).

Tyres have less sulfur than many eastern coals, which means lower SOx emissions, but many western coals have less sulfur than tyres.

Tyre Derived Fuel (TDF) has a lower carbon-to-hydrogen ratio, theoretically reducing the greenhouse gas CO_2 emissions. Therefore, if TDF were burned instead of coal, greenhouse gas emissions could be reduced.

Likewise lower nitrogen content of tyres can marginally decrease NOx. But the results in individual cases depends on exactly what type of fuel is being replaced by tyres and what configuration of boiler and air pollution control equipment exists at each site.

Tyres contain as much chlorine or more than many coals, but the chlorine has been reduced in many newer tyres as the chlorinated butyl inner liner has been replaced. Mercury also appears to be lower in TDF as compared to coal. [2][3][4].

Evaluation of shredded tyres and coal blends has already been done in considerable research works in the past from many different perspectives.

Williams *et al.* (2013) studied the Co-combustion of a South African coal (SAf) with waste tyre rubber (WTR) at the fuel fractions 4.1%, 14.1% and 19.7% along with the pure firing of WTR was conducted in an 80 kWh combustion test facility (CTF).This study assessed the potential slagging and fouling behaviour of the resultant ashes produced from co-firing SAf/WTR and pure fired WTR. it was determined that co-fired SAf/WTR and pure fired WTR ashes carry a low risk of slagging and fouling. ZnO is incorporated in the manufacturing of tyres as a compounding additive. In this study ash collected and analyzed from the pure fired WTR and co-fired SAf/WTR exhibited lower levels of Zn than anticipated. Experimental analysis found Zn enrichment at lower temperatures was not significant within the fly ash collected by the cyclone trap or ash deposits collected from the water cooled sections of the CTF. This suggests that Zn could be forming a submicron aerosol. It is further noted that ZnO/Zn is not likely to contribute significantly in the slagging/fouling mechanisms, due to its volatile nature.

Emerging novel applications of co-firing technologies using waste tyre rubber under air firing and air staged conditions has the potential to reduce NOx emissions and utilize a waste stream in one process. WTR is an ideal source of hydrocarbon radicals

possessing a low nitrogen content, low chlorine content, and a high calorific value of approximately 38 MJ/kg (Gross).[5]

R.K.Patil *et al.* (2012) The energy generation on incineration provides large amount of polycyclic aromatic hydrocarbon (PAH) emissions which is the cause of major environmental threat. Therefore, the combustion of coal and tyre were carried out in cement industry in order to generate heat energy at 1300^{O}C and the only remaining residue (steel powder) to enhance the strength of the cement. At the outset, the particle size of coal and tyre was cut into 63-75 and 180-212 μm respectively.

They found that the use of blended fuel is a key cost-effective strategy for energy efficiency improvement and CO2 emission reductions. They have performed experiment on combustion of waste tyre, high ash coal and tyre-coal blends with 10, 30 and 50% waste tyre were investigated by means of thermogravimetric analysis (TGA). They found that incorporation of waste tyre can improve the combustion characteristics of high ash coal, especially the ignition performance and the peak weight loss compared with the separate burning of waste tyre and coal. This indicates that the co-combustion of waste tyre and low qualities coal as fuel is feasible. [6]

Kristína Holíková *et al.* (2005) discussed the samples of coal and tyres with different weight ratios were combusted in a stream of air in a laboratory scale semi - batch fluidized bed reactor. The reactor was electrically heated to the initial temperature of 460°C -550°C inside the bed, and then it was charged with the samples of scrap tyres, coal or their mixtures. Coal particle sizes of 0.51- 0.7 mm and the fraction of waste tyres 0.8 - 2 mm were used. It is well known that scrap tyres possess a high-volatile and low ash content, with a heat value higher than that of coal or biomass. Therefore, the thermal treatment is a good way how to reuse tyres and old rubber. The waste rubber conserves a large amount of energy, the calorific value of approximately 3.3×104 kJ/kg, and if the waste rubber is not recycled the theoretical value of lost heat will reach 3.0×1014 kJ worldwide. [7]

Chiris Baglay *et al.* (2007) studied that tyres are a hydrocarbon-based material (polymerized rubber) derived from oil and gas (Gray 2004). Their heat content is 20-40% higher than coal: 7800 to 8600 kcal/kg [14,037 - 15,476 BTU/lb] for tyres compared to 5550 to 7200 kcal/kg [9988 - 12,957 BTU/lb] for coal. EPA testing shows that tyre-derived fuel has a higher BTU value than coal. Tyres typically have lower moisture content and (not counting the wire) a lower ash content than coal, which means higher energy use efficiency. Tyres also have a higher ratio of volatile to fixed carbon, which improves their ability to burn rapidly and completely. Facilities that can use TDF are cement kilns, industrial boilers at pulp and paper mills, electric utilities, waste-to-energy plants, and dedicated fuel facilities. Tyres can be burned whole at cement kilns, which reduces processing costs but increases capital costs. Alternately, they can be shredded and mixed with coal or with waste paper and wood in industrial boilers.

The chemical composition of tyres needs to be examined in order to determine the impact of burning them on air emissions. Tyres have less sulfur than many eastern coals, which means lower SOx emissions, but many western coals have less sulfur than tyres. TDF has a lower carbon-to-hydrogen ratio, theoretically reducing the greenhouse gas CO_2 emissions. Therefore, if TDF were burned instead of coal, greenhouse gas emissions could be reduced. Likewise lower nitrogen content of tyres can marginally decrease NOx emissions. [8]

In this paper the stability and rheological behavior of tyre water slurry is investigated by varying tyre water ratio and particle size.

2. EXPERIMENTATION

2.1 Marterial

TWS is prepared using scrap bus tyres. It's Proximate and Ultimate analysis is given in Tables 2 and 3.

Table 2 Proximate Analysis (% as Received Basis)

Fuel	C (%)	S (%)	H_2 (%)	O_2 (%)	N_2 (%)	Heating Value (Btu/lb)
Bus tyres	89.65	2.09	7.50	<0.01	0.55	14,968
Coal Lignite	38.04	1.8-6.5	4.43	7.74	0.7	7000-8000

Table 1 Ultimate Analysis (% as Received Basis)

Fuel type	Fixed Carbon (%)	Moisture (%)	Ash (%)	Volatile Matter (%)
TDF	27.96	0.3-2	3.9	66.64
Lakhra coal	20.7–39.2	13.5–39.4	7.4–25	26.3–42.5

2.2. Composition of tyre

The tyre used in TWS has the composition as in Table 4

Table 2 Composition of Bus Tyre

Raw Materials	Bus Tyre
Rubber/Elastomers	45%
Carbon Black	22%
Metal	25%
Textile	-
Zinc Oxide	2%
Sulphur	1%
Additives	5%
Carbon-based Materials, total	67%

2.3. Synthesis

Whole scrap bus tyres are bought from Shershah, Karachi.

2.4. Preparation of Pulverized Tyres

Steel wires are removed from the tyre and it is cut into rectangular strips. Those strips are then fed into the roller crusher, which pulverized the tyre. The finely pulverized tyre is now to be distributed into a range of different sizes, ranging between 800 microns-212microns. A sieving apparatus from NED Chemical Engineering, Particulate Technology lab is made into use.

2.5 Tyre Water Slurry Preparation

Sample consists of pulverized tyre and water which are weighed by mass balance. Slurry with a mass loading of 25%, consists of 50g pulverized tyre and 150g of tap water. Whereas, slurry sample with a mass loading of 20% consists of 50g pulverized tyre and 200g of tap water. The mixture is poured into the blender and is blended for almost 2 minutes till a homogenized mixture is achieved without any stabilizer and additives.

Figure 1 TWS-1

Table 3 TWS samples

Samples	Particle size (µm)	Mass of tyre (g)	Mass of water (g)	*Ratio	Tyre Loading (%)
TWS-1	212	50	150	1:3	25
TWS-2	212	50	200	1:4	20
TWS-3	425	50	150	1:3	25
TWS-4	425	50	200	1:4	20
TWS-5	600	50	150	1:3	25
TWS-6	600	50	200	1:4	20
TWS-7	800	50	150	1:3	25
TWS-8	800	50	200	1:4	20

*Ratio (Tyre: Water)

2.6 Stability Testing

After making the slurry, its stability is tested through the Standing Observation Method.

The standing observation method

In this method the tyre water slurry is stored in a glass beaker. And is observed at equal intervals of time (for 30 min) to determine the rate of settling and judging whether hard sedimentation of slurry occurs. [10][11][12]

Ratio = constant composition / total height at optimum loading of each type

The higher the ratio, the more the stability of tyre water slurry.

2.7 Rheological Testing

The rheological testing was carried out using the DV-E BROOKFIELD VISCOMETER. Disc spindle was used throughout the experiment 250 ml of slurry was measured each time and spindle depth(of about 2.4 inches) was kept constant The test was conducted at three different speeds 10, 50 and 100 rpm

2.8 Determination of behavior of fluid

Using Ostwald's power law model to fit the shear stress and shear rate data, for finding the values of flow behavior index (n) and the rheological constant (K).

Ostwald's Power law Equation:

$$\tau = K\gamma^{n} \quad (1)$$

Thixotropicity

Thixotropic is an extension of pusedoplastic behaviour. A thixotropic fluid undergoes a decrease in viscosity with time, while it is subjected to a constant shear rate

Sample TWS-1 at Temperature 30 °C was used and Total observation duration is 90 min with 30 min time interval.

Temperature dependence of viscosity

The experiment is conducted using a cold and hot water bath for the temperature range of 20-50^{O}C and Sample TWS-1 is used by keeping spindle speeds of 50 and 100 rpm. Just as the temperature is maintained, the readings are noted using Brookfield Viscometer.

2.9 Calorific Value Testing

This test is performed with the help of the Fuel Research Centre (FRC), PCSIR. Using ASTM D2013 and D 5865.

3. RESULTS AND DISCUSSION

3.1 Stability Testing

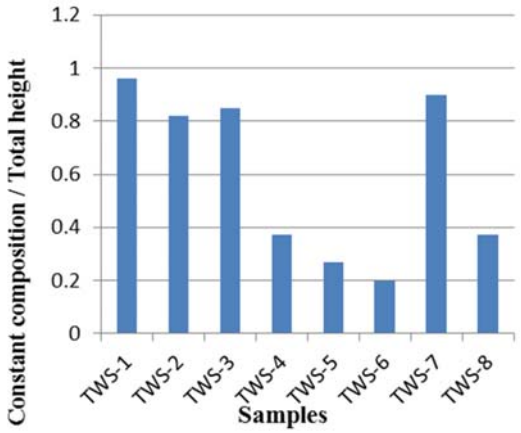

Figure 2: Stability trends of the tyre samples

Figure 2 displays the stability trend for the 8 samples. Showing clearly that TWS-1 has the most dominant trend out of all. Therefore, this sample is selected for further experimentation work.

Figure 3: showing the optimum result, TWS-1. (Notice there is just a tiny layer of sediment at the bottom of the beaker)

The difference in density between tyre and water is much greater of about 860kg/m^3 as shown in Table 1.This explains why tyre is able to suspend well in water

Highest stability is obtained in TWS-1 (size, 212µm and 25% tyre loading). Small particle size shows greater stability characteristics because the rate of settling of smaller particles is slower than larger particles. Also it can be inferred that TWS is greatly influenced by the amount of water present in the slurry. When water is increased from 100g to 200g, the stability of TWS decreases. A possible explanation of this could be the amount of water surrounding an individual particle and water between two particles has increased. Thus, the weight of the floc structure has increased which will in turn increase its rate of settling. Resulting in greater sediment zone at the bottom of the beaker.

3.2 Rheological Testing

Determination of behavior of fluid

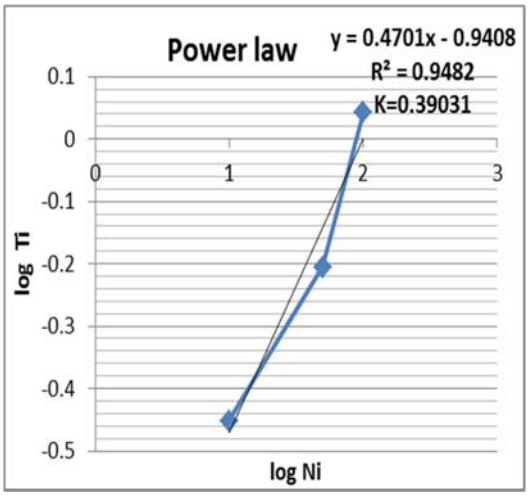

Figure 4: Graph of log (speed) against log (shear stress) to fit the graph in accordance with power law model.

This is a plot between log of rotational speed and log of shear stress. The slope of this graph gives the value of the flow behavior index (n) which is found to be 0.4701. And the intercept gives the value of K, which is 0.39.

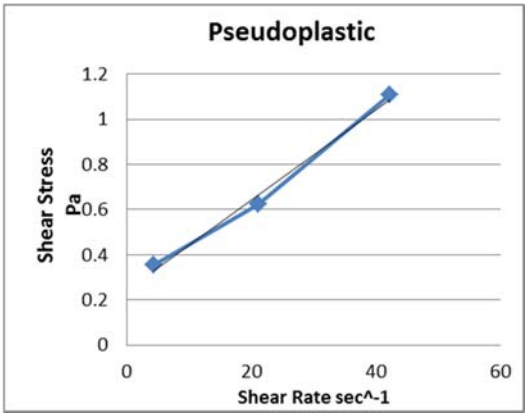

Figure 5 Graph of shear stress against shear rate to show behavior of fluid at 30^{o}C

Figures 4 and 5 shows pseudo plastic behavior, as shear rate increases shear stress also increases at a decreasing rate. This is consistent with the power law model fitted as the value of n< 1. The value of n obtained is 0.4701. And the yield stress is 245 mPa. Shear thinning occurs because the network structure is broken because of increasing shear rate.

Equation of our model:

$$\tau = 0.39\gamma^{0.4701} \qquad (2)$$

Thixotropicity

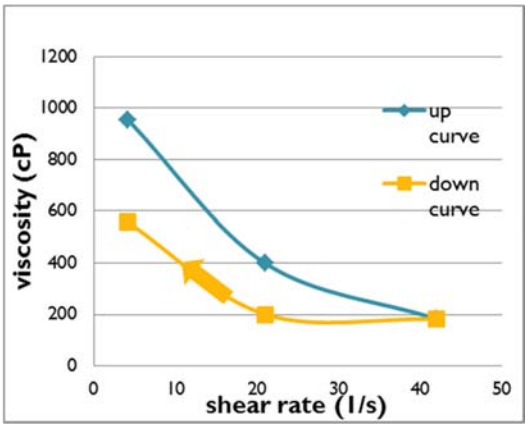

Figure 6: Effect of viscosity with time and different speeds using TWS-1

Up curve indicates the material's flocculated structure is destroyed with time, as it is sheared. The relinking rate of flocs after destruction is low, this explains why the

viscosity is lower at the same shear rate, in the down curve. This results in the thixotropic behavior. The area between the two curves defines the extent of thixotropicity.

Temperature dependence of viscosity

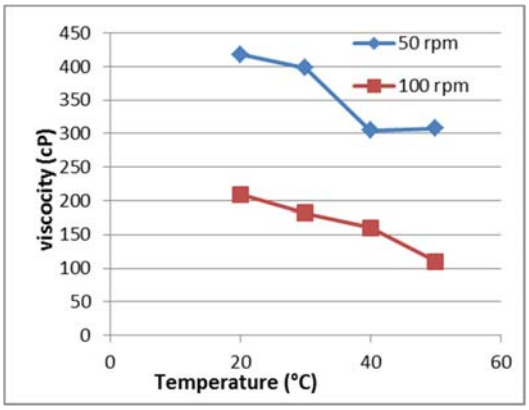

Figure 7: Graph of viscosity against temperature for different speeds using TWS-1.

3.3 Calorific Value Testing

The calorific value is found to be 2024 Kcal/kg. This value is comparable to the calorific value of CWS, which is 2000 Kcal/kg.

4. COMPARISON BETWEEN TYRE WATER SLURRY (TWS) AND COAL WATER SLURRY (CWS)

Tyre has a density significantly less than that of coal. Therefore TWS is more stable than CWS, even without the use of any additives. The higher carbon content in tyre attributes to the carbon black in tyres which, has the potential of enhancing the calorific value in comparison to that obtained by coal slurry fuels at a smaller mass loading of tyre. Furthermore, no additive usage to stabilize the tyre slurry gives it an advantage over coal slurry, as coal slurry requires additive usage Triton X 0.75% and Na CMC 0.25% which adds to the cost of slurry making. A smaller mass loading usage gives a significantly lower viscosity than coal slurry, therefore lowering pumping and atomizing costs.

Table 6 Comparison between CWS & TWS.

	Coal water slurry*	Tyre water slurry
Sizes µm	75-212	212
Optimum Loading %	50	25
Viscosity (cP) 10-100 rpm	6000- 3200	955-182
Additives	Triton X - 0.75% Na- CMC - 0.25%	No additives are used
Calorific value (Kcal/kg)	2000	2024

*Values obtained from the experiment performed by the students of Chemical Engineering Department, NED (2016) using DV-E Brookfield Viscometer

CONCLUSION

The ultimate goal of this study is to determine the feasibility of preparation and using the tyre water slurry (TWS). We aimed at introducing such a slurry fuel to the world, which would compare favorably to CWS in terms of its calorific value, utilizing a scrap material hence having less cost. Also a reduction in the amount of chemical additives added to stabilize the conventional CWS.

Pulverized Bus tyres without any stabilizer and additives were selected for this study. After performing 8 stability tests using different sizes and ratios we concluded that, bus tyre of size 212 µm and a mass ratio of tyre: water of 1:3 is most stable. As it exhibits the least constant composition/ total height ratio of 0.96.

Rheological tests were then performed on the selected size and ratio, to determine the behaviour of fluid. Concluded that bus tyre exhibits a viscosity range from 182-955 cP. Our TWS is showing pseudo plastic behavior, as shear rate increases shear stress also

increases at a decreasing rate. The value of n obtained is 0.4701.

Time dependent behavior of our slurry was also tested and it was found that as the time increases from 0 min to 90 min viscosity decreases signifying thixotropic behavior.

ACKNOWLEDGEMENTS

The authors are greatly thankful to the teachers of Department of Chemical Engineering NED University of engineering and technology, Karachi for their valuable suggestions and encouragement given time to time during the completion of the above project.

NOMENCLATURE

CWS Coal Water Slurry

TWS Tyre Water Slurry

REFERENCES

[1] Sunggyu Lee James G. Speight Sudarshan K. Loyalka, *Handbook of Alternative Fuel Technologies*, 2007

[2] Terry Gary, *TYRE DERIVED FUEL: ENVIRONMENTAL CHARACTERISTICS AND PERFORMANCE, New* York, 2004

[3] Joel I. Reisman, *AIR EMISSIONS FROM SCRAP TYRE COMBUSTION*, 1997

[4] R.K.Patil, *Environmental Pollution Reduction in Cement Industry for Co Combustion of Waste Tyre and Coal as a Fuel,* 2012

[5] Singh.S.Nimmo, *An experimental study of ash behaviour and the potential fate of ZnO/Zn in the Co-combustion of pulverized South African coal and waste tyre rubber Fuel*, 2013.

[6] Atal, Ajay, *Comparison of the combustion behaviour of pulverized waste tyres and coal,* 1995.

[7] Holikova, Kristina, *INVESTIGATION OF TYRES AND COAL COMBUSTION IN A LABORATORY SCALE FLUIDIZED BED COMBUSTOR,* 2005.

[8] Baglay, Chiris, *State Advisory Board Air Pollution Use of Tyre-Derived Fuel in Virginia,* 2007

[9] Evans, Anne and Russ, *THE COMPOSITION OF A TYRE: Typical component,* 2006.

[10] Hiromoto USUI, Takashi SAEKI and Yuji Sano, *STABILITY EVALUATION OF COAL-WATER MIXTURES BY INTERNAL STRUCTURAL STRESS*

[11] Fei Yi, Akshay Gopan, Richard L. Axelbaum *Characterization of coal water slurry prepared for PRB coal, 2014*

[12] Feridun Boylu, *The effect of chemicals on the*
viscosity and stability of coal water slurries, 2003

[13] P. Mitschka Rheologica Act, Rheol. Acta, *Simple conversion of Brookfield R.V.T. readings into viscosity functions*
21,207 *-209 (1982)*

[14] MORE SOLUTIONS TO STICKY PROBLEMS, Brookfield engineering laboratories

NEXT GENERATION CERAMIC BASED MEMBRANES FOR GAS

Hooria Batool[1,*], Tooba Ahmed[1], Fazila Waqar[1] and Urooj Fatima[1]
[1]lChemical Engineering Department, NED University of Engineering & Technology, Karachi, Pakistan
[*]Corresponding author. Tel.: 0307-2270496
E-mail address: hbtnaqvi@yahoo.co.uk (Hooria Batool)

ABSTRACT

The focus of this study is to provide cheap and feasible source kaolin as a ceramic membrane support material using sintering technique. Different membranes were prepared by varying composition of kaolin content. The prepared suspension included kaolin, solvent N-methyl-pyrrolidone (NMP), dispersant arlacel and binder polyvinylchloride (PVC) using a magnetic stirrer. A temperature of 150◦C was maintained for sintering and drying. Due to different kaolin content, the change in morphologies were observed. The reason to this was variations in suspensions viscousities. Membrane's pore size, roughness and strength were also affected by different percentages of kaolin.

Keywords: Kaolin; Ceramic membrane; Sintering; Gas separation

1. INTRODUCTION:

Membranes are thin and porous sheet of material able to separate contaminants and undesired products when a driving force is applied. Membranes importance comparitive to other separation processes includes its high performance, simple operation, environmentally friendly, less energy requirements and compact units.

Ceramic membranes have a promising future in industries because of its chemical and thermal stability [1]. A ceramic membrane can also work under harsh environment such as gas separation application [2]. Previously ceramic based membranes were made from metal oxides- a conventional method that was very expensive. However, provisions are being made to create a ceramic based membrane from a cheaper source kaolin [3]. Kaolin possess high refractory characteristics and preferred as a raw material for porous ceramics [4].

This study includes ceramic membrane characteristics altering kaolin content. The ceramic support composition is being inspired by the work of Sarbatly(Sarbatly, 2011).

2 EXPERIMENT

Following scheme of experiment was followed.

2.1 Material

Kaolin powder with particle size 212 μm was purchased from Sigma Aldrich was used as the ceramic particle. Binder Polyvinyl chloride (PVC), dispersant arlacel and solvent N-methylpyrrolidone(NMP) by MAAZ MM traders were used.

2.2 Ceramic Suspension Preparation

To remove the moisture from PVC and kaolin powder it was dried in an oven for a night at 60◦C. Ball milling of kaolin was done to reduce its particle size from 212μm to 8.96 μm. Before adding the kaolin powder, NMP and Arlacel were stirred at 60◦C. By using magnetic stirrer the suspension was stirred for 48 h at 60◦C to make sure that the ceramic particles, solvent and additive were mixed well. After the addition of PVC the stirring was continued for another 48 h to make sure that the polymer binder was fully dissolved.

2.3 Ceramic Support Fabrication

Using varying compositions of kaolin different samples were prepared as shown in table 1 and figure 1.

Table 1. Composition of the Ceramic Suspension

Membranes	Composition (g)			
	Kaolin	NMP	PVC	Arlacel
M1	13.5	37.5	6.7	1
M2	16.5	37.5	6.7	1
M3	20.5	37.5	6.7	1

The prepared ceramic suspension was poured glass plate at room temperature using a casting knife. The thickness of the membrane was controlled by using adhesive tape. Below 200◦C the cast film was placed into the oven for sintering process

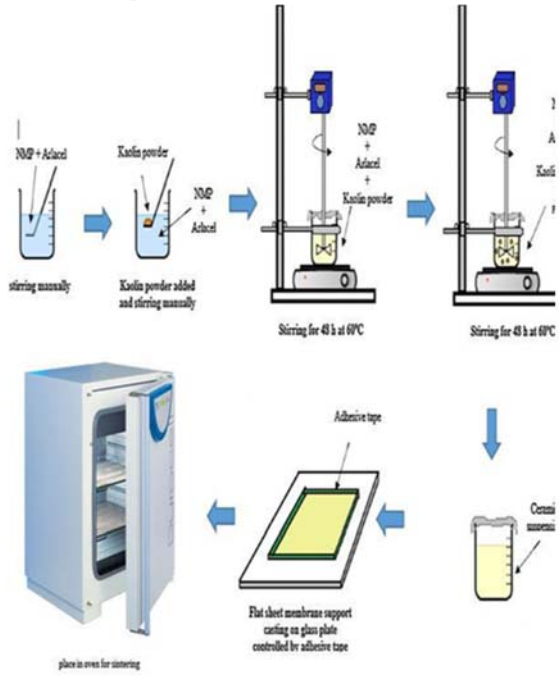

Figure 1. Kaolin based Ceramic Prepared from Sintering

3 CHARACTERIZATION METHODS

The following methods were considered.

3.1 Scanning Electron Microscopy

The scanning electron microscope (SEM) uses a focused beam of high-energy electrons to generate a variety of signals at the surface of solid specimens. The signals indicate the chemical composition, external morphology (texture), crystalline structure and orientation of materials making up the sample. Secondary electrons and backscattered electrons are commonly used for imaging samples.

3.2 Thermal Gravimetric Analysis

Thermal Gravimetric Analysis (TGA) tells about the amount of mass change of a material, either as a function of increasing temperature, or as a function of time, in an atmosphere of nitrogen, helium, air or in vacuum. Samples are analyzed in the form of powder so the interior sample temperature remains close to the measured gas temperature.

3.3 Ultimate Tensile Strength

Ultimate tensile strength is a property measured by the maximum pressure(force) that a material can bear while being stretched or compressed before breaking. It also provides information about the mechanical properties of material like elasticity, ductility and toughness.

This test includes taking a sample having a fixed cross-sectional area, and then pulling it with a tensometer force at a constant strain rate until the sample breaks.

4 CHARACTERIZATION RESULTS

4.1 Scanning Electron Microscopy Results

The figure 2 shows 3500 times magnified image of membranes. Figure 2 (A,C,E) contains 13.5gm, 15gm and 20gm kaolin respectively. Membranes have fine structure with big pores

The Figure 3 shows 10000 times magnified image of membranes. Figure 3(A,C,E) contains 13.5 gm, 15gm and 20 gm kaolin respectively. It can be obseved that as kaolin content decreases membrane's pore size increases. Pore sizes for figure 3(A,C,E) are 937nm, 721nm, 497nm respectively.

The figure 4 shows lateral view of membranes. Figure 4(a,b,c) contains 13.5gm, 15gm and 20gm kaolin respectively, thickness of all membranes are controlled by adhesive tape and lies in the range 180nm-200nm all of three membranes are of almost uniform thickness.

Whereas figure 4(d, e, f) shows the cross sectional view of membranes describing the structure obtained with respect to increasing kaolin content from 13gm to 20gm respectively. It is observed that we get a leaf like structure initially but as kaolin content increases, pore size reduces due to viscosity increases and membranes have very few pores and of very small pore size.

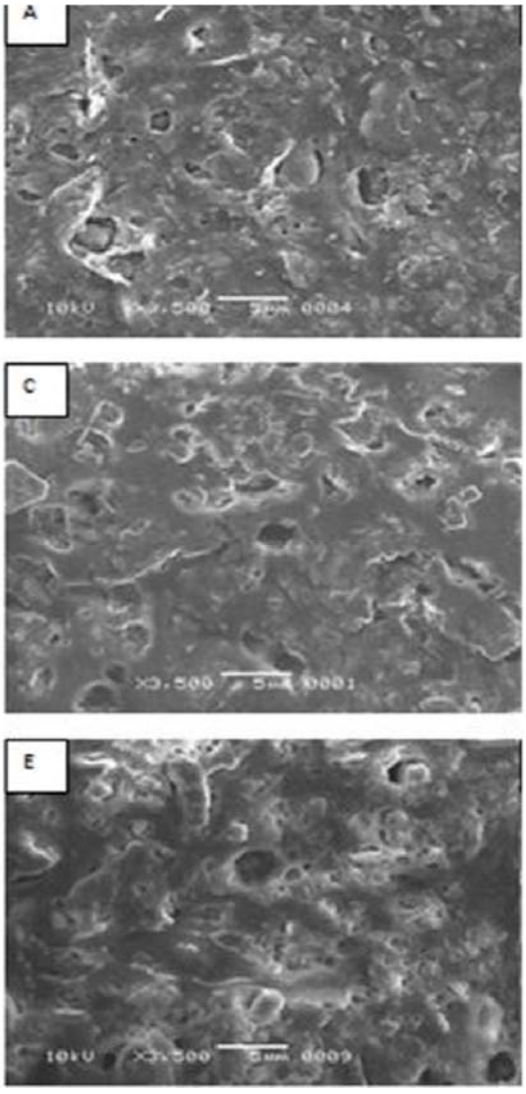

Figure 2. SEM 3500 Times Magnified Image

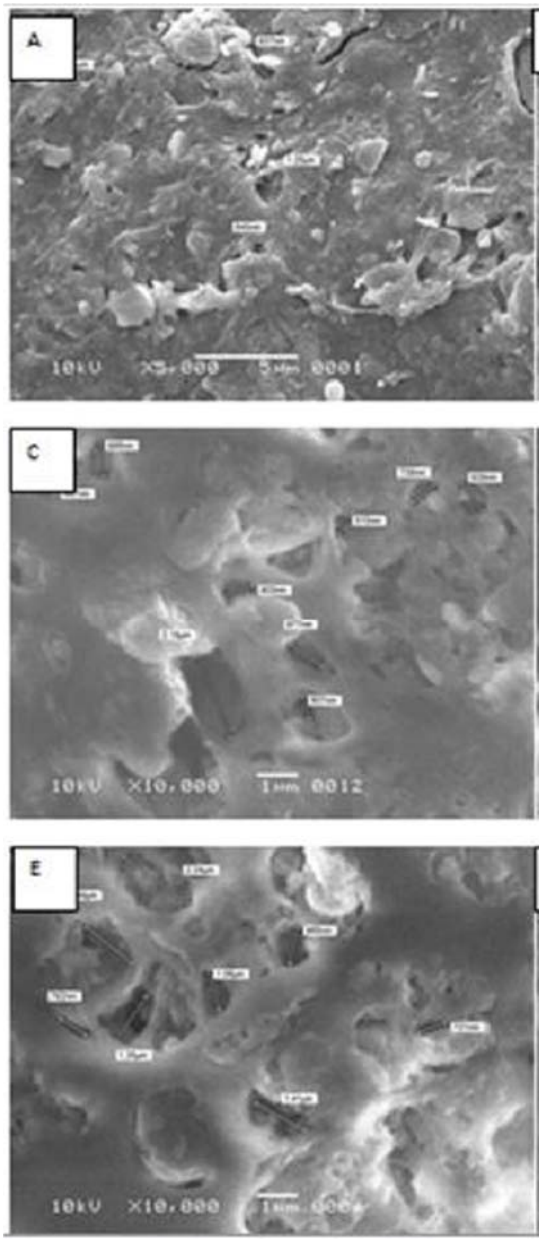

Figure 3. SEM 10000 Times Magnified Image

4.2 Thermal Gravimetric Results

Figure 5(a) represents the sample containing 13.5gm kaolin and 6gm PVC which adds up a total of 19.5gm in the sample other than solvent. In the start it was observed that moisture content is removed in the first bump of graph with some amount of surfactant (arlacel) around 10% weight loss occur. As the % of PVC in this sample is 29% and of kaolin is 69% so PVC is sintered off 20% in the range of 150-300^{o}C and the remaining is

removed till 450ºC. Now only kaolin remained in sample which is the desired result. Figure 5(b) represents the 20.5gm kaolin and 6gm PVC. At the start, moisture and some part of surfactant is removed then polymer PVC is removed before 250ºC.

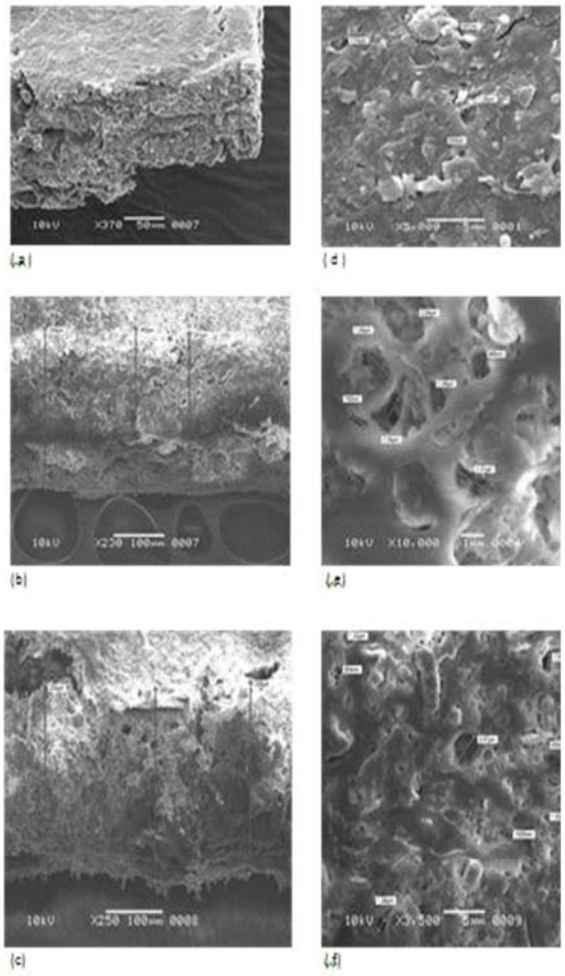

Figure 4. SEM Lateral View of Membranes

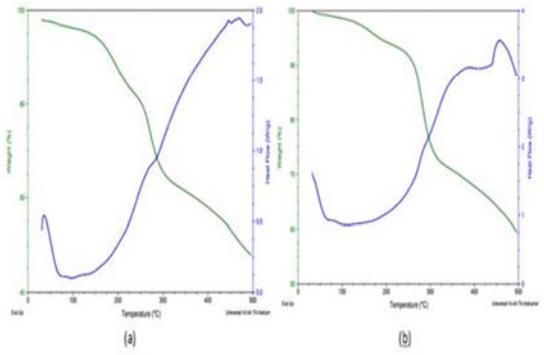

Figure 5. TGA of Kaolin Containing 13.5 gm & 20.5 gm

4.3 Ultimate Tensile Strength Results

Figure 6(a) represent the result of testing sample containing only 16gm of kaolin, it is observed that it can bear maximum force of 2.70N and maximum elongation of 8% and a tensile strength of 2.14MPa is obtained. Figure 6(b) contains 13gm kaolin and it can bear a maximum force of 8.23N and maximum elongation of 2 % is obtained with a tensile strength of 0.858MPa. Figure 6(c) represent the sample containing 20gm kaolin bearing a force sustaining capability of 2.79N with an elongation of 10% and a tensile strength of 3.24MPa.

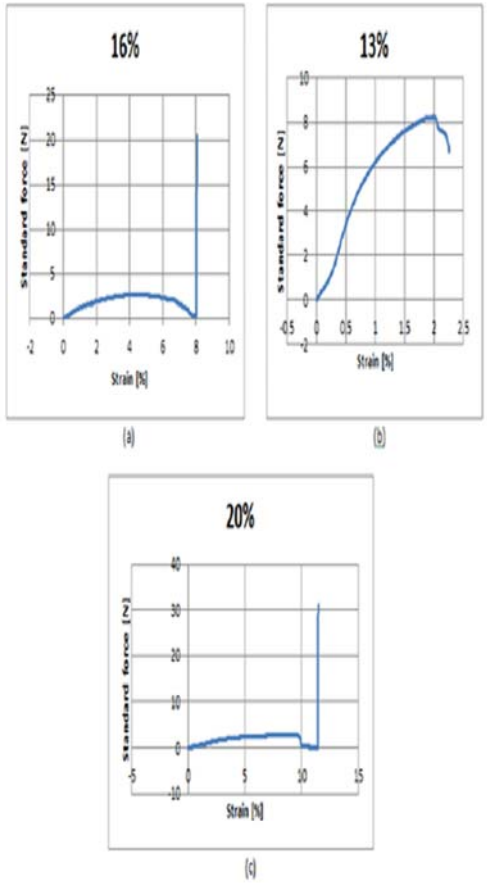

Figure 6. UTM of Kaolin Containing 13.5 gm, 16 gm & 20.5 gm

This conclude that with the increase of kaolin content in sample, force bearing capability of membrane reduces which makes it brittle (strength reduces) but elongation increases making it flexible.

Figure 7. Membrane Holder Assembly

5 GAS SEPARATION SETUP

An apparatus was fabricated to help with testing gas permeance and retention. This was a simple assembly consisting of a pipe, flanges, pressure gauges, two tee with npt connections, gaskets, ball valves and couplings.

The specifications included 1" galvanized carbon steel schedule 40 pipe, 1" slip on flat face flanges A216, standard 1" pressure gauge with pressure range of 2 bar, two equal tee galvanized carbon steel with npt connections, two carbon steel ball valves with npt connections, standard ½" carbon steel nuts and bolts, gasket from 3mm EPDM sheet, three couplings and a wooden mounting assembly as shown in figure 7.

5.1 Permeability and Selectivity

To evaluate the gas permeation properties of the developed kaolin ceramic support single gas permeation was conducted. The testing included use of O_2 (3.46˚A) and CO_2 (3.30°A) as test gases. Before testing gas permeation properties the membranes were bring in contact to a pure gas stream at 2 bar pressure for about 5 minute to eliminate residual gases if any.

Gas was passed through each sample thrice to get an average value. This gas permeation test results gave information about: (1) gas permeation and (2) gas selectivity (CO_2/O_2) which were calculated based on Darcy law as shown in equation (1).

$$Q = KA (P_b - P_a) / \mu L \qquad (1)$$

Where Q (m^3/s) is the total discharge which is equal to the product of the intrinsic permeability of the medium, , A (m^2) is the cross-sectional area to flow, and the total pressure drop $P_b - P_a$ (pascals), and the viscosity, μ (Pa·s) and the length over which the pressure drop is taking place L (m).

The selectivity of gas was calculated by equation (2).

$$P = P_A / P_B \qquad (2)$$

where $P_A$and P_B are the gas permeation of pure gases of A and B respectively.

RESULTS AND DISCUSSIONS

Figure 8 shows that as kaolin content increases permeability of CO_2 decreases. The reason behind this is the variation in pore size when kaolin content is increased. SEM images have shown a decrease in pore size. Therefore as pore size is increased the permeability will also be increased. Less gas will be passed as compare to the membrane with larger pore size.

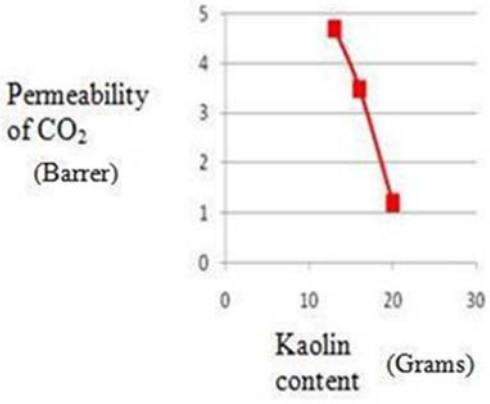

Figure 8. Permeability of $C0_2$ vs Kaolin Content

Figure 9 shows that as kaolin content increases permeability of air decreases. The reason behind this is the pore size as the kaolin content is increased sem images have shown a decrease in pore size. Therefore as pore size is increased the permeability have also increased. Less gas will be passed as compare to the membrane with larger pore size.

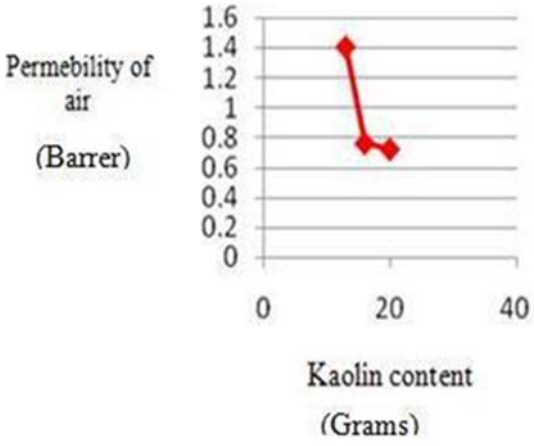

Figure 9. Permeability of Air vs Kaolin Content

Figure 10 clearly shows that as kaolin content is increased pressure drop is also increased. The reason behind this increase in pressure drop is the pore size. When the pore size is decreased the resistance to passage of gas is decreased which results in more pressure drop. Hence membrane with 16gm kaolin has more pressure drop than 13gm.

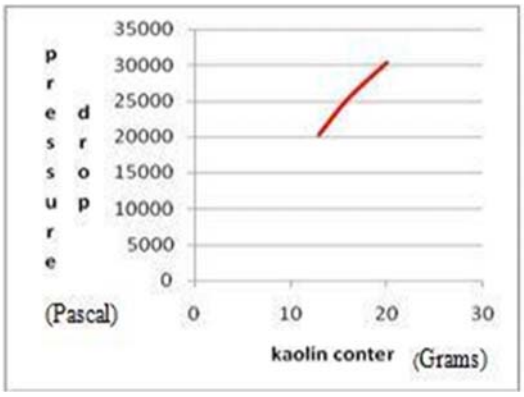

Figure 10. Pressure Drop vs Kaolin Content

6.1 CONCLUSION

Ceramic membranes were prepared from kaolin by the sintering technique in the presence of PVC polymer, arlacel and NMP.

By varying Kaolin content it was observed that the pore size decreses with increased kaolin content. Membranes having different kaolin content were prepared and tested for binary mixture. It was observed that as kaolin content increased pressure drop increased too. The permeation on the other hand decreased with increasing kaolin content.

ACKNOWLEDGEMENTS

We would like to express our sincere appreciation to our advisors, Dr. Saud Hashmi & Dr. Zahoor ul Hussain Awan whose contribution in stimulating suggestions and encouragement helped us to coordinate our project. Their support and supervision has been a significant part of our learning curve and we deeply appreciate it.

REFERENCES

[1] Fung and Wang, 2014; Harun et al, 2014; Hubadillah et al, 2014; Kingsbury and Li, 2009; Othman et al, 2010; Paimen et al, 2015.

[2] Donelson et al, 2014; Isobe et al, 2007; Li and Hwang, 1992.

[3] Bouzerara et al, 2016; Bouzerara et al, 2012; emani et al, 2014; Sarbatly, 2011.

[4] Ganesh and Ferreira, 2009; Bouzerara et al, 2008; Sahnoun and Baklouti, 2013.

[5] Siti Khadijah Hubadillah, Effect of kaolin content and non solvent coagulant bath, 2016.

SENSITIVITY ANALYSIS OF THE SHALE GAS FOR DECARBONIZAION USING IONIC LIQUID

Bilal kazmi[1], Dr. Zahoor ul Hussein Awan[1], Dr. Saud Hashmi[2], Hani kirmani[1]

[1]Department of Chemical Engineering
NED University of Engineering & Technology, Karachi, Pakistan

[2]Polymer & Petrochemical Engineering Department
NED University of Engineering & Technology, Karachi, Pakistan

ABSTRACT

Ionic liquid are rapidly receiving the attention of the world as the most effective and potentially suitable candidate for the capturing of the CO2 and make the process environment friendly. Still selection of the ionic liquid from its broader class is a tough task but with a suitable screening model and experimentation a large data can be generated for the decarbonization technology. A process simulation was performed for the decarbonization of the shale gas using ionic liquid using the physical absorption method. The simulation was developed based on the thermodynamics data available in the literature and with the help suitable thermodynamic mode of NRTL. Two processing options were used single stage as well as multi stage flashing after absorption. Both process results in the less amount of energy consumption in comparison as compare to the commercial process of amines. The results also revealed that a suitable amount of CO2 can be captured from the ionic liquid.

INTRODUCTION:

By and large, greater accentuation is begun to be put towards the control of environmental contamination. The significant wellspring of contamination is due to the consumption of petroleum derivative which is generally because of the high demand for the energy. So at the same time, it has turned out to be imperative to battle the energy emergency and in addition environmental effects. So it is important to search for the other options of energy that can essentially meet our demands for cleaner energy, for example, shale gas. Shale gas is not the same as the traditional petroleum gas shale gas is found in the concentrated reserves and is caught in substantially little pockets all through shale is a sort of sedimentary rocks. The main shale gas extraction was completed in the eighteenth century in Fredonia New York. The modern creation of the shale gas began not until 1970[2].

In 2013 division of energy in the United States led an investigation with the assistance of energy data organization (EIA) and recognized the capability of shale reserves in 41 unique nations. The report featured the geochemical attributes and furthermore recognized the measure of recoverable shale gas as appeared in figure 1[1]. In the report, it has been demonstrated that around approx 31000 trillion cubic feet (tcf) of shale saves are accessible of which actually recoverable shale gas is around 7000-8000 tcf [2].

Shale gas has reformed the economy of the United States with its less reliance towards the oil imports and it has likewise affected their economy with the increase in work opportunity on the enormous scale.

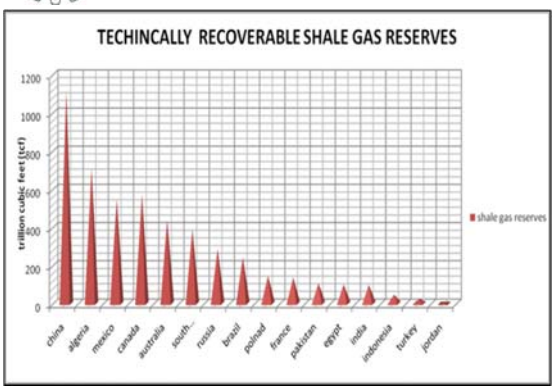

FIGURE1: technically recoverable shale gas in different countries according to EIA report[1]

Pakistan is honored to have such a geological area with around 827,365 km2 of sedimentary rocks enhanced with the shale saves and has a proven oil framework too [1-2].It has been additionally reported by Schlumberger in their reports in 2011 that one of the basins in southern Pakistan has the potential for the shale gas to be recovered while other basins in this region either lack thermal maturity or does not have enough information assessment [3]

Figure 2: shale basin in the subcontinent as reported by schlumberger in 2011 [3]

The current specialized examination conducted by the EIA has demonstrates that Pakistan is assessed to have around 586 tcf of shale gas stores of which the gas which can recoverable in fact is 100-200 tcf. Notwithstanding this 227 billion barrel of shale oil saves are additionally accessible and around 9.1 billion barrel is in fact recoverable as shown in figure 3 and 4. It has been evaluated that if these reserves are utilized we can beat the power and vitality necessities in Pakistan. It has likewise been called attention to in the report that the reserves in Pakistan are more than focal Asian state [1-2].

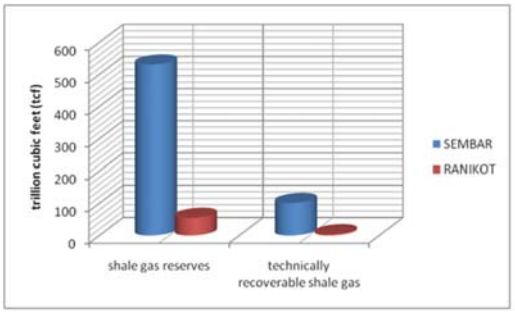

Figure 3: assessed shale gas reserves at the Indus basin of Pakistan according to EIA report 2013[1]

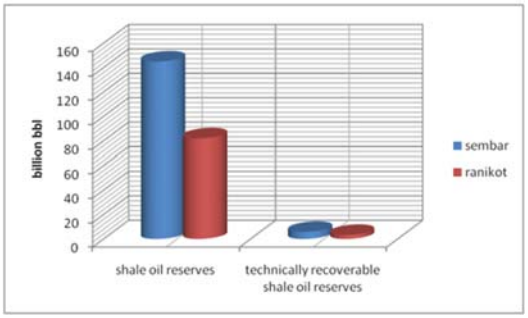

Figure 4: assessed shale oil reserves at the Indus basin of Pakistan according to EIA report 2013[1]

For the most part considering shale gas made chiefly out of methane and some measure of light hydrocarbon segments however before it can be utilized as a clean fuel it requires tobe cleaned. Since the outflows of CO2 are the real issue in the atmosphere and consideration is given toward CO2 discharge control.

Decarbonization is the major technology used these days to control the emission with the help of solvents. The most common solvents used in the decarbonization are N-methyl pyrrolidone, poly ethylene glycol di methyl ether, methanol, sulfolane, di ethanolamine,

monoethanolamine and methyl di ethanol amine. But generally these solvents have certain major drawbacks like high cost of energy for solvent regeneration, large lost of the solvent, corrosion causing agent due to alkalinity.

So to overcome these issues a new class of solvent has been studied widely known to be as “ionic liquids”. With their unique ability to work as an environmental friendly solvent The Ionic liquid are generally termed as the “green solvents”.This name was given due to their unique ability both physically and chemically. Ionic liquids (ILs) are the heterocyclic compounds belong to the molten salt group and mostly they are composed of asymmetric and bulky cations (organic) and anions (organic/inorganic)[5].They, by and large, have the one of a kind property of nonflammability which makes them nonhazardous for the modern scale industries. For the most part, the vast majority of the ionic liquids show insignificant vapor pressure under normal process conditions in this manner they can be effortlessly be regenerated and prevent a significant loss to the environment which results in less contamination. A large portion of the ILS is thermally steady and chemically steady as well. They are for the most part remains in the fluid state over the wide temperature range[4-7].They have the solvation capacity with regards to organics and inorganics sorts of mixes, additionally, with the best possible choice of cation and anion for the IL, this remarkable property can enable the researchers and designers to customize their process and fit this solvation ability into solutes. Because of their novel property of nonvolatility and great dependability they are being considered for the separation procedure.

So in view of the test comes about a simulation, contemplate was directed to screen out the potential ionic fluid out of the broader class of ionic fluids for the decarbonization of the shale gas. The simulation consider concentrates on the two sorts of process single stage streak division and multi-organize too. The theoretical plan of the procedure is to expel CO2 from the shale gas.it is performed in view of the accessible thermodynamic information, parameters for the fitting thermodynamic model are set up lastly two procedures has been considered against the traditional procedure.

SELECTION OF IONIC LIQUIDS:

it is extremely hard to choose a kind of ionic fluid having both high selectivity and solubility. Consequently to choose a fitting ionic liquid for the expulsion of CO2 is a noteworthy step to be taken into account.imidazolium based ionic liquid was chosen for the specific expulsion of CO2 from the blend of hydrocarbons. Imidazolium based ionic liquid is chosen among the huge characterization of an ionic liquid. this class of ionic liquid is chosen because CO2 is moderately more soluble in imidazolium based ionic liquids because of the formation of strong hydrogen bond between the carbon atoms of imidazolium ring and the CO2 atom[8]. The other reason is by and large a substantial information is accessible for the imidazolium based ionic to be used in the simulation. Thus it is smarter to choose [C4mim][BF4] as the potential ionic fluid for this simulation study figure 5.

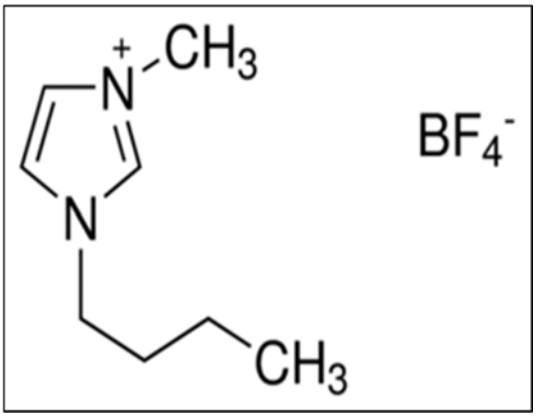

Figure 5: structural representation of [C_4mim][BF_4]

THERMODYNAMIC MODEL AND PROPERTIES:

Thermodynamic properties of the various ionic liquids and shale gas components involved in this study are demonstrated on the basis of NRTL (electrolyte non-random two liquid models). This model is used widely for the simulation of scrubbing process using amine. For ionic liquid the property prediction and equilibrium phase are modeled with the help of the data available at NIST data base for the ionic liquids.

Scalar properties incorporate the basic and volumetric properties of the gas and ionic liquids, the acentric factor, boiling point, etc which can be used in the further connections for the prediction of the different thermodynamic properties and binary parameters. The basic properties of the ionic fluid are extracted from the literature. The temperature dependent properties are corresponded by the empirical equations where the coefficients and the scope of the experimental information are utilized for the assurance of these condition esteems. These properties are imperative as they help in the simulation model to foresee and help to break down the energy requests of the process.

Table 1: Scalar properties of $[C_4mim][BF_4]$

PROPERTY NAME	unit	Value
molecular weight	-	226.02518
critical temperature	C	359.15
critical pressure	bar	20.4
critical volume	ml/mol	672
acentric factor	-	0.8489
normal boiling temperature	K	484.6

PROCESS SYNTHESIS:

The main objective of the process is the expulsion of CO2 from the shale gas utilizing ionic liquid. Routinely it is done with the assistance of amines. However, keeping in view the "green solvent" capacity of ionic liquids a process is being intended for the removal of CO2 from shale gas. The feed gas components for the shale gas comprises of light hydrocarbons and an extensive level of methane gas. The typical composition of the various components of the hydrocarbons in shale gas found in Pakistan is portrayed in table 2.it is assumed that sulfur based impurities are removed in the desulfurization step. The process simulation is designed for the state of 32oC and since the shale gas is recovered from the well at high pressure so the model is simulated at 1000 psi.

Table 2: typical composition of shale gas in Pakistan

Components	Mol %
METHANE	67.72%
ETHANE	6.57%
PROPANE	4%
BUTANE	0.52%
PENTANE	0.19%
CO2	15%
N2	6%
WATER	SATURATED

PROCESS DISCRIPTION:

In this work, we have utilized an outline procedure plot for the expulsion of CO2 from the shale gas to meet the necessity of the decontaminated gas and this re-enactment display was performed on the simulation platform of ASPEN plus®. Feed gas goes into the absorber column segment at 20oC and 68.95bar; reaching in the absorber column it interacts counter currently with the ionic liquid. Rich dissolvable stream from the absorber flows into the column (flash column) at 20bar which is utilized to reuse the lighter hydrocarbons once more into the process. The bottom of the main absorber column is additionally warmed to 27oC and enters into the second flash column at a decreased pressure of 1 bar. The bottom of the second

flash column is also further additionally cooled to 25oC and reused back to the absorber column. The stream schematic diagram is shown in figure 6a.

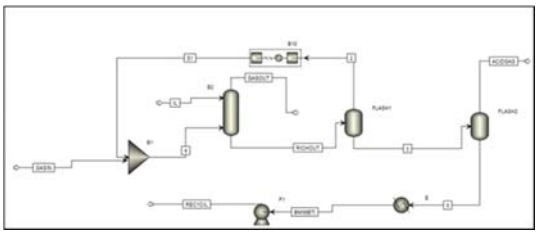

Figure 6a: ASPEN Plus flow sheet of the two single stage process of decarbonization

Besides the above mentioned process another process scheme was also evaluated. The scheme uses a series of the multistage columns to regenerate the solvent by reducing the pressure in each stage of the flash column. The schematic diagram of the process is shown in figure 6b.

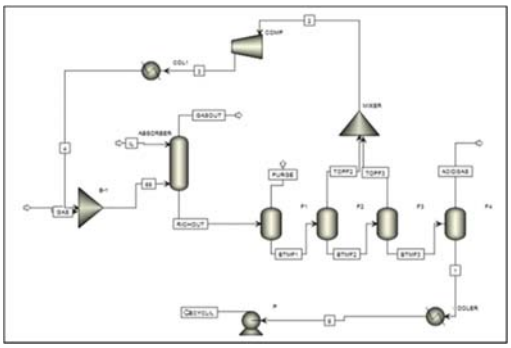

Figure 6b: multistage flashing process for the decarbonization using ionic liquid

RESULTS AND DISCUSSION:

1. EFFECT OF THEORETICAL STAGES ON CO2 REMOVAL:

It is very apparent that as the number of hypothetical stages in the absorber increases the separation of the CO2 from the shale gas increases as well. The outcomes for various stages and its separation performance are appeared in Fig 7a. It likewise delineates the performance of ionic fluid at various stream flows for the expulsion of CO2 from the shale gas. The outcome demonstrates that 8-10 theoretical plates of the absorber are sensible to get the coveted outcomes.

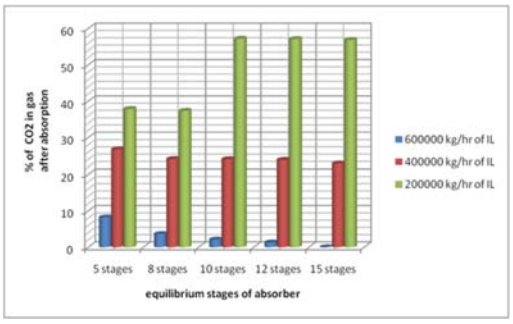

Figure 7a: effect of ionic liquid on CO_2 removal at different stages and at different mass flows

The stream flow of ionic liquid is likewise critical and with the outcomes it additionally imperative to choose an appropriate measure of the flow stream of ionic liquid for the process to run at an optimal point. The outcomes demonstrate that (4x105 - 6x105) kg/hr are the most reasonable mass stream of ionic liquid for the removal of the CO2 from the shale gas stream. In the wake of setting the equilibrium stages to 10 at 30oC, the impact of various mass streams of ionic liquids appear in fig 7b.

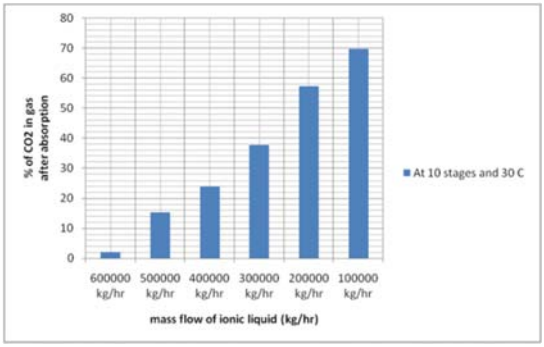

Figure 7b: % of CO_2 in gas after absorption at 10 stages at different mass flows

2. FLASH COLUMN:

In this procedure, we are utilizing two flash columns the reason for the flash column is for the regeneration of the methane and furthermore the recovery of the ionic fluid [C4mim][Bf4]. To accomplish the two things

you have to change the pressure of the flash column to recover the maximum measure of methane and maximum expulsion of CO2 from the process. From the figure 9, we can see that as we increment the pressure the recovery of the methane falls marginally while then again, CO2 recovery increments pointedly. So it implies that we have to modify the pressure of the flash columns with the end goal that we have a high recuperation rate of Ch4 and maximum removal of CO2 from the system. So the pressure of the flash column 1 is set at 20 bar which brings about the recovery of around 74.20% of CO2 from the feed gas stream and 75.59% of CH4 recovery is accomplished.

the second flash column is working at the lower pressure of 1 bar to regenerate the ionic liquid [c4mim][bf4] and remove the further amount acid gas from the system.

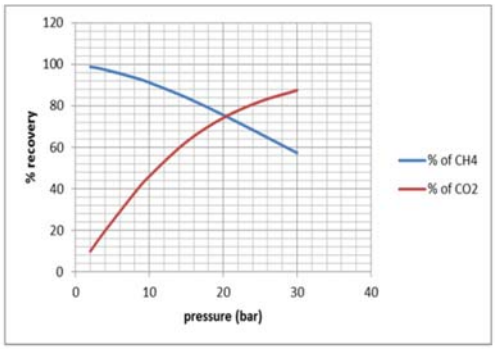

Figure 8: % recovery of CO_2 and CH_4 at various pressures of flash column 1

3. SOLVENT CONSUMPTION:

The amount of solvent is the most important factor to be considered for the both the process of amines and the process based on ionic liquid. The solvent consumption in ionic liquid based process is (6x105-7x105) kg/hr to achieve the recovery of the 90% methane. In contrast to the amine based process it requires lesser amount of amine as a solvent. On the other hand if the mutli stage process is utilized using ionic liquid it almost requires 40 % less amount of ionic liquid [8].

The main advantage of using ionic liquid is generally because of its thermal stability, less corrosive in nature, negligible vapor pressure resulting in less volatility and generally less amount is lost and can be easily regenerated. These factors make ionic liquid a suitable replacement for the amines and would result in longer benefit.

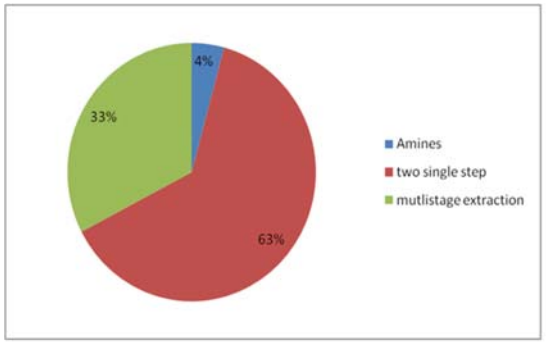

Figure 9: solvent demand of the various processes for the decarbonization of shale gas

4. ENERGY ANALYSIS:

The energy analysis results shows fig 10a and 10b that for the amine based process of decarbonization require a large amount of the total energy in comparison to the single stage and multi stage process using ionic liquid as solvent [8]. Also the thermal energy requirement of the amine based process is quite large as compare to the ionic liquid based processes

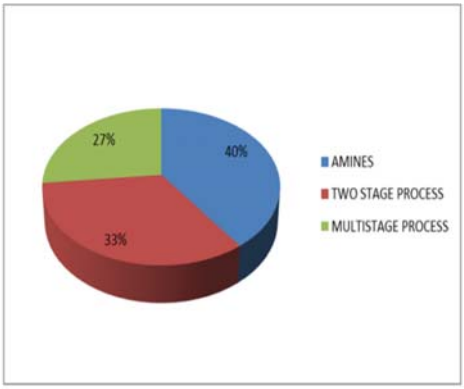

Figure 10a: total energy consumption comparison between the processes

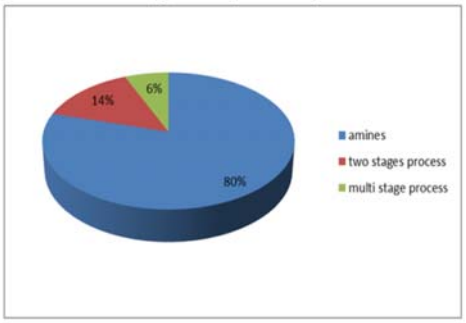

Figure 10b: total thermal energy comparison between the process

5 .COMPARISONS BETWEEN PROCESS SCHEMES :

We have demonstrated two processing options for the decarbonization process in the first option we have used a two single stage process in which an absorber is operating with two flash columns. Where as in the second scheme we have considered multistage process in which four adiabatic flash vessels is connect in series at different pressures. The flash vessels in the multi stage process leads to more energy consumption (3698.96kWe) during the process as compare to the two stage process (1532.911kWe) respectively. So it would be suitable to select two single stage process schemes for the process.

CONCLUSION:

In this work we have evaluated the importance of shale gas keeping in view the energy demands of Pakistan. Also we have worked towards the process of decarbonization of the shale gas with the help of ionic liquid as solvent. Two process schemes are being considered single stage absorption and multistage flashing as well. Both process results in the lower thermal energy consumption and effectively meets the requirements of the recovery of the methane as well as the lighter hydrocarbons.

NRTL thermodynamic model was used to model these processes on ASPEN plus.[C4mim][BF4] was chosen as the ionic liquid solvent for the process. [C4mim][BF4] was selected generally because a large amount of thermodynamic data required to in the simulation is available for it and it has high selectivity for the selective removal of CO2 form the stream of hydrocarbons without dissolving greater amount of hydrocarbons in it. Multistage flashing was considered as the optimal process for the decarbonization in terms of energy consumption as well as the performance for the removal of CO2.

Overall ionic liquid is proven to be a suitable replacement for the amines based process used commercially. Furthermore experimentation on the ionic liquid would enhance it further ahead in the future.

REFERENCES:

1. EIA/ARI World Shale Gas and Shale Oil Resource Assessment Technically Recoverable Shale Gas and Shale Oil Resources: An Assessment of 137 Shale Formations in 41 Countries Outside the United States

2. SDPI(sustainable policy development institute) drapt report for shale oil and shale gas :lifeline for Pakistan

3. Schlumberger report on “shale gas :a global resource” published in 2011

4. Swapnil A. Dharaskar,Kailas L. Wasewara, Mahesh. N. Varmaa, Diwakar. Z Shendea, Chang KyooYoo

5. Werner S, Haumann M, Wasserscheid P. Ionic liquids in chemical engineering. Annu Rev ChemBiomol 2010;1:203–30

6. Ana R. Ferreira , Mara G. Freire , Jorge C. Ribeiro , Fernando M. Lopes , João G. Crespo , João A.P. Coutinho , Ionic liquids for thiols desulfurization: Experimental liquid–liquid equilibrium and COSMO-RS description
http://dx.doi.org/10.1016/j.fuel.2014.03.020

7. Borja Rodríguez-Cabo, Héctor Rodríguez, Eva Rodil, Alberto Arce, Ana SotoExtractive and oxidative-extractive desulfurization of fuels with ionicliquidsFuel 117 (2014) 882–889

8. Xinyan Liu, Ying Huang, YongshengZhao,RafiqulGani, Xiangping Zhang, and Suojiang Zhang ionic liquid design and process simulation for decarbonization of shale gas DOI: 10.1021/acs.iecr.6b00029

To Explore Polymer Cure of De-Emulsified Cutting Fluids

R. Ahmed[1], H. Taqi[2], R.M. Khan[1], S.G.Hussain[2], H. Arif[3], K.A. Syed[1]
[1]Polymer & Petrochemical Engineering Department
NED University of Engineering & Technology, Karachi, Pakistan
ahmedr@neduet.edu.pk; rmkhan@neduet.edu.pk; drkausarali@neduet.edu.pk

[2]Department of Chemistry,
NED University of Engineering & Technology, Karachi, Pakistan
hasnain.taqi@yahoo.com
[3]Department of Industrial & Manufacturing Engineering,
NED University of Engineering & Technology, Karachi, Pakistan
hammad_aaa@hotmail.com

ABSTRACT

A novel method of re-generating the de-emulsified cutting fluid has been explored by adding water soluble polymer in addition to the anti-bacterial agent, pH modifier, and cutting fluid additives. The polymer loading was varied between 1 to 5 % holding other constituents constant. The polymer added samples (POLY samples) and de-emulsified samples (as-received samples) received from a local metalworking industry were studied for bacterial growth, changes in pH, changes in oil concentration, percent evaporation, and corrosion penetration rates using standard methods. Bacterial growth was modeled using modified Gompertz model. Significant increasing trend in lag time was observed with increase in polymer concentrations, > 800 % increase in POLY05, when compared to the as-received samples. The lower percent evaporation for all POLY samples indicated the enhanced thermal stability of these samples. POLY samples showed retarded corrosion rates than as-received samples. Similar decreasing trends in pH were observed for as-received and POLY samples. Almost all samples showed similar decreasing trend in oil concentration however POLY samples showed higher initial values. The findings of this research such as increase in lag time and higher thermal stability will not only make the metalworking process economical but will equally decrease the risk of environmental pollution.

Keywords: cutting oil, polymer, de-emulsification, bacterial growth, pollution.

1. INTRODUCTION:

Cutting fluids, also known as coolant, are liquids or gases applied to reduce the severity of the contact processes at the cutting tool-work piece interfaces. The main purposes of the cutting fluid is to avoid overheating at the tool-work piece interface, to reduce power consumption, to provide good finished surface, to wash scarf from the cutting area, and to avoid corrosion. Although the required properties of a cutting fluids depends on the final application but the most desirable properties of good cutting fluids include high thermal conductivity, high flash point, good lubricating qualities, stability against oxidation, must not promote corrosion and many more. Straight cutting oils, water emulsifiable oils (soluble oils), synthetic fluids (chemical fluids), semi-synthetic fluids and liquid nitrogen are the well-known cutting fluids available in the market.

Due to the wide range of applications in machining and grinding operations, water emulsifiable oils are the most popular cutting fluids in use today [1]. In addition to the combine lubricating qualities of oil and

cooling properties of water these fluids are quite adequate to adopt corrosion inhibitors and biocide. One of the major disadvantages of these fluids is de-emulsification, the process of breaking the emulsion into its individual incompatible phases, mainly water and oil. The resistance of a water/oil (w/o) emulsions to coalescence and their response to the de-emulsification methods essentially depends on the physical and chemical properties of oil, emulsification conditions, and aging. This means, w/o emulsion de-emulsification vary from one application to another [2]. Various methods for de-emulsification are reported in literature [3,4].

In view of the increasing demands for cutting fluids and environmental concerns bio-based oils such as esters and vegetable oils are getting enormous attention in industry and academia for the preparation of w/o emulsions. For example both castor and jojoba oils have shown quite distinct properties when compared to other vegetable oils [5,6]. But their low thermal stability is one of the major disadvantages in their widespread use [6].

The main purpose of this study is twofold: first, to re-generate the de-emulsified cutting oil making use of polymers, and second to use this novel method to explore the polymer content effect on the bacterial growth, thermal stability, oil concentration, and corrosion rate.

2. EXPERIMENTAL:

2.1 Materials

De-emulsified cutting oil was collected from Tank K32B of International Industries Limited (IIL), Karachi. Commercial grade raw materials were generously provided by the Hasnain Enterprises for the re-generation of de-emulsified cutting oil: cut emulsion 2057 (Hasnain Enterprises), caustic potash (pH modifier), triethylene glycol, oleic acid, triethanolamine, and a water soluble polymer (polyacrylamide (PAM), MFI = 30).

2.2 Re-generation of the De-emulsified Cutting Fluid

De-emulsified cutting oils samples (here after called as-received sample) were collected from a local metalworking industry IIL.

In a typical recipe various percentages (1 to 5% (w/v)) of a water soluble polymer along with the anti-bacterial agent, pH modifier, and cutting fluid additives were added to the de-emulsified samples. These samples here after will be called POLY samples. For example POLY01 means 1 % (w/v) of the water soluble polymer is added to the as-received sample along with other ingredients. The mixture was homogenously mixed under vigorous mixing conditions using overhead stirrer at room temperature. The mixture was used for further characterizations.

2.3 Characterizations

2.3.1 Bacterial Growth Measurements

Bacterial growth tests were performed at labtest, North Nazimabad Karachi. Measurements were done using plate count method at 37 °C and for incubation time of 48 hours by preparing serial dilutions of the sample (1:10, 1:100, 1:1000, etc.) in sterile water. Samples were cultivated on nutrient agar in a sealed and incubated dish. First set of plates was incubated at 22°C for 24 hours. Second set at 37°C for 24 hours. A recent method of using fluorescent agent was adopted so that counting of the colonies can be automated.

2.3.2 pH Measurements

pH measurements were performed on a digital CyberScan pH 1500 Benchtop pH Meter.

2.3.3 Determination of Oil Concentration

The oil concentrations were measured by measuring the changes in the refractive indices of the samples using a portable (OPTi digital

refractometer, Bellingham – Stanley, UK) refractometer.

2.3.4 Gravimetric Corrosion Study Technique

Corrosion study was performed on previously weighed mild steel (MS) coupons. The cleaned MS coupons were suspended with glass hook in the as-received sample and POLY samples in open beakers. The beakers were placed in a thermostated paraffin oil bath maintained at 35 °C. The coupons were retrieved progressively for 620 hours. Each time the coupons were washed with acetone, dried and re-weighed. The weight loss of the coupon was recorded as the difference in weight between the specimen before immersion and after immersion in each sample. Averages of four test samples are reported for each sample.

The following formula was used to determine the corrosion penetration rate (CPR) (mils per year (mpy)),

CPR = KW/ρAt

Where, W = weight loss (mg); exposure time t (inch^2); ρ = density (g/cm^3); A = exposed specimen area (inch^2) and K = 534, its magnitude depending on the system of units used.

3. RESULTS AND DISCUSSION:

3.1 Determination of Bacterial Growth Parameters

One of the major problems with the use of the cutting oil is the bacterial growth in de-emulsified cutting oil. Bacterial growth not only reduce the oil content of the cutting oil but also lead to the serious environmental concerns due to the bad smell and substantial increase in corrosion rates. Figure 1 shows relative population against time.

Various models are available to understand the bacterial growth such as Logistic, Gompertz [7,8], Richards [9], Stannard et al. [10], Schnute [11], and others [12]. The Gompertz model is well known for modeling of bacterial growth. Figure 2 shows the typical biological parameters that can be determined by fitting the population data with modified Gompertz model [13].

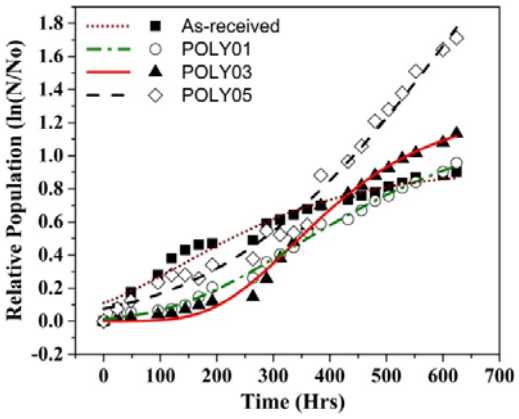

Figure 1: Relative population against time. The lines show the fit of modified Gompertz model.

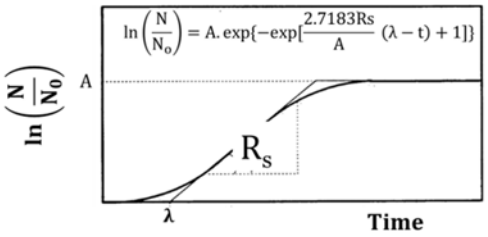

Figure 2: Modified Gompertz model typical curve. The mathematical equation shown on the graph is the modified Gompertz model. The parameters include R_s = specific growth rate, λ = lag time, and A = Plateau value ($\frac{N_\alpha}{N}$).

The purpose of the modified Gompertz model was to capture the biological parameters rather than to fit the data and only determine the number of organisms as a function of time. Figure 3 shows a typical representative curve fit to the POLY03 sample. The population growth curves were fitted with the modified Gompertz model that allowed the determination of three biological parameters: the maximum specific growth rate, R (the

tangent in the inflection point); the lag time, λ (intercept of the tangent); and the asymptote, $A\left(\ln\left(\frac{N}{N_0}\right)\right)$. The determined two parameters, considered in this study, are plotted in figure 4 (a and b).

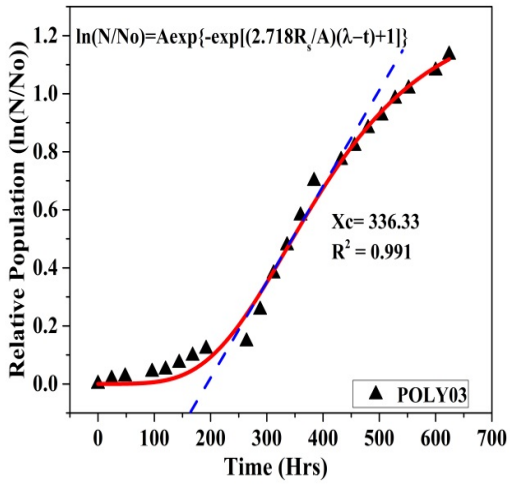

Figure 3: A representative curve showing modified Gompertz model, shown on the graph, fit on the POLY03 sample data: The solid line shows modified Gompertz model fit whereas the broken tangent line is drawn to guide the eyes to find the lag time.

It is evident from the figure 4a that as the polymer concentration is increased the lag time, the delay time between the zero growth rate and accelerated growth rate, increases. For example POLY05 sample reveals more than 800 % higher lag time when compared to the as-received sample. Therefore, the use of water soluble polymer will increase the shelf-life of the used cutting oil. On the other hand, the specific growth rate (Figure 4b), the maximum growth rate that when exponential increase in bacterial growth is observed, increases with the increase in polymer concentration. However, the POLY01 sample showed 40 % decrease in the specific growth rate when compared to the as-received sample. The thermal stability of the samples was determined by measuring the percent evaporation. Figure 5 shows that the POLY samples exhibit higher thermal stability when compared to the as-received sample. The thermal stability increases with increase in the polymer concentration. The lower values of the percent evaporation for POLY samples, at all times, correspondence to their higher thermal stability in comparison to the as-received sample.

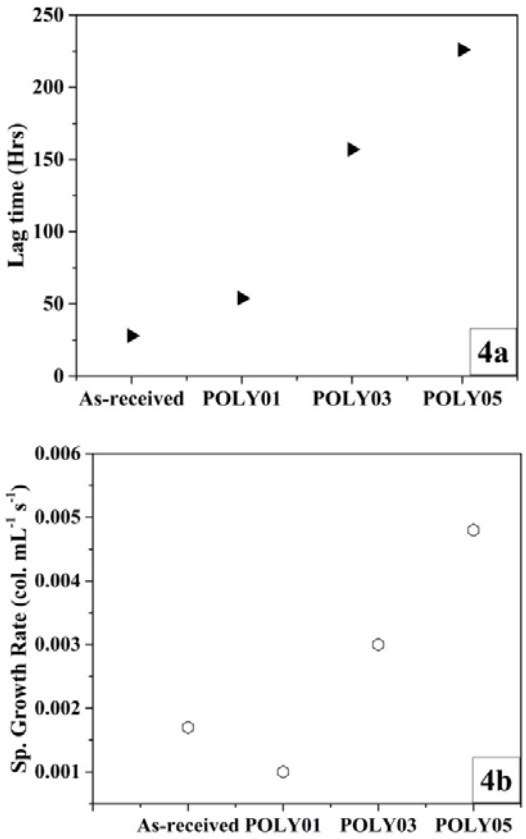

Figure 4: Biological parameters determined from the fit of modified Gompertz model for as-received and POLY samples; (4a) effect of polymer content on lag time (4b) effect of polymer content on specific growth rate.

3.2 Effect of Polymer Content on Oil Concentration

Figure 6 shows the effect of polymer content on the oil concentration, cutting oil concentration in emulsion. It is observed that the oil concentration decreases with time in all the samples. However, the oil concentration is higher for POLY samples when compared to the as-received sample. This might be attributed to the higher thermal stability of the POLY samples.

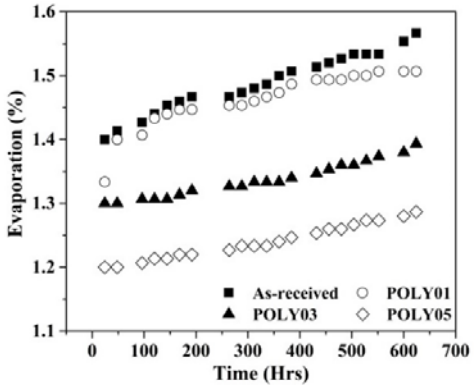

Figure 5: Effect of the polymer content on the percent evaporation.

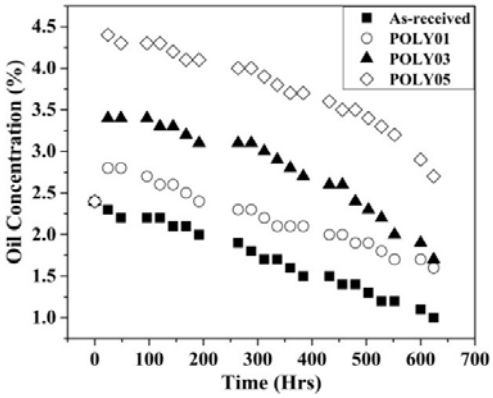

Figure 6: Effect of polymer content on oil concentration.

3.3 Effect of Polymer Content on pH

One of the major problems in use of cutting oils is the decrease in the pH of the samples. The lower acidic pH leads to the severe corrosion of metal surfaces in consequence to the sooner exhaustion of the cutting oil. Figure 7 shows the similar decreasing trend of pH in both as-received and POLY samples. However, POLY samples maintain higher pH (> 8) values for more than 12 days especially for POLY samples with higher content of polymer.

3.4 Effect of the Polymer content on the Corrosion Penetration Rate (CPR)

Figure 8 compares the CPR of the as-received and POLY samples. All the samples show similar trend of corrosion. However, the corrosion rate is decreased with increase in polymer content.

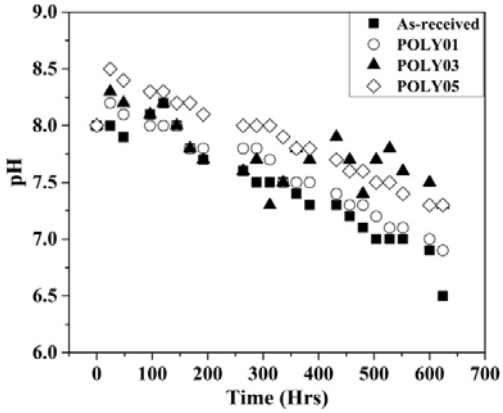

Figure 7: Effect of POLY content on the pH.

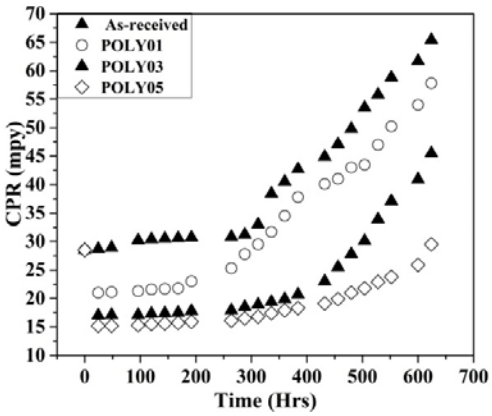

Figure 8: Effect of polymer content on the corrosion penetration rate.

4. CONCLUSIONS:

- Modified Gompertz model was successfully used to model the bacterial growth data.
- Higher lag time were observed for POLY samples which increases with POLY concentration.
- Lower evaporation rate were observed for POLY samples which increases with POLY concentration.
- Oil concentration varied in similar fashion for all samples however POLY samples showed higher initial oil concentration.
- No substantial changes in pH were observed for all samples.

- Corrosion rate decreases with POLY contents and the lowest CPR was observed for the 5 % POLY contents.

ACKNOWLEDGEMENTS

Authors are thankful to IIL for their permission to collect samples from their plant.

5. REFERENCES:

1. Issaka S.A., N our A.H., Yunus R.M., J Pet Environ Biotechnol, 2015, 6:2.
2. Kristiansen T.S., Lewis A., Daling P.S., Nordvik A.B., Spill Science and technology, 1995, 2: 133-141.
3. David D.D., Pezron I., Dalmazzone C., Noık C., Clausse D., Colloids and Surfaces A: Physic. chem. Eng. Aspects, 2005, 270: 257-262.
4. Kukizaki M., Goto M., Journal of Membrane Science, 2008, 32: 196-203.
5. Asadauskas S., Perez J.M., Duda J.L., Lubr Eng, 1997;53(12):35.
6. Allawzi M., Abu-Arabi M.K., Al-zoubi H.S., Tamimi A., J Am Oil Chem Soc 1998;75(1):57.
7. Gompertz B., Philos. Trans. R. Soc. London, 1825, 115:513-585.
8. Gibson A.M., Bratchell N., Roberts T. A., J. Appl. Bacteriol. , 1987,62:479-490.
9. Richards F.J., J.Exp. Bot., 1959, 10:290-300.
10. Stannard C.J., Williams A. P., Gibbs P. A., Food Microbiol., 1985, 2:115-122.
11. Schnute J., Can. J. Fish. Aquat. Sci., 1981, 38:1128-1140.
12. Ricker W.E., Fish Physiol., 1979,8:677-743.
13. Zwietering M.H., Jongenburger I., Rombouts F.M., Riet K. Van 'T., Appl. Environ. Microbiol.,1990, 56(6):1875-1881.

Microencapsulation of Halochromic Material and Inhibitor for Smart Coating to Detect and Control Corrosion

Danish Majeed[1, a], Shafaq Tassawar[1, b], Muhammad Mobeen Fasih[1, c] and Muhammad Tahir Siddiqui[1, d]

[1]*Department of Materials Engineering, NED University of Engineering & Technology, Karachi, Pakistan 75270*

[a]danish.majeed@neduet.edu.pk, [b]shafaq_tassawar506@yahoo.com, [c]mobin94@live.com and [d]tahirsiddique50@gmail.com

ABSTRACT

Corrosion of metals is one of the greatest industrial and economical problem leading to severe catastrophic failures. The versatile smart coating has been developed through microencapsulation of halochromic material and inhibitor for early indication and control of corrosion. This study starts with the selection of a compatible combination of prepolymer and surfactant. Different prepolymers along with their cross linkers are tested with different surfactants and after numerous experiments, prepolymer Epoxy was selected with surfactant Sodium Pyro Phosphate. The pH sensitive polymeric microcapsules were synthesized by interfacial polymerization and integrated into several coating systems. Coatings which are rigid and have acidic pH are unsuitable in this scenario. Therefore, transparent acrylic gel coating was found to be optimal selection for early detection of corrosion. The synthesized microcapsules when incorporated in defined coating showed a visible color change on corrosion sites within hours rather than in months & increased the inhibition effect. To ensure the thermal stability, TGA was performed before and after the UV exposure to check the effect of UV on thermal stability. And Stereomicroscopy was used to observe the morphology of microcapsules.

Keywords: Halochromic Material, Corrosion Indication, Corrosion Inhibition, Corrosion Control, Microencapsulation, pH-sensitive coatings, Interfacial polymerization.

1 INTRODUCTION

Corrosion of metals is a problem with great economic and social impact and if it is not indicated and prevented, it can lead to catastrophic failure. Corrosion is a costly problem for a wide range of industries and it affects nearly every facet of our lives. [1-3] pH and other electrochemical changes are often associated with localized corrosion, so it is expected that materials that are pH or otherwise electrochemically responsive can be used to detect and control corrosion. [4-5] Encapsulation of the active corrosion-control ingredients allows the incorporation of desired autonomous corrosion-control functions such as early corrosion detection, hidden corrosion detection, corrosion inhibition, and self-healing of mechanical damage into a coating. The technology offers the versatility needed to include one or several corrosion-control functions into the same coating. Microencapsulation is a commercially successful technology that has been used for controlled-release of active ingredients. In recent years, this technology has attracted increased interest from the coatings industry as well as the research community in the field of corrosion protective coating. [6-10]. Paint systems containing color-change compounds are found to be sensitive to underlying corrosion processes by reacting to the pH increase associated with the cathodic reaction that accompanies corrosion. The incorporation of encapsulated halochrome and inhibitor that can be protected by a coating until their release is triggered by the onset of corrosion will result in a smart coating that is both environment-friendly and cost-effective. [11]

One critical aspect of a corrosion protective smart coating is the selection of corrosion inhibitor for encapsulation and comparison of the inhibitor function before and after encapsulation. [12] Some of the new inhibitor chemistries exhibit excellent corrosion protection, such as organic inhibitors, but their incorporation into coatings has been difficult due to their high reactivity with resin systems,

or high solubility that lead to blistering and leaching. Smart coatings with pH-sensitive microcapsules can be used to overcome these challenges by isolating the inhibitor from the environment through encapsulation. [13]

Many approaches have been done that are circumscribed by corrosion prevention only but the early detection or indication of corrosion will help in alarming the danger and may prevent the catastrophic failure. It is essential to detect corrosion when it occurs, and preferably at its early stage, so that action can be taken to avoid structural damage or loss of function of metals and their alloys. Many different sensors and techniques are being developed to detect corrosion. [14-17]. Among different technologies, corrosion sensing coatings are highly desired for corrosion control, especially if the signal can be detected through visual inspection by the naked eye, at a stage much earlier than the appearance of the observable corrosion products. [18-23]

This paper presents the development of microcapsules that encapsulates halochromic material, one of the categories of smart materials that change color when a change in pH takes place, as corrosion indicator and inhibitor and the results obtained by introducing these microcapsules into the acrylic transparent coating to test their corrosion indication and inhibition effectiveness. Also technical details on the characterization of defined microcapsules using Thermogravimetric analysis before and after UV exposure and stereomicroscopy.

Method

In this study Interfacial polymerization was used to synthesized microcapsules which follows oil and water phase formation and then merging both phases while mixing as shown schematically in figure 1 and 2.

2.1. Synthesis of oil core microcapsules with halochrome phenolphthalein

Reagent	Mass in grams
Oil Phase	
Epoxy	8
Hardener	2
Toluene	20
Isopropanol	4
Phenolphthalein	0.2
Water Phase	
Sodium pyrophosphate	0.1
Water	100
Catalyst	
H_2SO_4	0.5

Table 1. Formula for oil core microcapsule formation with halochrome

2.1.1. Formation of Water phase and Oil Phase

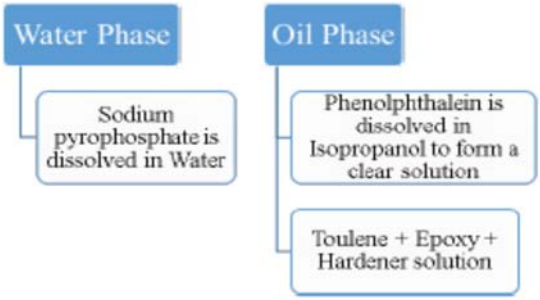

Figure 1. Schematic representation of oil and water phase formation with halochrome

2.1.2. Process of microcapsules formation

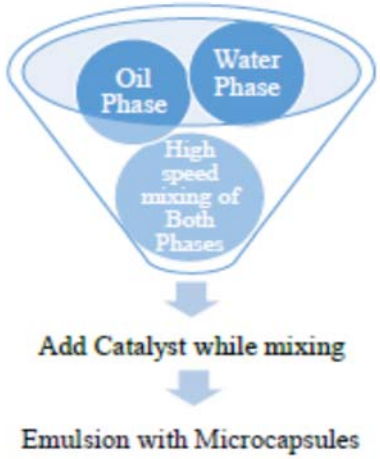

Figure 2. Schematic representation of process of microcapsules formation with halochrome

2.2. Synthesis of oil core microcapsules with halochrome phenolphthalein and inhibitor beta-lactamase

Reagent	Mass in grams
Oil Phase	
Epoxy	8
Hardener	2
Toluene	20
Isopropanol	4
Phenolphthalein	0.2
Beta lactamase	0.2

Water Phase	
Sodium pyrophosphate	0.1
Water	100
Catalyst	
H_2SO_4	0.5

Table 2. Formula for oil core microcapsule formation with halochrome and Inhibitor

2.2.1. Formation of Water phase and Oil Phase

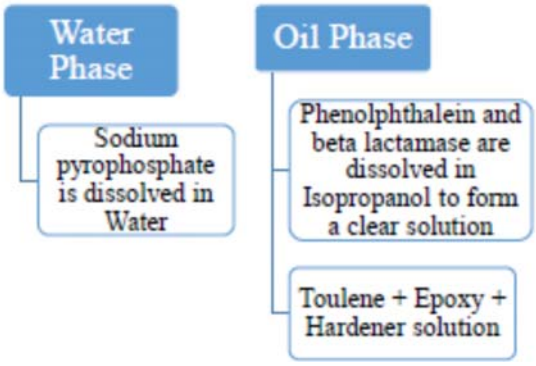

Figure 3. Schematic representation of oil and water phase formation with halochrome and inhibitor

2.2.2. Process of microcapsules formation

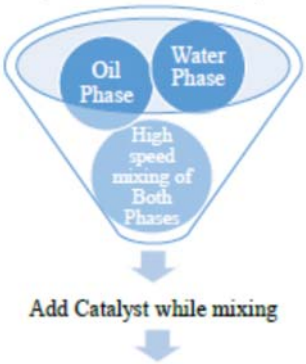

Figure 4. Schematic representation of process of microcapsules formation with halochrome and inhibitor

Results and Discussion

3.1. Corrosion Indication

Synthesized capsules with halochrome were added to acrylic transparent coating and the coating containing capsules was applied on a mild steel sample and allowed to dry. After that, the sample was scribed with a scriber and observed for corrosion indication. The coating showed a visible color change (pink) in wet condition when the corrosion occurred.

- **3.2. Corrosion Inhibition**

Both microcapsules with and without inhibitor were added to acrylic transparent coating and then applied to two mild steel samples. The sample coated with the coating containing inhibitor showed the inhibition effect and protect from corrosion with the detection phenomenon unchanged whereas another sample shows the early detection of corrosion.

- **3.3. UV Stability**

Synthesized capsules were exposed to ultraviolet light using an Ultraviolet lamp for 4 hours and added to the acrylic transparent coating. The coating containing capsules was applied to mild steel sample. The coating containing microcapsules which had exposed to UV light showed a visible color change in wet conditions when corrosion occurred. Hence, showed no major effect on detection of corrosion.

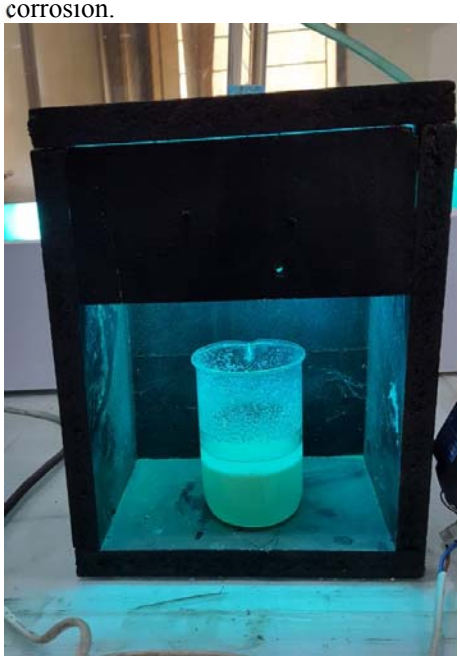

Figure 5. Exposure of UV light to microcapsules in Ultraviolet Lamp

3.4. Stereomicroscopy

As shown in figure 6, the size of microcapsules is around 1000-2800 µm and showing the size distribution of 1800 µm. Then, we enhanced the speed of magnetic stirrer which resulted in better size distribution as shown in figure 7. Hence, the size of

microcapsules was reduced to 300-1300 µm and reduced the size distribution to 1000 µm.
Figure 8, 9 and 10 show the physical stability of microcapsules at 20X, 30X and 30X respectively. Figure 11 shows the physical stability of better microcapsules dispersed in the transparent acrylic coating and the core content encapsulated in microcapsules.

3.5. Thermogravimetry

Figure 12 and 13 show the change in mass percent with respect to temperature. The first decrease in slope in the graph is showing the evaporation of isopropanol, water and toluene as they have boiling points of 89°C, 100°C and 110°C respectively.
The second dramatic decrease in slope is showing the degradation of epoxy polymer around 325°C as it has thermal degradation temperature at around 350°C and completely degraded at 475°C and after it, the remaining weight percent is about 12.6%.
The last decrease in slope is showing that the epoxy is completely degraded while the remaining constituents will start to degrade after it while the thermal degradation temperature of phenolphthalein and inhibitor is around 550°C and 545°C.
Figure 14 (TGA graph after UV exposure) shows a decrease in the first slope which shows the evaporation of isopropanol, water and toluene as they have boiling points of 89°C, 100°C and 110°C respectively.
The second dramatic decrease in slope is showing the degradation of epoxy polymer around 325°C as it has thermal degradation temperature at around 350°C and completely degraded at 475°C.It is observed that after UV exposure, the remaining weight percent at the similar temperature is 24.44% which is higher than before UV exposure TGA sample results.
The last decrease in slope is showing that the epoxy is completely degraded while the remaining constituents will start to degrade after it while the thermal degradation temperature of phenolphthalein is around 550°C.

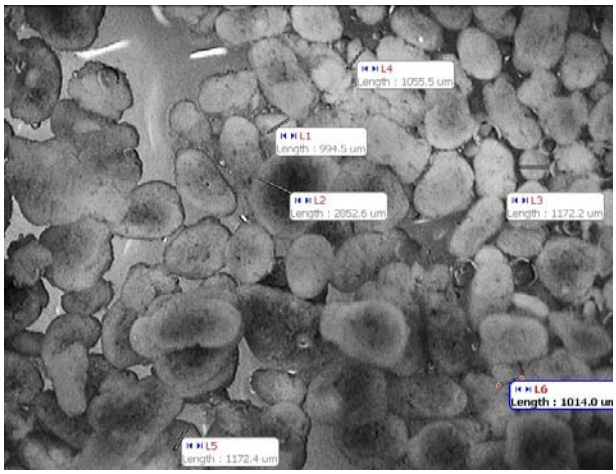

Figure 6. Stereomicroscopic Image of pH-sensitive microcapsules at 30X

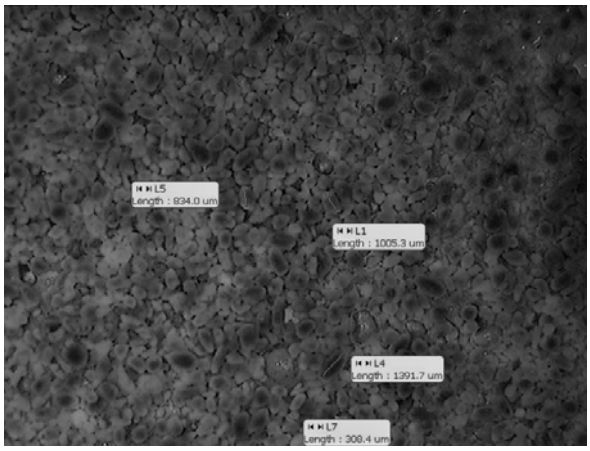

Figure 7. Stereomicroscopic Image of pH-sensitive microcapsules at 15X

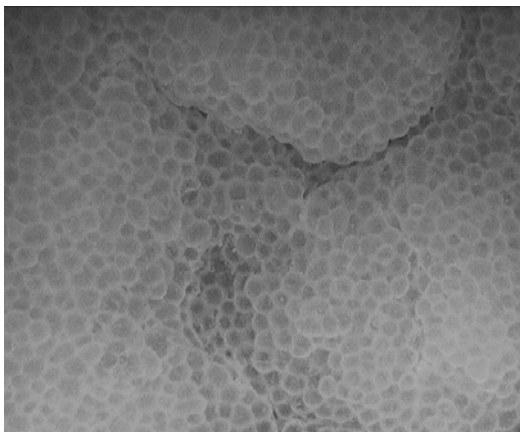
Figure 8. Stereomicroscopic Image of pH-sensitive microcapsules at 20X

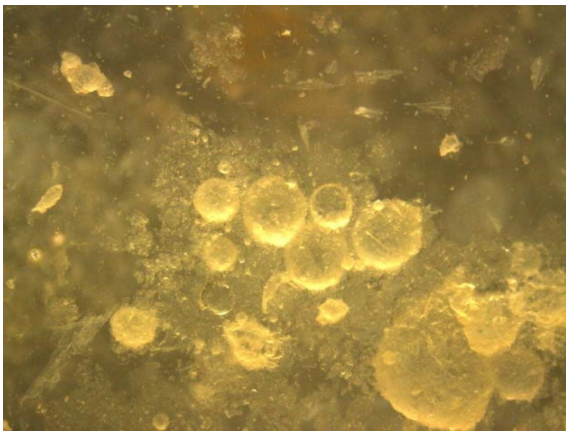

Figure 9. Stereomicroscopic Image of pH-sensitive microcapsules at 30X

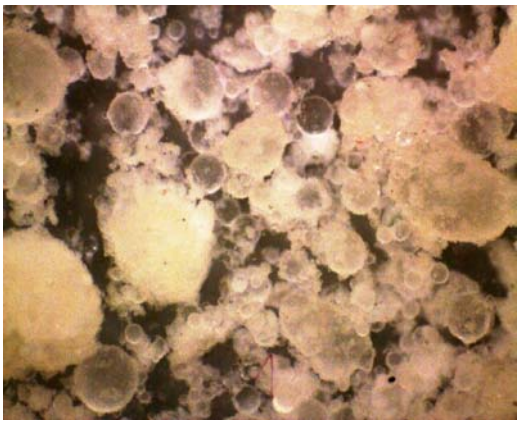

Figure 10. Stereomicroscopic Image of pH-sensitive microcapsules at 30X

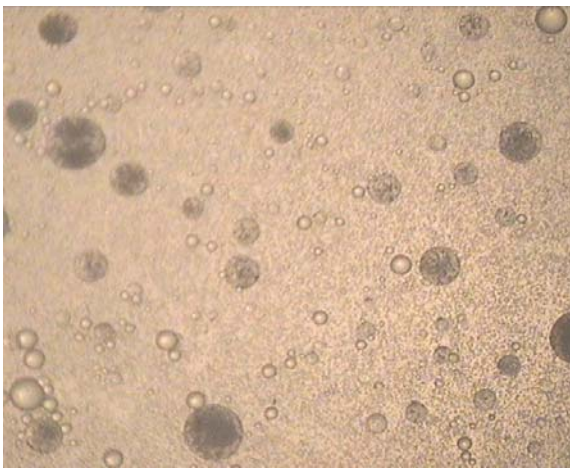

Figure 11. Visible encapsulated content of microcapsules in Acrylic Gel through stereomicroscope

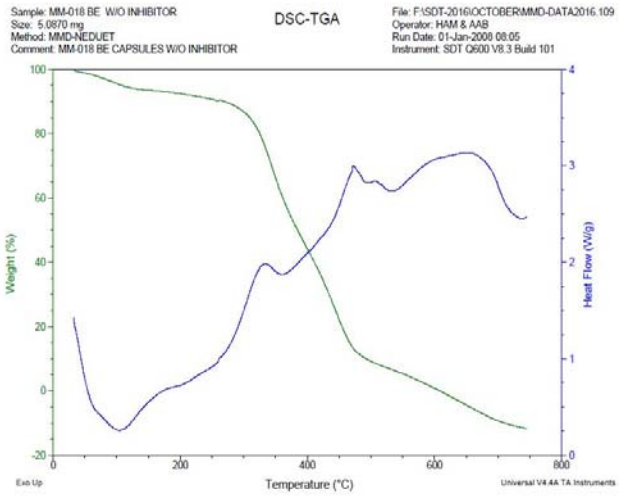

Figure 12. TGA graph of microcapsules with Indicator before UV exposure

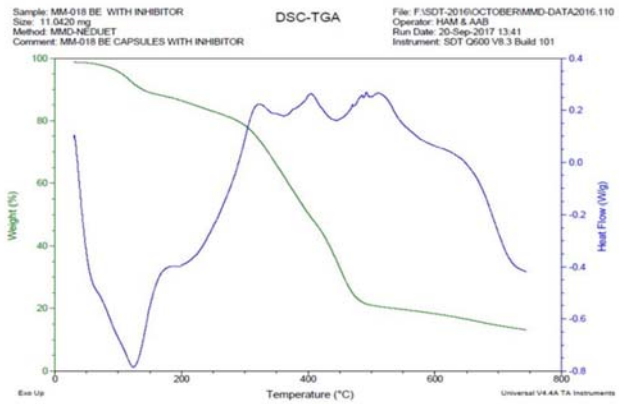

Figure 13. TGA graph of microcapsules with Inhibitor

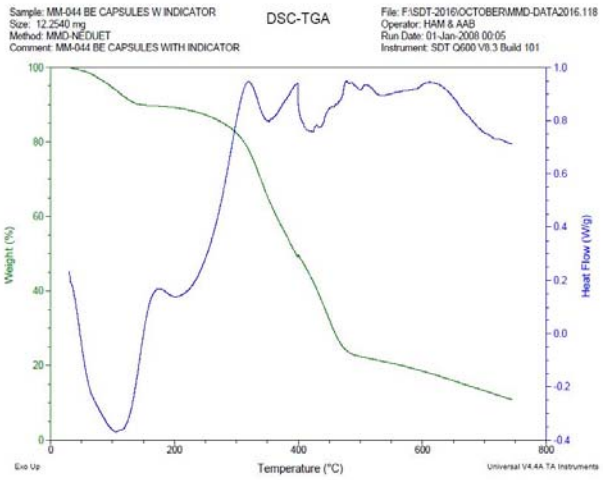

Figure 14. TGA graph of microcapsules with Indicator after UV exposure

Conclusion

The industrial world is on track to meet the target on reducing corrosion issues. We have successfully developed the effective smart coating that will surely help to deal with the corrosion issues. The microencapsulation was performed by interfacial polymerization to encapsulate phenolphthalein and β-lactamase as corrosion indicator and inhibitor respectively. A general formulation has been obtained for new emerging materials that can encapsulate by simply changing the core content of microcapsules. Our smart coating with microcapsules showed a visible color change when corrosion occurred underneath it, giving early detection as well as inhibit corrosion to some extent before indication.
The temperature, pH, mixing speed has a remarkable influence on the formation of microcapsules. The major degradation on TGA curve at 300-450°C showed the degradation of epoxy polymer makes it suitable to use in normal environments. The UV exposure slightly enhanced the thermal stability as it cured the uncured polymer. We can conclude from our results that the size of microcapsules is mixing speed dependent. The coating system should have the pH of around 7 after addition of microcapsules. Although there are still some technical challenges associated but the coating is still fulfilling the great promise for industrial application.

References

1. Wenyan Li, Jerry W. Buhrow, and Scott T. Jolley, Luz M. Calle, Joshua S. Hanna and James W. Rawlins, *MICROENCAPSULATION OF CORROSION INDICATORS FOR SMART COATINGS,* NTRS(NASA Technical Reports Server)
2. W. Li and L. M. Calle, "A Smart Coating for the Early Detection and Inhibition of Corrosion," Proceeding of the Smart Coatings 2007, p.191, Orlando, Florida, February 2007
3. W. Li and L. M. Calle, "Controlled Release Microcapsules for Smart Coatings," NACE Corrosion 2007, Paper 07228 (Nashville, TN, 2007).
4. Research Opportunities in Corrosion Science and Engineering, Committee on Research Opportunities in Corrosion Science and Engineering, National Research Council, S6, 2010.
5. M. G. Durrett, R. E. Johnson, and V. S. Agarwala, ICI, Intelligent corrosion indicator, and its use for the early detection of corrosion on aluminum alloy surfaces by florescence, Corrsoionl2000, Paper No. 00285
6. R. E. Johnson and V. S. Agarwala, Mater. Performance, 33, 25 (1994)
7. Microencapsulation Methods and Industrial Applications, 2nd edition, edited by Simon Benita, CRC Press Taylor & Francis Group, Marcel Dekker, New York, 2006.
8. D. E. Bryant and D. Greenfield, Prog. Org . Coatings 57, 416 (2006)
9. BP Pearman, LM Calle, X Zhang, W Li, JW Buhrow… - 2015 - ntrs.nasa.gov
10. W Li, JW Buhrow, LM Calle, M Gillis, M Blanton… - 2015 - ntrs.nasa.gov
11. Zhang and G.S. Frankel, Corrosion 55, 957 (1999)
12. MN Johnsey, W Li, JW Buhrow, LM Calle, BP Pearman… - 2015 - ntrs.nasa.gov
13. J Buhrow, W Li, S Jolley, LM Calle, B Pearman… - 2015 - ntrs.nasa.gov
14. W. L. Dunn, A. M. Yacout, "Corrosion Detection in Aircraft by X-ray Backscatter Methods," Applied Radiation and Isotopes 53, 4-5 (2000): p. 625.
15. M. Z. Silva, R Gouyon, and F. Lepoutre, "Hidden Corrosion Detection in Aircraft Aluminum Structures Using Laser Ultrasonics and Wavelet Transform Signal Analysis," Ultrasonics, 41, 4 (2003): p.301.
16. J.H. Ali, W. B. Wang, P. P. Ho, R R Alfano, "Detection of Corrosion Beneath a Paint Layer by Use of Spectral Polarization Optical Imaging," Optics Letters 25,17 (2000): p.1303.
17. V. Agarwala, S. Ahmad, "Corrosion Detection and Monitoring - A Review," Proceedings of Corrosion 2000, paper nO.271 (Houston, TX: NACE International, 2000).

18. J. Zhang and G. S. Frankel, "Corrosion-Sensing Behavior of an Acrylic-Based Coating System," Corrosion 55 (1999): p. 957.
19. RE. Johnson and V.S. Agarwala, Fluorescence Based Chemical Sensors for Corrosion Detection, Corrosion1997, paper no. 304 (Houston, TX: NACE International, 1997).
20. RE. Johnson and V.S. Agarwala, Using Fluorescent Compounds as Early Warning Detectors for Corrosion, Materials Performance, April 1994, pp.25-29.
21. G. S. Frankel, et aI., Corrosion-Sensing Composition and Method of Use, US patent application 20030068824.
22. Kumar and L.D. Stephenson, "Smart Coatings," 23rd Army Science Conference, Orlando, Florida, December 2002.
23. Augustyniak, J.Tsavalas, and W. Ming, "Early Detection of Steel Corrosion via "Turn-On" Fluorescence in Smart Epoxy Coatings," Applied Materials & Interfaces 1, 11 (2009): p. 2618.

Chitrosan and Graphene Oxide based Nano-Composite Hydrogel for the removal of heavy metal ions from industrial waste water

Sarah Faheem[1], Muhammad Sohail[1*] ,. Fayaz Hussain[1], Muhammad Maaz[1], Bilal Abbas[1]

Department of Materials Engineering, NED University of Engineering & Technology, Karachi, Pakistan, 75270
[*] Corresponding Author: msohailhanif@neduet.edu.pk

ABSTRACT

Chitosan is a natural polymer that has proved its uses in many research areas because of its wide range of properties. Its Adsorption properties can purify water by sticking metallic ions to its surface. Chitosan was extracted from the shrimp shell and its properties and existence differs with different type of shrimps obtained area wise. The Chitosan-Graphene Oxide Hydrogel was prepared by socializing Graphene Oxide sheets and Chitosan chains. The CS-GO nanocomposite hydrogel has a high adsorption capacity towards various contaminants, including heavy metal ions, as well as cationic and anionic dyes. The hydrogel is treated with different samples of wastewater from industries, as well as self-prepared sample of Copper Sulphate, Zinc Chloride, and Nickel Sulphate. The results were studied, and finally it was demonstrated that the CS-GO hydrogel can be used for the purification of wastewater via adsorption mechanism.

1. INTRODUCTION:

Sea food is consumed in every part of the world leaving tons of waste behind. Exo-skeleton, heads and in case of crabs and shrimps legs are dumped either in landfills or in sea after taking out the meat only for the consumption. Even with the property of biodegradability it can take months to degrade the whole mass and not to mention the smell that spreads with the decomposition.

Using this waste to produce Chitosan commercially can be the way to reduce waste and to use it for different purposes can make a positive impact. However Extraction yield and appearance is differs with the different type of shrimps and also the region those shrimps were captured on. Different Researchers from different areas reported different yields with the slight change in process.

Chitosan is a natural polymer that can be extracted from shrimp shells', crabs' and fishes' exo-skeleton. It is a linear aminopolysacchride of [1-4] linked N-acetyl glucosamine and glucoseamineunit. It is a hard white, hard, inelastic, and nitrogenous polysaccharide. Chitosan has a biodegradable nature, and also maintains non-toxicity and antimicrobial activities hence can be used in a lot of applications including genetics, food sciences, food packaging, antimicrobial coatings & Water treatment plants.

Due to the use of chemicals in its extraction, Extraction processes of Chitosan can be expensive and some of them also report less yields hence currently a lot of scientists and researchers are working for the economic and commercial extraction processes.

2. Experimental Details

Chemicals:

Shrimp Shells (obtained from local fish markets), Sodium Hydroxide, Hydrochloric Acid (35%), Potassium per Magnet, Oxalic Acid, Sulphuric Acid (99.998% pure), Potassium Per Magnet, Graphite Powder (99.998% pure), Hydrogen per Oxide (30%), Distilled Water, Ultrapure Water & Glacial Acetic Acid (100%).

Extraction of Chitosan:

Chitosan was extracted by the combination of processes. 20gm Shrimp Shells and were cleaned and washed with tap water, dried and then refrigerated (fig 1) and were soaked in 4% NaOH solution for 20hrs (fig 2).

Figure 1 shells after 24hr treatment with NaOH

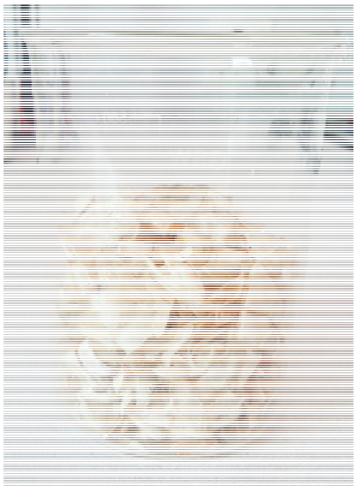

Figure 2 the cleaned dried shrimp shells

NaOH was drained and washed under running water and then then was soaked it in 4% HCl Solution for 10hrs (fig 3). Acid solution was drained off and sample was washed until its pH dropped to neutral with Distilled water. Sample was then again treated with NaOH but with 2% Concentration for 24hrs and washed till neutrality with running tap water and then Distilled water and the again soaked in 1% HCl for 12hrs and washed with Distilled water (fig 4). Treatment with NaOH deprotienize the shrimp shell and HCl is supposed to demineralize the sample.

Figure 3 the sample in HCl after 12hrs

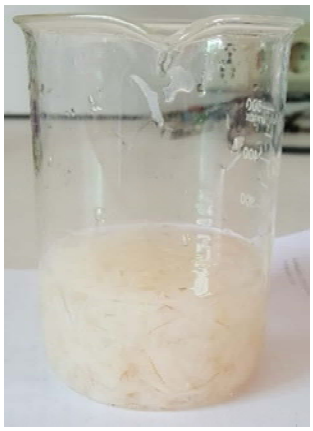

Figure 4 sample deprotienization & Demineralization

Figure 5 sample after being treated by $KMnO_4$

Deprotienized and Demineralized samples were then decolorized with 1% $KMnO_4$ for 1hr (fig 5). Sample was then treated by it 1% Oxalic Acid for 3hrs. Sample was then washed with ample amount of water. Decolorized Sample is called Chitin and is Brilliant white in color (fig 6).

Figure 6 Chitin obtained

Figure 7 Chitosan soaked in NaOH

Obtained sample was then soaked in 65% NaOH Solution for around 70hrs. Extracted Chitosan was 8.05gm in weight and was brilliant white in color with translucent appearance when dried (fig 8) & (fig 7).

Figure 8 the dried Chitosan Sample

Synthesis of Graphene Oxide:

46 ml of 98% H_2SO_4, 2gms of natural graphite powder, 1gms Sodium Nitrate were mixed in 500 ml conical flask and was magnetically stirred for 30 minutes in ice bath. 6gms of $KMnO_4$ was added with beaker still in ice bath, Beaker was then put on hot plate and after temperature is given oxidation reaction start and heated it for 30 minutes under 35˚C. 100ml of distilled water was added during this half hour under constant stirring. Solution was additionally stirred for 45min at 98˚C. Sample solution was mixed with the solution of 20ml of 30% H_2O_2 and 280ml of Distilled water and stir for 5 minutes and solution changed its color to luminous Yellow with obtained Graphene Oxide settled down. Sample was then centrifuged and washed with 5% HCl Solution and then with distilled water 5 times each. Sample was then mixed with acetone to drain it out in dishes and dried at ambient temperature.

Synthesis of Chitosan graphene Oxide Nano Composite:

0.5gms of Graphene Oxide powder was dispersed in 100ml of ultrapure Water through ultrasonification for 30 minutes. 3ml of glacial Acetic Acid was poured slowly into the graphene oxide dispersion under constant stirring and 8gms of Chitosan was added into the mixture under constant stirring at room temperature. Solution was the stirred at room temperature for 30 minutes

Figure 9the synthesized CS-GO Hydrogel

and at 95°C for 30 minutes. Gel obtained marked 75ml mark in the beaker (fig 9).

Yield Calculation:

Weight of extracted Chitosan and synthesized Hydrogel was measured and yield was measured.

Water Testing:

A Solution of known concentration of a heavy metal compound was made that shows its presence with a color. 3000ppm of Copper Sulphate, Zinc Chloride & Nickel Chloride Solutions and an untreated textile industrial waste water sample with unknown concentration of dye was taken separately. 3ml CS-GO Hydrogel was poured in every solution sample and within 4-5 seconds Water showed visible clarity and removal of Blue, Translucent White and Celadon color from Copper Sulphate, Zinc Chloride & Nickel Chloride Solutions respectively and Violet Color from Industrial Waste.

Characterization:

pH Measurement: pH of both graphene Oxide Solution and Chitosan were measured by pH meter. pH of tested samples was measured after filtering out the gel from Water.

FTIR Analysis: Functional groups present in Chitosan are amino/acetamido groups as well as both primary and secondary hydroxyl group. These Functional groups were detected by FTIR. As CS-GO Hydrogel is a polymer based composite hence its characterization was also done through FTIR and it's supposed to contain the peak of both Graphene oxide and Chitosan. Samples were studied between 4000 m-1 to 400 m-1.

XRD Analysis: CS-GO Hydrogel sample was characterized by XRD analysis by finding out its characteristic peak.

UV-Vis Spectroscopy: Graphene Oxide was tested between 200nm to 800nm.

Purified and unpurified water samples of CuSO4 and Dye were taken for the UV-Vis spectroscopy and were tested between 290nm to 550nm.

3. Results & Discussions:

Yield was supposed to be 46% but was calculated to be 40%.pH was measured to be 7.5 after washing it with running water and then with distilled water. Peak at 1632.8, 1437.9, 1380.0, 1320.8, 1158.5, 1111.9 m^{-1} shown in figure x are obtained as they are usually in the standard chitosan corresponding to some of the functional groups and bond stretching.

UV-Vis spectroscopy of graphene oxide shows the characteristic peak of GO at 212nm.CS-GO Hydrogel was made by following instructions in the reference article but ratios were changed in which chitosan and graphene oxide were combined together. Chitosan was set for 8 wt. % and graphene oxide was set for 0.5wt. %. Figure xii shows that there is a sharp peak present at 3447.2m^{-1} because of GO, -OH, -COOH, C-OH and N-H stretching. Peak at 1648.4 m^{-1} corresponds to some of the functional groups in Chitosan and other peaks in the range of 1112.0 m^{-1} to 1160.1 m^{-1} corresponds to the Alcoholic group present. Peak at 1746 m^{-1} represents C=O stretching and at 1648.4m^{-1} represents carbonyl group Stretching

.

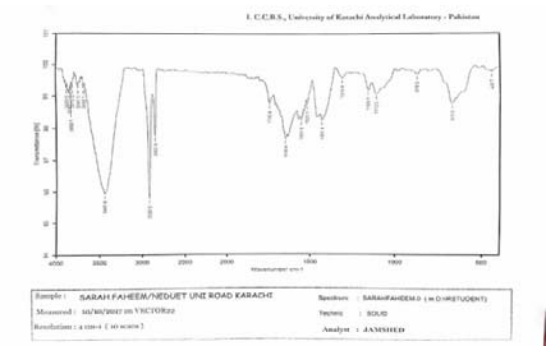

Figure 10 IR spectrum of CS-GO Hydrogel

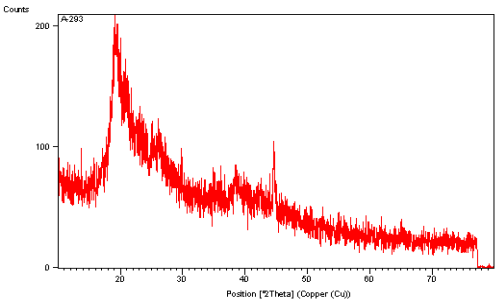

Figure 11 the XRD of CS-GO Hydrogel

In figure 9 peak close to 20° shows a chitosan peak indicating crosslinking wasn't done right

between chitosan and graphene oxide. Decrease in intensity can be clearly analyzed through the graph. Sample absorption is decreased by a huge margin as water was purified and colored heavy metal ions and dye particles were removed.

4. CONCLUSIONS

The chitosan was synthesized from locally available bio waste. The grapheme oxide was synthesized separately. A gel is formed from Chitosan (CS) and Graphene Oxide (GO). The FTIR results showed the characteristic peaks of chitosan while UV-Vis spectroscopy of graphene oxide also confirmed the formation of grapheme. The Hydrogel obtained from CS-GO was also characterized through XRD and FTIR spectroscopy. The hydrogel was tested to purify the industrial waste water containing Industrial Dye, Copper Sulphate, Zinc Chloride and Nickel Sulphate and it was shown that all the colored solutions were either became transparent or their transparency was increased due to the treatment with CS-GO hydrogel. Further analysis could also be performed to remove more heavy metal ions from the water.

5. ACKNOWLEDGEMENT

The authors are thankful to the Department of Materials Engineering, NED University of Engineering and Technology for providing the necessary support for conducting this project

REFERENCES

[1] Flornica Alca Ahing* & Newati Wid, Transactions on Science and Technology 2016, Extraction and Characterization of Chitosan from Shrimp Shell Waste in Sabah, Faculty of Science and Natural Resources, Universiti Malaysia Sabah, Jalan UMS, 88400, Kota Kinabalu, Sabah, MALAYSIA. June,2016.

[2] Bhattarai, N.; Gunn, J.; Zhang, M. Q. Elsevier, Chitosan-based hydrogels for controlled, localized drug delivery. Adv. Drug Delivery Rev. 2010, 62 (1), 83−99. 2010

[3] Chih-Ling Huang, Chin-Ho Chuang, Yu-Lung Lo, Evaluation of anisotropic chitosan hydrogels using analytical Mueller matrix method and scanned laser pico-projector, In Carbohydrate Polymers, Volume 96, Issue 2, 2013

[4] Guanru Chang, Yan Chen, Yanjie Li, Shikuo Li, Fangzhi Huang, Yuhua Shen, Anjian Xie, Self-healable hydrogel on tumor cell as drug delivery system for localized and effective therapy, In Carbohydrate Polymers, Volume 122, 2015

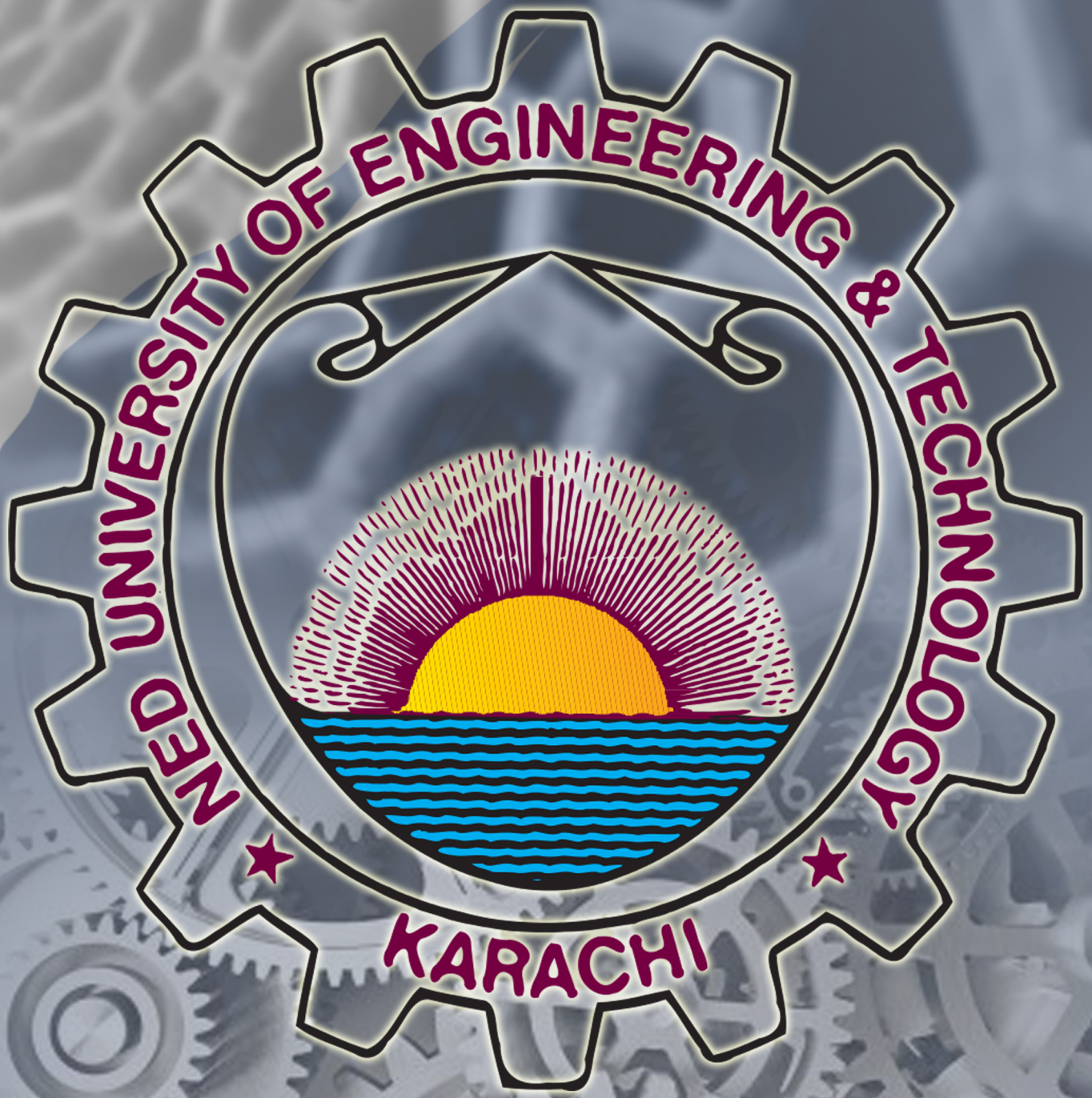

CONTACT

FACULTY OF CHEMICAL AND PROCESS ENGINEERING

NED UNIVERSITY OF ENGINEERING & TECHNOLOGY

KARACHI PAKISTAN

PHONE: (+92-21)99261261 EXT 2577,2286,2404

FAX: (+92-21)99261255

Email: ampe@neduet.edu.pk

www.nedampe.com